

Development of the $\overline{\text{PANDA}}$ MVD Trapezoidal Sensors and a Feasibility Study of the $\overline{p}p \rightarrow \overline{\Lambda}_c \Lambda_c$ Reconstruction

Dissertation zur Erlangung
des Grades eines Doktors der Naturwissenschaften
in der Fakultät für Physik und Astronomie
der Ruhr-Universität Bochum

von
Dariusch Deermann
aus
Siegburg

Bochum 2015

Versicherung gemäß §7 Abs. 2 Nr. 6 PromO 2011

Hiermit versichere ich, dass ich meine Dissertation selbstständig und ohne unerlaubte fremde Hilfen angefertigt und verfasst habe und keine anderen als die angegebenen Hilfsmittel und Hilfen benutzt habe. Meine Dissertation habe ich in dieser oder ähnlicher Form noch bei keiner anderen Fakultät der Ruhr-Universität Bochum oder bei einer anderen Hochschule eingereicht.

1. Gutachter: Prof. James Ritman, Ph.D.

2. Gutachter: Prof. Dr. Ulrich Wiedner

Tag der Disputation: 02.07.2015

Contents

1	Motivation	1
2	Experimental Facility	3
2.1	FAIR	3
2.1.1	Scientific Program	4
2.1.2	Accelerator Facility	5
2.2	The PANDA Experiment	6
2.2.1	Physics Program	7
2.2.2	Detector	13
2.2.3	Data AcQuisition (DAQ)	19
2.2.4	Simulation Framework	19
3	Micro Vertex Detector	23
3.1	Overview	23
3.2	Requirements	24
3.2.1	Hit Rates	24
3.2.2	Radiation Hardness	24
3.2.3	Radiation Length	24
3.2.4	Spatial Resolution	25
3.3	Silicon Sensors	25
3.3.1	Sensing Ionising Radiation with a p-n Junction	26
3.3.2	Strip Sensors	28
3.3.3	Hybrid Pixel Sensors	30
3.4	Readout	31
3.5	Support Structure and Cooling	32
3.5.1	Support Structure	32
3.5.2	Cooling	34
4	Strip Sensor Characterisation	35
4.1	Trapezoidal Strip Sensor Prototype	35
4.2	Measurement Setup	36
4.3	Characterisation with a Probestation	39
4.4	Characterisation with a Dedicated Test Board	42
4.5	Conclusion	46

5	Spatial Resolution Determination	49
5.1	Methods of Position Reconstruction	49
5.2	Implementation of the η Method into PandaRoot	50
5.2.1	Simulation of the η Distribution	50
5.2.2	Adjustments to the η Distribution	52
5.2.3	Hole in the inter-strip distribution of two-strip clusters	56
5.3	Resolution Results	57
5.4	Conclusion	59
6	Test Measurements of a Strip Prototype	61
6.1	Test Beam Setup	61
6.1.1	Beam Conditions	61
6.1.2	Mechanical Setup	61
6.1.3	Readout Chain	61
6.2	Analysis of Test Beam Data	66
6.2.1	Data Selection	67
6.2.2	Vertical Pattern in n-side Signal	73
6.2.3	Energy Resolution	75
6.2.4	Noise Analysis	77
6.2.5	Signal to Noise Ratio	80
6.2.6	HV Scan	82
6.2.7	Determination of η Distributions	83
6.3	Conclusion	86
7	$\bar{p}p \rightarrow \bar{\Lambda}_c \Lambda_c$ Simulation with PandaRoot	87
7.1	Event Generation	87
7.2	Simulation and Reconstruction of the Decay Channel	89
7.2.1	Detector Setup	91
7.2.2	Track Reconstruction	91
7.2.3	Λ and $\bar{\Lambda}$ Reconstruction	94
7.2.4	Λ_c and $\bar{\Lambda}_c$ Reconstruction	99
7.2.5	Exclusive $\bar{\Lambda}_c \Lambda_c$ Reconstruction	103
7.2.6	$\bar{p}p \rightarrow \bar{\Lambda}_c \Lambda_c$ Cross Section	107
7.2.7	Non-resonant Background	107
7.3	Conclusion	110
8	Conclusion	111
A	Sensor Characterisation	113
A.1	Software	113
A.2	Measurements of Prototype Sensors	115
B	Results from December Test Beam	119
C	Momentum Resolution of the Final State Particles	125
D	$\bar{p}p \rightarrow \bar{\Lambda}_c \Lambda_c$ Cross Section Predictions	129

CONTENTS	vii
Bibliography	131
Acronyms	137
List of Figures	139
Acknowledgements	147

Motivation

1

Nothing Lasts... But Nothing Is Lost

Shpongile

Throughout history, the origin and nature of matter has always found big interest. From macroscopic objects such as rocks down to molecules, atoms, and quarks, smaller and smaller structures have been found.

Today, the smallest known particles are quarks and leptons. Both are sorted into 3 groups or *families*. Those particles together with the gauge bosons form the [Standard Model \(SM\)](#) of particle physics. For each of those particles an antiparticle of the same mass but opposite charge-like quantum numbers can be found.

The current state of the [SM](#) combines the knowledge about the weak, strong, and electromagnetic interaction. But it is still far from being a complete theory. It has a lot of free parameters which cannot be accessed by theory but must be measured. And some phenomena cannot be quantitatively explained by it. An example is the mass of hadrons, which has only a minor contribution from the interaction of the valence quarks with the Higgs field. In order to fill the gaps in understanding of hadron physics and [Quantum ChromoDynamics \(QCD\)](#) in general, different hadrons have to be produced and studied in experiments.

Accelerators are good tools to investigate a great number of differently flavoured hadrons in their ground states as well as excited states. One facility under construction is the [Facility for Antiproton and Ion Research \(FAIR\)](#), which is being build at the [Helmholtz Centre for Heavy Ion Research \(GSI\)](#) in Darmstadt.

The goal of [FAIR](#) is to provide particle beams of high precision as well as high intensity. At [FAIR](#), antiproton beams with momenta from 1.5 GeV/c to 15 GeV/c will be produced and stored in the [High Energy Storage Ring \(HESR\)](#). The antiproton beams will then be used to create hadrons in an annihilation process that can be studied with the [antiProton ANnihilation at Darmstadt \(PANDA\)](#) detector which will be located inside [HESR](#). The experimental setup is described in detail in Chapter 2.

In this thesis, a prototype of trapezoidal silicon strip sensors, a sensor type that will be used in the [PANDA Micro Vertex Detector \(MVD\)](#), is characterised (Chapter 4) and tested (Chapter 6). Furthermore, a method for the improvement of the spatial resolution of two-strip signals (η method) has been investigated and implemented to the PandaRoot simulation framework (Chapter 5). The η method depends on the measurement of the charge distribution between two neighbouring strips. A method to correct the measured charge distribution of a sensor for noise and threshold effects has been developed and is presented in Chapter 6.

Finally, the reaction $\bar{p}p \rightarrow \bar{\Lambda}_c \Lambda_c$, which requires the [MVD](#), is simulated and one of its decay channels ($\Lambda_c \rightarrow \Lambda \pi^+$) is analysed in a feasibility study (Chapter 7).

Experimental Facility

2

2.1 FAIR

FAIR is an accelerator facility which is specifically designed to produce phase space cooled beams of precise energy and high intensity with antiprotons as well as ions. As seen in Figure 2.1 a linear accelerator called UNILAC is already in existence at the **GSI** and will be used for ion injection to the further **FAIR** accelerators. Another linear accelerator, called the p-LINAC, is under construction and will be used as an injector for protons into the further **FAIR** accelerators.

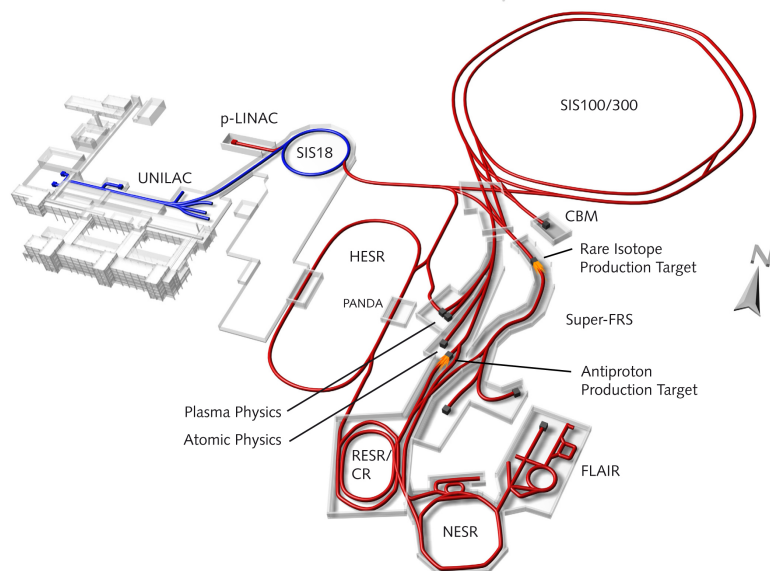


Figure 2.1: Overview on **FAIR** and the location of the different experiments. The existing part of the facility is shown in blue and the new parts which are currently under construction in red [1].

2.1.1 Scientific Program

A variety of experiments is planned to be set up at [FAIR](#). These experiments are divided into four scientific fields, namely:

- [Atomic, Plasma Physics and Applications \(APPA\)](#)
- [Compressed Baryonic Matter \(CBM\)](#)
- [NUclear STructure, Astrophysics and Reactions \(NUSTAR\)](#)
- [PANDA](#)

APPA While hot plasmas in low pressure environments have already been studied and understood quite well, this is not the case for cold plasmas in high pressure environments as they exist e.g. inside large planets. The [APPA](#) program includes five projects [2]:

- **BIOMAT**: The **BI**ology and **MA**terial Science collaboration works on biophysical experiments and experiments for ion-induced changes in solids.
- **SPARC**: A goal of the **S**tored **P**articles **A**tomics **P**hysics **R**esearch **C**ollaboration is to research extreme atomic conditions by using heavy, highly charged ions at relativistic velocities.
- **FLAIR**: The **F**acility for **L**ow-energy **A**ntiproton and heavy **I**on **R**esearch aims at testing [Charge Parity Time \(CPT\)](#) violation and [Quantum ElectroDynamics \(QED\)](#), studying the gravitational behaviour of antimatter, antiprotons as hadronic probes, and medical applications such as tumour therapy.
- **HEDgeHOB**: The **H**igh **E**nergy **D**ensity matter **g**enerated by **H**heavy **i**On **B**eams collaboration plans to investigate high energy density samples under very low temperature and density gradients.
- **WDM**: The **W**DM collaboration will investigate **W**arm **D**ense **M**atter which is a state where on one hand the density is too high for current plasma models to give a good description and on the other hand the energy density is too high for condensed matter models.

CBM The [CBM](#) experiment will use high energy nucleus-on-nucleus collisions to study the [QCD](#) phase diagram for high baryon densities and their phase transition to a quark-gluon plasma. The goals of [CBM](#) include the search for chiral phase transitions and the deconfinement, and the investigation of the equation-of-state of nuclear matter at high densities [3].

NUSTAR The [NUSTAR](#) collaboration is working on several experiments, which will make use of the [Superconducting FRagment Separator \(Super-FRS\)](#) facility. Rare isotopes and exotic nuclei with up to relativistic energies can be separated in-flight within several hundreds of nano seconds by the [Super-FRS](#). Thus, even short-lived nuclei can be studied [4].

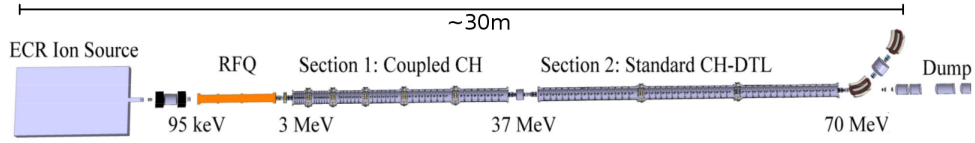


Figure 2.2: Schematic view on the p-LINAC [5].

$\bar{\text{P}}\text{ANDA}$ In the $\bar{\text{P}}\text{ANDA}$ experiment, antiproton annihilations will be used to produce hadrons of all quantum numbers. This also enhances the production of glueballs or exotic hadrons with more than three valence quarks, if they exist. A detailed description of the scientific program for $\bar{\text{P}}\text{ANDA}$ is presented in Chapter 2.2.1.

2.1.2 Accelerator Facility

p-LINAC and SIS 18 The existing linear accelerator UNILAC is well suited for heavy ion acceleration but less so for proton acceleration. As some of the experiments at FAIR are planned to use a proton beam, a new linear accelerator for protons needs to be built. This accelerator is the p-LINAC, which is going to accelerate protons up to kinetic energies of 70 MeV, and its schematic can be seen in Figure 2.2.

After this first acceleration step the protons are injected into the SIS 18, which is a synchrotron of 216 m circumference and has a maximum magnetic rigidity of 18 T m. Within SIS 18, the proton beam energy is increased to up to 4.5 GeV before being extracted and injected into the SIS 100/300.

SIS 100/300 The SIS 100/300 is a superconducting double-synchrotron with a circumference of 1,084 m and a maximum magnetic rigidity of 100 T m or 300 T m. Its purpose is to further increase the proton or ion beam energies delivered by SIS 18. Some experiments at FAIR like CBM or several atom and plasma physics experiments will use the particle beams from SIS 100/300 directly. Experiments like $\bar{\text{P}}\text{ANDA}$, that require an antiproton beam, will make indirect use of the beam from SIS 100/300.

For the antiproton production, the proton beam in SIS 100 will be accelerated to a kinetic energy of 29 GeV with an intensity of $4 \cdot 10^{13}$ protons per cycle and extracted during 25 ns. This proton beam will then be used for antiproton production via the reaction $pA \rightarrow \bar{p}X$. Here, A represents the antiproton production target and X represents all possible outgoing particles in the final state.

Collector Ring (CR) and Recycled Experimental Storage Ring (RESR) The antiprotons are then collected in the CR, which has a circumference of 212 m, and get a first stochastic cooling. After this pre-cooling step the antiprotons are transferred with a kinetic energy of 3 GeV to the RESR, which has a circumference of 245 m and surrounds the CR. The RESR accumulates the antiprotons and stores them until they can be injected to HESR [6].

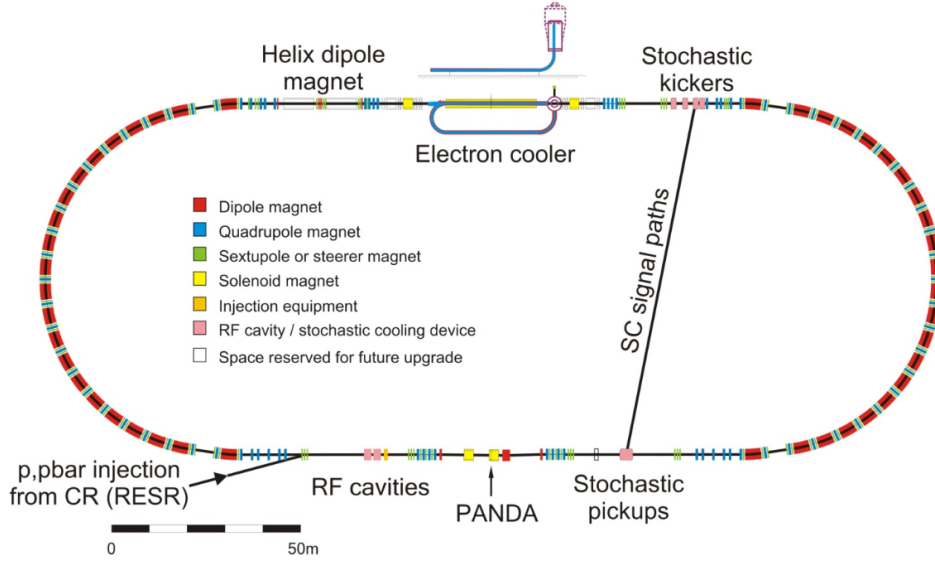


Figure 2.3: Overview on [HESR](#), with position of [PANDA](#), electron cooler, stochastic pickups and kickers, and \bar{p} -injection. Picture taken from [8].

HESR [PANDA](#) will be located inside the [HESR](#) as shown in the overview of [HESR](#) in Figure 2.3 and will contain a proton target to study antiproton annihilation products. [PANDA](#) will also support alternative targets with heavier nuclei. The [HESR](#) has a circumference of 575 m and will be used to further accelerate or decelerate the injected antiproton beam within a beam momentum range of 1.5 GeV/c up to 15 GeV/c.

A **High Resolution mode (HR)** is foreseen in the beam momentum range of 1.5 GeV/c to 9 GeV/c and shall provide a luminosity of $\mathcal{L} = 2 \cdot 10^{31} \text{ cm}^{-2} \text{ s}^{-1}$, with a beam momentum spread of $\frac{\sigma_p}{p} \sim 3 \times 10^{-5}$. Another mode is the **High Luminosity mode (HL)** which is planned to produce an approximately 10 times higher luminosity at the cost of an increase in the momentum spread of the beam. The **HL** is planned for operation in the full [HESR](#) antiproton momentum range from 1.5 GeV/c up to 15 GeV/c [7].

2.2 The [PANDA](#) Experiment

Figure 2.4 shows a [CAD](#) representation of the full [PANDA](#) detector with a height of ~ 5 m and a length of ~ 13 m. [PANDA](#) will be one of the main experiments at [FAIR](#) and is planned as a fixed target experiment. It will explore $\bar{p}p$ and $\bar{p}A$ reactions in the charm mass region with intense, phase space cooled beams with momenta between 1.5 and 15 GeV/c. Due to momentum conservation, the decay products in a fixed target experiment have a preference to small polar angles, especially at high beam momenta. To cope with the expected difference in particle track rates for different polar angles, the detector is planned to consist of two sections, the **Target Spectrometer (TS)** and the **Forward Spectrometer (FS)**.

Due to the broad physics program with many very different decay channels, it is not possible to define easy global trigger properties. Therefore, [PANDA](#) will be operated without a first-level

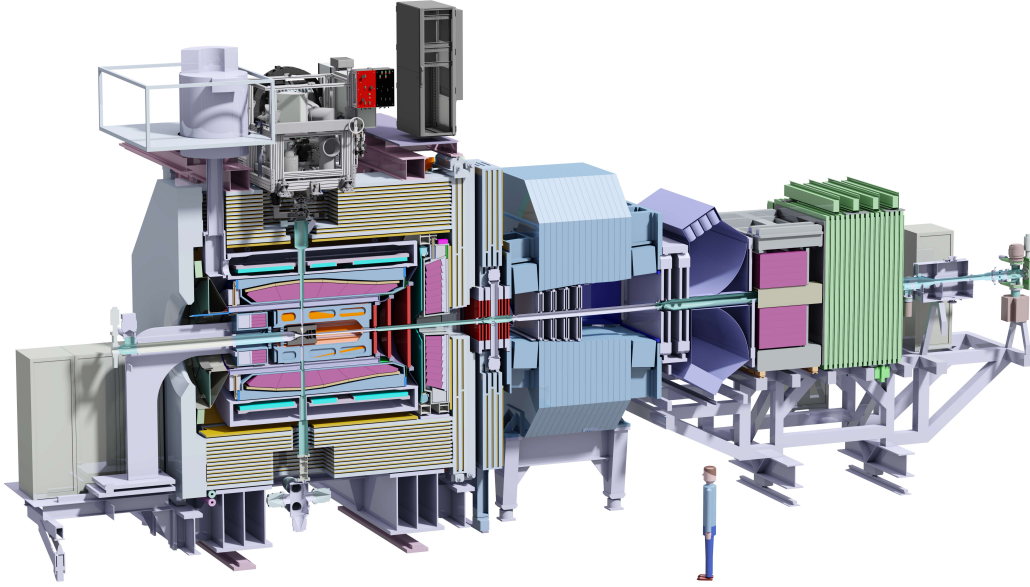


Figure 2.4: CAD representation of the $\overline{\text{PANDA}}$ detector [9].

hardware trigger. This means that every subdetector has to be self-triggering and provide a time stamp for the event building, where a software trigger should decide whether an event matches the criteria of an interesting decay channel or not.

2.2.1 Physics Program

The $\overline{\text{PANDA}}$ experiment will study the strong interaction and the structure of hadrons. The strong interaction can be well described for processes with high momentum transfer with perturbative quantum chromodynamics. But in the transition region between the non-perturbative and the perturbative regime, a theoretical framework that results in plausible predictions is still missing. The available centre of mass energy region for $\overline{\text{PANDA}}$ ($2.25 \text{ GeV} < \sqrt{s} < 5.47 \text{ GeV}$) is well suited for this purpose, as can be seen in Figure 2.5. A summary of the main research goals of $\overline{\text{PANDA}}$ is given below.

Charmonium Spectroscopy Charmonium describes a class of particles that are composed of a charm quark and antiquark ($c\bar{c}$). Such systems have no charge or flavour and therefore are referred to as *hidden charm*. The nature of charmonium states is similar to that of positronium states, as both are particle-antiparticle systems. Thus, it seems natural to compare these systems. Figure 2.6 shows this comparison, and indeed they show similar relative distances of their energy levels, despite the huge difference in their energy scales.

Electron positron colliders have been used intensely to study charmonium states. But, since e^+e^- annihilation requires a virtual photon to first order, only those charmonium states with the same quantum numbers as a photon ($J^{PC} = 1^{--}$) can be produced directly. Those states

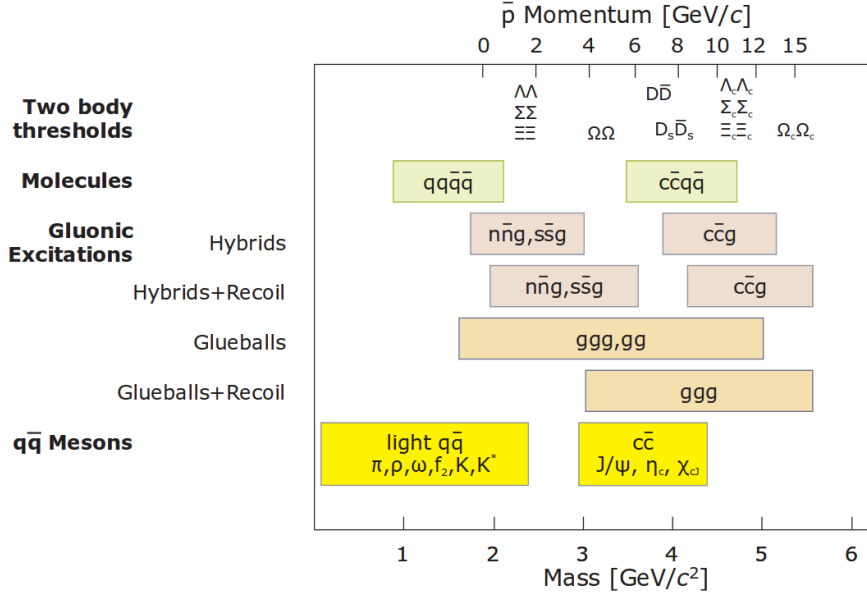


Figure 2.5: This figure shows the accessible mass range of hadrons with antiproton beams in HESR. The necessary antiproton momenta for charmonium spectroscopy, potential charmed hybrids and glueballs, as well as the production of D meson pairs and the production of Σ baryon pairs for hypernuclear studies are indicated in the upper part. Figure taken from [10].

POSITRONIUM		CHARMONIUM		RATIO
5×10^{-6} MeV	2^1S_0	650 MeV	2^1S_0	1.3×10^{-8}
4.1×10^{-11} MeV	$\begin{cases} 1^3P_2 \\ 1^3P_1 \\ 1^3P_0 \end{cases}$	140 MeV	$\begin{cases} 1^3P_2 \\ 1^3P_1 \\ 1^3P_0 \end{cases}$	3.4×10^{12}
8.4×10^{-10} MeV	1^3S_1	115 MeV	1^3S_1	1.4×10^{11}
	1^1S_0		1^1S_0	
$m_e = 0.5$ MeV, $\alpha_{em} = 1/137$		$m_c = 1500$ MeV, $\alpha_S = 1/3$		
FS, HFS $\alpha_{em}^4 m_e = 1.4 \times 10^{-9}$		$\alpha_S^4 m_c = 18.5$		1.3×10^{10}

Figure 2.6: A comparison of positronium and charmonium spectra together with a ratio of their energy scales. Figure taken from [11].

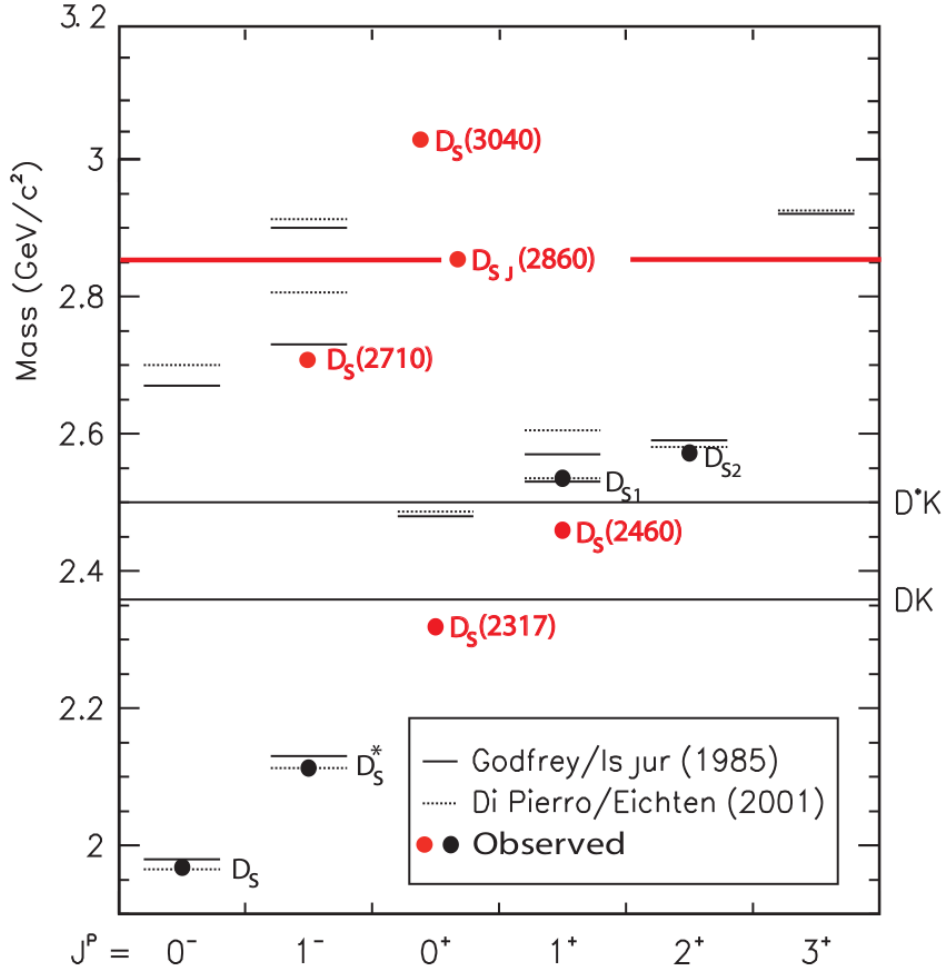


Figure 2.8: The spectrum of D_s mesons with predictions shown as solid lines [12] and dotted lines [15]. The points represent experimental data for old measured states (black) and newly discovered states (red). Figure taken from [13].

order to support or reject those theories. With $\bar{p}p$ annihilations, $\bar{\text{PANDA}}$ provides an environment where all charmonium states can be produced directly. This, in combination with the highly phase space cooled beam of HESR can bring a vast improvement for the resolution of mass and width.

Open Charm Spectroscopy Mesons which contain one light quark or antiquark ($u, d, s, \bar{u}, \bar{d}, \bar{s}$) and one charm quark or antiquark (c, \bar{c}) are called D or D_s mesons. They have a charm flavour quantum number $\neq 0$ and are therefore referred to as *open charm*. Such a system of a light and a heavy particle is quite similar to the hydrogen atom with its light electron and the heavy nucleus. While the study of the hydrogen atom contributed to the understanding of the electromagnetic force, the open charm particles may give hints to a better understanding of the strong interaction. Figure 2.8 shows measured and predicted states of the D_s meson spectrum.

The spectrum of the D and D_s mesons has not yet been studied with high precision. Several newly found D_s states, which do not fit into the classical picture of heavy-light systems, are good candidates for four quark states. In order to reveal their true nature, a precise measurement of their width is essential.

For example, up to now the $D_{s0}^*(2317)$ is only known to have an upper limit of several MeV on its width. A simulation study has shown that $\overline{\text{PANDA}}$ can achieve a resolution better than 0.1 MeV for that state [16].

Heavy Baryons For baryons formed from light quarks, quark model calculations are already not perfect at explaining the excitation spectrum. For heavy baryons on the other hand, quark model predictions do not reproduce at all what has been observed until now [17].

One goal of $\overline{\text{PANDA}}$ is to perform measurements in the multi-strange and charmed baryon region in order to determine with high statistics and precision the baryon excitation spectrum. As the lifetime of heavy baryons is rather short, a high precision tracking detector setup as it is planned for $\overline{\text{PANDA}}$ can help to find and identify the decay products of heavy baryons.

Search for Gluonic Excitations The existence of hadrons that contain gluons as main components that contribute to the overall quantum numbers is one of the big question marks in hadron physics and the search for such particles is a big challenge.

There are two basic types of gluonic excitations. Particles from the first type are called *glueballs* and form their quantum numbers with gluons and no additional valence quarks. Particles from the other type are *hybrids*, which are particles with valence quarks plus additional excited gluons that contribute to the particles' quantum numbers. Figure 2.9 shows a predicted mass spectrum of glueballs. These predictions were made by lattice QCD calculations and most of the predicted masses lay within the energy range of $\overline{\text{PANDA}}$. Furthermore, $\overline{p}p$ annihilations provide a good environment to produce gluonic excitations.

Hadrons in Nuclei When hadrons are produced in a medium their spectral properties can be modified. This modification can be explained by a partial restoration of the chiral symmetry [19]. With heavy nuclear targets this effect can be studied. Most experiments regarding this topic have focussed on the light quark regime, with the high energy \overline{p} beam, $\overline{\text{PANDA}}$ can cover the light quark regime as well as the charm regime.

$\overline{\text{PANDA}}$ can study the charmonium-nucleon interaction, e.g. the J/Ψ dissociation in a medium by measuring the cross section [20]. Furthermore, $\overline{\text{PANDA}}$ may help in the search for bound systems of D mesons with two nucleons, which have been predicted [21].

Nucleon Structure Exclusive $\overline{p}p$ annihilation into two photons can be described by the theoretical framework of *Generalised Parton Distributions (GPD)* [22]. Count rates of several thousand $\gamma\gamma$ events per month have been predicted for a luminosity of $2 \cdot 10^{32} \text{ cm}^{-2} \text{ s}^{-1}$ and an energy of $\sqrt{s} = 3.2 \text{ GeV}/c^2$. One goal of $\overline{\text{PANDA}}$ is to measure the crossed-channel Compton scattering as well as the exclusive annihilation processes with a scalar meson pair, a vector meson pair, or a lepton pair in the final state. Comparing the differential cross sections of these decay processes can lead to a better understanding of the annihilation process.

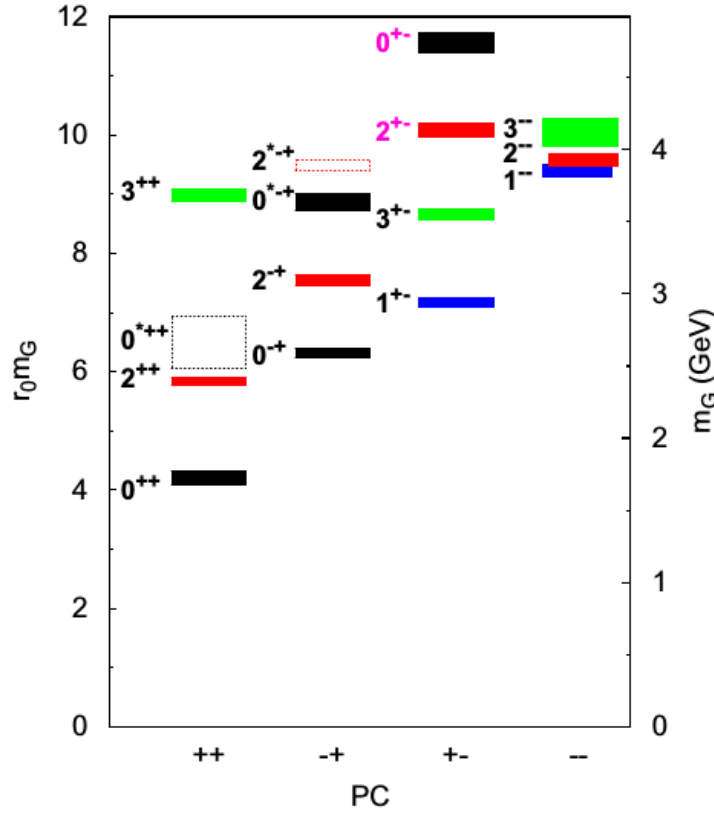


Figure 2.9: The spectrum of glueball masses predicted by lattice QCD calculations [18].

Hypernuclei A hyperon is a baryon with strangeness. Hypernuclei are atomic nuclei that contain at least one hyperon [23]. $\overline{\text{PANDA}}$ aims to produce hyperons in large quantities, which can be absorbed by the nuclei of a secondary target to form hypernuclei. Hyperons decay via the weak interaction and therefore have a relatively long lifetime, which allows them to become bound by the nucleus.

Since hyperons contain strangeness, they are not restricted by the Pauli principle within a nucleus that otherwise only contains nucleons without strangeness. Therefore, a hyperon in a nucleus can occupy any excited nuclear state and are good probes for nuclear structure investigations.

At $\overline{\text{PANDA}}$, it is planned to produce double Λ hypernuclei. This will be done by a multi-step reaction. The $\bar{p}p \rightarrow \Xi^- \bar{\Xi}^+$ reaction is used to generate Ξ^- . The Ξ^- are then captured in a nucleus of a secondary target in which the Ξ^- hyperons decay via $p\Xi^- \rightarrow \Lambda\Lambda$. In order to do this, the MVD must be replaced by an active secondary target.

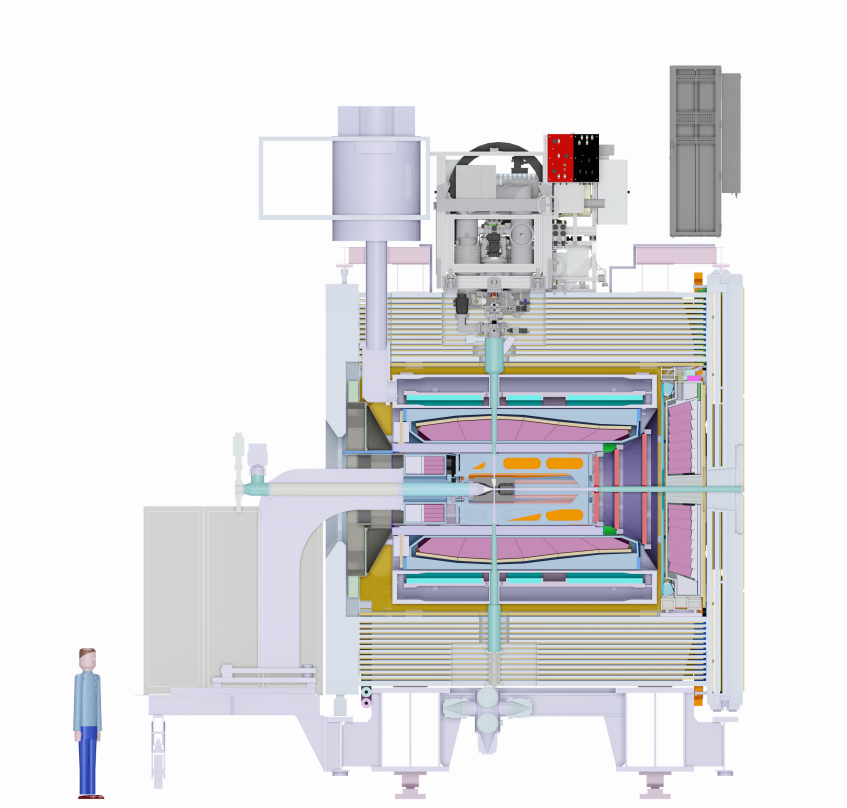


Figure 2.10: CAD rendering of the target spectrometer. Figure taken from [9].

2.2.2 Detector

The whole detector is about 5 m tall and 13 m long. These 13 m are divided into an approximately 5 m long part for the **TS** and an approximately 8 m long part for the **FS**. While the **TS** surrounds the target area and aims at covering almost 4π of the solid angle, the **FS** aims at precise tracking of the particles with small polar angles. An overview of the technology and purpose of the different subdetector systems of the **TS** and the **FS** are presented in the following sections.

Target Spectrometer The **TS** contains the target as well as a number of tracking and **Particle IDentification (PID)** systems. A schematic view on the **TS** can be seen in Figure 2.10. It covers polar angles $\geq 5^\circ$ in the vertical and $\geq 10^\circ$ in the horizontal direction.

Target There are two target systems in development for $\bar{\text{PANDA}}$. A cluster-jet target is produced by releasing pre-cooled gas through a de Laval nozzle. When passing the convergent-divergent de Laval nozzle, the gas is cooled down adiabatically and forms a supersonic stream. Due to the cooling process the gas atoms can form clusters with a size in the nm scale. Since the clusters are of such small dimension a homogeneous distribution of target material within the stream can be assumed.

	cluster target	pellet target
effective target thickness	1×10^{15} atoms/cm ²	5×10^{15} atoms/cm ²
target thickness adjustable	yes (0-max)	yes (by reduction of pellet rate)
volume density distribution	homogeneous	granular
size transversal to \bar{p} beam	2 – 3 mm	≤ 3 mm
size longitudinal to \bar{p} beam	15 mm	≤ 3 mm
target particle size	nm scale	20 μ m
mean vertical particle distance	$\leq 10 \mu$ m	2 – 20 mm
target material	H ₂ , D ₂	H ₂ , D ₂ , N ₂ , Ar
	heavier gases optional	heavier gases optional

Table 2.1: Summary of the cluster-jet and pellet target properties from already achieved results [24].

Another option is a pellet target which uses a triple-point chamber with a mixture of liquid and gaseous target material. Periodic excitations are induced on a nozzle by a piezoelectric transducer. This results in an oscillating jet that forms drops along its beam in regular distances. On their way to the vacuum, where the interaction point is, the drops cool down due to surface evaporation and form frozen pellets. The pellets have a diameter of about 20 μ m and can be tracked by an optical tracking system [24].

As the pellet density is very high, many reactions will occur within the same pellet. For those annihilation events the tracked pellet position can be used to enhance the primary vertex resolution. Table 2.1 summarises the properties of the two target options.

MVD The **MVD** is made of silicon pixel and strip sensors and is the innermost tracking system directly surrounding the interaction point. It aims at a high resolution for primary and secondary vertices. A detailed description of the **MVD** is presented in Chapter 3.

Straw Tube Tracker (STT) After the **MVD**, the **STT** follows as the second tracking device in the **TS**. Figure 2.11 shows a schematic of the **STT** and its profile. The **STT** is arranged in a cylindrical volume that surrounds the **MVD** and is the main tracking device in the **TS**. The device is 1.5 m long and has a diameter of about 82 cm. It contains a total of 4,636 individual straw tubes and has the task to reconstruct the helical trajectories of charged particles in the solenoidal magnetic field.

The specific energy loss dE/dx measured with the **STT** can be used for **PID**, especially for kaon, proton, and pion separation in the momentum region below ~ 1 GeV/c. The green tubes in Figure 2.11(b) represent tubes that are aligned parallel to the beam axis, while the red and blue tubes are skewed by $\pm 2.9^\circ$. The purpose of the skewed tubes is to improve the resolution along the beam direction.

Each straw has an inner diameter of 1 cm and a 27 μ m thick aluminium coated Mylar foil as the cathode. A 20 μ m diameter gold-plated tungsten-rhenium wire is used as the anode in the centre of the tube. The tubes are filled with a mixture of 90% Ar and 10% CO₂ at an overpressure of 1 bar, which results in a wire tension of 50 g. Because of the overpressure, the straws are self supporting so that the size and weight of mechanical support structures can be

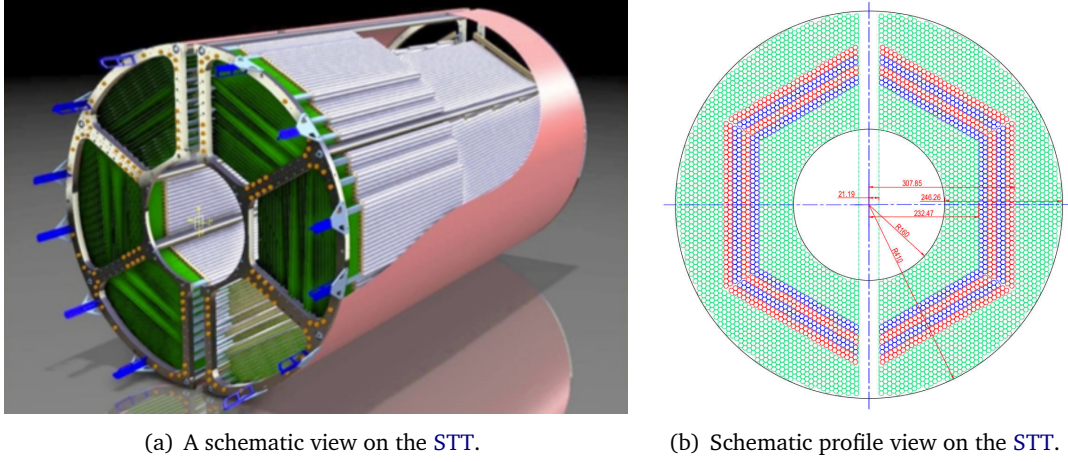


Figure 2.11: Schematic of the STT and its profile. Figures taken from [25].

minimised. The drift time of the electrons inside the tube can be used to determine the radial distance of the ionising tracks to the anode wire, this results in a resolution $\sim 150\mu\text{m}$ in the xy -plane. In combination with the skewed tubes, a resolution of $\leq 3\text{ mm}$ for single track points in beam direction can be achieved [25].

Gas Electron Multipliers (GEM) To cover the polar angle range below 22° , which is not totally covered by the STT, three GEM stations will be placed at 1.1 m, 1.4 m, and 1.9 m downstream from the interaction point [25]. The GEM stations have diameters of 0.9 m, 1.12 m, and 1.48 m, respectively [26]. All three GEM stations have an inner radius of 2.5 cm. Figure 2.12 shows the components of a single GEM station.

The main components of a GEM station are a gas drift volume and GEM foils. A GEM foil consists of a thin Kapton layer ($\sim 50\mu\text{m}$), with a copper coating on both sides. A voltage is applied between the two copper layers, and the foil is covered with a pattern of holes with a diameter and separation of several $10\mu\text{m}$. Due to this geometry, a high electric field in the order of 50 kV/cm is reached inside the holes, so that electrons will be accelerated when passing a hole and multiply in an avalanche. These electrons can then be detected as hit points.

Detector for Internally Reflected Cherenkov Light (DIRC) When a charged particle passes a medium of refractive index n with a velocity $v \geq \frac{c}{n}$, it emits Cherenkov light in a cone. The opening angle of the cone depends on v as follows:

$$\cos(\Theta_C) = \frac{1}{\beta n}$$

This circumstance is used in the DIRC in order to calculate $\beta = \frac{v}{c}$ of the particle tracks by measuring Θ_C . This information will help to calculate the particle's mass and can therefore be used for PID. \bar{P} ANDA will have two DIRCs. A barrel shaped DIRC between the Time-Of-Flight (TOF) detector and the electromagnetic calorimeters surrounding the STT will cover the polar angle range from 22° to 140° , and a disc DIRC in forward directions covering the polar angle range from 5° to 22° in vertical directions and from 10° to 22° in horizontal directions [27].

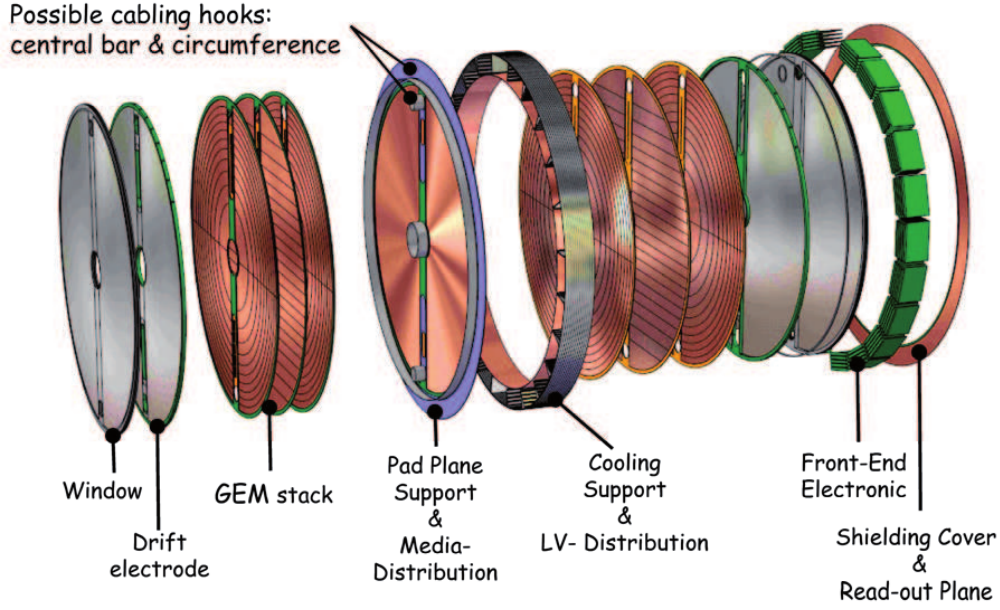


Figure 2.12: Schematic of the components inside a GEM station. Figure taken from [26].

The medium in the DIRCs is an artificially fused quartz with a refractive index of $n = 1.47$, which has a Cherenkov light threshold for kaons at a momentum of $p_K = 460 \text{ MeV}/c$ [10]. The Cherenkov light is internally reflected, thereby preserving Θ_C , and finally the light is projected on solid state photosensors.

Time-of-Flight Detector A scintillator tile barrel will be placed just outside the barrel DIRC volume, and will be used for the PID of slow particles emitted at large polar angles. This detector will consist of 5,760 scintillator tiles, each with a size of $28.5 \times 28.5 \text{ mm}^2$. All tiles will be read out individually by two silicon photomultipliers per tile. It will provide a fast signal with a time resolution of about 100 ps.

Besides PID, the precise timing information can also be used as a time stamp for tracks to help the event building process. Additionally, the time information with a good spatial resolution can be used as input for online pattern recognition [28].

Electro-Magnetic Calorimeters (EMC) The EMC will cover almost 4π solid angle with a barrel part as well as forward and backward endcaps. Its main purpose is the energy measurement of the particle tracks. This can be used for the PID of neutral particles, but it can also supplement the PID from the DIRC and TOF to help distinguishing pions from electrons and kaons. The barrel part is by far the largest part with 11,360 crystals, followed by the forward endcap with 3,600 crystals, and finally the backward endcap with 592 crystals. A schematic overview of the EMC is presented in Figure 2.13. All crystals face towards the interaction point and have a length of 20 cm, which corresponds to 22 radiation lengths.

The chosen scintillating material is PbWO_4 (PWO), because of its high radiation hardness and a fast response time which are both important features especially for the forward endcap

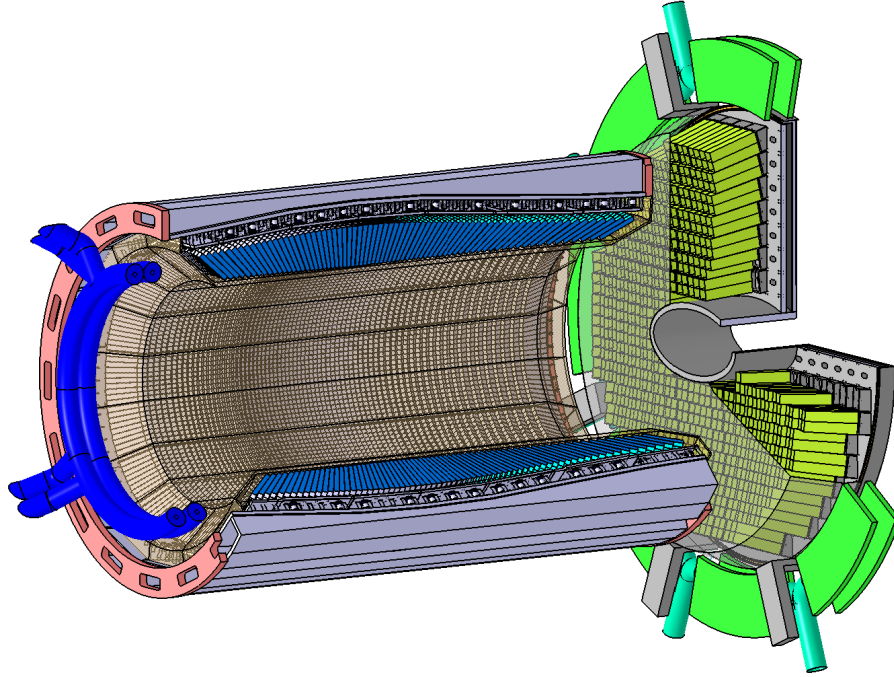


Figure 2.13: Schematic view on the EMC. Figure taken from [29].

due to the high luminosity provided at $\bar{\text{PANDA}}$. Furthermore, it has low energy thresholds, and good energy and spatial resolution. In order to achieve a good light yield, the crystals will be operated at a temperature of $T = -25^\circ\text{C}$ which increases the yield by a factor of 4 compared to operation at room temperature [29].

In the barrel part, the backward endcap, and the outer 80% of the forward endcap, two **Large Area Avalanche PhotoDiodes (LAAPD)** per crystal have been chosen for the read out. These are very compact and fulfil all requirements for the read out at the expected rates of $\leq 100\text{ kHz}$. For the inner 20% of the EMC forward endcap, rates of up to 500 kHz are foreseen, which require a faster and radiation hard read out system, therefore **Vacuum Photo-TeTrodes (VPTT)** have been chosen for the read out in this region [30].

Muon Detectors In order to make muons distinguishable from other charged tracks a muon system is implemented at $\bar{\text{PANDA}}$. The muon detectors are **Mini Drift Tubes (MDT)** which are the most external detectors at $\bar{\text{PANDA}}$. They are arranged in thirteen alternating layers with the return yoke of the solenoid magnet in the TS barrel part and in alternating layers with iron plates behind the EMC forward endcap. Each iron layer is 3 cm thick and has the purpose of filtering out hadrons, therefore the tracks measured by the MDTs are purely muon tracks. Each 3 cm layer of MDT has a resolution of $\sim 1\text{ cm}$ which is sufficient to match the muon track to its corresponding track from the tracking system [31]. A schematic overview is given in Figure 2.14.

Solenoid Magnet The requirements for the $\bar{\text{PANDA}}$ solenoid magnet are to produce a homogeneous magnetic field of 2 T pointed along the beam axis, while keeping that volume empty for

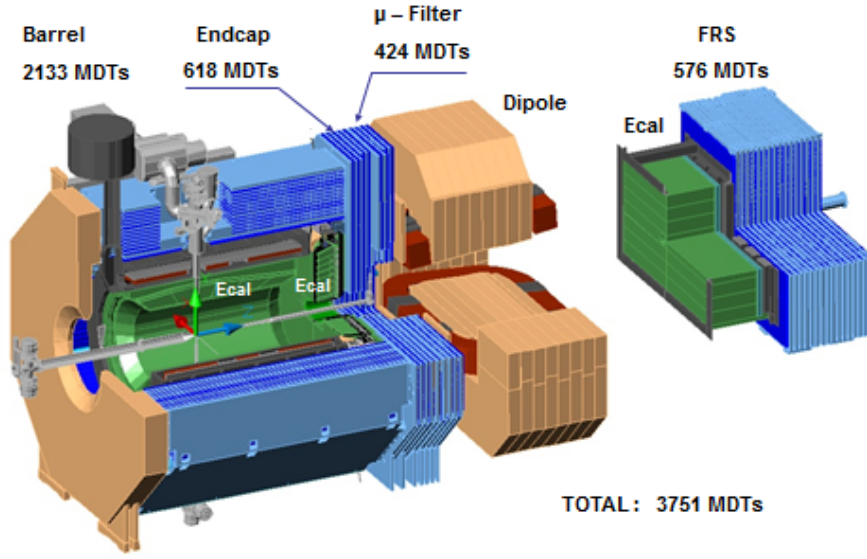


Figure 2.14: Schematic view on $\overline{\text{PANDA}}$ with the muon system. Figure taken from [31].

the tracking and PID systems. This will be realised by a superconducting solenoid magnet with a Rutherford cable carrying 5 kA. The field homogeneity will reach $\leq 2\%$ within the volume of the STT. The magnet will have a total length of 4.9 m with an outer radius of 2.3 m and a weight of 300 t [32].

Forward Spectrometer Tracks with polar angles smaller than 10° in the horizontal direction and smaller than 5° in the vertical direction will be covered by the FS.

Dipole Magnet The FS lies outside of the solenoidal magnetic field and uses a dipole magnet. Due to the different magnetic field orientations, charged tracks are bent in the horizontal plane by the FS dipole. The opening of the magnet will be about $1 \text{ m} \times 3 \text{ m}$ and will have a length of 2.5 m. A bending power of up to 2 T m will be provided.

Forward Tracking System (FTS) The FTS will consist of six tracking stations. Two before the magnet, two within the magnet and two behind the magnet. Each station will contain four double layers of straw tubes of which two will be oriented vertically and the other two double layers will be rotated by $\pm 5^\circ$ with respect to the vertical straw tubes [33]. The straw tubes will have a diameter of 10 mm and will be filled with a mixture of 90 % Ar and 10 % CO_2 at an overpressure of 1 bar, just like the straw tubes of the STT.

Ring Imaging Cherenkov detector (RICH) The RICH will measure the Cherenkov light cone directly without internal reflection. The RICH will have two radiators of different refractive indices, silica aerogel ($n = 1.0304$) and C_4F_{10} gas ($n = 1.00137$). A lightweight mirror will

focus the Cherenkov light on an array of photo-tubes placed outside the active volume [28]. The **RICH** will provide $\pi/K/p$ separation for momenta from 2 to 15 GeV/c.

Forward TOF In forward directions a **TOF** system is planned as a wall of scintillator bars set up 7 m downstream from the interaction point. A similar setup will be placed inside the dipole magnet gap to detect slow particles that are not able to leave the dipole magnet. A time resolution in the order of 50 ps is planned to be achieved for the forward **TOF** system, which will allow π/K separation up to momenta of 2.8 GeV/c and K/p separation up to momenta of 4.7 GeV/c [28].

Forward EMC In the **FS** a sampling calorimeter covering 4.6 m^2 with 54×28 cells of a shashlyk type design is planned to be installed. Each module has a cross section of $5.5 \text{ cm} \times 5.5 \text{ cm}$ and contains 380 double layers of $275 \mu\text{m}$ thick lead absorbers and 1.5 mm thick plastic scintillator tiles, this adds up to 19.6 radiation lengths. Optical fibres are used to transport the scintillation light to photomultipliers. The **FS EMC** was designed to achieve a low detection threshold so that photons with an energy below 100 MeV can be detected [34].

2.2.3 DAQ

As $\bar{\text{PANDA}}$ will run without a global trigger, every subdetector sends its data together with a time stamp in a continuous data stream. The total raw data rate of all the subdetectors will reach about 200 GB/s. In order to handle this amount of data, compute nodes will combine the information from the different subdetectors to form track candidates and rebuild the event. After the event building process, it is possible to select events of defined criteria, which may contain interesting data for a research channel. Only those promising events are then forwarded to a data farm for further analysis and storage. In this way the continuous data stream of $\sim 200 \text{ GB/s}$ from the subdetectors will be reduced by a factor 1,000.

2.2.4 Simulation Framework

The simulation of events in $\bar{\text{PANDA}}$ is realised with the PandaRoot simulation framework. PandaRoot is part of the FairRoot project which is a common software framework for the future **FAIR** experiments [35]. It is based on ROOT [36] and Virtual MonteCarlo with Geant3 and Geant4 [37]. PandaRoot contains all the detector geometry and material information for the active sensors as well as for the mechanical holding structures, cooling systems, and magnets. It offers several ways for the initial event generation. A short list of options is presented here:

- **FairBoxGenerator**

The FairBoxGenerator generates a user defined number of particles from a user defined particle type with a momentum and angle range defined by the user. With this generator the effect of precisely known initial situations can be studied.

- **PndDpmDirect**

With the PndDpmDirect event generator $\bar{p}p$ reactions are simulated. This is done accordingly to the **Dual Parton Model (DPM)** with a total of 773 predefined reactions of which one is chosen with a probability according to their relative cross sections. Furthermore,

the PndDpmDirect event generator can be set to create only elastic reactions, only inelastic reactions, or both.

- **PndEvtGenDirect**

The PndEvtGenDirect event generator needs a decay file as input which defines all the reactions which should be created. In this way reactions with a small cross section can be generated and can be forced into a predefined decay chain. All non-stable particles whose decay chain is defined by the user's decay file, are generated to decay according to a common decay file which includes the decay branches and cross sections as given from the [Particle Data Group \(PDG\)](#) [38].

- **Pythia**

PandaRoot is also able to use the Pythia [39] event generator, which is specialised for high energy reactions.

- **Ultrarelativistic Quantum Molecular Dynamics (UrQMD)**

As [PANDA](#) also plans to study reactions with heavy ions as target instead of protons, the [UrQMD](#) event generator can be used to create events for such targets [40].

The generated events are the input for the further simulation process. This process with PandaRoot is split into five parts:

Simulation The first part is called *simulation* and it takes care of propagating the generated particles through all detector material and magnetic fields. This means that all energy loss and scattering processes from particles in detector material and deflection from the magnetic field is processed in this step. Furthermore, all secondary particles which may be created from the initial particles by interaction with detector material are being generated and propagated by the simulation step. Also, for all crossings of a track with an active sensor a [Monte Carlo point \(MCPoint\)](#) is created, which contains the entry and exit locations of the track through the sensor as well as the deposited energy.

Digitisation The *digitisation* step creates *digi* points for each [MCPoints](#). A single [MCPoint](#) can result in multiple digis as each sensor channel creates its individual digi. A [MCPoint](#) may also result in no digi, as for each sensor the corresponding detection thresholds are considered. Additionally, if the sensor is capable of measuring the deposited energy this value is smeared accordingly to the sensors estimated noise and saved within the digi. Furthermore, the digis should be as close as possible to real detector data, so that PandaRoot can be used as an analysis tool for real data by exchanging the digitisation output with real detector output.

Reconstruction The next step is called *reconstruction* and arranges digis together that belong to the same track. At first, digis from neighbouring sensor channels are grouped together to form hit clusters. Then each cluster is considered as a track point, and pattern recognition algorithms are used to determine which points belong to the same track.

Particle Identification In the [PID](#) step, the momentum, energy, charge, and mass for each found track is determined. Then, a particle type is assigned to each found track by taking the particle type which has the highest probability to create the reconstructed values.

Analysis The last step is the *analysis* of the detected tracks in the event. In this thesis the analysis of the simulated reaction $\bar{p}p \rightarrow \bar{\Lambda}_c \Lambda_c \rightarrow \bar{\Lambda} \pi^- \Lambda \pi^+$ is presented in Chapter [7](#).

Micro Vertex Detector

3

3.1 Overview

The **MVD** is the innermost tracking detector of **PANDA** and its purpose is to measure the first part of tracks from charged particles with high precision to determine their origin and to improve the momentum resolution. It is composed of silicon sensors in four barrel and six disc layers. A schematic overview of the **MVD** is given in Figure 3.1.

The outer radius of the **MVD** is limited to 15 cm due to the surrounding detector. Its extent along the beam axis is about ± 23 cm with respect to the interaction point. The inner two barrel layers will use silicon pixel sensors while the outer two barrel layers will use double sided

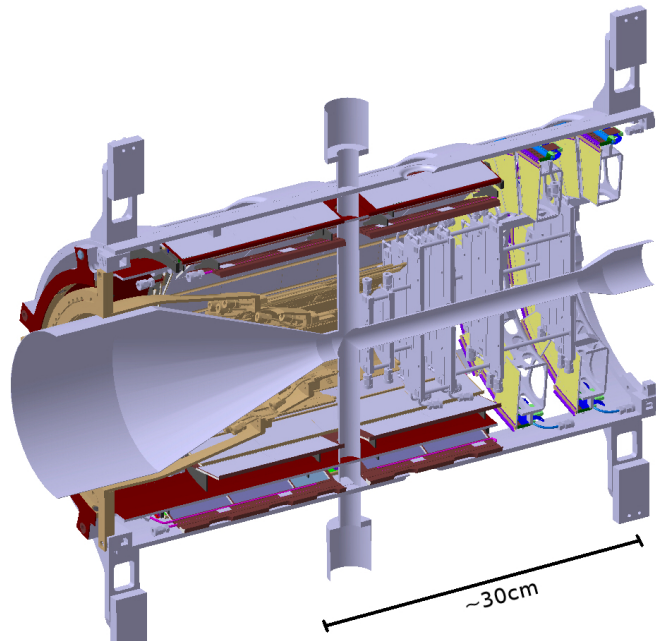


Figure 3.1: An overview on the **MVD**, which shows its mechanical holding structure and sensor layers [41].

silicon strip sensors. All the six disc structures will contain pixel sensors in their centre, and the last two discs at $z = 16$ cm and 23 cm will additionally contain trapezoidal silicon strip sensors that are arranged in a double ring structure around the pixel discs. The first two pixel discs have a diameter of 75 mm while the other four pixel discs are larger with a diameter of 150 mm. The two strip rings will extend the diameter of the last two discs to a diameter of ~ 27 cm [28].

3.2 Requirements

3.2.1 Hit Rates

Pixel sensors have a number of signal channels proportional to their area, while the number of signal channels for strip sensors is proportional to their active perimeter. This results in a higher number of readout channels which usually also leads to a higher material budget for pixel sensors compared to strip sensors, but also provides the advantage of unambiguity of hits when several hits are measured at the same time. This is because there is always exactly one pixel cluster per hit, while a strip sensor generates k^2 possible combinations of p- and n-side clusters when k hits are measured at the same time. Wrong combinations lead to hit positions that did not really occur and are therefore called *ghost hits*.

Additionally, each channel has a specific deadtime after a hit, during which a following hit cannot be measured individually. Each strip in a strip sensor covers a larger fraction of the area of the whole sensor than a pixel in a pixel sensor, therefore the deadtime of a strip also affects a larger area than the deadtime of a pixel. Furthermore, pixel sensors are usually more radiation tolerant than strip sensors.

Due to these reasons, pixel sensors have to be used in the inner parts of the [MVD](#) where the highest hit rates per area are expected, while the outer two barrel layers and the outer ring of the fifth and sixth forward discs can be equipped with strip sensors which have a lower total material budget. In order to separate individual events, the [MVD](#)'s time resolution should be in the order of 10 ns [28].

3.2.2 Radiation Hardness

As the innermost detector, the [MVD](#) has to withstand a high radiation dose and should remain functional over the planned life time of [PANDA](#). During the first ten years of [PANDA](#) operation, a radiation dose of $10^{14} \times 1$ MeV neutron equivalent particles per square centimetre is expected at the [MVD](#) position [42]. Furthermore, an ionising radiation dose of 100 kGray is expected [43].

3.2.3 Radiation Length

As the [MVD](#) is the innermost detector, it is the first detector that influences the particle tracks by multiple scattering, energy loss, and photon conversion. In order to allow good resolution results from all the subdetectors that follow the [MVD](#), the material budget of the [MVD](#) has to be kept as small as possible. To achieve a material budget of less than 10 % of one radiation length, thinned sensors are developed, and low density materials are used for the mechanical support and cooling structures [28].

3.2.4 Spatial Resolution

As the name **MVD** implies, the **MVD**'s main task is to determine the vertex of particles. This is needed to identify short lived particles that decay with small distances to the primary interaction point. For example, the mesons $D^0(c\tau = 123\text{ }\mu\text{m})$ or $D^\pm(c\tau = 312\text{ }\mu\text{m})$ have a decay distance to the primary interaction point in the sub-millimetre range for the typical laboratory momentum of $P/M = \beta\gamma \approx 2$. More details on the achievable spatial resolution of the strip sensors will follow in Chapter 5.

3.3 Silicon Sensors

Semi-conductor detectors are ideal for vertex reconstruction. Compared to gaseous detectors, silicon detectors are of high density so that a larger energy loss per unit distance is reached for charged particles passing the detector. Therefore, it is possible to build very thin silicon detectors. The energy loss of charged particles in a semi-conductor mainly happens by inelastic scattering with shell electrons. Additionally, Rutherford scattering, Bremsstrahlung, and Cherenkov light emission can happen. The average energy loss per unit distance for a particle is well described by the Bethe-Bloch formula [44]:

$$-\frac{dE}{dx} = 2\pi N_A r_e^2 m_e c^2 \rho \frac{Z}{A} \frac{z^2}{\beta^2} \left[\ln\left(\frac{2m_e \gamma^2 v^2 W_{max}}{I^2}\right) - 2\beta^2 - \delta - 2\frac{C}{Z} \right] \quad (3.1)$$

with:

N_A	:	Avogadro number
r_e	:	classic electron radius = $2,817 \cdot 10^{-15}\text{ m}$
m_e	:	electron mass
I	:	mean excitation potential
Z	:	mean nuclei charge of the absorber material
A	:	relative atomic mass of the absorber material
ρ	:	mean density of the absorber material
z	:	charge of the passing particle
c	:	speed of light
β	:	speed of the particle normalised to c , $\beta = \frac{v}{c}$
γ	:	$\gamma = \frac{1}{\sqrt{1-\beta^2}}$
δ	:	density correction
C	:	shell correction
W_{max}	:	maximum energy transition for a single collision

The energy loss per unit distance for a particle plotted against the particle's momentum shows a characteristic curve for each particle type and can be used for **PID**. Figure 3.2 shows a section of the Bethe-Bloch function for different absorber materials.

Nevertheless, these characteristic curves only represent the mean values of a Landau distributed statistical process. For thin sensors with only a few interactions between the particle

and the sensor the statistical fluctuation can be big. Figure 3.3 shows the energy loss distribution for pions with a momentum of 500 MeV/c in silicon. Especially in the higher momentum region where the difference in $\frac{dE}{dx}$ for different particle types is low, the semi-conductors energy loss measurement may only give an additional information that can be used for PID, but cannot provide sufficient identification by itself. Additionally, for PID the total momentum of the particles must also be known. This can be determined by the shape of the reconstructed tracks inside the known magnetic field.

3.3.1 Sensing Ionising Radiation with a p-n Junction

In order to suppress the number of intrinsic charge carriers compared to the number of charge carriers created by an ionising particle, a p-n junction in reverse bias mode is used to create a depletion zone. Silicon belongs to the forth main group of elements, it has four electrons in its outer electron shell that are able to bond with electrons from neighbouring atoms. In a pure silicon crystal this means that each silicon atom binds with four adjacent atoms. Doping the silicon means to implement atoms from other elements into the otherwise pure silicon crystal.

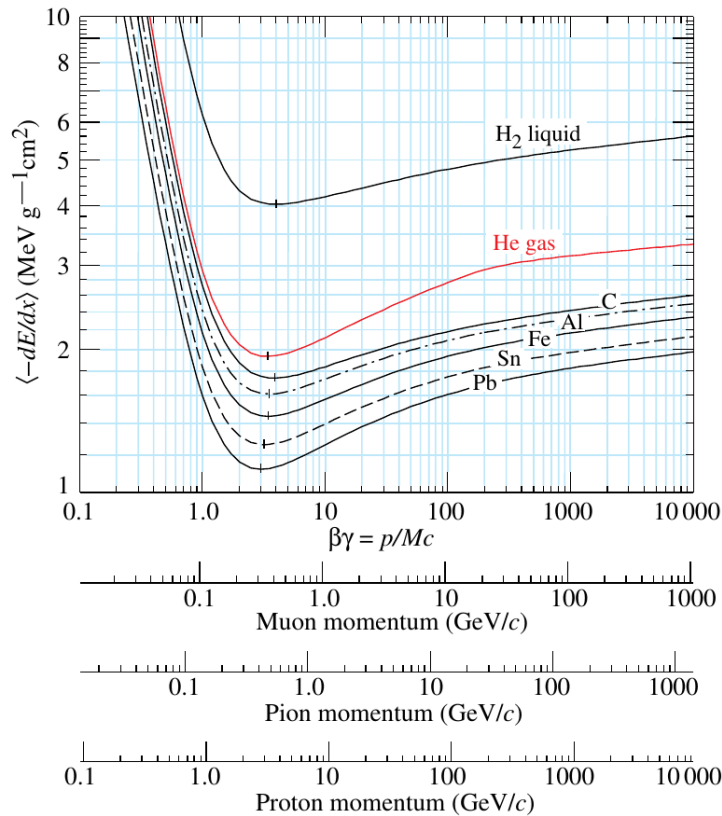


Figure 3.2: Mean specific energy loss per unit distance for different absorber materials, the momentum scale on the x-axis is scaled by the particle mass so that a combined measurement of p and $\frac{dE}{dx}$ can be used for PID. Figure taken from [38].

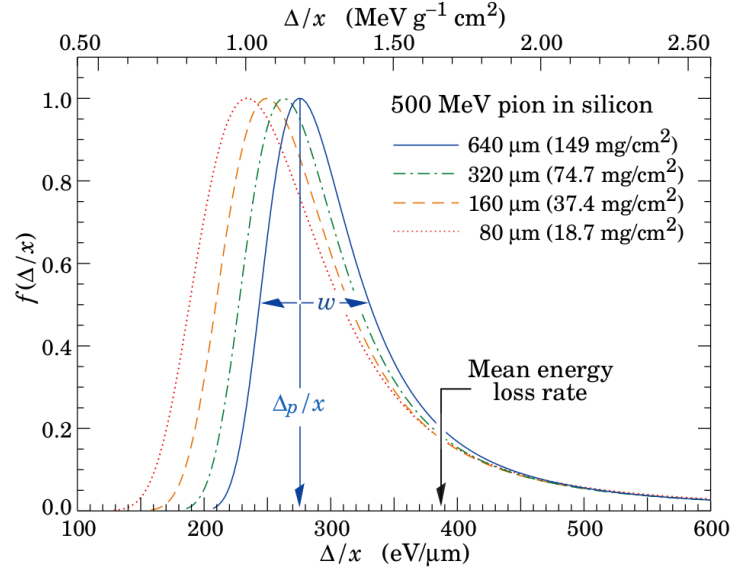


Figure 3.3: Distribution of the energy loss per unit distance for pions with a momentum of 500 MeV/c in silicon, calculated for several thicknesses of the absorber. Figure taken from [38].

p-doping Adding elements of the third main group into the silicon crystal is called p-doping. Since elements of the third group have only 3 electrons in the outer shell, the implemented atom will form only three complete bonds with neighbouring silicon atoms, and another bond with just the one electron from a silicon atom. That bond still can accept one more electron, this can happen by pulling in an electron from a neighbouring bond. In this way the missing electron site can move through the crystal and p-doping adds one free positive charge carrier to the crystal.

n-doping If an atom of the fifth main group is implemented into the crystal it brings an additional fifth electron in its outer shell which is unable to bond with a neighbouring silicon atom. This implementation of an atom of the fifth main group is called n-doping and adds with the electron one negative charge carrier to the crystal.

When p-doped and n-doped volumes are brought in contact, some of the free electrons from the n-doped volume will drift into the p-doped volume, while some of the electron holes from the p-doped volume can drift into the n-doped volume. As free electrons and electron holes drift inside the same volume, they can combine and get locally trapped. A consequence of this transfer of electrons and electron holes from the n-doped volume into the p-doped volume and vice versa is that the p-doped volume becomes slightly negatively charged and the n-doped volume becomes slightly positively charged. This non-homogeneous charge distribution generates an electric field \vec{E} that points from the n-doped volume to the p-doped volume and hinders more electrons and electron holes to make the same transition.

If an ionising particle passes the crystal, electrons and electron holes are created in the crystal. Without an electric field present, the electron-hole pairs would just recombine and leave the crystal with no signal. But within the depleted zone of the p-n junction, the electric

field separates the electrons from the electron holes, and brings the electrons to the n-side of the crystal and the holes to the p-side of the crystal.

The separated charges can then flow back through the readout electronics. This generates a measurable current and the information that an ionising particle has passed the sensor. In order to maximise this effect, a reverse bias voltage should be added to the crystal, so that the depletion zone fills the whole silicon volume and therefore all the created electron-hole pairs can be separated from each other. Additionally, the size of the depletion zone should be maximised in order to suppress the number of free charge carriers which otherwise would contribute to the noise.

3.3.2 Strip Sensors

Besides the basic information that an ionising particle has passed the sensor, the spatial information where it has passed the sensor is an essential parameter that should be measured. To achieve this, the sensors contain more than a single p-n junction. In particular the p- and n-doped areas are divided into individually contactable segments. Typical components for silicon strip sensors, which have been considered for the [PANDA MVD](#), are listed here:

- **substrate**

The bulk substrate of the sensor is n^- -doped silicon.

- **p-side strips**

On the p-side of the sensor there are p^+ -doped strips. On the surface over the strips is a resistive silicon oxide layer, which is covered by metallic strips on top of the strips. Each strip has a pad close to the sensor's edge, which provides an AC coupled connection to the front end electronics. Another DC coupled contact pad is placed at the beginning of each strip, these pads are separated from the metallic strip layer and contact the strip implants directly without a resistive silicon oxide layer in-between.

- **n-side strips**

On the n-side of the sensor there are n^+ -doped strips. Just as the p-side the n-side also has a resistive silicon oxide layer and metallic strips on the surface. Each strip has an AC coupled and a DC coupled contact pad.

- **p spray**

The n^- -doped substrate does not form a depletion layer to the n^+ -doped strips and therefore no electric field forms that could stop crosstalk between the n-side strips. In order to prevent this crosstalk between the n-side strips, the n-side is slightly p-doped in-between the strips at the surface. This procedure is called p-spray. When the sensor is depleted with a reverse bias voltage, the only conductive area left is at the surface. Due to the p-n junction at the surface created by p-spray, an electric field forms that pushes electrons towards the n-strips thereby preventing crosstalk. This method will be used in the [PANDA MVD](#) sensors.

- **p stop**

An alternative solution to create n-side strip separation is the p stop technique. Instead

of p-doping the whole area between two strips, only a narrow area is p-doped with a higher doping density.

- **moderated p spray**

There is also the possibility to use a mixture of p-spray and p-stop with a strong p-doping in the centre between two strips and a gradient towards weaker doping with less distance to a strip implant.

- **bias ring**

Both sensor sides have a bias ring surrounding all strips close to the sensor's edge. On the p-side this ring is p^+ -doped and on the n-side this ring is n^+ -doped, both are covered with a metallic layer. In contrast to the metallic layers on the strips, the metallic layer on the bias rings are directly on top of the doped silicon without an isolating silicon oxide layer in-between. The biasing voltage for the sensor is provided via the bias rings.

- **guard rings**

The guard rings are surrounding the p-side bias ring and have the task to shield the conducting sensor edges from the depletion voltage. Furthermore, they help to provide a homogeneous electric field.

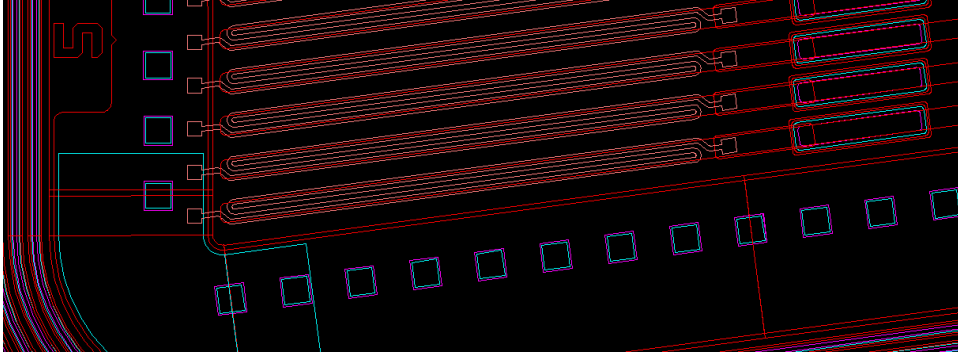
- **poly-silicon resistors**

If the p- and n-side strips were in direct contact to the bias ring, they would also be in contact with each other and share their signals. In order to prevent signal sharing between the strips via the bias line, a resistor is placed in-between each strip and the bias ring. These resistors are realised with a poly-silicon material. Furthermore, the resistors delay the drain of the collected charges from the strips by the bias voltage supply. This is necessary to provide a time frame during which the collected charge can be detected by the front end electronics. This technique is planned to be used in future [MVD](#) trapezoidal sensor prototypes.

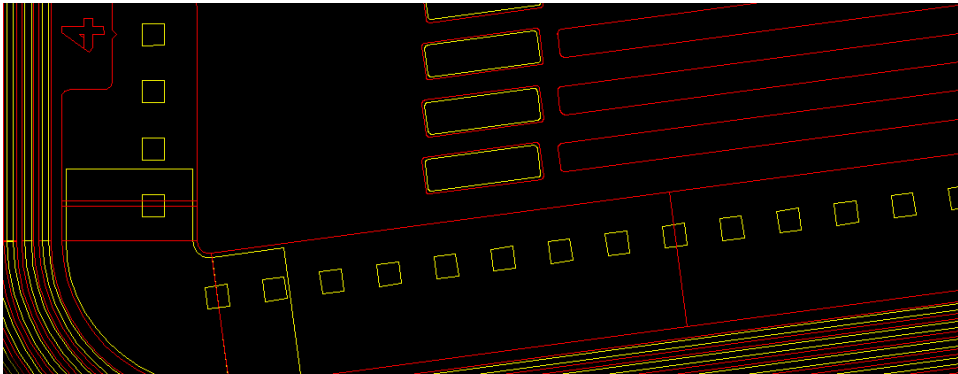
- **punch through method**

Alternative to the poly-silicon resistors, the so called punch through method can be used. This means that the bias ring is not connected to the implanted strips but a gap of n^- -doped substrate is placed in-between the strip implants and the bias ring. In this case the connection of the strips to the bias voltage happens after the depletion zone bridges this gap. The initial biasing voltage needed to make the depletion zone large enough to bridge that gap defines the resistance needed to separate the strip signals from each other and from the bias voltage supply. The punch through method was applied to the sensors tested in this thesis.

Some of these described elements can be seen in Figure [3.4](#). A sensor with the punch through technique has a shorter distance between the bias ring and strips, and therefore its strips, which define the active area of the sensor, are longer by a few $100\mu\text{m}$ compared to a sensor with poly-silicon sensors. This can be seen by comparing Figure [3.4\(a\)](#) and Figure [3.4\(b\)](#), where the strip pitch is $67.5\mu\text{m}$.



(a) Corner segment of a trapezoidal strip sensor's p-side. This layout was designed with poly-silicon resistors. The snake like shaped structures in pink colour are the poly-silicon resistors connecting the strips to the bias ring.



(b) Corner segment of a trapezoidal strip sensor's p-side. This layout was designed with punch through strip separation.

Figure 3.4: Corner segments of the p-side from two sensor's are shown in this figure. Parts of the p-side strips, p-side bias ring, and guard rings can be seen. The two pictures were extracted from layout files given by [CiS](#) who also produced the sensors which are described in Chapter 4.1. a) with poly-silicon resistors, b) with punch through method.

3.3.3 Hybrid Pixel Sensors

As the name suggests, the segmentation on a pixel sensor is organised in individual cells or pixels on one sensor side. The other sensor side is not segmented but doped as a single area. Only the segmented sensor side is connected via bump bonds to the readout electronics. Figure 3.5 shows a schematic profile of a hybrid pixel sensor together with its readout chip, the bumpbonds in-between sensor and readout chip, and a cooling pipe which is placed inside a carbon foam holding structure. The hybrid sensors for $\overline{\text{PANDA}}$ will be produced by growing an epitaxial silicon layer on a Czochralski substrate. Afterwards, most of the Czochralski substrate can be removed to obtain thinned sensors. This technique produces sensors with exceptionally high radiation hardness [45].

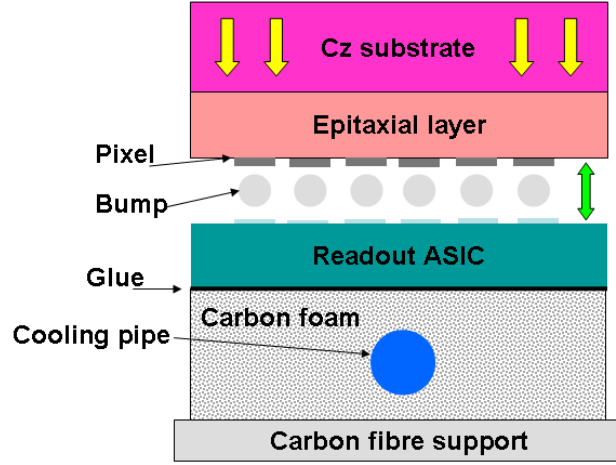


Figure 3.5: Scheme of a hybrid pixel sensor. Graphic taken from [28].

Pixel Size	$100\,\mu\text{m} \times 100\,\mu\text{m}$
Noise Level	$200\,e^- \text{ rms}$
Linear dynamic range	Up to 50 fC
Power consumption	$< 20\,\mu\text{W}$
Input polarity	Selectable
Leakage compensation	Up to 50 nA

Table 3.1: Summary of the requirements for the [ToPix](#) readout chip [46].

3.4 Readout

The [MVD](#) will contain over ten million pixel channels and over 200,000 strip channels. The front end chip for the pixel sensors will be an [Application Specific Integrated Circuit \(ASIC\)](#) called [ToPix](#) which is currently in development. The requirements for the [ToPix](#) readout chip are summarised in Table 3.1.

The [ToPix 4](#), a reduced size prototype, was tested at 160 MHz and its analogue performances are in accordance with the requirements. Additionally, tests for total ionisation doses and single event upsets have been performed and showed that [ToPix](#) can be operated in the radiation environment foreseen for [PANDA](#) [47].

For the strip sensor readout another [ASIC](#) will be used, called the [PANDA STRip ASIC \(PASTA\)](#). [PASTA](#) is being developed based on an existing [ASIC](#), the [Time-Of-Flight Positron Emission Tomography \(TOFPET\)](#) [48], because [TOFPET](#) already fulfils many of the requirements that are needed for [PASTA](#). Table 3.2 shows a comparison of the requirements for [PASTA](#) with the properties of [TOFPET](#). The only requirements not fulfilled by [TOFPET](#) are the smaller pitch size and the need to consume less than 4 mW per channel. Furthermore, [PASTA](#) will include a dual threshold system in order to provide a fast signal that can be used as a time stamp, and a second threshold discriminates noise that may cross the first threshold, as can be seen in Figure 3.6. The current status of [PASTA](#) foresees a size of $4.2\,\text{mm} \times 5\,\text{mm}$.

	TOFPET	PASTA
Area [mm ²]	7.1×3.5	$< 8 \times 8$
Ch. pitch	102 μm	60 μm
Hit rate	$< 100 \text{ kHz}$	$< 40 \text{ kHz}$
Time bin.	50 ps	$< 10 \text{ ns}$
CLK	80 – 160 MHz	155.56 MHz
Deadtime	$\sim 20 - 40 \text{ ns}$	$< 6 \mu\text{s}$
Power	7 – 8 mW/ch	$< 4 \text{ mW/ch}$

Table 3.2: Comparison of the requirements for [PASTA](#) with the properties of [TOFPET](#) [49].

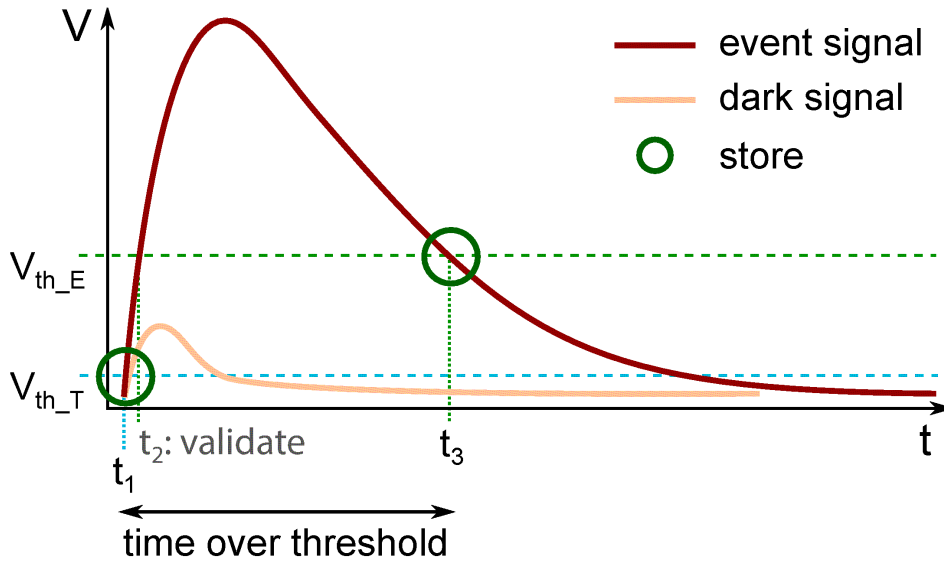


Figure 3.6: Dual threshold scheme for [PASTA](#). The lower threshold provides a fast time stamp and the higher threshold validates a hit and gives the second point for the ToT measurement [50].

3.5 Support Structure and Cooling

3.5.1 Support Structure

The four subsystems (pixel barrel and disc, strip barrel and disc) in the [MVD](#) will be mounted on the [MVD](#) frame with a relative positioning error better than 100 μm . The [MVD](#) frame is composed of two half barrels made by a high modulus composite of unidirectional carbon fibre cyanate ester resin as the skin which is filled with carbon foam as the core material. The total thickness is 4 mm.

A displacement study for gravitational load with a safety factor 2 has determined the maximum displacement to be 96.8 μm [28]. The top part of Figure 3.7 shows the central frame, which holds the entire central tracking system and serves as a reference frame to the external setup. It has fixation points to the beam pipe, target pipe, and the rail system to provide a stable positioning to those objects. The two [MVD](#) frame halves will each be separately fixed to three points on the central frame so that their position is well defined.

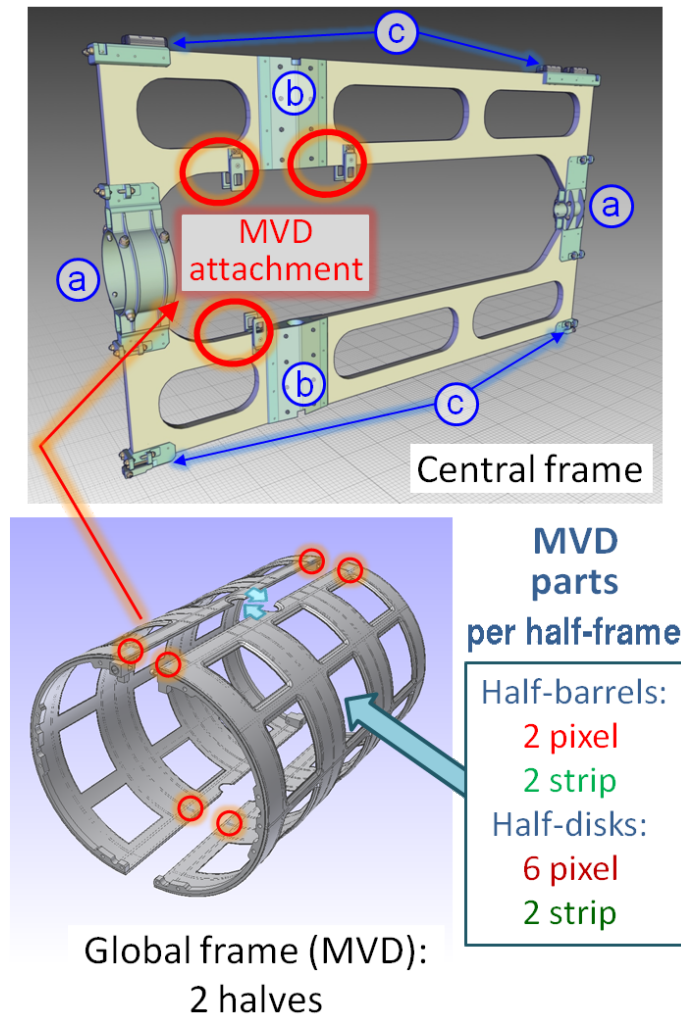


Figure 3.7: The two MVD frame halves are mounted on the central frame separately with a three point fixation. The central frame includes fixation points to the beam pipe (a), target pipe (b), and rail system (c). Figures taken from [28].

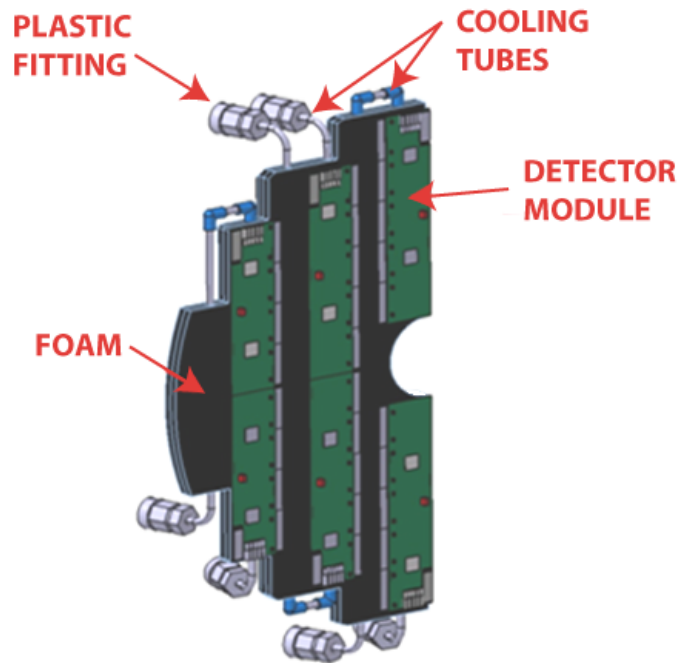


Figure 3.8: Schematic of a larger pixel disc with its cooling tubes and connections to the depression system. Figure taken from [28].

3.5.2 Cooling

The cooling system is needed to guarantee an operation temperature $< 35^{\circ}\text{C}$. Water of 16°C has been chosen as the cooling fluid, since the need to operate at a moderate pressure has led to discard evaporative fluids in favour of a depression system. A depression system has the advantage of avoiding leaks and taking away stress from fittings and connections. The temperature was chosen as it is important to operate above the dew point in order to protect the electronics from condensation water.

The water will be provided to the front end electronics with tubes of a 2 mm diameter. In order to place the cooling tubes close to the front end electronics, a material is needed that has low density, high thermal conductivity, and a low thermal expansion coefficient. Furthermore, it should be machinable and glueable, as well as stable at different temperatures, and radiation resistant.

All those requirements can be fulfilled by carbon foam. The cooling tubes are glued into the carbon foam holding structures of the front end electronics. Figure 3.8 shows this for the larger pixel discs. The connection from the cooling tubes to the cooling system is realised by glueing plastic fittings on the openings of the cooling tubes, which can be connected to further tubes that provide the water from the depression system.

Strip Sensor Characterisation

4

In order to learn more about the characteristics of the sensors as well as for [Quality Assurance \(QA\)](#) it is important to perform sensor characterisations. An important value for QA is the leakage current, which can directly be compared to the measurements of the manufacturer. Those measurements are typically done before the sensors are cut out of the wafer, so the comparison of leakage currents may also be an indicator for the cutting quality. The bias voltage needed to fully deplete the sensor must be known to operate the sensor.

4.1 Trapezoidal Strip Sensor Prototype

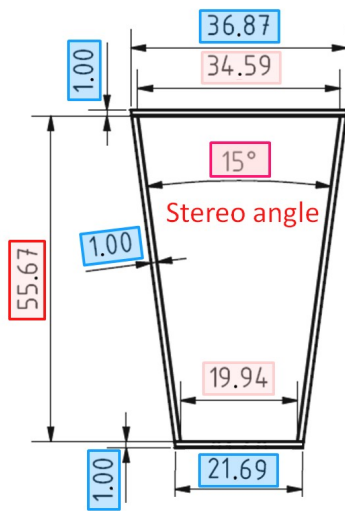
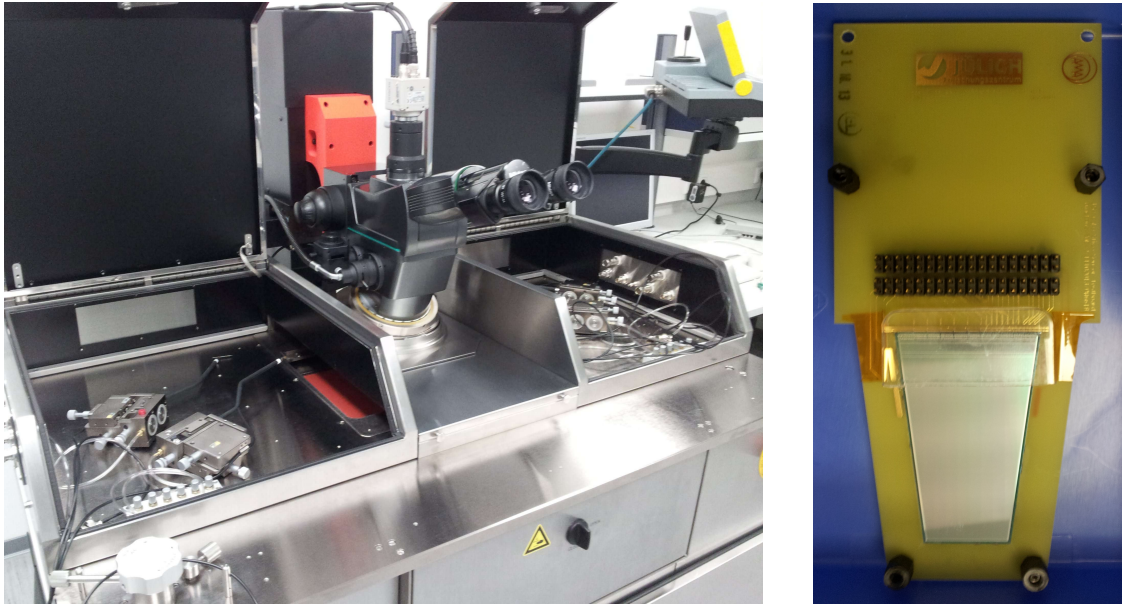


Figure 4.1: Trapezoidal strip sensor geometry. Sizes are in mm. Figure taken from [51].

The strip discs consist of trapezoidal silicon strip sensors. A first series of prototype sensors was produced by CiS [52]. Their geometry was chosen according to the [MVD Technical Design Report \(TDR\)](#) [28] and [51], and is shown in Figure 4.1. The sensors have a n^- -doped silicon bulk material with n^+ -doped strips on the n -side and p^+ -doped strips on the p -side.

Both sides have 512 strips with a $67.5\mu\text{m}$ pitch. The p-spray technique was used for n -side strip separation, otherwise the situation of n^+ -doped strips inside a n^- -doped material would result in massive cross talk between the channels. Each sensor has a stereo angle of 15° between the two long edges as well as between the p -side and n -side strips which are aligned parallel to the two long sensor edges. Therefore, it takes a total of 24 sensors to complete a 360° disc.

The sensor thickness is $285\mu\text{m}$ and each sensor has a passive border of 1 mm. The biasing voltage is supplied via a bias ring on both sensor sides. The electric connection from the bias ring to the strips is realised by the punch through mechanism on both sensor sides. Each strip provides two AC contact pads and one DC contact pad. All the DC pads are arranged



(a) Model PA 300, probestation from Suess.

(b) Picture of the dedicated test board with a sensor.

Figure 4.2: A picture of the probestation and the dedicated test board, which were used for sensor characterisation.

side by side, while the AC pads are arranged in a double row in order to give them more space. In this chapter, when the upper, lower, left, or right sensor edge is mentioned, it is always referred to the view as described above and shown in Figure 4.1. Here, the strips are parallel to the left edge. The strip number $n \in (1, 512)$ refers to the n^{th} strip counting from left to right. Due to the geometry of the sensor, the strips are not all of the same length. Starting with the full length of 56.1 mm from the left they stay constant until strip number 295, and then linearly decrease in length towards the upper right sensor corner.

4.2 Measurement Setup

A probestation was used to perform non-destructive measurements on the sensors. The probestation has a holding plate called a *chuck* where the sensors can be placed. A picture of the probestation can be seen in Figure 4.2(a). The chuck can be remotely controlled by a PC to change its position in all three dimensions plus rotations around a vertical axis through its centre. To secure the sensor's position on the chuck there are vacuum holes which can be switched on or off to fixate or release the sensor from the chuck. Contacts between measurement devices and the test subject on the chuck are realised with probe needles.

These needles are held by metallic stands with three micrometre callipers and vacuum fixation to the table, one probe needle can be seen in Figure 4.3. The red button at the side of the needle stand releases the vacuum so that the stand can be easily moved to the needed position and fixated there by releasing the button again. The three micrometre callipers can adjust the needles position on a fine scale in all three dimensions. A maximum of 16 probe

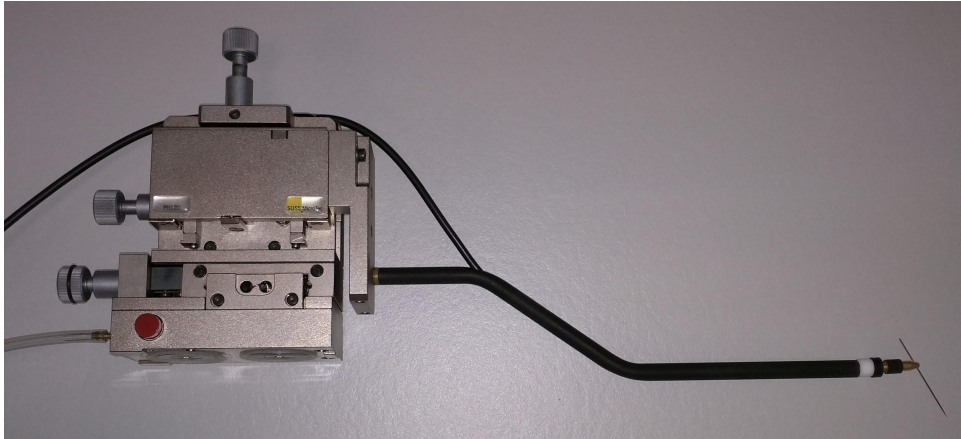


Figure 4.3: Photograph of a probier needle.

needles can be mounted onto the probestation. During these studies, not more than four needles were needed, allowing the freedom to select up to four pads on the sensor for contact so that one can easily change the measurement setup. A PC is connected to the probestation and can be used to fully control the probestation. The probestation has a combination of microscope and camera to view the probier needle and its target which can be seen in Figure 4.4.

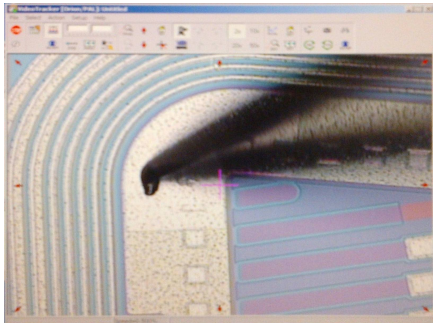


Figure 4.4: The corner of a sensor and a probier needle viewed with the video-tracker from the probestation PC.

Besides the probestation, a dedicated test board was designed for the characterisation of a single sensor with very high precision and the possibility to contact all the 1024 strips at the same time. It can be seen in Figure 4.2(b). The test board requires a sensor to be mounted and bonded to the board, consequently the sensor cannot be used in another device later on. The measurement equipment consisted of a LCR meter¹ and a source meter². Both measurement devices and the probestation are controlled by a measurement software from a PC.

Communication between the PC and the probestation, as well as the LCR meter were realised by Ethernet. The communication between PC and source meter was realised by a RS232 connection. For all three devices, classes have been written in C++ to allow remote control from the PC and to program automated measuring routines. The devices can also be controlled manually from a [Graphical User Interface \(GUI\)](#). While the probestation has its own set of commands, the two measurement devices communicate via the [Standard Commands for Programmable Instruments \(SCPI\)](#) format. More information about the software and SCPI is presented in Appendix A.1.

As can be seen in Figure 4.5 the source meter and LCR meter are not directly connected to the sensor, but they have both a separation box in-between them and the sensor. Schemes of the

¹Agilent, model E4980A

²Keithley, model 2410

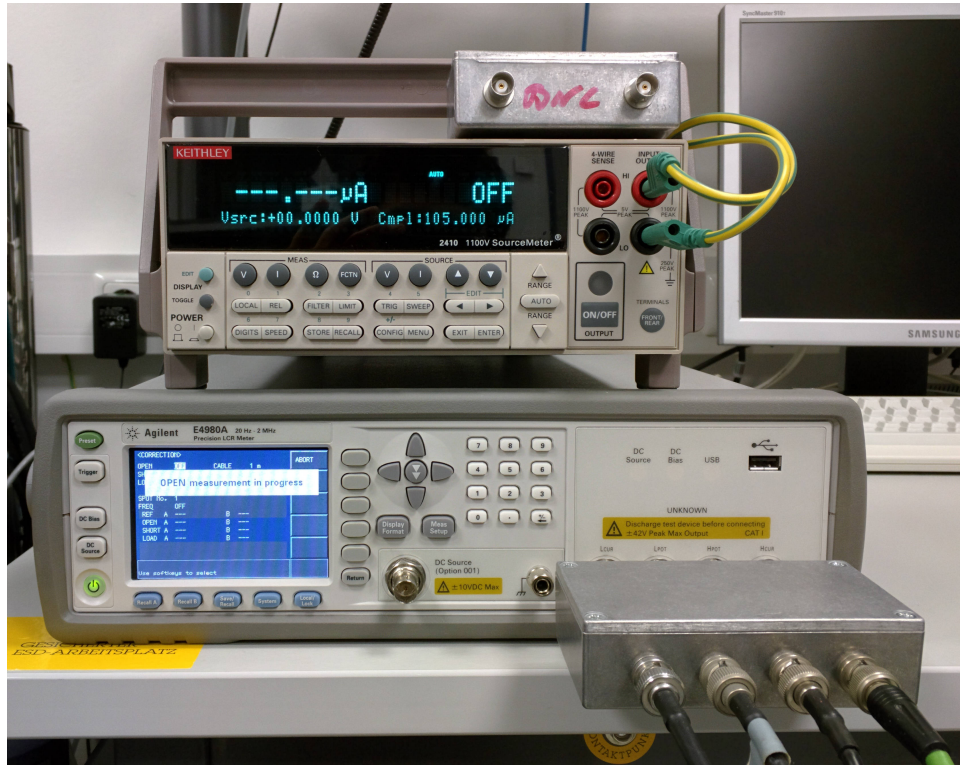


Figure 4.5: A picture of the LCR meter and the source meter used for the measurements in this chapter.

inside of the separation boxes, which have been created specifically for the test measurements in this chapter, are shown in Figure 4.6. The total resistance of $1\text{ M}\Omega$ in Figure 4.6(a) has the purpose of limiting the output current in order to have a safe testing environment for the sensor. Additionally, the LCR meter sees the source meter in some test setups as a parallel device to the sensor, and measures the sum of the capacitance of the sensor and the source meter's capacitance in these cases. Therefore, two coils have been added to the separation box of the source meter. The two coils represent only a very small resistance for the source meter's DC output, but they represent an additional huge resistance for the LCR meter's testing frequency and suppress the source meter's capacitance in the LCR meter measurements.

In those setups where the source meter is connected in parallel to the sensor, the LCR meter's input ports are directly connected to the biasing voltage. The LCR meter is only specified for an input voltage of up to 40 V , but the tested voltage range by far exceeds 40 V . This could harm the LCR meter or result in corrupted measurement data. Therefore, the separation box for the LCR meter contains a capacitor at each input port in order to separate the device from the DC biasing voltage.

Figure 4.6(b) shows the layout of the LCR meter separation box. The Agilent E4980A has four connection ports, two of them are used to provide the test frequency and the other two are used as input channels for measurements. In this way influencing effects of cable capacitances can be minimised. For the LCR meter separation box, capacitors of 100 nF have been chosen. Since the capacitances that are characterised are expected to be well below 1 nF these should

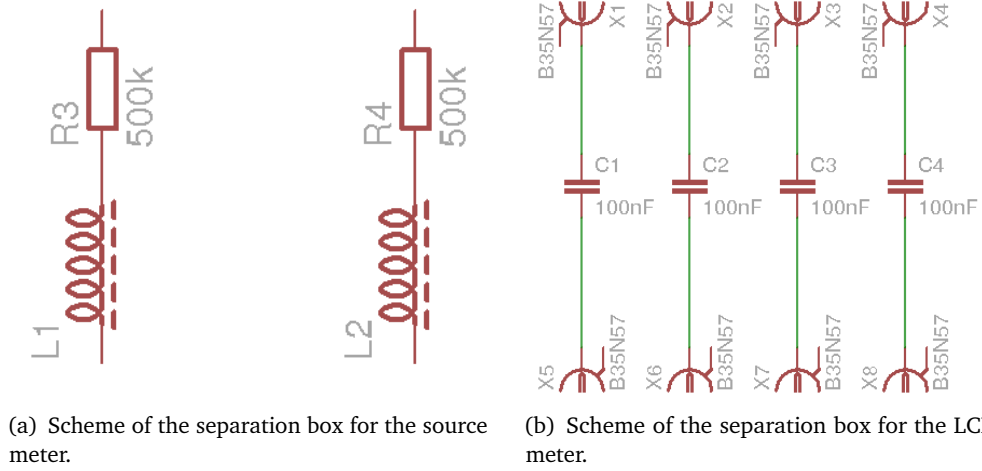


Figure 4.6: Schemes of the separation boxes for the LCR meter and source meter.

not influence the measured capacitance C_M as only the two capacitors on the measurement input ports are in series to the measured device $C_{TD} < 1 \text{ nF}$, see Equation 4.1.

$$C_M = \frac{1}{\frac{1}{100 \text{ nF}} + \frac{1}{C_{TD}} + \frac{1}{100 \text{ nF}}} = \frac{100 \text{ nF} \cdot C_{TD}}{2C_{TD} + 100 \text{ nF}} \approx C_{TD} \quad (4.1)$$

4.3 Characterisation with a Probestation

When a sensor is placed on the chuck, it is impossible to directly contact the under side of the sensor. This means that the bias ring of the bottom lying side can not be accessed. Nevertheless, it is possible to provide a bias voltage to the sensor by contacting the sensor's edge. The edge contact is a direct contact to the sensor substrate, which is n^- doped. Since the edge provides contact to the n-side of the sensor the only available option to provide a bias voltage is to lay the sensor with its n-side down on the chuck, leaving the p-side accessible on top. The sensor can be biased with one needle contacting the p-side via the p-side bias ring and another needle contacting the n-side via the edge contact.

Leakage Current Figure 4.7 shows the leakage current of one sensor compared to the leakage current measured by CiS. The measured leakage current is slightly higher than what was measured by CiS. This can be explained by a strong dependence of the leakage current on the sensor's temperature. The leakage current is directly connected to the number of intrinsic charge carriers n_i inside the sensor, which is dependent on the temperature [53]:

$$I_{leak} \propto n_i \propto T^{\frac{3}{2}} \exp\left(-\frac{E_g}{2kT}\right) \quad (4.2)$$

Here, E_g is the energy difference between the largest valence band energy and the lowest conduction band energy, which is 1.11 eV for silicon at room temperature. The measurement from CiS was performed at 20°C. While the laboratory provides a stable room temperature of 19.5°C the probestation itself can be slightly warmer due to its power consumption.

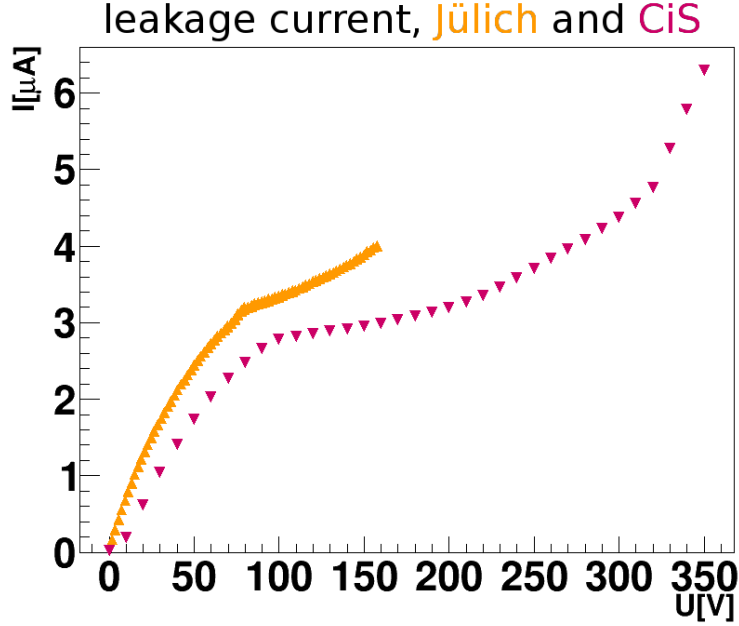


Figure 4.7: Leakage current of sensor 1 from wafer 8 (322635-8.1). The orange measurement was done in Jülich with the probestation and the purple measurement was done by CiS.

A temperature difference of ΔT results in a leakage current change of:

$$I_{T+\Delta T} = I_T \cdot \frac{(T + \Delta T)^{\frac{3}{2}} \exp(-\frac{E_g}{2k(T+\Delta T)})}{T^{\frac{3}{2}} \exp(-\frac{E_g}{2kT})} \quad (4.3)$$

With a temperature difference of $\Delta T = 2^\circ\text{C}$ and an initial temperature of $T = 20^\circ\text{C}$, this corresponds to $I_{22^\circ\text{C}} = 1.17 \cdot I_{20^\circ\text{C}}$ or an increase of 17%.

Thermal Runaway The sensor's power consumption heats up the sensor, and therefore the leakage current increases due to Equation 4.2. Then, because of the increased leakage current the power consumption increases which further heats up the sensor. Thus, the two effects amplify each other, which is called thermal runaway.

The power consumption of the sensor is $P = U_{bias} \cdot I_{leak}$, while the convective heat transfer to the surrounding air can be calculated as [54]:

$$\frac{dQ}{dt} = h \cdot A \cdot (T_S - T_{env}) \quad (4.4)$$

In Equation 4.4, h is the heat transfer coefficient, A is the surface of the heat transferring object, T_S the sensor temperature, and T_{env} the environment temperature. For gases or air the heat transfer coefficient is $h \sim 5 - 37 \text{ W}/(\text{m}^2\text{K})$ [55]. As $\bar{\text{PANDA}}$ will be operated in a closed room without a fan blowing onto the MVD, $h = 5$ is assumed here. Neglecting the sensor edges, its surface is $A = 2 \times 57.67 \text{ mm} \times \frac{36.87 \text{ mm} + 21.69 \text{ mm}}{2} = 33.77 \text{ cm}^2$. For a bias voltage of $U_{bias} = 150 \text{ V}$ and a room temperature of $T_{room} = 300 \text{ K}$ the resulting stable sensor temperature T'_S can be

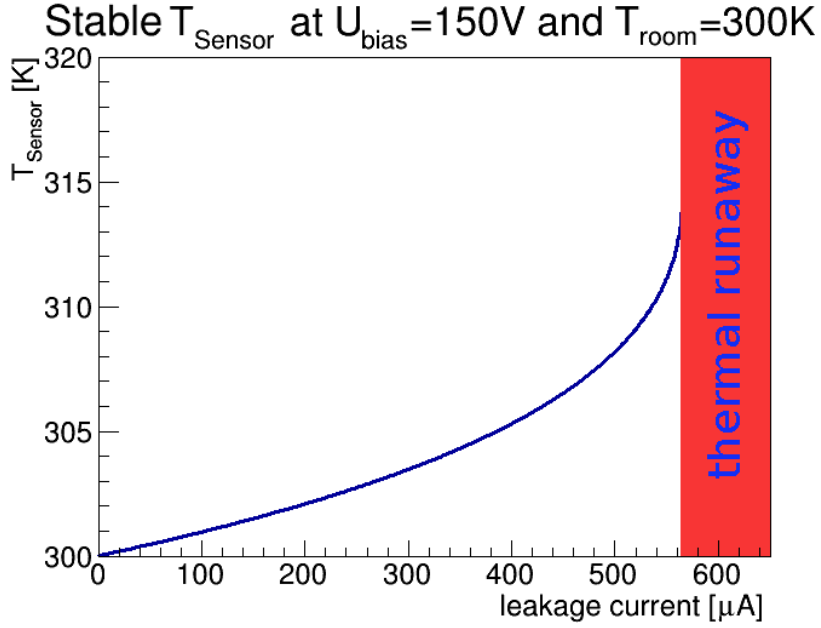


Figure 4.8: Stable sensor temperature as a function of the leakage current at room temperature.

calculated numerical as a function of the leakage current at room temperature by satisfying the following equation:

$$U_{\text{bias}} \cdot I_{\text{leak}} \cdot \frac{T_S'^{\frac{3}{2}} e^{-\frac{E_g}{2k \cdot T_S'}}}{T_{\text{room}}^{\frac{3}{2}} e^{-\frac{E_g}{2k \cdot T_{\text{room}}}}} = h \cdot A \cdot (T_S' - T_{\text{room}}) \quad (4.5)$$

The result can be seen in Figure 4.8. For leakage currents above 565 μA at room temperature no stable sensor temperature is reached and thermal runaway occurs.

Capacitance Measurements The same setup with two needles as described in the previous paragraph is used to measure the sensors capacitance. Since the cables and needles themselves give a contribution to the total measured capacitance it is important to calibrate the LCR meter every time the setup has changed. For the calibration the chuck is lowered so that the sensor is disconnected from the LCR meter, while everything else is in the right position for the next measurement. The calibration will set the LCR meter to ignore the cables' and needles' contribution to the total capacitance by running an open measurement for a set of 51 predefined frequencies to determine the 0 F capacitance [56]. The calibration for other test frequencies is done by an internal interpolation of the calibration parameters.

As explained in Chapter 3.3.1, the CV-curve of a sensor shows the depletion status of the sensor with full depletion being reached when the capacitance stops decreasing. Figure 4.9 shows the capacitance of the sensor that was measured with the LCR meter with a testing frequency of 100 kHz, and shows full depletion around 105V to 110V. Since the contact is realised via the bias ring and the edge contact, this should not be understood as the absolute capacitance between the p-side and n-side, which should be measured by contacting all p-side

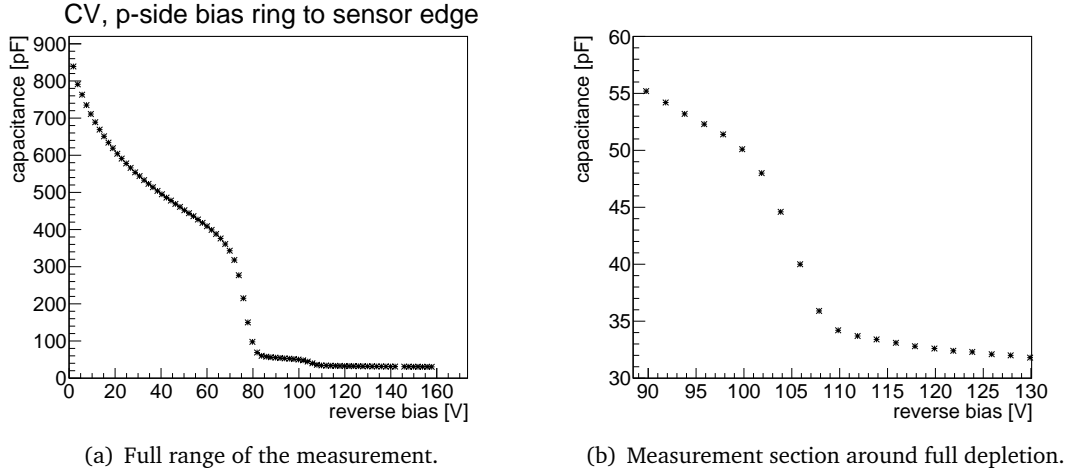


Figure 4.9: Sensor capacitance at 100 kHz measured for bias voltages from 0 V to 160 V.

strips and all n-side strips, but as that capacitance with two resistors in series. These resistors are the punch through resistors on p- and n-side, which separate the strips from the bias rings.

The LCR meter measures a resistance and calculates the corresponding capacitance via $R = \frac{1}{\omega C} \Leftrightarrow C = \frac{1}{\omega R}$. With $R = R_C + 2R_{PT}$, where R_C is the capacitive created resistance and R_{PT} is the punch through resistance which is created by the n^- doped gap in-between the bias rings and the strips. Figure 4.10 shows the measured capacitance per strip length with the probestation. The measurement was done using three prober needles. The biasing voltage was supplied as described before. The needle on the edge contact was used as backside contact and an additional third needle was used to contact individual p-side strips of various lengths.

As the needles together with the whole setup are comparably huge against the capacitance of an individual strip, this measurement did not return very precise results, but the tendency of a linear growth in capacitance per strip length can be seen. A linear fit on the measured points with a forced point on the origin of ordinates returned $C(l) = (0.12 \pm 0.01) \text{ pF/mm} \cdot l$, with l being the strip length. Also in this measurement the values should not be taken as absolute values as the punch through resistance from the edge contact influences the result.

4.4 Characterisation with a Dedicated Test Board

With the dedicated test board it is possible to test the whole sensor as well as individual strips, in particular strips of different lengths. The board has been designed to provide an environment in which all sensor strips can be contacted simultaneously. To achieve this goal the test board has a bonding line³ over the full range of the upper sensor edge to which the AC pads of all but a selected number of individual strips are bonded to.

³Since the AC pads are arranged in a double row on the sensor, two bonding lines have been implemented on the test board in order to keep the bonding procedure simple. But it was later found that the bonding to just one line could be done without extra effort, so the second line was left unused.

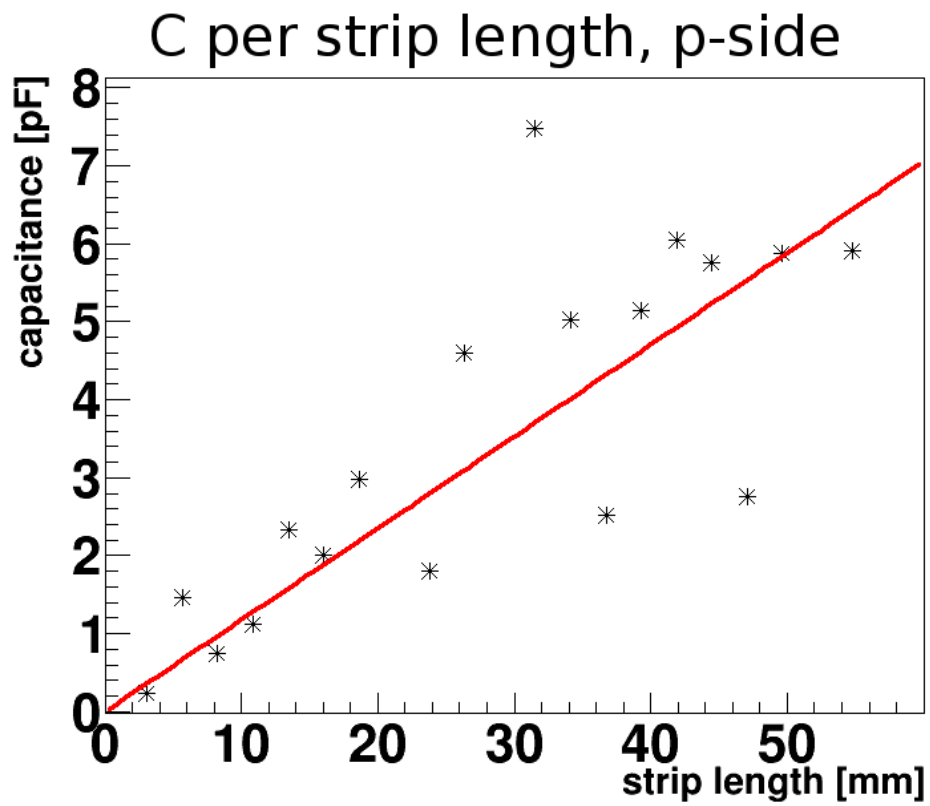


Figure 4.10: Capacitance per strip length of the p-side strips, measured with the probestation at 1 MHz

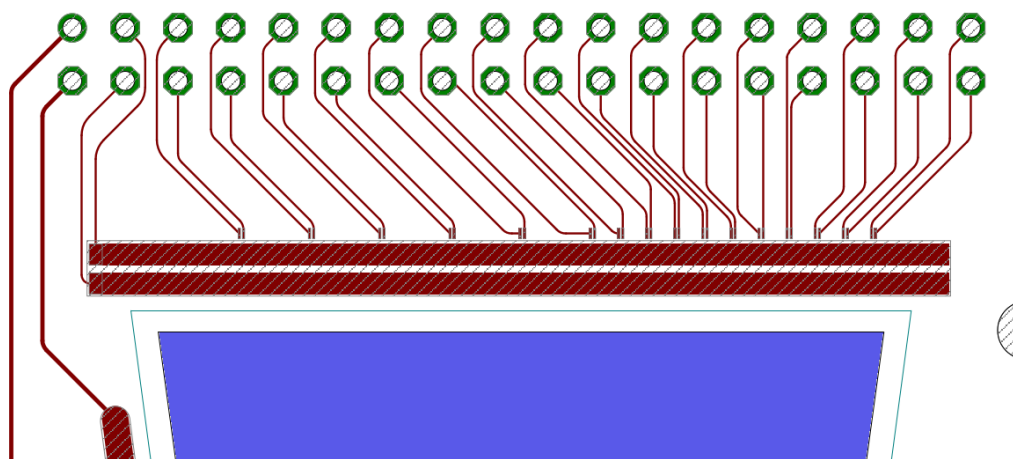


Figure 4.11: A section of the test board layout, with two contact lines for the majority of strips and some pads for the connection of individual strips. The blue area indicates the sensor.

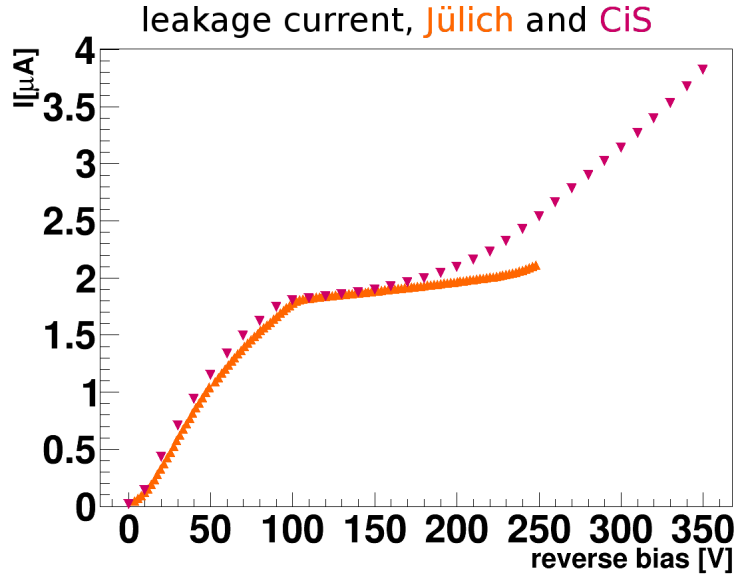


Figure 4.12: Leakage current of sensor 1 from wafer 7 (321589-7.1). The orange measurement was done in Jülich with the test board and the purple measurement was done by CiS.

Those individual strips are strip number 50, 100, 150, 200, 250, 300, 320, 340, 360, 380, 400, 420, 440, 460, 480, and 500. This means every fiftieth strip of full length and every twentieth strip of the strips of varying length has an individual contact. The layout of that section of the test board can be seen in Figure 4.11. For each of the individually connected strips, two pads are implemented on the test board, one for bonding to the AC pad of that strip and one for bonding to the DC pad. A second test board without a sensor was used for the LCR meter calibration. In this way the test board structure won't affect the measurement, but there is no way to compensate the effect of the wire bonds.

Leakage Current Figure 4.12 shows the leakage current of a sensor measured by CiS and then measured again with the test board in Jülich. The test board measurement is in good agreement with the data provided from CiS but slightly lower. In contrast to the probestation, the test board has no power consumption besides the power consumption of the sensor itself, and therefore has room temperature. The room temperature in the laboratory is stable at 19.5°C, which is half a degree colder than the test environment used by CiS and may explain the slightly lower leakage current measured with the test board.

Since both measurements are in good agreement, it is safe to assume that the sensor remained unharmed during the cutting procedure from the wafer. At a bias voltage of 150V, this sensor has a power consumption of less than 300 μW, and is with $I_{leak} < 2 \mu A$ far below a potential thermal runaway.

Capacitance Measurements With the test board the capacitance between p- and n-side can be measured directly by connecting one LCR meter connection to the test board connection with contact to the majority of the p-side strips and the other LCR meter connection to the test

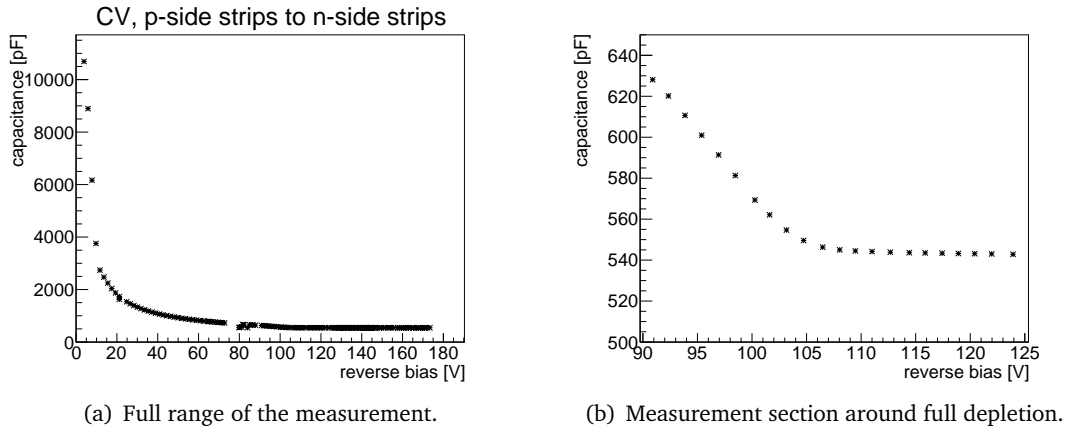


Figure 4.13: Sensor capacitance at 200 kHz measured for bias voltages from 0 V to 250 V.

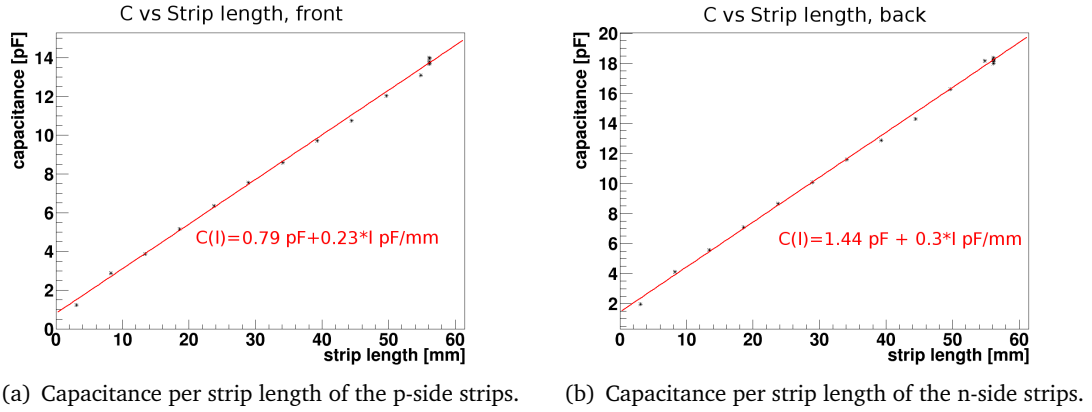


Figure 4.14: Capacitance per strip length, measured above full depletion (150 V) with 200 kHz.

board connection with contact to the majority of the n-side strips. The result can be seen in Figure 4.13. Full depletion is reached at about 105 V as can be seen in Figure 4.13(b).

With the 16 individual strip contacts per sensor side the test board also provides the possibility to measure the capacitance per strip length for p- and n-side. For each of the 16 strips the capacitance to the majority of strips from the other sensor side was measured above full depletion (150 V). Figure 4.14 shows the capacitance per strip length for the p-side and n-side strips. A linear fit results in $C(l) = (0.793 \pm 0.106 \text{ pF}) + (0.230 \pm 0.003 \text{ pF}) \cdot l \text{ pF/mm}$ for the p-side strips and $C(l) = (1.435 \pm 0.126 \text{ pF}) + (0.299 \pm 0.003 \text{ pF}) \cdot l \text{ pF/mm}$ for the n-side strips.

Both sensor sides show a small offset, this is due to the missing calibration of the LCR meter for the wire bonds. Since the sensor is bonded to the test board, the calibration of the LCR meter can not be run with the test board already connected. Therefore, in addition to the strip capacitance, the LCR meter also measures the capacitance of the wire bonds that connect the sensor with the test board. The n-side wire bonds from the test board to the sensor are about 1 mm longer than the p-side connection wires. This results in a slightly bigger offset for the

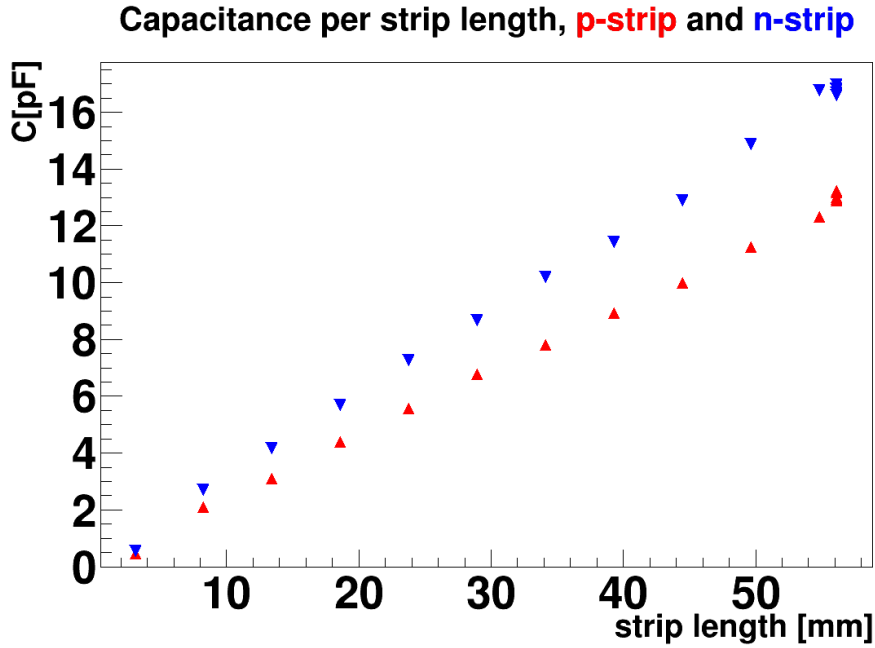


Figure 4.15: Capacitance per strip length. The red entries show measurements between individual p-side strips and the majority of n-side strips. The blue entries show measurements between individual n-side strips and majority of p-side strips.

n-side than for the p-side. Figure 4.15 shows the capacitance per strip length for p- and n-side in one plot with both measurements being corrected by their initial offset.

With the test board it is also possible to compare the CV measurement of an individual p-side strip to an individual n-side strip. This measurement is shown in Figure 4.16. The capacitance of the p-side strip is already quite low without a biasing voltage and decreases a bit while nearing full depletion voltage. The capacitance of the n-side strip on the other hand shows a much bigger difference between its unbiased capacitance and its capacitance above full depletion. This is due to the fact that the n-side strip are connected to their adjacent strips through the n^- -doped bulk material. Therefore, when measuring the capacitance of an n-side strip the capacitances of the neighbouring strips are automatically measured as well. When the depletion zone grows into the p-spray region, n-side strip separation is established and the measured capacitance has a sharp drop. As the p-spray doping does not reach far under the sensor surface, the sharp drop in this measurement happens just before full depletion. To make use of the n-side strips, the sensor has to be operated at a reverse bias above this value.

4.5 Conclusion

With the use of the probestation a test system for sensors has been set up that can run non-destructive sensor characterisation. It was used on a first set of prototype sensors of the trapezoidal strip sensors in the MVD.

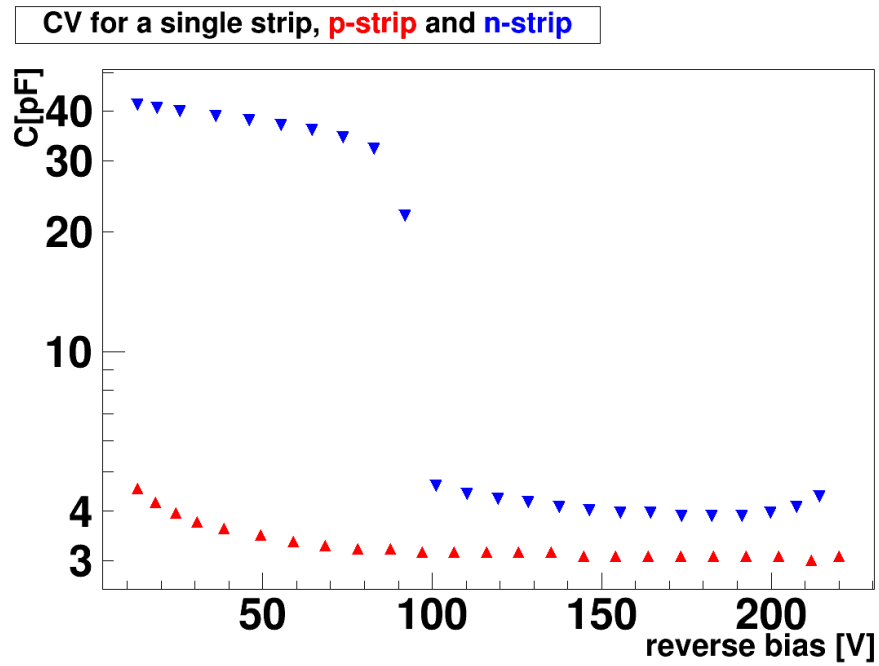


Figure 4.16: In this figure the capacitance of an individual p-side strip shown in red and the capacitance of an individual n-side strip is shown in blue.

The sensors reach full depletion at a bias voltage of 100V to 110V and have a leakage current in the order of several μA at full depletion.

Furthermore, a dedicated test board has been designed to perform high precision measurements on a single sensor. This was especially helpful to determine the capacitance per strip length with sub pF/mm resolution.

Spatial Resolution Determination

5

5.1 Methods of Position Reconstruction

When only a single channel of a multi strip detector gives a signal for a passing ionising particle, the best guess for the hit position is the centre of the strip associated with that channel. For uniformly distributed hits, the actual hit point of a single channel event has the same probability to be at any position within the active area. Therefore, the spatial resolution can be calculated

as $\sqrt{\int_0^d \frac{(\frac{d}{2}-x)^2}{d} dx} = \frac{d}{\sqrt{12}}$ with d being the strip pitch.

When dealing with a signal of two neighbouring channels, the first estimate for the hit position could be the centre in-between the two strips that created the signal. Together with the charge information of the detector, the spatial resolution of a silicon strip detector can be enhanced beyond the limit of $\frac{d}{\sqrt{12}}$ for hits that were created by signals from two or more strips.

Two methods of spatial resolution improvements will be shown in this section. The [Centre of Gravity \(CoG\)](#) method is an often used method to enhance the resolution for hits with the input of two or more strip signals and it can be used directly. The η method on the other hand is a more sophisticated approach to enhance the spatial resolution. Using it demands an additional study of the charge division for two-strip signals.

Centre of Gravity Method Instead of taking the centre between the two strips, a charge weighting algorithm can be applied to both strips. The hit position is then calculated by the following equation:

$$x = \frac{\sum_{i=1}^n q_i x_i}{\sum_{i=1}^n q_i} \quad (5.1)$$

Here, q_i are the measured charges on the strips in the cluster, and x_i are the central positions of the strips in the cluster. This method already promises an improvement over just taking the centre in-between the two strips, but it assumes a linear behaviour of the collected charge division to the distance between the hit and the strips.

η Method The η method takes the actual charge division distribution of a sensor into account instead of simply assuming a linear dependence, as for the CoG method [57][58]. In this thesis the η value, which describes the charge division between the two strips, is defined as $\eta = \frac{q_r}{q_r + q_l}$. In other works a slightly different definition for η ($\eta = \frac{q_r - q_l}{q_r + q_l}$) is often used.

In order to use the η value for spatial resolution reconstruction the distribution of the charge division between the two strips for homogeneously distributed hits on the sensor has to be known. Therefore, the η method cannot be used before this distribution is measured for the sensor it is planned to be used on. When the distribution of charge division $\frac{dN(\eta)}{d\eta}$ is known, the position reconstruction for a two-strip signal with η' is done by:

$$x(\eta') = x_l + \frac{\int_0^{\eta'} \frac{dN(\eta)}{d\eta} d\eta}{N_0} \quad (5.2)$$

In this equation x_l is the position of the centre of the left strip and N_0 is $\int_0^1 \frac{dN(\eta)}{d\eta} d\eta$. The η method as it is described here works only for cluster sizes of 2 strips. It is possible to define η in a similar manner to apply the method on clusters with three or more strip entries. But the count rate for clusters with more than two strips makes only a small contribution to the total number of hits, so that higher statistics would be required to measure the η distribution. At the same time, the dependence of the hit position to the η value becomes more linear for three hit clusters compared to two-strip clusters. Therefore, the η method has not been applied to three hit clusters in this study.

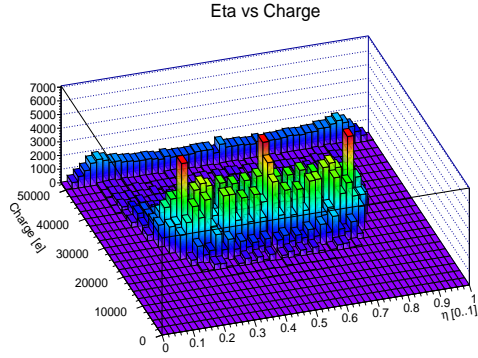
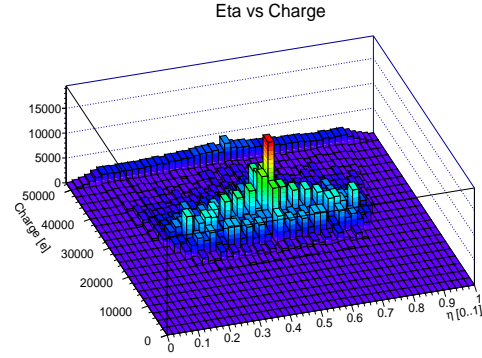
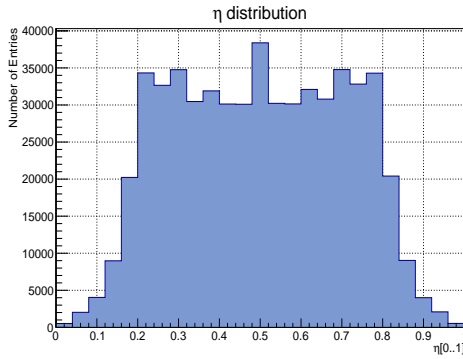
5.2 Implementation of the η Method into PandaRoot

5.2.1 Simulation of the η Distribution

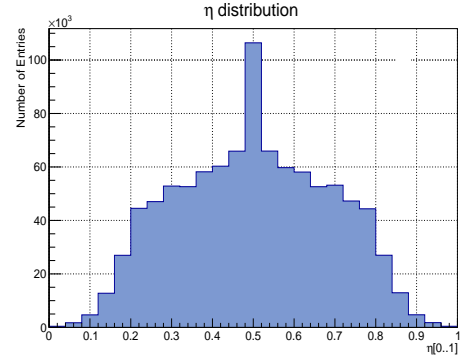
Besides the implementation of the algorithm for calculating the hit position with the η method in the PandaRoot framework, it is also necessary to create the corresponding η distribution $\frac{dN(\eta)}{d\eta}$ in order to use the algorithm.

The η distribution for a real sensor can be related to the energy deposited in the sensor by the ionising particles. The reason for this is that a higher energy deposition may result in a higher total charge inside the created charge cloud as well as a larger sized charge cloud. Additionally, the relation between total charge, noise, and sensor threshold influences the η distribution. Therefore, the η distributions presented in this section are created for charge deposition ranges individually instead of having one η distribution for all hits. The threshold in this simulation is 5,000 electrons and the charge deposition ranges have a width of 2,500 electrons.

The η distribution of the trapezoidal sensors was determined by simulating one million muons of random momenta in the range of 0.01 GeV/c to 15 GeV/c using the BoxGenerator provided within the PandaRoot framework. The muons were shot evenly distributed in the azimuth angle $\phi = [0^\circ, 360^\circ]$ and in the polar angle range of $\theta = [5^\circ, 15^\circ]$, this is where the trapezoidal sensors are located. Another one million muons with the same range of energy and azimuth angle were simulated in the polar angle range of $\theta = [15^\circ, 165^\circ]$ for the η distribution of the rectangular strip sensors within the MVD. The total number of created cluster signals is

(a) Simulated η distribution for two-strip signals with the trapezoidal sensors.(b) Simulated η distribution for two-strip signals with the rectangular sensors.

(c) Integral over the charge, trapezoidal sensors.



(d) Integral over the charge, rectangular sensors.

Figure 5.1: Simulated η distributions for two-strip signals for the trapezoidal and rectangular sensors. The colours indicate the number of entries per combination of η and charge, and the highest charge range contains all entries with a charge deposition greater or equal to 50,000 electrons. Figures c) and d) show the η distribution integrated over the charge deposition.

2,398,666 for the trapezoidal sensors and 6,085,216 for the rectangular sensors. 559,716 of the clusters from the trapezoidal sensors and 1,155,299 of the clusters from the rectangular sensors contained two-strip signals and therefore contributed to the η distributions which can be seen in Figure 5.1.

The peak at $\eta = 0.5$ for trapezoidal and rectangular sensors, especially visible in Figure 5.1(c) and 5.1(d), is due to two reasons. The highest chance for a hit to deposit a charge above threshold in two strips is when the hit's charge is distributed evenly ($\eta = 0.5$) among the strips. Additionally, the digitisation of detected charge also results in a discretisation of the charge values and therefore a discretisation of the η values. One effect of the discretisation is that not all η values are possible for all charge depositions, but $\eta = 0.5$ is always among the possible values for η .

Due to the threshold of 5,000 electrons, η values close to zero or one are only possible for large charge depositions. As the majority of hits deposits less than 30,000 electrons, η values

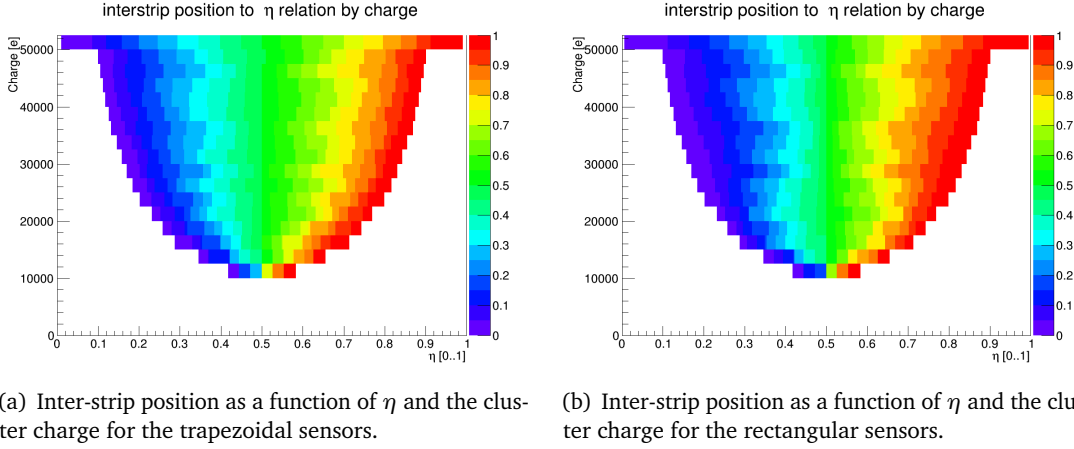


Figure 5.2: η to inter-strip position relations according to Equation 5.2. The colours indicate the inter-strip position from the centre of the left strip (0 or purple) to the centre of the right strip (1 or red). The white space indicates combinations of η and q that did not occur. The highest energy range contains all entries with energies greater or equal to 50,000 electrons.

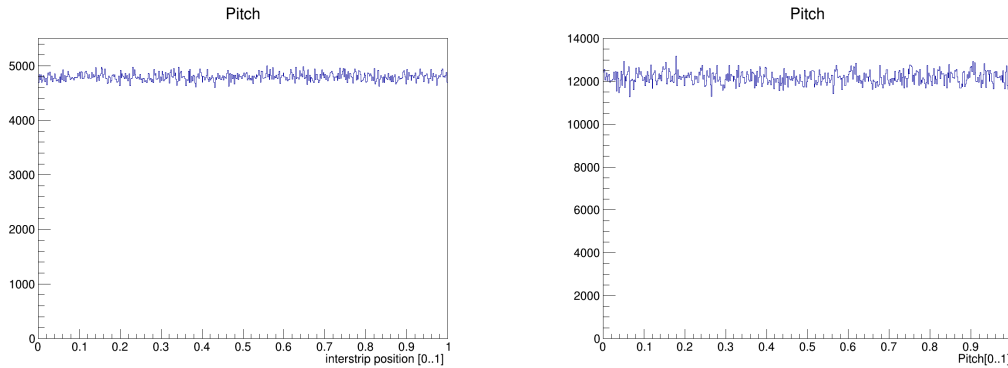


Figure 5.3: These plots show the uniform distribution of the hit locations.

lower than $\eta = \frac{5,000}{30,000} \approx 0.17$ or greater than $\eta = \frac{25,000}{30,000} \approx 0.83$ only contribute a small fraction to the total distributions shown in Figure 5.1(c) and 5.1(d). The corresponding η to inter-strip position relation shown in Figure 5.2 was created based on Equation 5.2.

5.2.2 Adjustments to the η Distribution

As mentioned before, it is vital for the η method that the η distribution is created with hits which are homogeneously distributed over the full range of inter-strip positions. Since in a simulation not only the sensor's output but also the simulation input is accessible, it is possible to plot the incoming spatial distribution of sensor hits. This is done in Figure 5.3 and it shows that the muons have hit the sensor at all possible inter-strip positions equally often. Nevertheless, one should keep in mind that only the hits which create signals in two strips will actually contribute

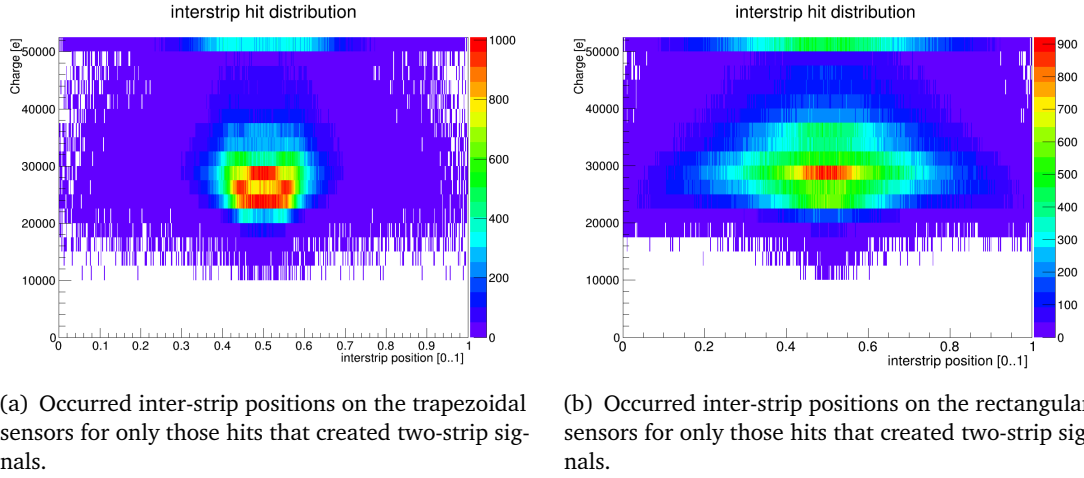


Figure 5.4: Inter-strip position distribution of two-strip signals separated for different energy ranges. The highest bin in the y-axis contains all entries with energies greater or equal to 50,000 electrons.

to the η distribution. For a two-strip hit, both contributing strips must collect a charge greater than their threshold. This is obviously more probable for hits just in-between two strips where the created charge cloud divides more or less equally to the two strips than for hits just in the centre of a strip, where the created charge cloud will almost entirely be collected by that strip. This behaviour can be seen in the inter-strip position distribution of two-strip signals as shown in Figure 5.4.

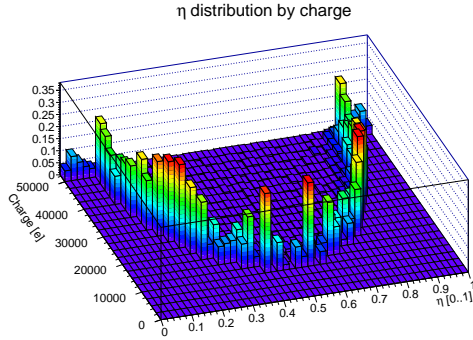
While all of the hits are homogeneously distributed over the inter-strip positions, the hits with two-strip signals are more likely to be in-between two strips than close to the centre of a strip. The inter-strip position distribution of two-strip hits on the trapezoidal sensors in Figure 5.4(a) shows a hole in the centre of the distribution that can be explained by discrete strip charges due to the used front end clock. For more information on this see Chapter 5.2.3.

The inter-strip position distribution of two-strip hits will subsequently be referred to as $\frac{dD(p)}{dp}$. The inhomogeneous distribution $\frac{dD(p)}{dp}$ should be taken into account when reconstructing a hit position. For this p' must be determined in order to fulfil Equation 5.3.

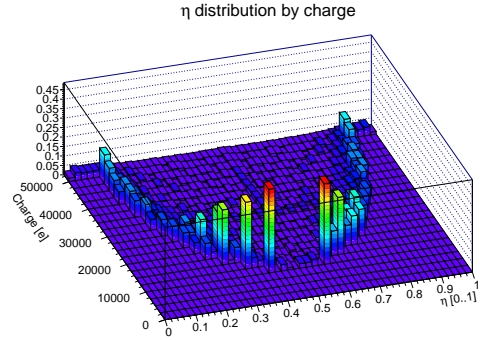
$$\frac{\int_0^{p'} \frac{dD(p)}{dp} dp}{D_0} = \frac{\int_0^{\eta'} \frac{dN(\eta)}{d\eta} d\eta}{N_0} \quad (5.3)$$

Here p' is the inter-strip position, D_0 is $\int_0^1 \frac{dD(p)}{dp} dp$, and the total reconstruction of the hit position is $x(\eta') = x_l + p'$. The corrected η to inter-strip position relations are shown in Figure 5.6. The measured η distributions can also be transformed to the η distributions that one would have measured if the two-strip signals were homogeneously distributed. This is done by taking the derivations of the corrected η to inter-strip position relations, which are the integrals over the true η distributions. The result can be seen in Figure 5.5.

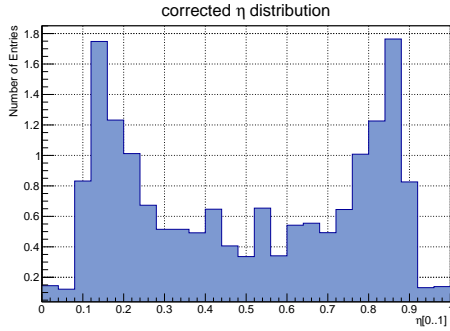
In simulation studies, $\frac{dD(p)}{dp}$ can be easily determined and taken into account to create a better matching η distribution. When attempting to make this correction on the η distribution



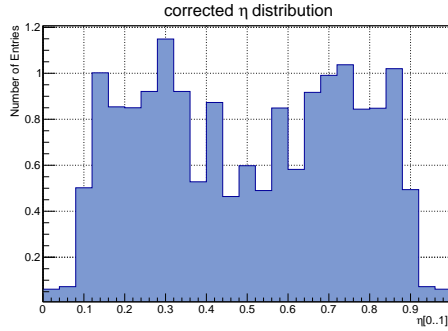
(a) Corrected η distribution for the trapezoidal sensors. The z-axis shows the number of entries in arbitrary units.



(b) Corrected η distribution for the rectangular sensors. The z-axis shows the number of entries in arbitrary units.

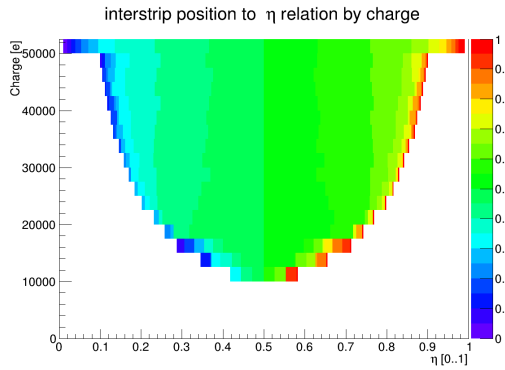


(c) Integral over the charge, trapezoidal sensors.

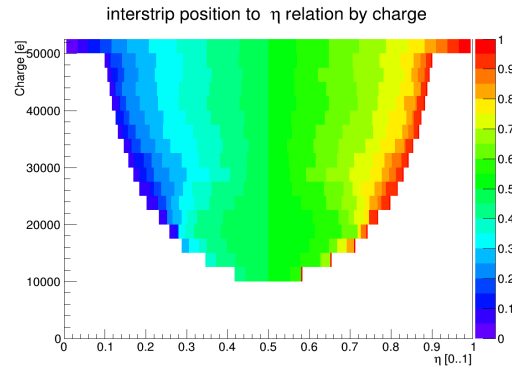


(d) Integral over the charge, rectangular sensors.

Figure 5.5: Plots of the η distributions after performing a correction due to the inhomogeneously distributed two-strip signals. Figures a) and b) show the η distribution per charge deposition range. Figures c) and d) show the η distribution integrated over the charge deposition.



(a) Corrected inter-strip position as a function of η and the cluster charge for the trapezoidal sensors.



(b) Corrected inter-strip position as a function of η and the cluster charge for the rectangular sensors.

Figure 5.6: Plots of the η to inter-strip position relations, after performing a correction.

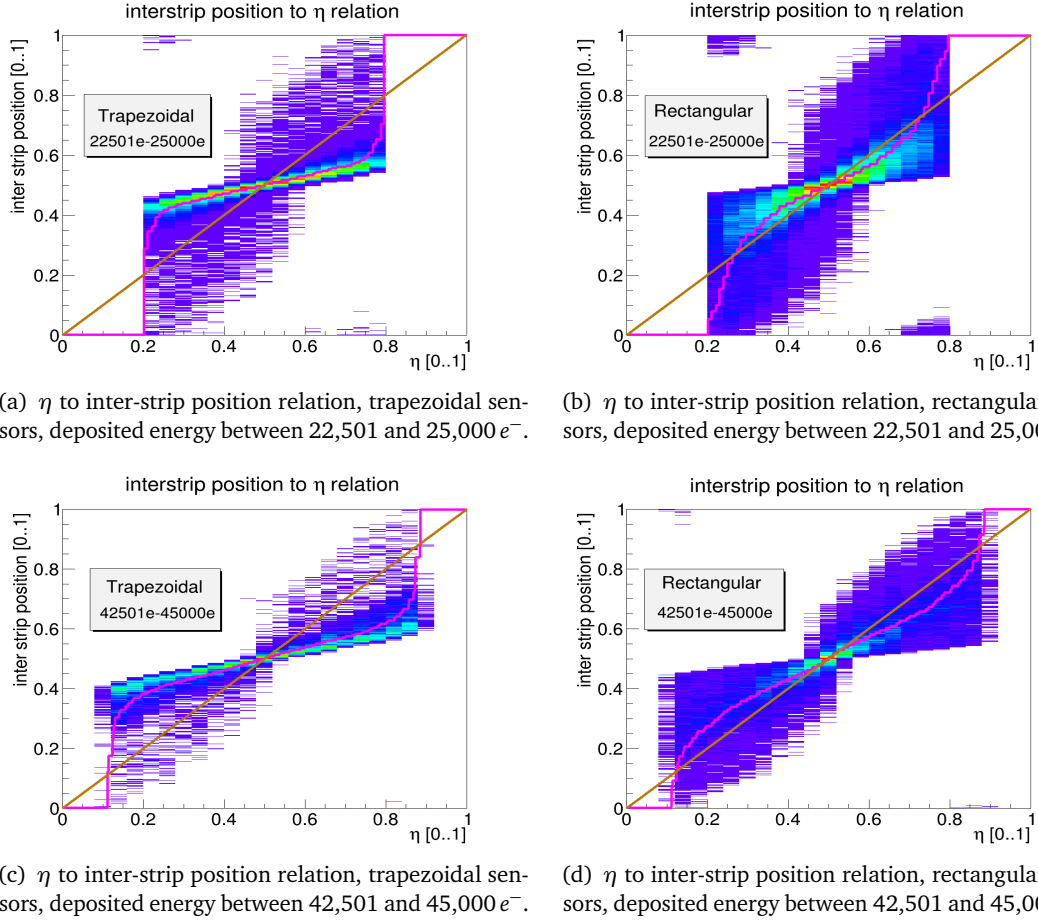


Figure 5.7: η to inter-strip position relation together with the reconstructed relation (pink) and the linear relation which represents the reconstruction with the CoG method (brown), shown for two ranges of deposited charge and both sensor geometries. The plots on the left are for the trapezoidal sensors, and the plots on the right are for the rectangular sensor. The plots on the top are for the range of deposited charge from 22,501 to 25,000 e^- , and the plots on the bottom are for the range of deposited charge from 42,501 to 45,000 e^- .

of a real sensor, a sensor telescope with a greater resolution than the strip pitch of the studied sensor is needed in order to gain access to $\frac{dD(p)}{dp}$. If such a sensor telescope is not available, an alternative method to gain a correction on the measured η distribution, based on calculating the probability function $P(\eta)$ for a two-strip signal to be registered as only a single strip signal due to noise and threshold, is provided in Chapter 6.2.7.

In Figure 5.7 the η to inter-strip relations for all two-strip signals in a low deposited energy range from 22,501 to 25,000 electrons and a high deposited energy range from 42,501 to 45,000 electrons are shown together with the reconstructed relations. There are a few entries with a low η value and an inter-strip position close to 1 as well as some entries with a high η value and an inter-strip position close to 0 in the histograms in Figure 5.7. The entries with a low η value but a high inter-strip position were created by events in which a hit happened

slightly left from the centre of a strip, which results in an inter-strip position close to 1, and have induced a three strip signal with the mentioned strip being in the middle. The left strip from this cluster then fell below threshold due to noise, so that only the middle strip and the right strip of the cluster are left and are registered as a two-strip cluster. As the middle strip is the left strip inside this two-strip cluster and carries the majority of charge, the two-strip cluster returns a low η value while the inter-strip position is close to 1. A similar situation with a hit slightly right from the centre of a strip creating a three strip signal of which the right strip falls below threshold due to noise can result in a high η value with an inter-strip position close to 0. Such a situation occurs only seldomly and cannot be reconstructed correctly, because the actual hit position does not lie between the two strips that created the cluster signal.

Finally, the corrected η to inter-strip position relations for the trapezoidal and rectangular sensors seen in Figure 5.6 are saved as a parameter file to PandaRoot and are integrated in the digitisation process.

5.2.3 Hole in the inter-strip distribution of two-strip clusters

Figure 5.8 shows the inter-strip position distribution for two-strip clusters inside the trapezoidal sensors from a simulation with PandaRoot.

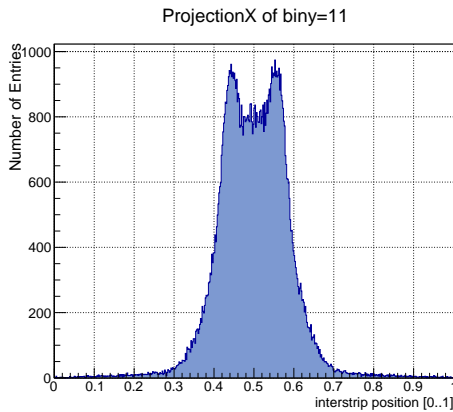
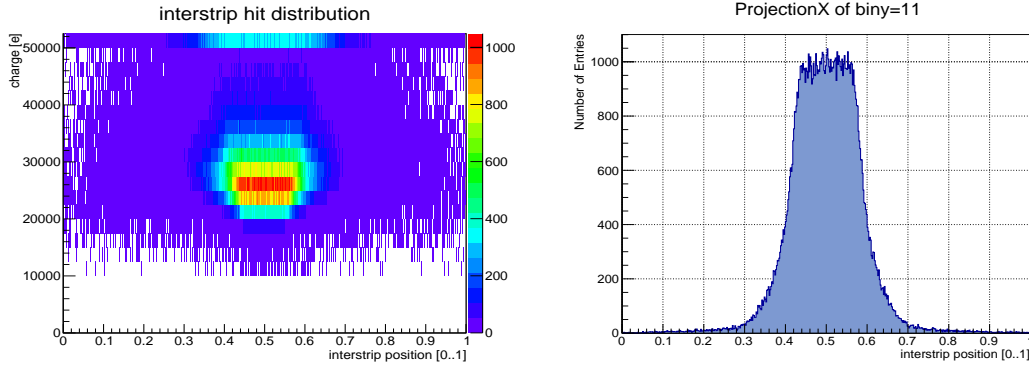


Figure 5.8: Inter-strip position distribution for two-strip clusters in the cluster charge range from 25,000 to 27500 e^- .

A hit directly between two strips has the highest chance to deposit sufficient charge in both strips for both of them to reach threshold. Thus, a maximum rate of two-strip clusters is expected from hits at an inter-strip position of 0.5. Nevertheless, for clusters with charge between 25,000 and 27500 e^- , two peaks around the inter-strip position of 0.5 with a small but obvious drop at 0.5 is observed, as shown in Figure 5.8.

The reason for this lies in the front end chip's clock which defines the time resolution for the time-over-threshold measurements, and therefore ultimately defines the charge resolution with discrete charge values corresponding to the clock cycle length. A realistic clock setting for the front end chip is 30 MHz, which was also used for the

simulation. Possible charge values from the simulation with that clock were [$10,305 e^-$, $11,265 e^-$, $12,245 e^-$, $13,265 e^-$, $14,295 e^-$, $15,355 e^-$, $16,425 e^-$..]. A hit at the inter-strip position of 0.5 has the biggest chance to equally split its charge to the two strips surrounding it. For a two-strip cluster with equal charge in both strips to land in the cluster charge range of 25000 to 27500, the only option is that both strips carry a charge of 13265 which makes a cluster charge of 26530. All other charge combinations that make it into that cluster charge range are not equally split ($\eta = 0.5$), but have $\eta \geq 0.539$ or $\eta \leq 0.461$. Due to this reason hits with an η value slightly off 0.5 have the highest probability for a cluster with charge between 25,000 and 27500 e^- .



(a) Inter-strip position distribution for two-strip clusters per cluster charge.

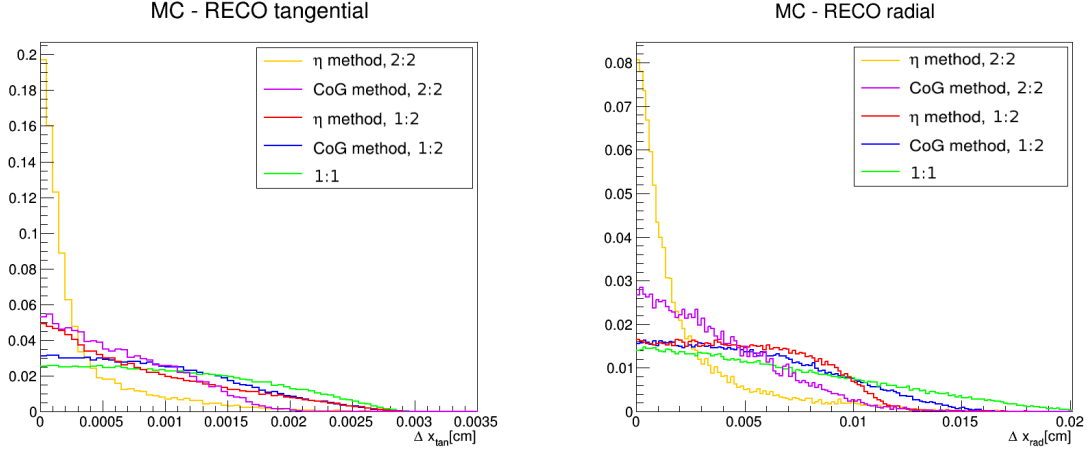
(b) Projection of Figure 5.9(a) to the x-axis for cluster charges between 25,000 and 27500 e^- .

Figure 5.9: Inter-strip position distribution for two-strip clusters with a simulated front end chip clock frequency of 300MHz.

In order to ensure that this is the only reason for the drop at 0.5, a simulation with a front end clock frequency of ten times the real frequency has been performed for which the discretisation of measured charge values has a correspondingly smaller step size. Figure 5.9 shows the corresponding inter-strip position distribution for two-strip clusters with the higher frequency, and it shows no local minimum at 0.5. This proves that the drop at 0.5 is caused by a discretisation effect from the front end chip clock setting.

5.3 Resolution Results

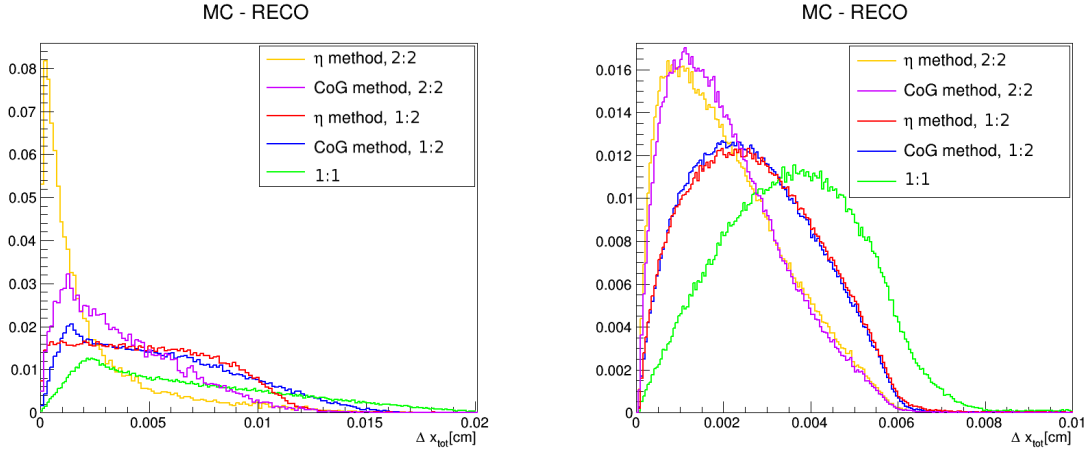
For the comparison of the CoG method and the η method another set of 1,000,000 muons with momenta in the range of 0.01 GeV/c to 15 GeV/c have been simulated with the box generator. The full range of polar and azimuth angles were used. The hits have been reconstructed with the CoG method and with the η method. As described in Chapter 4.1 the trapezoidal sensor's resolution differs in horizontal and vertical direction. Or in the case of the strip discs, the resolution differs in tangential and radial direction relative to the beam pipe. Figure 5.10 shows the resolution in tangential and radial direction to the beam line achieved with the trapezoidal double sided silicon strip sensors. The hits with just one strip signal per sensor side have no charge division that could improve the reconstructed position. Therefore, these hits naturally show the worst resolution. Those hits which have only one strip signal on one sensor side but two-strip signals on the other sensor side can use the charge division from one sensor side to improve the resolution. For that case, a slight improvement of the resolution from using the η method instead of the CoG method can be observed for the trapezoidal sensors. This is especially visible for the tangential resolution shown in Figure 5.10(a). In the case of two-strip signals per sensor side, charge division can be used on both sensor sides to improve the resolution. Here, the η method shows a great improvement over the CoG method in both radial and tangential directions for the trapezoidal sensors. The total resolution can be seen in Figure 5.11 and confirms the good improvement in resolution with the η method for the trapezoidal sensors. For the rectangular sensors the difference between CoG method and η



(a) Distribution of the residual between the reconstructed position and the generated position in the tangential direction.

(b) Distribution of the residual between the reconstructed position and the generated position in the radial direction.

Figure 5.10: These plots show the spatial resolution in tangential and radial direction of the trapezoidal sensors for different combinations of p- and n-side cluster sizes. The numbers in the legend give the sizes of the two clusters that have been combined to a hit point. For better comparison all graphs in this figure are normalised to an area of 1.



(a) Distribution of the residual between the reconstructed position and the generated position of the trapezoidal sensors.

(b) Distribution of the residual between the reconstructed position and the generated position of the rectangular sensors.

Figure 5.11: These plots show the total resolution of the trapezoidal and rectangular sensors for different combinations of p- and n-side cluster sizes. The numbers in the legend give the sizes of the two clusters that have been combined to a hit point. All graphs in this figure are normalised to an area of 1.

	single strip	CoG	single + CoG	η method	single + η method
tangential	10.9 μm	6.4 μm	9.3 μm	3.3 μm	8.2 μm
radial	66.0 μm	37.0 μm	53.9 μm	22.8 μm	50.0 μm
total	68.0 μm	38.3 μm	55.5 μm	23.4 μm	50.9 μm

Table 5.1: Summary of the achieved spatial resolutions of the trapezoidal sensors in a simulation with PandaRoot. All values in this table represent the mean values from their corresponding plots.

	single strip	CoG	single + CoG	η method	single + η method
total	36.1 μm	20.8 μm	27.0 μm	20.9 μm	27.4 μm

Table 5.2: Summary of the achieved spatial resolutions of the rectangular sensors in a simulation with PandaRoot. All values in this table represent the mean values from their corresponding plots.

cluster sizes	1 and 1	1 and 2	2 and 2	2 and 3 (or higher)
Trapezoidal	49.8 %	35.2 %	8 %	7 %
Rectangular	21.3 %	39 %	27.3 %	12.4 %

Table 5.3: Summary of the frequency of different combinations of cluster sizes for the trapezoidal and rectangular sensors.

method is very small. This can be understood by looking at the inter-strip position to η relations shown in Figure 5.7, which show that the inter-strip position to η relations for the rectangular sensors are much closer to a linear behaviour than the ones for the trapezoidal sensors. A linear relation would result in the same reconstructed positions for both methods η and CoG.

The different results for rectangular and trapezoidal sensors from this simulated studies is due to the different pitch lengths of both devices. While the trapezoidal sensors have a pitch of 67.5 μm , the rectangular sensors have a pitch of 130 μm ¹.

5.4 Conclusion

The η method has been implemented in PandaRoot and can be used when a parameter file with the η to inter-strip position relation for a sensor is available. This parameter file can either be created by simulations of the sensor, or for the usage with real data can be exchanged with a measured parameter file for a sensor.

The simulation results show an improvement of the spatial resolution with the η method for the trapezoidal sensors. All resolution results are summarised in Table 5.1 for the trapezoidal sensors and in Table 5.2 for the rectangular sensors. For the trapezoidal sensors the η method improves the resolution for hits with a two-strip cluster on both sides by 63.7% compared to the CoG method. The resolution for hits with a two-strip cluster on one sensor side and a single-strip cluster on the other sensor side improved by $\sim 9\%$ for the trapezoidal sensors.

¹The actual pitch is 65 μm but only every second strip is read out. Within the PandaRoot simulation, the intermediate strip is ignored and the device is handled as though it had read out every strip given a pitch of 130 μm .

Table 5.3 shows the fractions for combinations of cluster sizes for both sensors. The higher number of two-strip clusters in the rectangular sensors is due to the geometric placement. As the trapezoidal sensors are placed in the forward discs, they mostly face tracks perpendicular to their surface. The rectangular sensors are mounted with a small tilt in the barrel structure of the MVD, and cover a larger solid angle, therefore more shallow angles are common, which result in longer distances of the tracks through the sensor material.

Due to the smaller pitch of the final version of the trapezoidal sensor and the read out scheme with every second strip left unconnected as a passive strip in-between two active strips, the fraction of two-strip clusters is expected to be bigger for the final sensor version [59].

Test Measurements of a Strip Prototype

6

A prototype sensor of the same design as described in Chapter 4.1 has been tested in a proton beam at [COoler SYnchrotron \(COSY\)](#). The goal for this test beam was to study the performance of the prototype sensor.

6.1 Test Beam Setup

The test beam times were held in December, 2013 and January, 2014 at [COSY](#), a particle accelerator that is operated by the Institut für Kernphysik within the research centre Jülich.

6.1.1 Beam Conditions

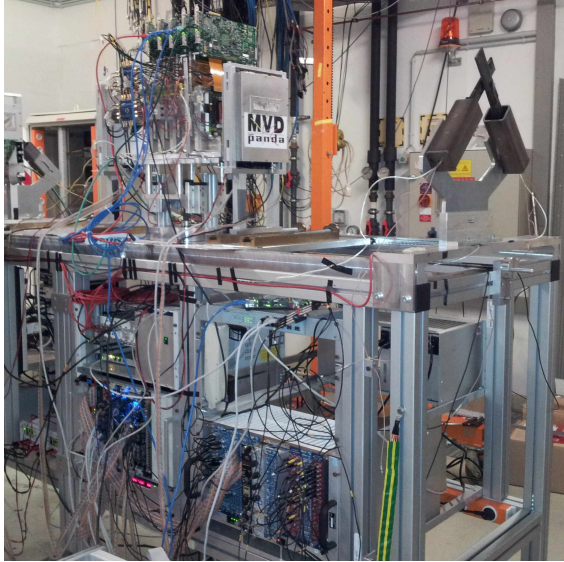
During the beam time in December, 2013 [COSY](#) provided a proton beam with a momentum of 2.95 GeV/c and a rate of ~ 5 kHz. The second test in January, 2014 was done with a proton beam with a momentum of 800 MeV/c and a rate of ~ 20 kHz. The beam is produced in spills, which means that [COSY](#) is injected with protons which are then accelerated and finally extracted over a period of ~ 50 s. The time gap between extractions was ~ 18 s. The beam intensity mentioned above was measured as the rate for scintillator coincidences and is a mean value over the extraction times.

6.1.2 Mechanical Setup

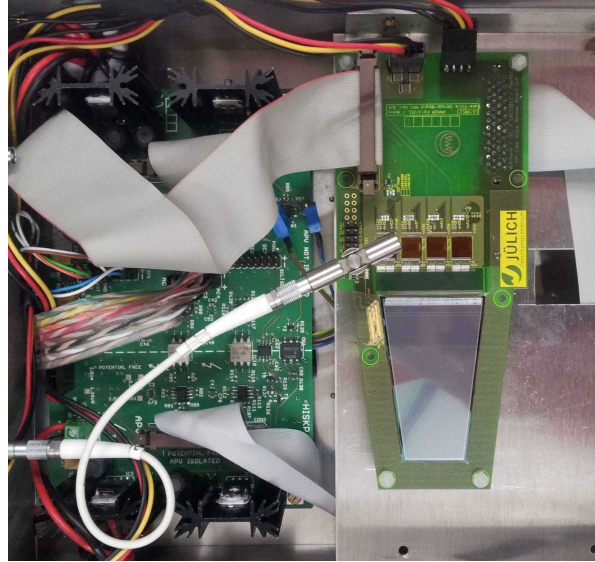
Figure 6.1(a) shows the full setup of the test beam. Two scintillators are placed at each end of the table as trigger system for the APV25 front end chip. The electronic devices mounted to the table contain power supplies, [FPGA](#) boards and [ADC](#) cards. The box with the label *MVD panda* contains the trapezoidal strip sensor together with its sensor board and supply board. Figure 6.1(b) shows the contents of the box.

6.1.3 Readout Chain

The readout chain is presented schematically in Figure 6.2. The sensor board carries the sensor and the APV25s, and the communication to it is routed via the supply board. From a PC the



(a) Experiment table with four pixel sensors and two strip sensors fixed on top, power supplies, ADC cards and FPGA boards in the table.



(b) The sensor board together with a mounted sensor, four APV25 chips per sensor side, connected power cables, and the supply board.

Figure 6.1: Photographs of the mechanical setup for the test measurements.

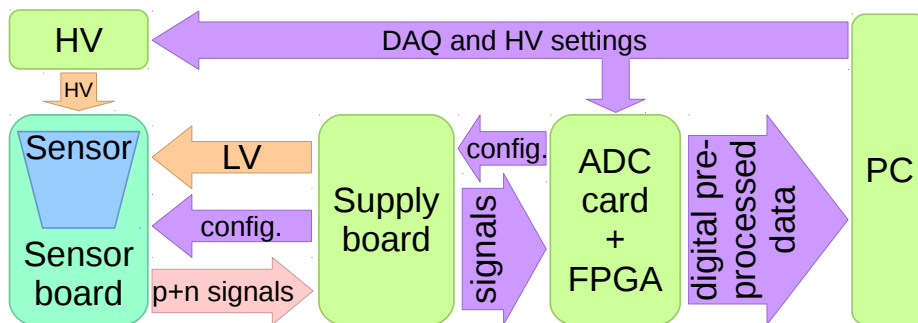


Figure 6.2: Schematic of the readout chain.

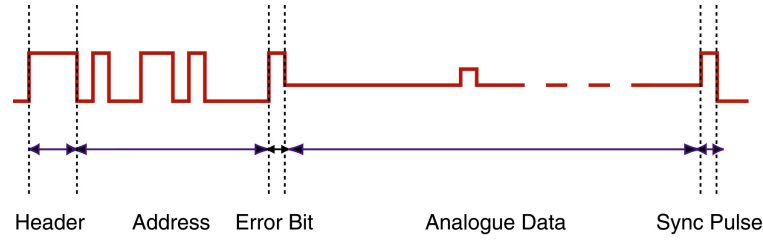


Figure 6.3: The APV25's data output scheme. Figure taken from [62].

settings of the DAQ and HV supply can be set. The APV25 data are routed via the supply board to an ADC card with an integrated FPGA where the analogue APV25 data are digitised and preprocessed before being sent to the PC for storage and analysis.

Sensor Board The sensor board for the trapezoidal sensors was designed taking a sensor board [60] for rectangular sensors of the same technology but different geometry as template. For the rectangular sensors, a L-shaped board is used that can readout one sensor side. The rectangular sensors are readout from two adjacent edges. In order to readout both sensor sides simultaneously, two of these boards of which one is flipped upside down and rotated by 90° are attached to a rectangular sensor. Due to the different geometry of the trapezoidal sensors, both sensor sides must be readout from the longer edge among the two parallel edges. Therefore, in addition to the geometrical changes the readout board for the trapezoidal sensors has more PCB layers, so that it can contain the components and routing of two L-shaped boards inside one trapezoidal board to read out both sensor sides.

The sensor is wire bonded to the board from both sides, and the p-side is visible in Figure 6.1(b). The main components of the sensor board are the sensor itself, four APV25 [61] chips per sensor side, capacitors for DC stabilisation, a pitch adaptor, and several connectors for the data cables, HV cables, and LV cables. Additionally, a bias resistor for the HV of $1\text{ M}\Omega$ is present on the sensor board. A detailed description of the trapezoidal sensors can be found in Chapter 4.1. The other components are described in this chapter.

APV25 The APV25 is an analogue readout chip with 128 channels and is powered with 2.5 V DC voltage. 2.5 V is also the limit for the maximum outgoing signal. Each channel can be wire bonded to one sensor strip. Since the trapezoidal strip sensors have 512 strips per sensor side, four APV25s are needed per sensor side to readout all the strips. The geometrical size of a APV25 chip is $8.1\text{ mm} \times 7.1\text{ mm}$ and its pitch size for the input channels is $44\text{ }\mu\text{m}$. Inside the APV25, the strip signals are amplified and used to load buffer capacitors. These buffers are chained to a 192 cell pipeline for each channel. If a trigger signal indicates a data request, the charges saved in the pipelines are amplified again and multiplexed on the outgoing data line. The output is provided as a differential current that ranges from -4 mA to $+4\text{ mA}$ [61].

Figure 6.3 shows the data output scheme which is composed of five parts. The first part is a 3 bit header with all three bits being a logical one. Next is an 8 bit address of the pipeline column from where the data was taken. The third part is an error bit which is by default a logical 1 and switches to a 0 in case that the APV25 senses an error. In that case the error register can

be read out via an [Inter-Integrated Circuit \(IIC\)](#) connection, which is a serial data bus with two bidirectional open drain lines of which one is used for data transmission and the other carries the clock. After the error bit the actual data follows in the form of 128 analogue data sets, one for each channel. The chip can either be run in 20 MHz or 40 MHz mode, and depending on the mode a sync pulse is sent as the fifth part of the output scheme either every 70th (20 MHz) or every 35th (40 MHz) clock cycles [62]. One set of these four -or five, when a sync pulse is sent- parts is called a *frame*.



Figure 6.4 shows the digitised data from an APV25 from the sensor's p-side for several frames. In this sample the logical ones from the header, address, and error bits are the dots at the top of the figure. These make it easy to find the beginning of a new frame. The dots at the bottom of the figure are the logical zeros from the 8 bit address.



Figure 6.4: The APV25's data output, digitised and recorded over several frames.

The 128 strip signals are all the dots in-between the digital headers. They are closer to the logical zero than to one and have a plateau of entries from empty strips. Within each frame a single dot can be found a little higher than that plateau, these dots originate from a strip channel which contained a signal. The signal rises for the first few frames and then decreases back to the plateau. The time needed for that channel to decrease back to the plateau is dependent on the signal height and determines the dead time of that channel.

For this signal it took about 10 frames, which corresponds to a time of 0.5 μ s, as the APV25 was operated with a 20 MHz clock.

Capacitors for DC Stabilisation It is necessary for the APV25s to have a ground level of their DC voltage in the same region as the sensor strip signal's potential. As the sensor is biased with a voltage of $\gtrsim 100$ V compared to the 2.5 V operating voltage of the APV25, the n-side and p-side APV25s can not share the same ground potential but the n-side APV25s' ground potential is floating with the sensor's biasing voltage over the potential of the p-side APV25s. Since both sides have a different ground potential, those might have fluctuations relatively to each other. As the APV25 is designed to amplify very small signals, these fluctuations can induce a noise signal because every channel is composed of capacitors, which are basically small antennas and very sensitive to fluctuations in the surrounding electric field. Capacitors with different capacitances are used to filter out any AC part in the difference between the two ground potentials of p-side and n-side electronics and therefore suppress noise.

Pitch Adaptor On the sensor side the channel pitch is 67.5 μ m while the APV25 has a channel pitch of 44 μ m and a small gap in-between channel 64 and channel 65 [62]. In order to connect

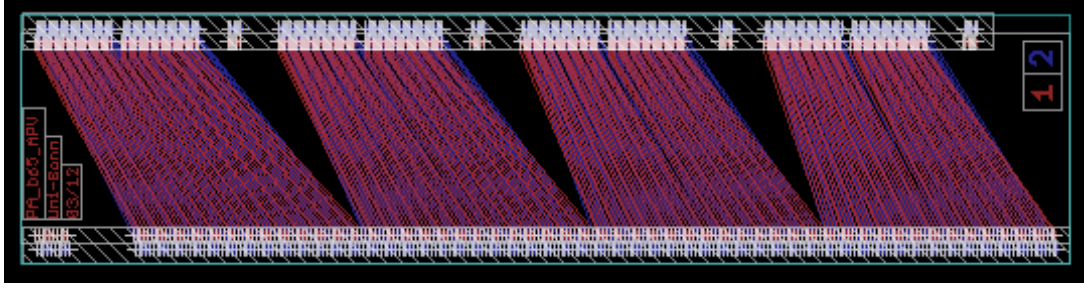


Figure 6.5: A schematic view on the pitch adaptor with the matching pitch size for the APV25 chips at the top and the matching pitch size for the sensor at the bottom.

the sensor strips directly to the APV25s' channels one would have to make wire bonds that vary in their angle to compensate the pitch difference, the gaps in-between two APV25 chips, and the small gaps in-between the channels 64 and 65. For an easier bonding procedure with straight and parallel wire bonds, a pitch adaptor is used. This pitch adaptor is a collection of thin wires with contact pads of sensor pitch size on the side facing the sensor and contact pads with the pitch of the APV25 and a separating gap in-between the APV25s on the side facing the APV25. A schematic overview on the pitch adaptor can be seen in Figure 6.5.

HV In both test beams, the HV supply for the sensor board was set to 150V. Due to a leakage current of $21.5 \mu\text{A}$ at that voltage, 21.5 V of the 150V dropped at the $1 \text{ M}\Omega$ bias resistor. Therefore, the HV at the sensor was at 128.5V

Supply Board and DAQ All communication between the operator and any part of the DAQ starts from the DAQ software on a PC. The DAQ used for this measurements has originally been developed for the rectangular sensors of the MVD and could be used for the trapezoidal sensors as well [63]. For the $2.95 \text{ GeV}/c$ beam momentum the trigger rate for the DAQ had a mean value of $\sim 70 \text{ Hz}$, and during the beam with $0.8 \text{ GeV}/c$ momentum a mean trigger rate of $\sim 650 \text{ Hz}$ was reached. The further components of the DAQ are described in this section.

ADC with integrated FPGA Board The configuration of readout parameters on the APV25 is realised via IIC which uses two lines, one data line and one clock line. A configuration request from the computer is sent to the FPGA board which translates it into an IIC-conform signal for the APV25. As mentioned above, the APV25 provides an analogue signal output. In order to receive data that can be interpreted and saved by a computer an ADC is necessary. The digitised data is then preprocessed by a FPGA before being transferred to a computer. Since an ionising particle creates a signal in only a few strips close to its point of penetration, most of the channels do not carry relevant signal information. Therefore, the main task of the FPGA is to filter the data for relevant information in order to reduce the amount of data. The process of filtering is done by setting a threshold value to discriminate noise from signal.

Before this is possible, the signal height of a channel has to be determined. In order to do this a baseline (zero value) is defined for each APV25 as the mean value of all channels without a hit signal from that APV25. This is realised in three steps. First the mean value m_1 of all 128

channels is determined. There are typically only a few hit signals in the 128 strip channels connected to an APV25, so that m_1 is much closer to the empty channels than to the signal hits. To get the mean value of only those channels without a hit signal, a mean value m_2 of only those channels that are in a close range to the first mean value m_1 is calculated. m_2 is usually already a good value for the baseline, but in some cases with high signal entries, m_1 could have been too large for some of the lower empty channels to fall into the range of m_1 . Therefore, this step is repeated to determine the baseline as the mean value of all channels that are in a close range to m_2 [64]. This procedure is repeated for every frame, in this way this also compensates for shifts of the baseline, e.g. due to common mode noise.

Furthermore, every channel has a pedestal which can vary over time, e.g. due to temperature changes. The [FPGA](#) tracks that pedestal for all channels by calculating the average signal height over the last 128 frames in which a channel was lower than threshold. The [FPGA](#) output to the [DAQ](#) software on the PC finally contains an [ADC](#) channel which is corrected by both, the baseline and the pedestal for each channel, and is above threshold. In this test beam the threshold was set to an [ADC](#) channel of 50 as a significant reduction of noise was reached at that point.

Another task of the [FPGA](#) is a noise measurement, which is done individually for each strip by taking the root mean square [ADC](#) channel of each strip from the past 30 seconds, taking only those [ADC](#) channels into account which were below threshold. Entries below threshold are considered to be no real hits and should have an [ADC](#) channel of 0 (i.e. should be equal to the instantaneous baseline plus pedestal of the channel), therefore the given [ADC](#) channel can be understood as noise contribution. [ADC](#) channels above threshold are considered to be real hits and no information about the noise contribution to that specific hit is available. A detailed analysis of the noise is presented in Chapter 6.2.4.

Supply Board The supply board is the routing point for all the data lines from and to the sensor board and also contains voltage regulators that provide the power for the APV25s. Additionally, the APV25s' signals from the n-side of the sensor board, which have a ground potential that is shifted by the sensor's biasing voltage, are transformed to p-side potential on the supply board. This is important because otherwise it would not be possible to use the same [ADC](#) for signals from both n-side and p-side. A picture of the supply board with labels to the main components can be seen in Figure 6.6. From the supply board the APV25s' differential output can be connected to the [ADC](#) via twisted pair cables.

6.2 Analysis of Test Beam Data

Out of the eight APV25 chips used, one chip was broken and could not be read out. That was the chip connected to the 128 shortest strips of the sensor's n-side. Besides the broken APV25, other technical problems during the December beam prevented the acquisition of a larger data sample. Therefore, in this section all data which is not explicitly denoted otherwise is produced with the 0.8 GeV/c proton beam from January. The results from the 2.95 GeV/c beam can be found in Appendix B.

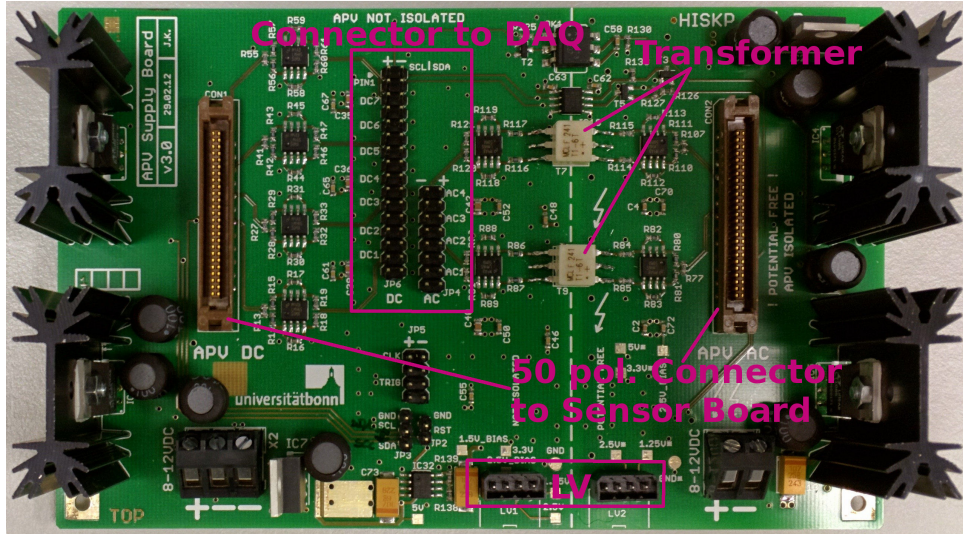


Figure 6.6: Photograph of the supply board with labels for the main components. The two white components on the dashed line are two of the transformer. Two more transformers are on the back side of the supply board.

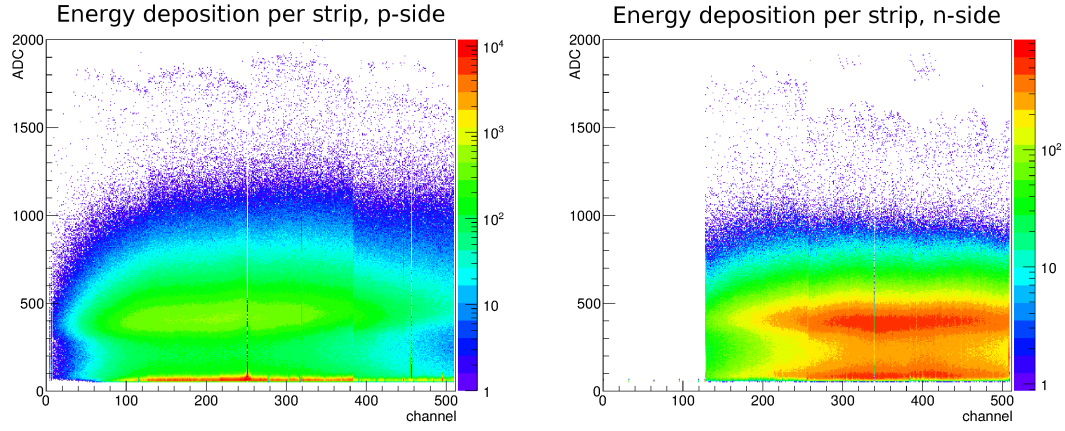
6.2.1 Data Selection

A first step in data analysis is to separate signal from noise entries. This can be done by analysing the energy deposition, the start frame, and the p- to n-side correlation of the hits.

Energy Deposition As all protons passing the sensor have the same beam energy all of them have the same mean energy loss per unit distance described by the Bethe-Bloch formula (Equation 3.1). Since the energy loss is a statistical process, the actual energy loss for each particle deviates from the mean value with a Landau distribution, especially in the case of such thin sensors where the energy loss happens over a relatively small number of collisions between the protons and silicon atoms. The energy loss per strip signal is received in ADC channels from the DAQ for all channels above threshold and the unfiltered data can be seen in Figure 6.7.

Two peak regions can be seen for both p- and n-side, one is at about an ADC channel of 420 whereas the other is at about 50 to 100. The mean energy loss of the protons contribute to the peak at around 420. Especially the p-side data contain a lot of noise entries which occupy the region of ADC channels from 50 to 100.

Beside noise entries, also entries of hits that distributed their energy loss over more than one strip are present in the low ADC channel region. Therefore, cutting all signals below an ADC channel of 100 would reduce noise, but would also affect a big fraction of the real signal. When the individual signals are grouped to clusters of neighbouring strips that gave a signal, most of the noise entries will become individual clusters since they appear at random positions and are unlikely to have a neighbouring strip that gave a signal as well. In contrast, entries in the low energy region, which belong to real hits, are likely to have a neighbouring signal induced by the same hit, as most hits deposit an energy equivalent to an ADC channel of about 420. Figure 6.8 shows the energy loss per cluster. While the n-side shows only a small peak in



(a) ADC channels measured per strip signal, p-side. (b) ADC channels measured per strip signal, n-side.

Figure 6.7: Energy loss per strip signal measured in ADC channels.

the ADC region of 50 to 100 for the energy loss per cluster, the p-side shows a big peak. But for both sensor sides the noise peak is clearly separable from the signal peak.

As the p-side shows a lot of noise entries above the threshold of 50 ADC, some of the noise entries are by chance from neighbouring strips and therefore form two-strip clusters with both strips above threshold. This results in the second smaller noise peak at an ADC channel of about 130, i.e. two times the main noise peak value which is at about 65 ADC channels. That peak can be seen in Figure 6.8(c) or more clearly in Figure 6.9, which shows the energy loss only for clusters with a cluster size of two.

For the energy loss per cluster, the minimum number of entries in-between the signal and the noise peak is at an ADC channel of 175 for the p-side and at 150 for the n-side. These values have been applied for the data selection as indicated by the red lines in Figure 6.8(c) and 6.8(d). With the cuts on the cluster energy being applied, the energy deposition per strip does not show a noise peak but still contains entries in the low energy region from 50 to 100 ADC channels from strips that belong to a cluster. The energy per strip distribution with cuts applied can be seen in Figure 6.10.

Start Frame As the APV25 works with a trigger signal, this can be used to distinguish signal from noise. When the scintillators coincide and fire the trigger signal, the APV25s start to send frames of its recorded signal. The number of frames per second is determined by the APV25 clock which was operated at 20 MHz. That relates to a time difference of 50 ns between frames. The drift velocities of the electrons and holes in the sensor is constant as it is defined by the electric field in the depletion zone which is defined by the reverse biasing voltage which was held at 128.5V.

Therefore, the time between a trigger signal and the rise of the hit signal above threshold is constant. Figure 6.11 shows the distribution of that time difference for each channel. It is determined by multiplying the start frame number of the first signal above threshold with 50 ns

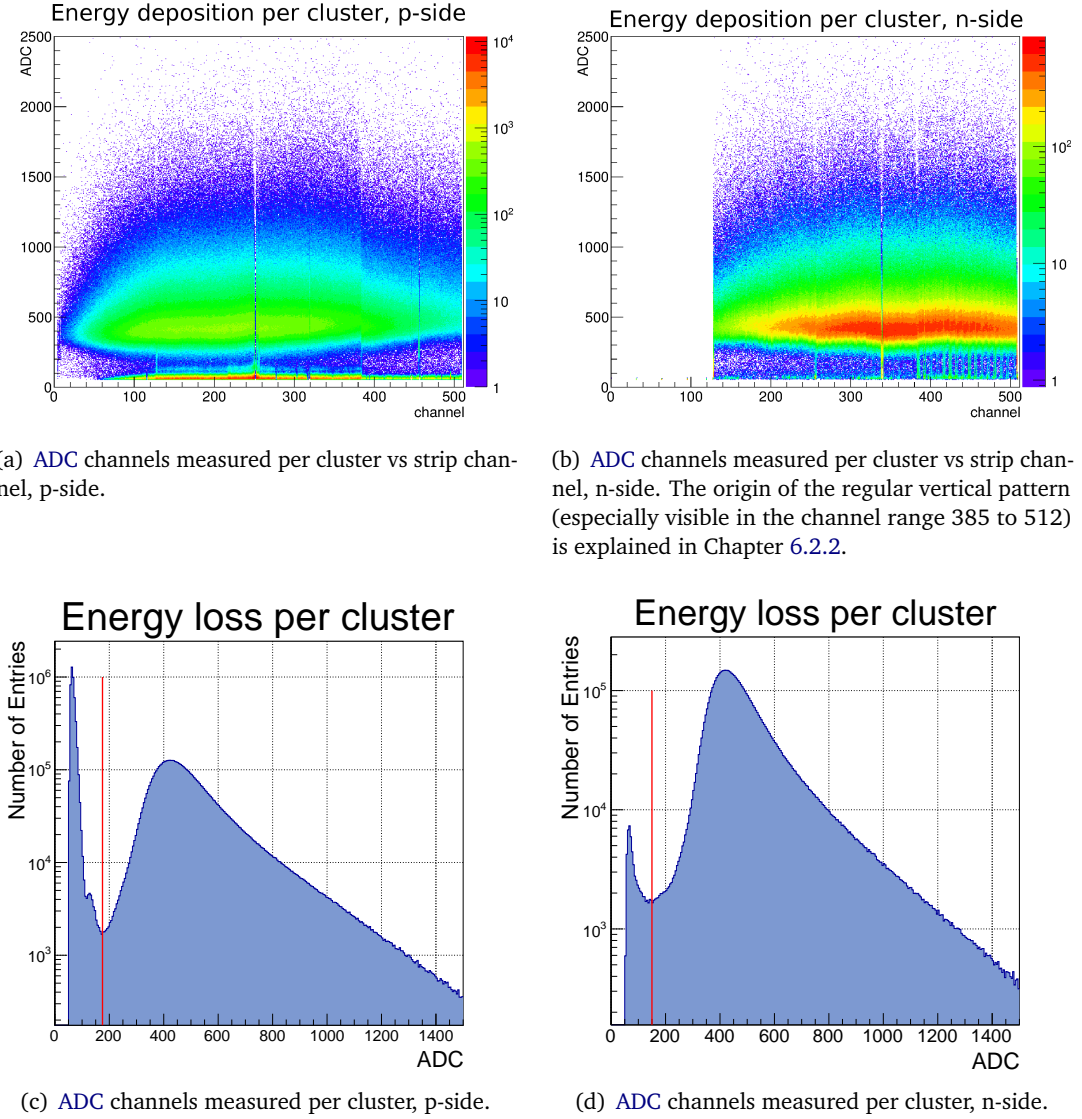


Figure 6.8: Energy loss per cluster measured in ADC channels. a) and b) show the cluster energy vs the strip channel, while c) and d) show the projection on the y-axis together with a red line that indicates the software threshold.

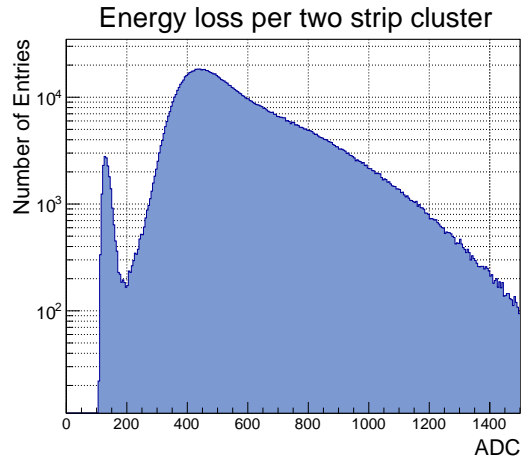
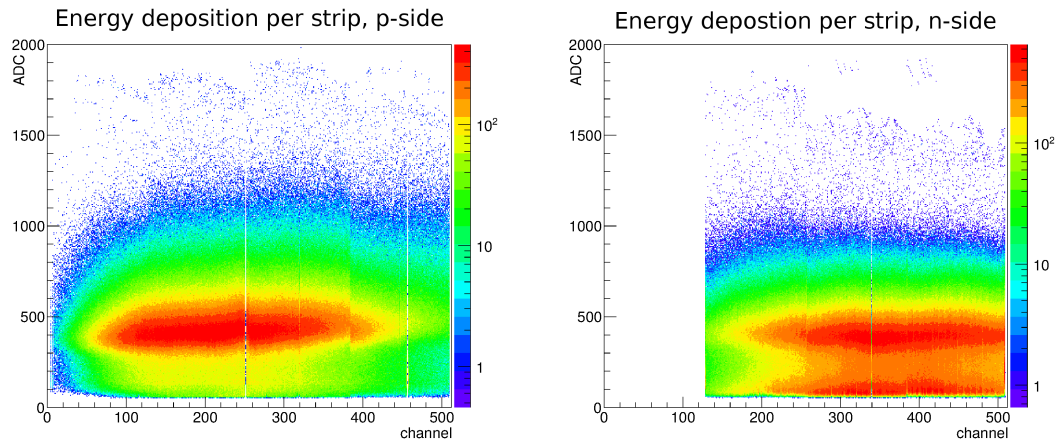


Figure 6.9: Energy loss of two-strip clusters measured in ADC channels.



(a) ADC channels measured per strip signal, after cuts, p-side.

(b) ADC channels measured per strip signal, after cuts, n-side.

Figure 6.10: Energy loss per strip signal measured in ADC channels.

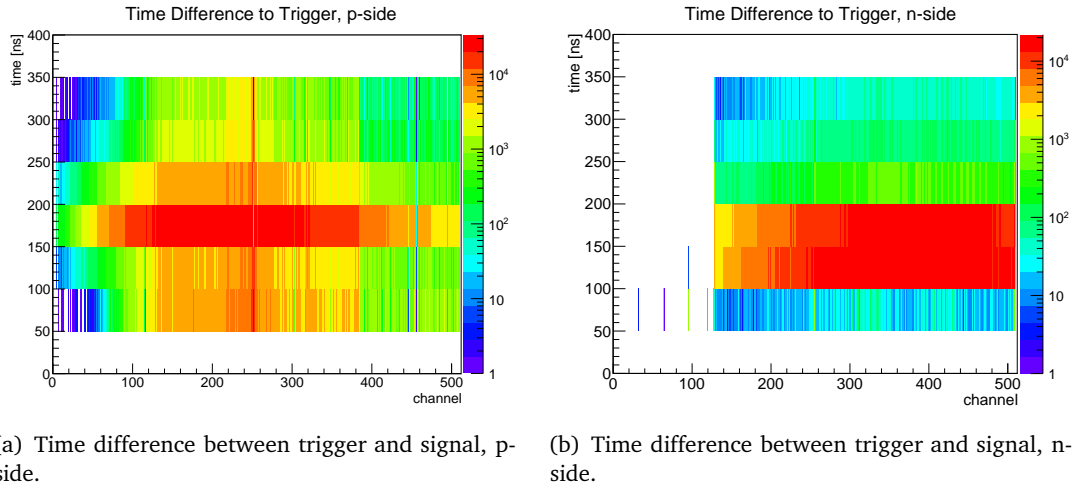


Figure 6.11: Distribution of the time difference between trigger and signal for p- and n-side.

which is the time per clock cycle. There are no entries above a start frame number of 6 because a hardware selection has been applied there. As electrons have a higher mobility than holes in silicon [65], the time difference between trigger signal and hit signal is slightly lower for the n-side strip signals. This effect can be seen in the start time of the signals of the n-side which is 100 ns to 200 ns for most entries, while most p-side entries have a start time of 150 ns to 200 ns.

Noise signals are unrelated to the triggered event and therefore have a random start time. To reduce noise entries the start time can be used to reject all p-side signals with a start time < 150 ns or > 200 ns and all n-side signals with a start time < 100 ns or > 200 ns.

p- to n-side Correlation The correlation between p- and n-side can be used to reject noise and ghost hits. As real hits deposit the same charge amount on the p- and n-sides, they populate the diagonal in Figure 6.12(a).

Noise Hits The entries parallel to the x-axis (y-axis) with p-side (n-side) ADC channels of less than 175 (150) originate from noise entries on the p-side (n-side) that get combined to random n-side (p-side) clusters from the same event. This part of the correlation already gets rejected by the cuts for energy depositions on p- and n-side.

Ghost Hits Ghost hits occur when two or more hits occurred on the sensor at the same time. For k hits at the same time there are k^2 possible combinations of p- and n-side clusters, with only k correct combinations that lead to the real hits and $k(k - 1)$ wrong combinations that lead to ghost hits. The entries in Figure 6.12(a) off the diagonal with p- or n-side ADC channels above the corresponding cut values are mostly ghost hits, because they carry strong signals in their p- and n-side clusters and are therefore unlikely to be noise. But they do not show the same energy deposition which should be the case for real hits. The difference in cluster energy between a p- and a n-side cluster defines the resulting distance to the diagonal in the correlation

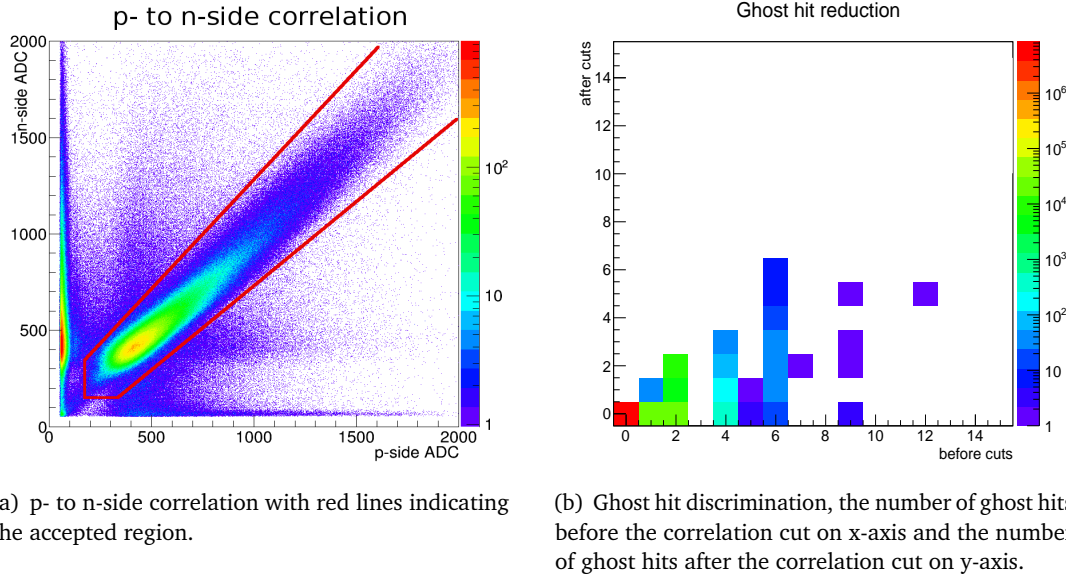


Figure 6.12: Correlation between p- and n-side energy loss and ghost hit discrimination. a) shows the correlation and the position of the applied cut. b) shows the ghost hit discrimination.

plot. Therefore, ghost hits from combinations of clusters with an energy difference greater than the sensor's energy resolution can simply be sorted out, while ghost hits from combinations of clusters with similar energy can hardly be distinguished from true combinations. In that case one can still take the combinations which are closest to the diagonal as a best guess if there are no additional information available that may help to identify the true hit point. At [PANDA](#), such information could come from the tracking information from other sensors that can project the particle's track towards the ambiguous sensor and limit the plausible region for the hit point within the sensor.

In order to discriminate noise and ghost hits, all combinations of p- and n-side clusters that are not along the diagonal are rejected as indicated by the red lines in Figure 6.12(a). Due to noise, or in this beam test also due to one missing APV25 on the n-side, k hits do not always produce k clusters on p- and n-side, but can leave k_p and k_n clusters on the p- and n-side. This results in situations where the number of ghost hits is not always clear. Therefore, the number of ghost hits before and after applying the correlation cut have been approximated by $N_{\text{ghosts}} = k_p \cdot k_n - \sqrt{k_p \cdot k_n}$ and $N'_{\text{ghosts}} = k'_p \cdot k'_n - \sqrt{k'_p \cdot k'_n}$, with $k'_{p,n}$ being the number of clusters from p- and n-side that could be combined with a cluster from the other sensor side so that they survive the correlation cut. From a total of 56,617 ghost hits 21,398 survived the correlation cut, which gives a suppression rate of 62%.

Figure 6.12(b) shows the number of ghost hits before and after applying a cut on the correlation. Because most of the hits were unambiguous from the beginning, the bin with the maximum number of entries is at (0|0). As expected, all entries are in or below the bins on the diagonal, because no additional ambiguities can be created by the correlation cut. The figure also shows that the suppression rate for events with an unequal number of clusters per sensor

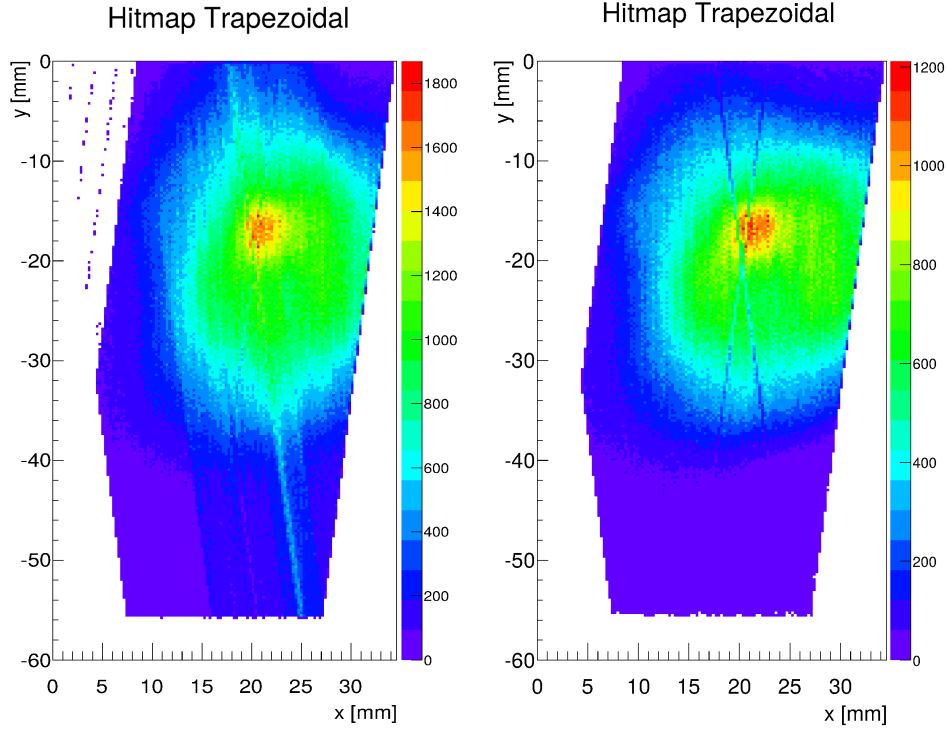


Figure 6.13: The hitmap of the sensor, without (left) and with (right) data selection.

side ($k_p \neq k_n$) is the highest. This would be ghost hit entries without correlation cut of 1, 3, 4, 5, 7, 8, and 9.

Hitmap Figure 6.13 shows the hitmap of the sensor before and after the data selection has been applied. Due to the high noise contribution on the p-side of the sensor, some structures parallel to the left sensor edge can be seen in the hitmap without data selection. These structures disappear and the beam spot has an overall more round shaped structure in the hitmap with data selection as expected from the beam profile. Strip number 252 of the p-side and strip number 129 and 340 of the n-side are defect, so that almost none of their data was utilisable. Two lines of reduced data rate can be found in the hitmap after data selection, these correspond to strip number 252 of the p-side and strip number 340 of the n-side. The strip number 129 of the n-side is at the edge (strips 1-128 from the n-side were connected to the broken APV25) of the hitmap and therefore the reduced data rate is not visible here.

6.2.2 Vertical Pattern in n-side Signal

Figures 6.7(b), 6.8(b), and 6.10(b) for the n-side energy deposition show a regular vertical pattern, especially for the APV25 data from channel 385 to 512. This structure can be explained by the signal transformation on the supply board. While the p-side signals can directly be forwarded to the ADC system, this is not the case for the n-side signals. Due to the n-side's floating ground potential which is shifted by the reverse biasing of the sensor, the n-side signals

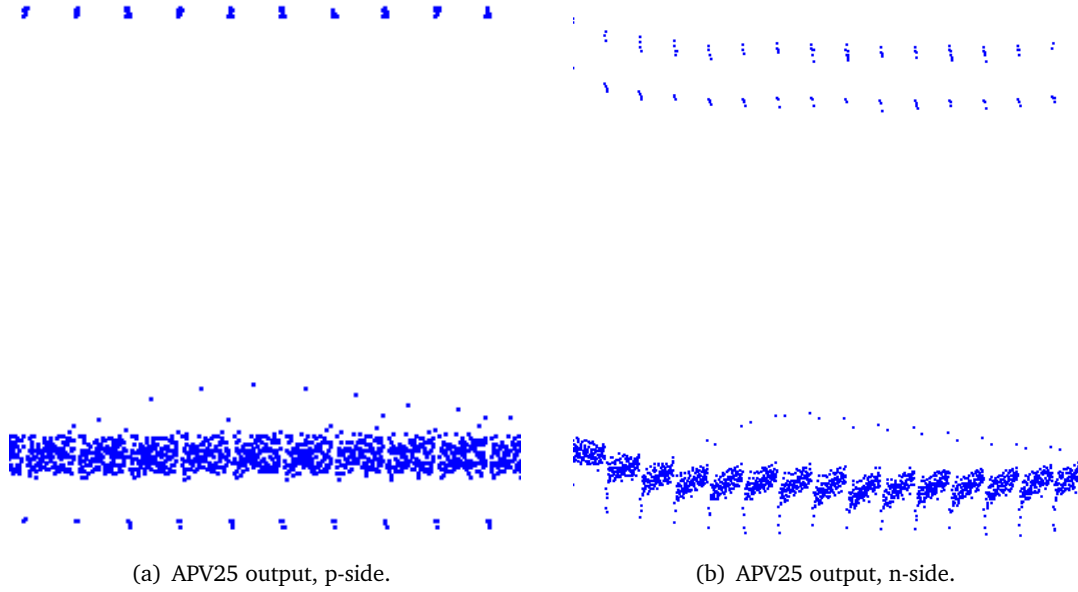


Figure 6.14: The output of a single APV25 for several frames. (a) p-side, (b) n-side.

have to pass a transformer to be shifted to the p-side ground potential before their signal can be forwarded to the common ADC card. As described in Chapter 6.1.3, each APV25 frame starts with a header and an 8 bit address which both contain logical zeros, followed by the analogue data of all 128 APV25 channels which are closer to the logical zero than to the logical one. The 128 strip channels take a time of $128 \cdot 50 \text{ ns} = 6,400 \text{ ns}$ to be sent. During that time, the potential on the transformer input does not vary much, as there are no logical signals in-between the 128 channel signals. As transformers do not show the same loss for all frequencies, this means that the channel signals are shifted by the transformer with time.

A view on the output of a single APV25 over several frames for the p- and n-side can be seen in Figure 6.14. Within each frame, this shows a constant mean level for the p-side and an increasing level over time for the n-side channels. The vertical pattern in the energy deposition figures origins from this shift. The channel ordering within each APV25 frame is:

$$Ch.(n) = 32 \cdot (n \bmod 4) + 8 \cdot \text{INT}(n/4) - 31 \cdot \text{INT}(n/16) \quad (6.1)$$

Therefore, the vertical pattern has a slight increase over 8 channels before it drops and increases over 8 channels again repeatedly.

Another noticeable feature in Figure 6.14 is the difference between the p- and n-side digital part of the APV25 output. While the p-side (Figure 6.14(a)) shows a well defined position for zeros and ones, the n-side (Figure 6.14(b)) shows two rows for the ones and a stretched zero position. The reason for this is that the n-side signals have a slightly longer signal route from the APV25 to the ADC due to the transformation to p-side potential on the supply board. Because of this, the n-side signals arrive a little later than the p-side signals at the ADC. The ADC system has a global setting for all channels for the phase of the clock. This phase shift was set to match the p-side signals, therefore the n-side signals are not perfectly matched to the

ADC and get a few percent of their signal cut off and shifted to the next signal. This results in two situations for the digital ones. Either a one is followed by another one and the ADC sees a one through the whole clock cycle or it is followed by zero so that the lost part of the signal reduces its total height to the lower row of ones. For zeros which are not followed by zero a slight increase of the signal can be observed.

6.2.3 Energy Resolution

The resolution of the deposited energy inside the sensor is important for the p- to n-side correlation in order to discriminate ghost hits, but it is also important for the PID as the deposited energy is dependent on the particle type and momentum. In order to quantify the energy in eV instead of ADC channels, a calibration has to be done first.

Calibration As mentioned above, the energy loss of a particle passing a silicon sensor is a statistical process whose mean value is defined by the Bethe-Bloch formula (Equation 3.1). The mean energy loss for 800 MeV/c protons in silicon without the density and shell correction terms is:

$$-\frac{dE}{dx} = 2\pi N_A r_e^2 m_e c^2 \rho_{Si} \frac{Z}{A} \frac{z^2}{\beta^2} \left[\ln\left(\frac{2m_e \gamma^2 v^2 W_{max}}{I^2}\right) - 2\beta^2 \right] \quad (6.2)$$

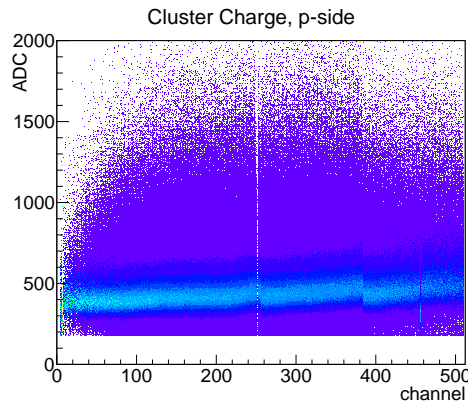
$$\Leftrightarrow \frac{dE}{dx} = -1.08 \cdot 10^{-10} \text{ J/m}$$

In Equation 6.2 $\rho_{Si} = 2.336 \frac{\text{g}}{\text{cm}^3}$ and W_{max} according to [38]:

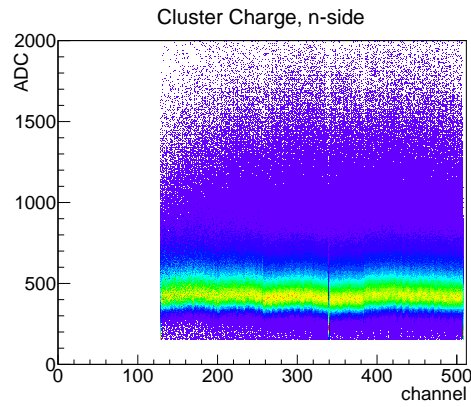
$$W_{max} = \frac{2m_e c^2 \beta^2 \gamma^2}{1 + 2\gamma m_e / M + (m_e / M)^2} \quad (6.3)$$

Here, M is the proton mass. For a 285 μm thick sensor, $\frac{dE}{dx} = -1.08 \cdot 10^{-10} \text{ J/m}$ results in a mean energy loss of $dE = -192 \text{ keV}$.

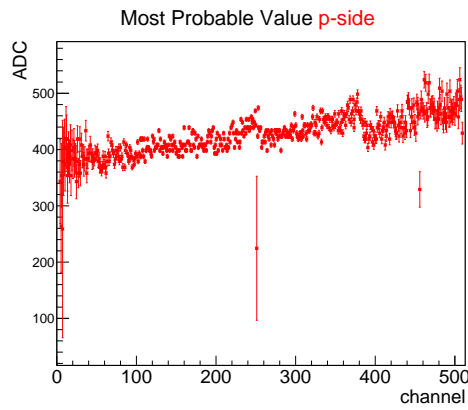
Since the measured data from the test beam contains noise in addition to the signal, the mean energy deposition value maybe influenced by the noise entries. Therefore, it is better to take the most probable value as a reference point instead of the mean value. The most probable signal value in Figure 6.8(c) and 6.8(d) is the peak position at an ADC channel of 420. But those figures show the projection over all channels, while the amplification of the APV25s is not the same for all APV25s and all their channels. Therefore, the energy loss per cluster is shown again in Figures 6.15(a) and 6.15(b) for all channels and both sensor sides, but only for those clusters that pass the data selection. The figures are also normalised to the number of entries per channel to make shifts of the most probable value more obvious. For sub-millimetre thick silicon, the most probable value of energy deposition is about 30% lower than the mean value [66], which means that the peak ADC channel relates to an energy loss of $dE = -0.7 \cdot 192 \text{ keV} = -135 \text{ keV}$. The most probable value per strip channel can be seen in Figures 6.15(c) and 6.15(d). The resulting energy deposition per ADC channel for each strip channel can be seen in Figure 6.16. The mean value for each APV25 is shown in Table 6.1. The non-linearity of the APV25 is $< 2\%$ [61] and is the largest contribution to the errors shown in Table 6.1. This error describes how well the energy calibration could be done, it does not describe the energy resolution per hit, though. The achieved energy resolution per cluster is presented in the paragraph *Cluster Energy Resolution* shown below.



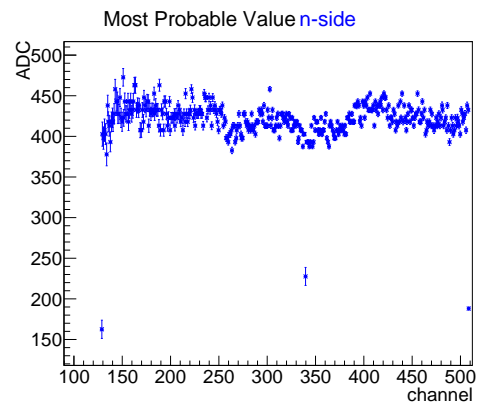
(a) ADC channels measured per cluster vs strip channel, p-side.



(b) ADC channels measured per cluster vs strip channel, n-side.



(c) Most probable energy loss ADC channel vs strip channel, p-side.



(d) Most probable energy loss ADC channel vs strip channel, n-side.

Figure 6.15: Energy loss per cluster measured in ADC channels. a) and b) show the cluster energy vs the strip channel, normalised to the number of entries per channel. c) and d) show the most probable value of energy loss for each channel.

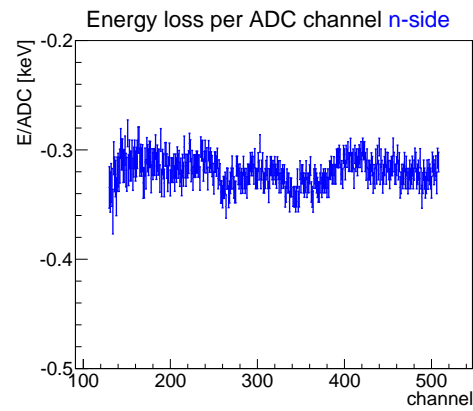
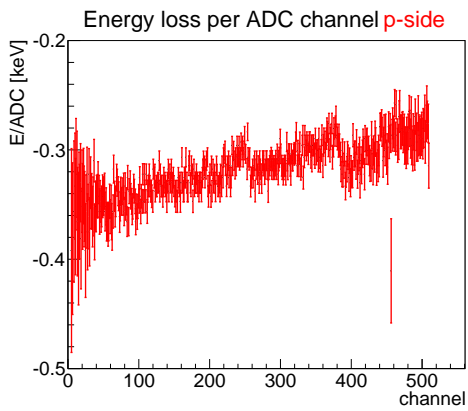


Figure 6.16: Energy loss per ADC channel for each strip channel, (left) p-side and (right) n-side.

APV25	ch. 0-128	ch. 129-256	ch. 257-384	ch. 385-512	all
p-side [eV/ADC]	-349 ± 8	-326 ± 7	-306 ± 6	-297 ± 6	-320 ± 7
n-side [eV/ADC]	—	-318 ± 6	-330 ± 7	-323 ± 7	-323 ± 7

Table 6.1: Mean values of the energy loss per ADC channel for each APV25.

Particle Identification with the Cluster Energy The energy deposition in the sensors of the MVD gives an additional possibility for particle identification that can be used. Particle identification with the MVD cluster energy can be done if several hits inside the MVD exist. Then a truncated mean of the deposited energy from those hits can be calculated to determine the most probable value of deposited energy.

In this way $\frac{dE}{dx}$ is measured, and combined with the momentum information from the whole tracking system the particle type can be determined by comparing the combined set of p and $\frac{dE}{dx}$ with the corresponding Bethe-Bloch function (Figure 3.2). As the distribution of deposited energy is relatively broad and only a limited number of MVD hits per track will exist, the reliability of this PID method will be limited to the resolution of $\frac{dE}{dx}$.

Cluster Energy Resolution The energy resolution of a cluster is mainly important for ghost hit discrimination. As shown above, the ghost hit discrimination depends on an energy difference between ambiguous hits. With a better energy resolution a smaller energy difference is sufficient to separate the ambiguous hits and discriminate the ghost entries.

Before calculating the resolution, the calibration, which has been determined above, has been applied on the energy entries. The three defect strips (strip number 252 of the p-side, and strip number 129 and 340 of the n-side) could not be properly calibrated, therefore these three strips have been excluded from the energy resolution determination. The calibration gives an estimate of the deposited energy in the sensor dE for both p- and n-side. Therefore, the best guess for the deposited energy is $dE = \frac{dE_p + dE_n}{2}$. Then, half of the energy difference between p- and n-side $\frac{dE_p - dE_n}{2}$ is plotted versus dE for each hit point, which is shown in Figure 6.17. The standard deviation of $\frac{dE_p - dE_n}{2}$ is considered as the error of the reconstructed energy σ_{dE} . Figure 6.18 shows the absolute and relative energy resolution. While deposited energies of 200 keV or more are reconstructed with a resolution of about 4.5 %, the lower energy region has a peak at $dE \approx 75$ keV with a resolution of about 11.5 %.

6.2.4 Noise Analysis

As mentioned above, the FPGA returns averaged noise values for all strips every 30 seconds. Those have been recorded over the time of measurement and the averaged values over the measuring time can be seen in Figure 6.19. A capacitor's induced mean square fluctuation of the voltage in a system is [67]:

$$\Delta V^2 = kT/C \quad (6.4)$$

Since the noise on each strip is measured in ADC channels, which means a monotonically rising function of the collected charge, the fluctuation of the charge on each strip is a more

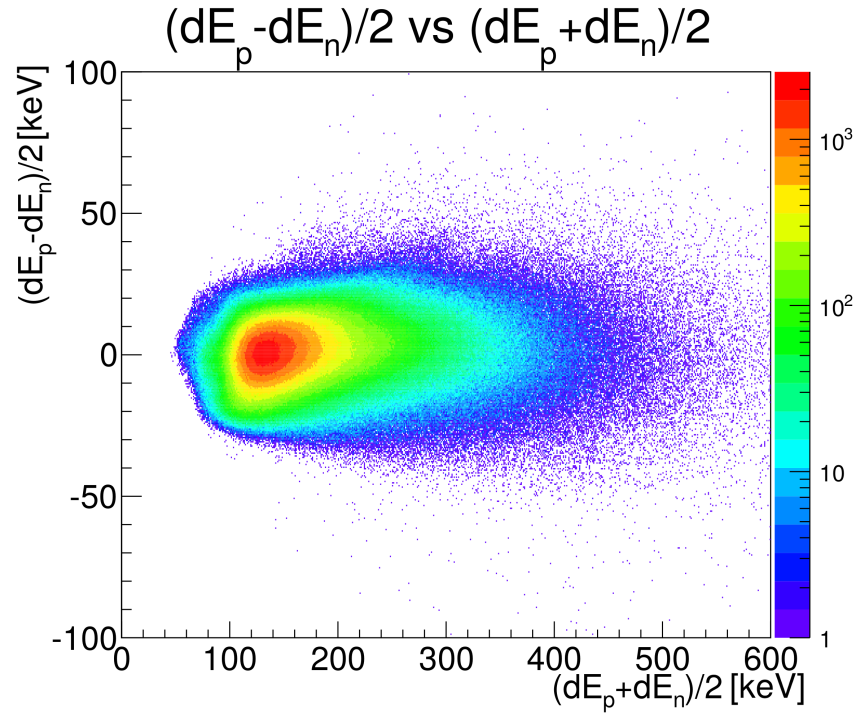


Figure 6.17: Energy difference between p- and n-side versus the energy sum of p- and n-side.

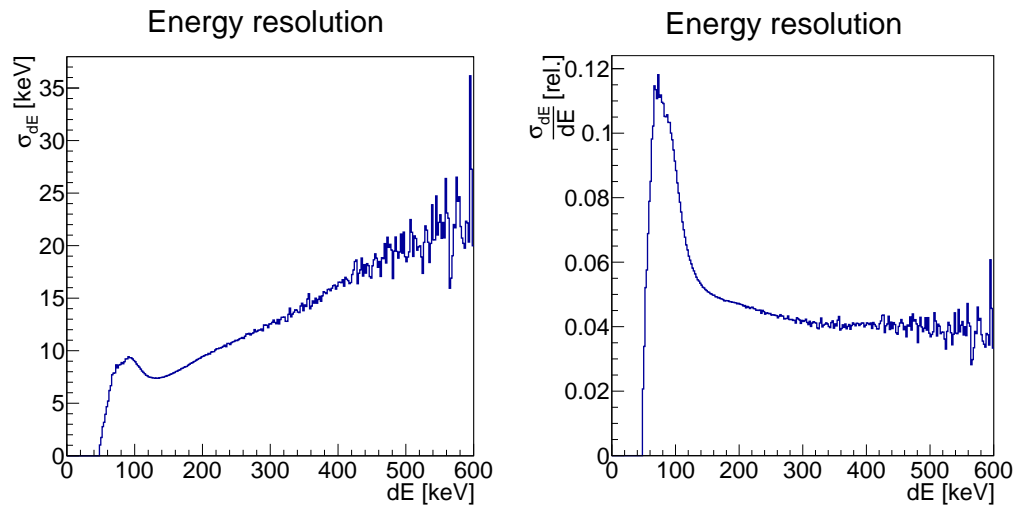


Figure 6.18: The absolute (left) and relative (right) energy resolution of sensor hits.

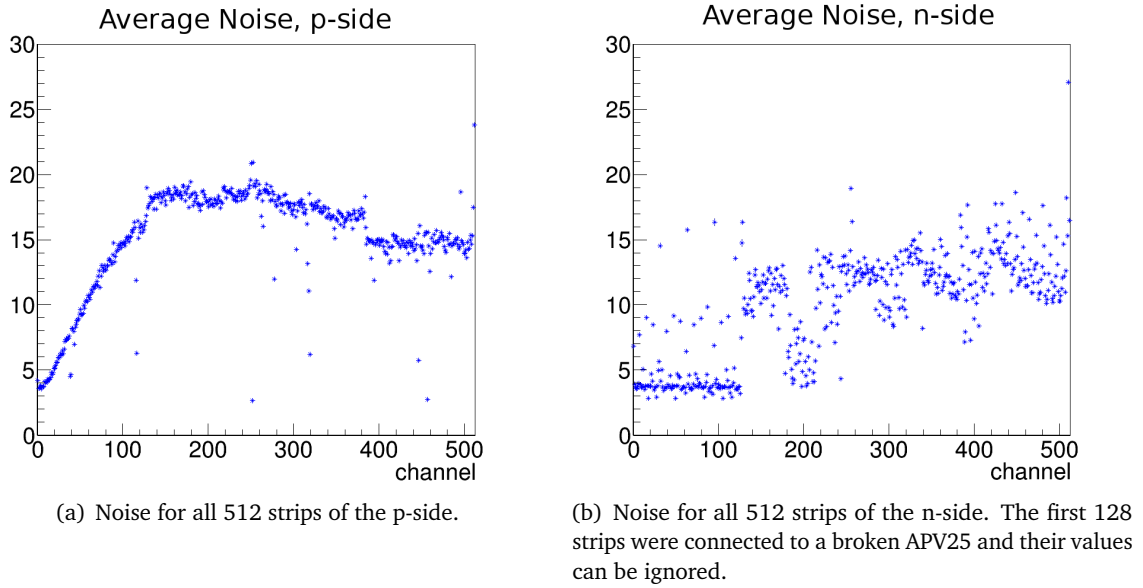


Figure 6.19: The measured noise in ADC channels during the time of measurement with the trapezoidal sensor.

meaningful expression. With $Q = C \cdot U$ Equation 6.4 can be transformed to show the charge fluctuation for a strip n :

$$\Delta Q_n = \sqrt{kTC_n} \quad (6.5)$$

As described in Chapter 4.1 the sensor strips have varying lengths. On both sides of the sensor strip number 1 is the shortest strip with a linear increasing strip length up to strip number 217, which is the first strip with full length. Figure 6.19(a) nicely shows the dependence of the strips' noise to their lengths in the first APV25 range. As the dependence of the strips' lengths to their capacitance was shown in Chapter 4.4, this also shows the dependence between strip capacitance and strip noise. Chapter 4.4 showed a linear relation between strip length and strip capacitance. Therefore, with Equation 6.5 a square root shaped strip number to noise relation could be expected for the strip numbers 1 to 217. That this relation is a little washed-out can be explained by the fact that the strip capacitance is not the only noise source. Two other noise sources are the leakage current of the sensor, which generates a shot noise when the electrons pass the potential barrier at the p-n junction, and the input transistor of each channels preamplifier inside the APV25 [61].

Figure 6.19(a) shows that the APV25 which connects to the strips 385 to 512 on the p-side has a lower noise output than the other APV25s as there is a step visible between the noise of those strips and the noise of the other full length strips. This can be interpreted in two ways, either that there was less physical noise on that APV25 or it provided an overall lower amplification. Chapter 6.2.5 will show that the latter is the case.

The channel range 180 to 220 from the n-side has exceptional low noise entries, these channels are all within the same APV25 and make about one third of that APV25's channels.

There are no special conditions for this channel range or that APV25, the reason for these distinct low noise entries is unknown. In this case these channels had less physical noise, as can be seen in Chapter 6.2.5.

6.2.4.1 Noise Correction

Noise contributions of more than the threshold value of 50 are falsely considered as hits and therefore are lost for the calculation of the average noise value. Thus the calculated average noise value given by the FPGA is biased towards lower values. To compensate this effect, a corrected noise value has been calculated. This is done under the assumption of a Gaussian shaped noise distribution:

$$N(x) \propto e^{-kx^2} \quad (6.6)$$

Since only noise contributions of up to 50 are seen, the average noise value given by the FPGA can be written as:

$$Noise_{FPGA} = \frac{\int_{-\infty}^{50} |x| e^{-kx^2} dx}{\int_{-\infty}^{50} e^{-kx^2} dx} \quad (6.7)$$

The value k in Equation 6.6 can be calculated numerical, with Equation 6.7, as $Noise_{FPGA}$ is available from the FPGA. The corrected noise value can then be calculated as the average absolute value from Equation 6.6 with the determined value for k :

$$Noise_{corrected} = \frac{\int_{-\infty}^{+\infty} |x| e^{-kx^2} dx}{\int_{-\infty}^{+\infty} e^{-kx^2} dx} \quad (6.8)$$

Figure 6.20 shows the corrected noise for the p- and n-side of the sensor. This correction has been applied on all noise values and in further sections of this chapter the term noise always refers to the corrected noise.

6.2.5 Signal to Noise Ratio

The mean signal values for each strip have been divided by their corrected noise entries to determine the **Signal to Noise Ratio (SNR)** for each channel. As the short strips have low noise entries, high SNR entries are reached from the corresponding channels and can be seen in Figure 6.21(a). The strips 385 to 512 from the p-side do not show a step like improvement of their SNR as could be expected due to the step in Figure 6.20(a). This absence of a step like improvement shows that the shift in signal for that APV25 compared to its neighbouring APV25 as it can be seen in Figure 6.8(a) is of the same amplitude than that APV25's shift in noise. Therefore, it can be concluded that this APV25 produces an overall smaller amplification for noise as well as for signal.

The previously mentioned strip region 180 to 220 from the n-side shows a high SNR as it is expected from the low noise in that strip range. The average value of SNR is 30.9 ± 0.8 for the p-side and 30.9 ± 0.3 for the n-side. In the beam test data the p-side showed more noise than the n-side. This is not represented in the mean SNR due to the fact that the APV25 for the

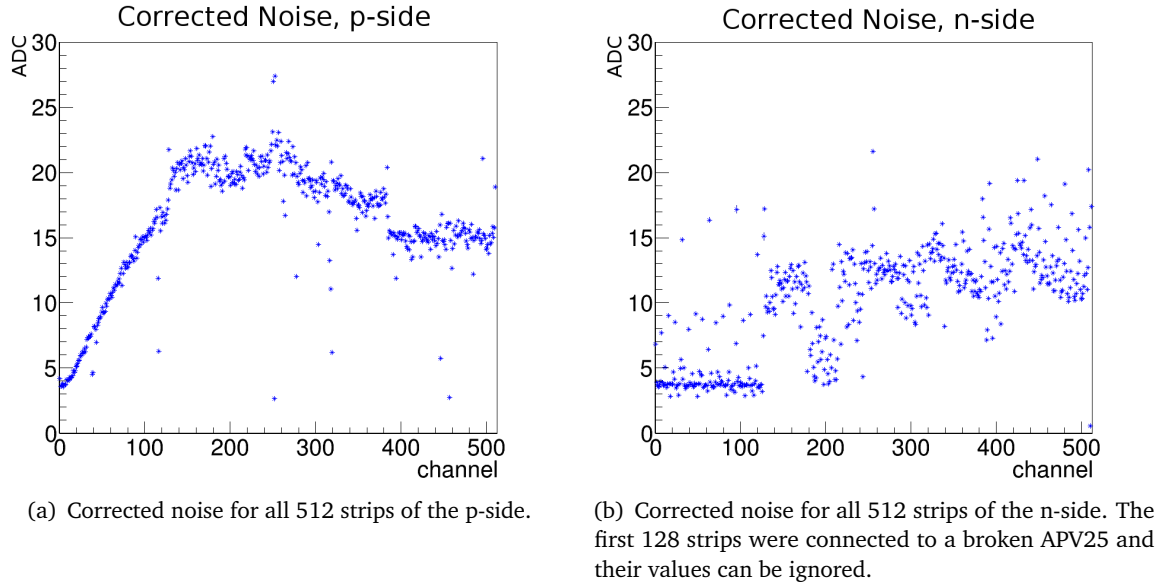


Figure 6.20: Corrected noise in ADC channels.

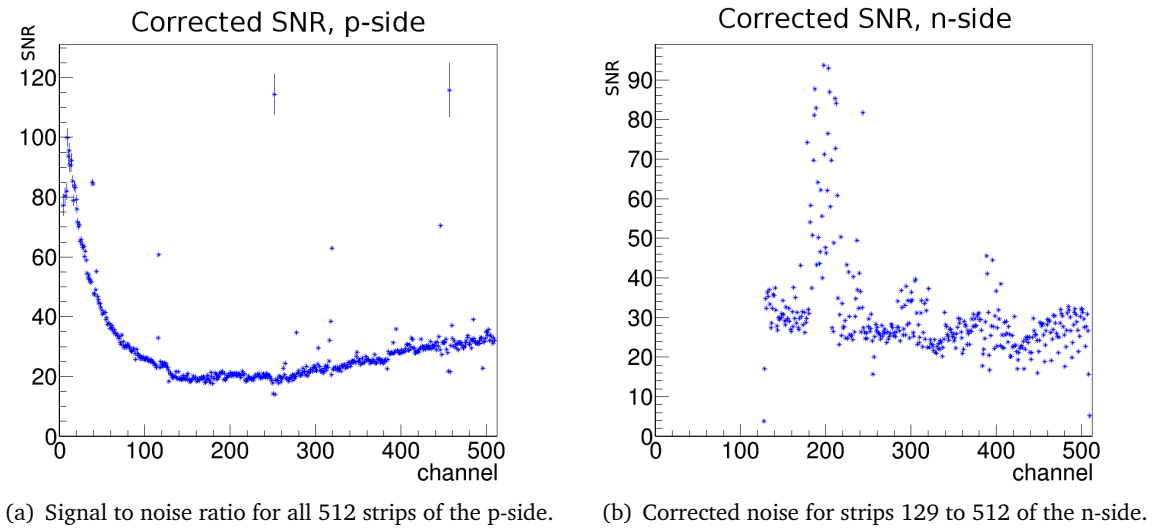


Figure 6.21: This figure shows the signal to noise ratio for the p- and n-sides of the sensor.

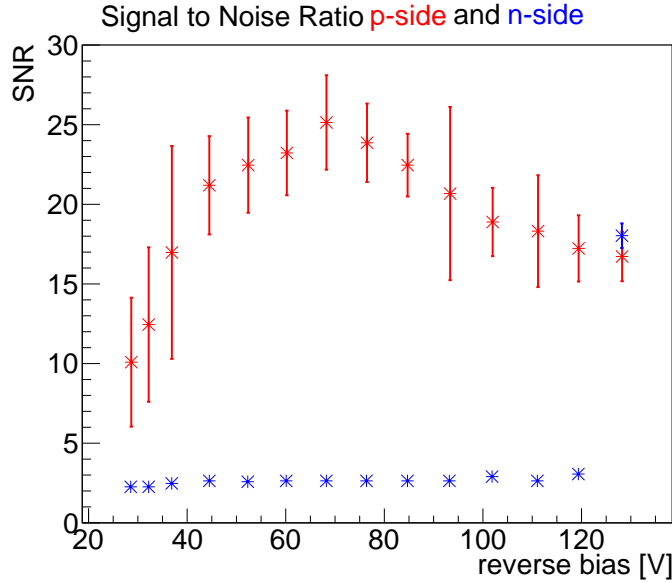


Figure 6.22: The mean **SNR** for different reverse bias voltages shown in red for the p-side and in blue for the n-side.

shortest strips on the n-side was broken, while the APV25 for the shortest strips on the p-side worked correctly. As the short strips carry the lowest noise, the data from this APV25 increase the mean **SNR** of the p-side. A more comparable value is the average **SNR** from p- and n-side excluding the 128 shortest strips on both sides. The average **SNR** for the channels 129 to 512 is 26.5 ± 0.7 for the p-side and 30.9 ± 0.3 for the n-side.

For a **Minimal Ionising Particle (MIP)** with $\beta\gamma \geq 3$, the expected energy loss in the sensor can be calculated with Equation 6.2. For a proton with a momentum of 3 GeV/c, this results in 113 keV. With the same noise, this would result in an average **SNR** for **MIPs** in the channel range 129 to 512 of ~ 15.6 for the p-side and ~ 18.2 for the n-side.

6.2.6 HV Scan

A HV scan was performed during the December test beam. For different reverse biasing voltages the signal and noise strength was recorded. In this measurement the mean **SNR** from p- and n-side after noise correction is shown in Figure 6.22. For the p-side the signal increases with increasing reverse biasing and reaches a maximum at 68.3 V. A further increment of the reverse voltage is still increasing the depletion zone, as 68.3 V is below full depletion. This results in a higher signal, but an increasing reverse bias voltage also increases the leakage current which results in more noise. Thus, the **SNR** drops for higher bias voltages. The n-side does not show any valuable signal before the n-side separation is established by full depletion at > 120 V. When n-side separation is established the **SNR** of the n-side is a bit higher than the **SNR** of the p-side but comparable within their error bars.

As the HV scan was done with a 2.95 GeV/c proton beam, the results shown here are lower than in Chapter 6.2.5 since a higher beam momentum results in a lower deposited energy

according to the Bethe-Bloch formula, while the noise entries are the same in both cases.

6.2.7 Determination of η Distributions

As the noise is not constant for all strip channels, the corrections performed in this section would be more precise if the η distribution would be provided not only as a function of η and cluster charge but additionally as a function of strip channel. Doing this would drastically decrease the number of entries per η distribution slice for one set of channel and cluster charge compared to the number of entries per η distribution slice for a cluster charge range. Therefore, the noise values used for the correction in this section are mean noise values for the corresponding sensor side. These are 16.2 ADC channels for the p-side and 11.8 ADC channels for the n-side, and they correspond to $k_p = 1.1 \cdot 10^{-3}$ and $k_n = 2.3 \cdot 10^{-3}$.

When a hit creates enough electron-hole pairs that two strips can collect enough charge to be above threshold, it is still possible that one or even both of them fall below threshold due to noise contributions to the total signal strength. This case is most probable for η values close to one or zero when one of the two strip signals carries much less charge than the other, so that a small noise contribution can already be enough to put the smaller signal below threshold. For η values around 0.5 the charge is more evenly distributed between both strips, so that both of the signals have a similar distance to threshold. And, it would require a bigger noise contribution for one of the signals to fall below threshold. The probability for the noise contribution to a signal to be in the range of $[x_0, x_1]$ is:

$$P(x_0, x_1) = \frac{\int_{x_0}^{x_1} e^{-kx^2} dx}{\int_{-\infty}^{+\infty} e^{-kx^2} dx} \quad (6.9)$$

For a two-strip hit with q_r and q_l being the ADC channels of the right and left strip without noise contribution, the probability for them to fall below threshold can be calculated as:

$$P_r(q_r) = \frac{\int_{-\infty}^{50-q_r} e^{-kx^2} dx}{\int_{-\infty}^{+\infty} e^{-kx^2} dx}; \quad P_l(q_l) = \frac{\int_{-\infty}^{50-q_l} e^{-kx^2} dx}{\int_{-\infty}^{+\infty} e^{-kx^2} dx} \quad (6.10)$$

$P_r(q_r)$ and $P_l(q_l)$ can also be written as functions of η and $q = q_r + q_l$ by using the following relations:

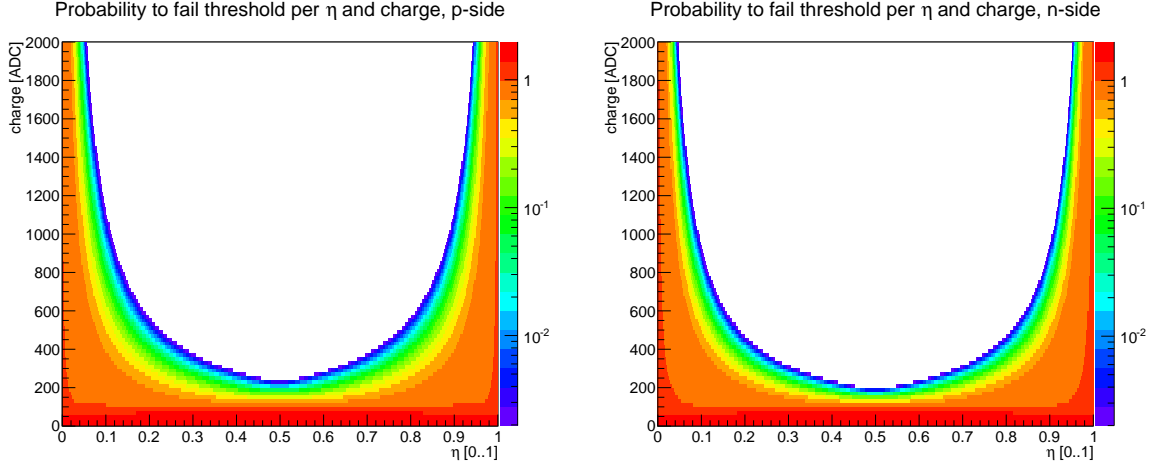
$$q_r = \eta \cdot q \text{ and } q_l = (1 - \eta) \cdot q$$

The combined probability for a two-strip hit to have at least one strip entry falling below threshold due to noise would correctly be calculated as:

$$P(\eta, q) = 1 - (1 - P_r(\eta, q)) \cdot (1 - P_l(\eta, q))$$

But, the overlap of $P_r(\eta, q)$ and $P_l(\eta, q)$ is negligibly small for cluster charges above the cut limit of an ADC channel 175 for the p-side or an ADC channel 150 for the n-side so that it can be approximated by $P(\eta, q) = P_r(\eta, q) + P_l(\eta, q)$, which results in:

$$P(\eta, q) = \frac{\int_{-\infty}^{50-\eta \cdot q} e^{-kx^2} dx}{\int_{-\infty}^{+\infty} e^{-kx^2} dx} + \frac{\int_{-\infty}^{50-(1-\eta) \cdot q} e^{-kx^2} dx}{\int_{-\infty}^{+\infty} e^{-kx^2} dx} \quad (6.11)$$



(a) Probability for a two-strip p-side cluster to be measured as a one-strip cluster.

(b) Probability for a two-strip n-side cluster to be measured as a one-strip cluster.

Figure 6.23: Probability functions $P_p(\eta, q)$ and $P_n(\eta, q)$ that indicate the probability for a two-strip cluster to be measured as a one-strip cluster by colour.

Here, $P(\eta, q)$ is the probability for a two-strip hit for each combination of q and η to be measured as a one-strip hit. Figure 6.23 illustrates $P_p(\eta, q)$ and $P_n(\eta, q)$ with η on the x-axis and q on the y-axis. This information can be used to correct the measured η distribution $N(\eta)$ by calculating the fraction of lost entries and adding those to the measured η distribution.

$$N_{corr.}(\eta, q) = N(\eta, q) + N(\eta, q) \frac{P(\eta, q)}{1 - P(\eta, q)} \quad (6.12)$$

The calculated part of the η distribution that has been lost due to noise $N(\eta, q) \frac{P(\eta, q)}{1 - P(\eta, q)}$ from Equation 6.12 can be seen in Figure 6.24, and the corrected η distribution $N_{corr.}(\eta, q)$ is shown in Figure 6.25. The correction fills the η distribution with additional entries from the single strip clusters. In both figures the y-axis shows the deposited energy, which has been calculated from q with the calibration presented above. For the probability functions $P_p(\eta, q)$ and $P_n(\eta, q)$, the mean calibration values per sensor side (Table 6.1) have been used, and the η distributions have been calibrated with the individual values for each strip channel (in accordance with Figure 6.16).

The remaining number of single strip clusters $N_{single, corr.}(q)$ per cluster energy range can be treated as two-strip clusters with one of the two strip signals being zero.

$$N_{single, corr.}(q) = N_{single}(q) - \int_0^1 N(\eta, q) \frac{P(\eta, q)}{1 - P(\eta, q)} d\eta \quad (6.13)$$

In this way $\frac{N_{single, corr.}(q)}{2}$ clusters are considered to have $\eta = 0$ and the same fraction of clusters are considered to have $\eta = 1$.

After this last adjustment, the η to inter-strip position relation can be calculated by Equation 5.2 for each cluster energy range. The final η to inter-strip position relation corrected by

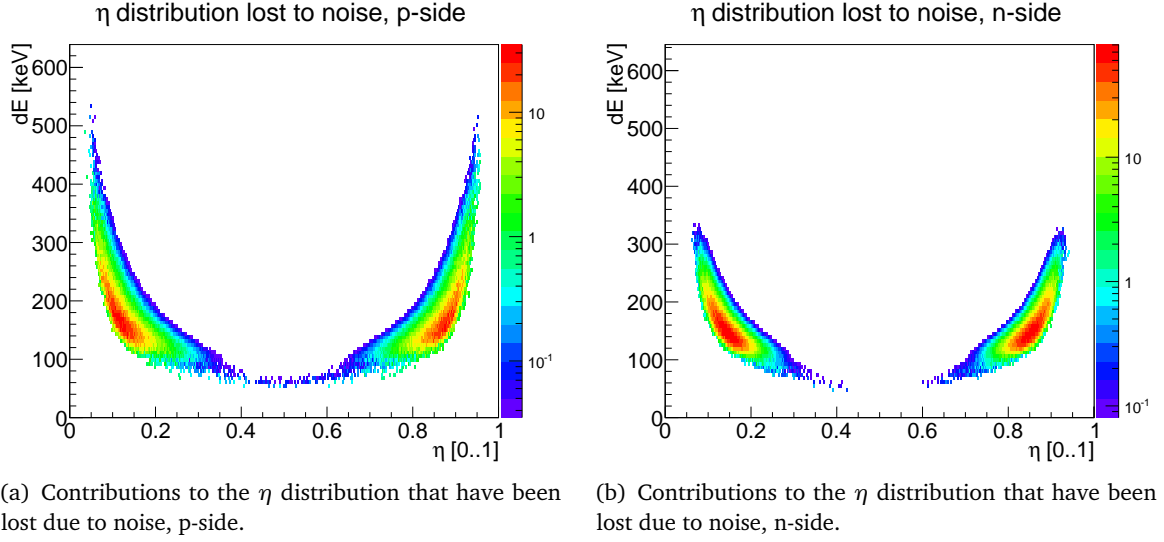


Figure 6.24: Contributions to the η distribution that have been lost due to noise. This result has been calculated by $N(\eta, q) \frac{P(\eta, q)}{1-P(\eta, q)}$.

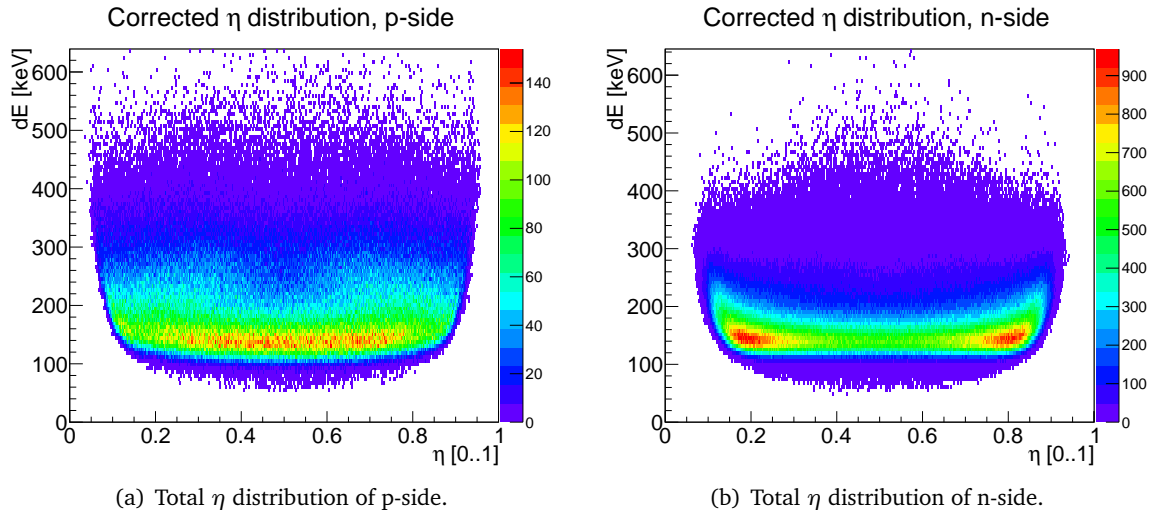


Figure 6.25: Plots of the corrected η distributions $N_{corr.}(\eta, q) = N(\eta, q) + N(\eta, q) \frac{P(\eta, q)}{1-P(\eta, q)}$ for p- and n-side.

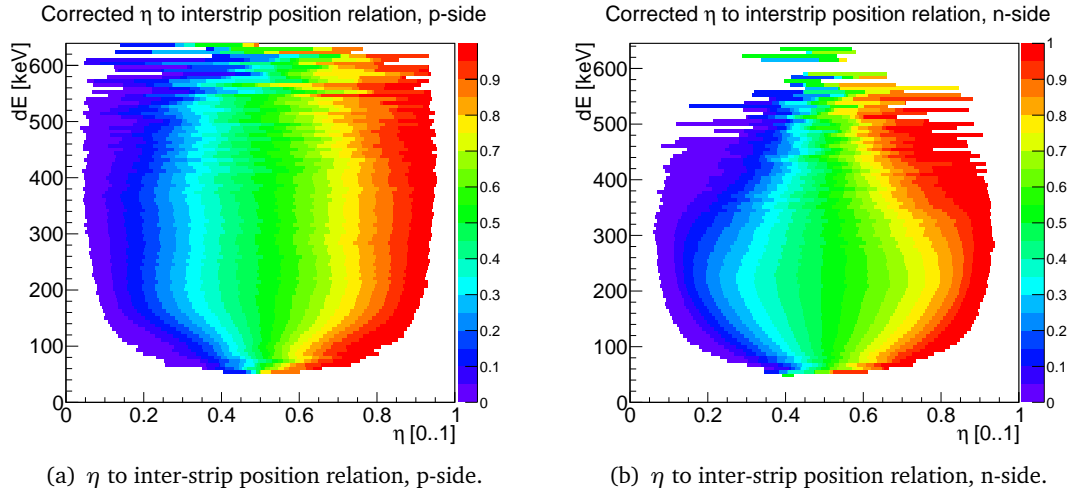


Figure 6.26: η to inter-strip position relation for the p- and n-side. The colour scale indicates the inter-strip position, with purple representing the centre of the left strip and red the centre of the right strip. White areas are combinations of η and cluster charge that have not occurred.

considerations about noise and threshold, and the amount of one-strip clusters is shown in Figure 6.26 for p- and n-side. A high amount of statistics in the η distribution results in a high precision of the η to inter-strip position relation. Due to a decreasing number of entries in the η distribution for cluster charges above the signal maximum, the η to inter-strip position relation is less precise for increasing cluster energies. This is especially visible for cluster energies $dE > 400$ keV, where each horizontal layer of the η to inter-strip position relation can be slightly shifted.

6.3 Conclusion

The successful first test beam with a $\overline{\text{PANDA}}$ trapezoidal prototype sensor showed the functionality of the sensor. The majority of noise and ghost hits can be discriminated by a p- to n-side correlation cut, and reduced the ghost hit entries by 62 %. The suppression factor to be expected for $\overline{\text{PANDA}}$ may differ depending upon the multiplicity distribution. At the $\overline{\text{PANDA}}$ experiment, the remaining ghost hits may be rejected by tracking algorithms, which include the track information from the whole detector setup.

The SNR for the 0.8 GeV/c proton beam was between 20 and 30 for most of the full length strips, with an exception in the n-side channel range from 180 to 220 which showed a SNR of up to 90. An estimation of the average SNR for MIPs on the p-side strips with full length is ~ 15.6 and ~ 18.2 for the n-side strips with full length. The shortest strips on the p-side reached a SNR of up to 100, or up to 60 in an estimation for MIPs . The energy resolution was determined to be about 4.5 % for deposited energies of more than 200 keV, and to have a peak at a deposited energy of about 75 keV with 11.5 %.

Furthermore, the η distribution was determined with a correction for noise and threshold effects.

$\bar{p}p \rightarrow \bar{\Lambda}_c \Lambda_c$ Simulation with PandaRoot

7

The Λ_c is the lightest charmed baryon with a mass of $2.286 \text{ GeV}/c^2$. The production threshold for the reaction $\bar{p}p \rightarrow \bar{\Lambda}_c \Lambda_c$ lies at an antiproton beam momentum of $10.16 \text{ GeV}/c$. Therefore, the decay products are expected to be strongly boosted in forward direction.

In this thesis the decay channel $\bar{p}p \rightarrow \bar{\Lambda}_c \Lambda_c \rightarrow \bar{\Lambda} \pi^- \Lambda \pi^+ \rightarrow \bar{p} \pi^+ \pi^- p \pi^- \pi^+$ has been studied. Its final state products are all charged and include no kaons that could be misidentified as pions. Additionally, with a branching fraction of $(1.07 \pm 0.28)\%$ it is one of the bigger decay channels [38]. Since there are two π^+ and two π^- in the final state, they must be correctly assigned to their mother particles in order to avoid ambiguity.

7.1 Event Generation

The Monte Carlo input for the feasibility study is produced with the *EvtGenDirect* event generator with a beam momentum of $p_{\bar{p}} = 10.2 \text{ GeV}/c$. In order to study the correctness of the event generation as well as the initial properties of the Λ_c , $\bar{\Lambda}_c$, and their decay products, Monte Carlo data for four million events is examined in this section.

These four million events have been produced with the tool *simpleEvtGenRO*. This tool is a compiled version of EvtGen which produces Monte Carlo data of just the primary particles from the event without the further simulation process of propagation through the detector. The initial distribution of the Λ_c and $\bar{\Lambda}_c$ is isotropic in the centre of mass reference system, as can be seen in Figure 7.1. The assumed isotropy is plausible considering the low excess energy, and thus dominant s-wave nature of the final state. Figure 7.2 shows the ratio between transverse and longitudinal momentum of the produced Λ_c and $\bar{\Lambda}_c$ particles. In this chapter, longitudinal always means the direction parallel to the antiproton beam direction, which also defines the z-axis.

The combined momentum of the Λ_c and $\bar{\Lambda}_c$ equals the beam momentum. With a beam momentum exactly on threshold, this would result in $p_t = 0$ and $p_l = \frac{p_{\text{beam}}}{2}$ for both Λ_c and $\bar{\Lambda}_c$. With a beam momentum of $10.2 \text{ GeV}/c$, the excess energy is conserved in the deviation

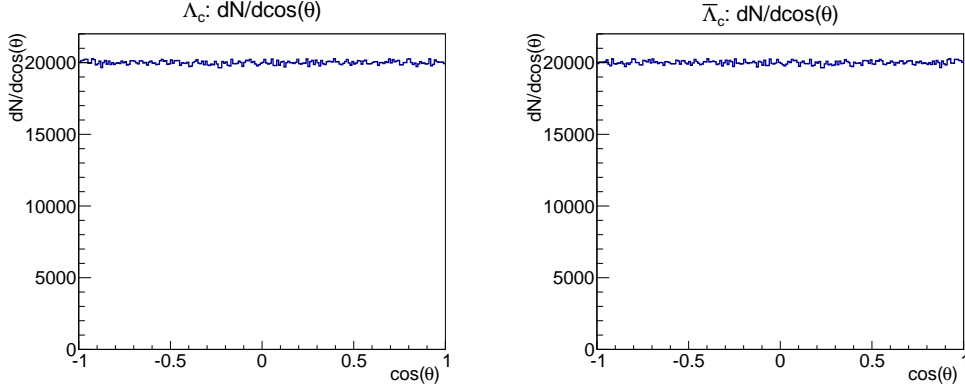


Figure 7.1: The simulated Λ_c and $\bar{\Lambda}_c$ particles are isotropically distributed in their centre of mass system.

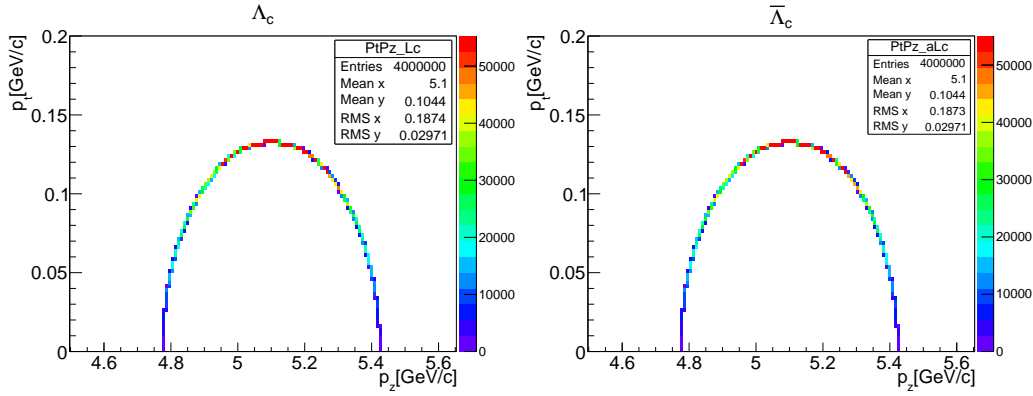


Figure 7.2: The simulated Λ_c and $\bar{\Lambda}_c$ particle's transverse to longitudinal momentum distributions.

of p of the two particles from $\frac{p_{beam}}{2}$. This results in the ellipse shaped ratio of p_t to p_l shown in the figure with the axes lengths being defined by the additionally available energy of the antiproton beam beyond production threshold. The ellipse is a precise curve since this is a two body decay, $\bar{\Lambda}_c \Lambda_c$.

In Figure 7.3 the decay length distributions of the simulated Λ_c and $\bar{\Lambda}_c$ are shown in the z direction and in the xy -plane. An exponential decrease can be observed with a mean value of $134 \mu\text{m}$ in the z direction and a mean value of $3 \mu\text{m}$ in the xy -plane for both Λ_c and $\bar{\Lambda}_c$.

The Λ and $\bar{\Lambda}$ particles show an exponential decrease as well. Their mean value for the decay length along the z direction is 22.3 cm and their mean value for the decay length in the xy -plane is 4.8 cm . The decay length distributions of the Λ and $\bar{\Lambda}$ can be seen in Figure 7.4.

The proper time distributions of the Λ_c and $\bar{\Lambda}_c$, and the Λ and $\bar{\Lambda}$ can be seen in Figure 7.5 and has a mean value of $59.9 \mu\text{m}$ for the Λ_c and $\bar{\Lambda}_c$, and a mean value of 78.9 mm for the Λ and $\bar{\Lambda}$. These numbers are in accordance with the values given by the [PDG](#), which have been the input for EvtGen.

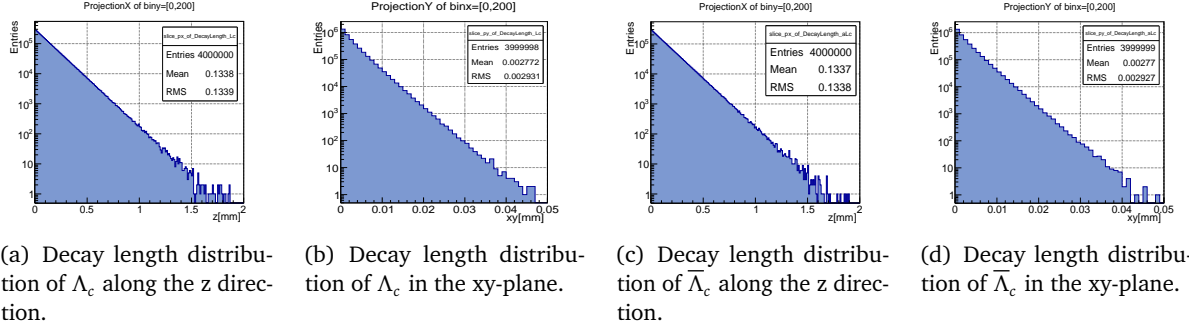


Figure 7.3: The simulated decay length distributions of the Λ_c and $\bar{\Lambda}_c$ in the laboratory frame.

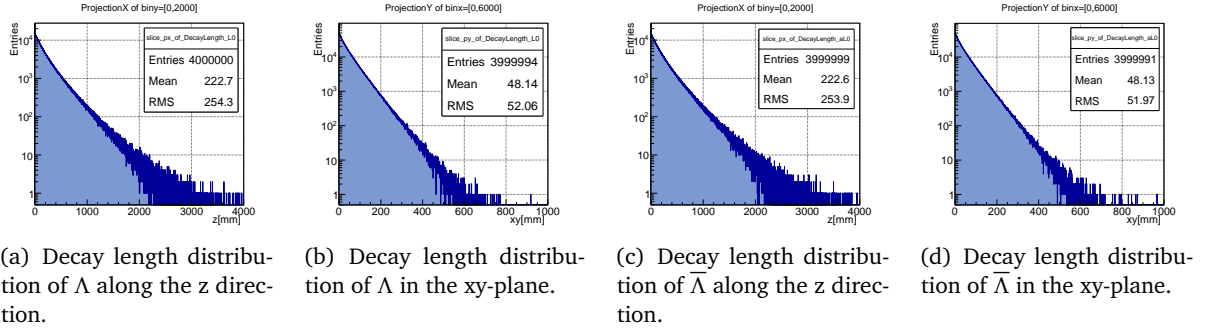
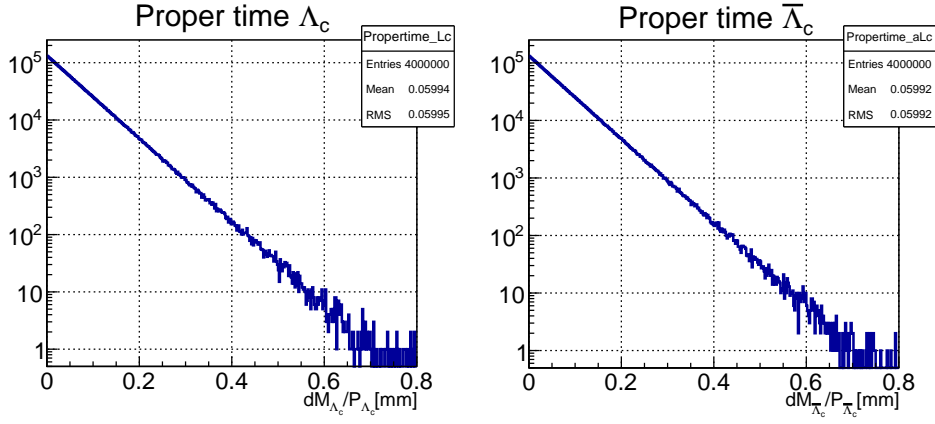
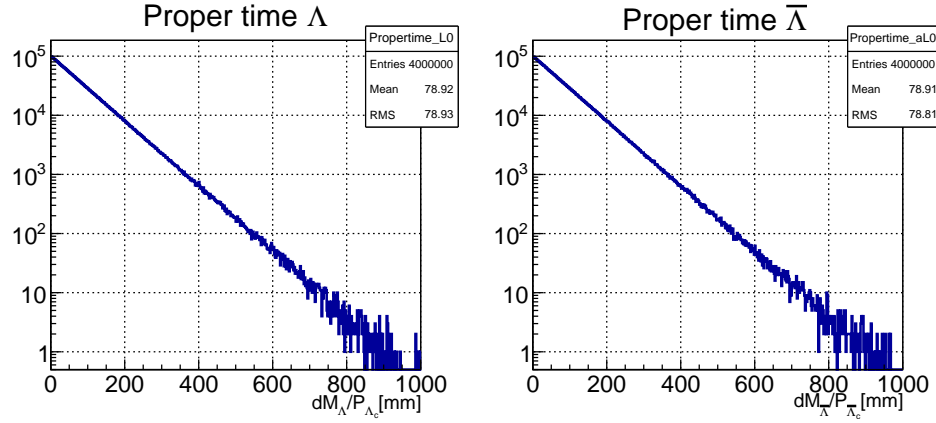
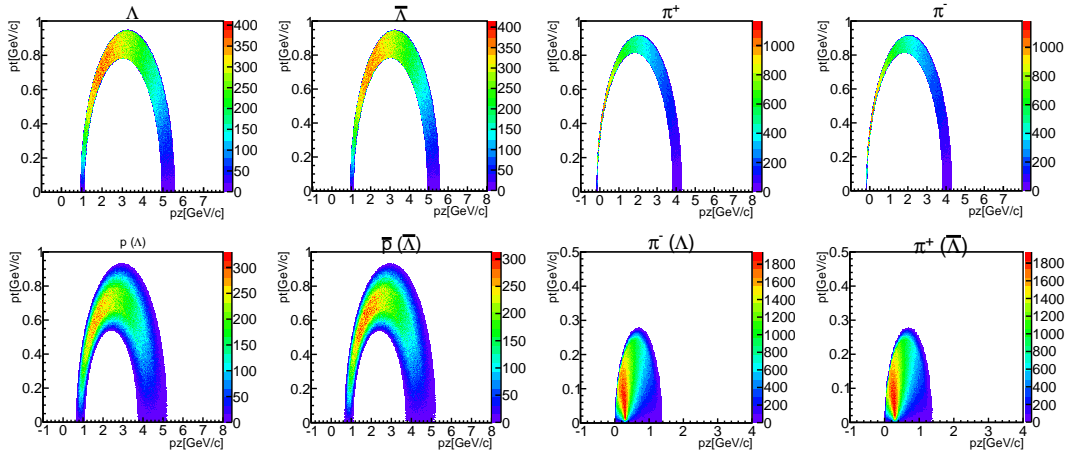


Figure 7.4: The simulated decay length distributions of the Λ and $\bar{\Lambda}$ in the laboratory frame.

Figure 7.6 shows the transverse to longitudinal momentum distributions of the final state particles from the decay channel $\Lambda_c \rightarrow \Lambda \pi^+$. The decay products have again an ellipse shaped distribution of their transverse to longitudinal momenta relation. In contrast to the distributions of Λ_c and $\bar{\Lambda}_c$ which have a precisely defined ellipse, the ellipse shaped distribution of their decay products are broader as their production conditions are varying by the transverse to longitudinal momentum distributions of Λ_c and $\bar{\Lambda}_c$, while the production conditions for Λ_c and $\bar{\Lambda}_c$ are precisely defined by the beam momentum.

7.2 Simulation and Reconstruction of the Decay Channel

A total of 798,000 events has been produced and processed through the whole chain of simulation, digitisation, reconstruction, [PID](#), and analysis. In this section the used detector setup and all steps of reconstruction from the track candidates of the final state particles to Λ_c and $\bar{\Lambda}_c$ candidates are presented.

(a) Proper time distributions of the Λ_c and $\bar{\Lambda}_c$ (b) Proper time distributions of the Λ and $\bar{\Lambda}$ **Figure 7.5:** This figure shows the proper time distributions of the Λ_c and $\bar{\Lambda}_c$, and the Λ and $\bar{\Lambda}$.**Figure 7.6:** Distributions of the transverse momenta of the different decay products plotted versus their longitudinal momenta.

7.2.1 Detector Setup

Within the PandaRoot simulation framework the different substructures of $\bar{\text{PANDA}}$ can be included or excluded to the simulation process. In this study the most complete setup possible was used, this considered the following components:

- Both magnets, the superconducting solenoid in the TS , and the dipole in the FS
- The beam and target pipe
- The complete STT
- The MVD with the forward discs
- All three GEM stations
- The EMC
- The barrel TOF and forward TOF
- The barrel and disc DIRC
- The complete muon system
- The FTS
- The RICH

7.2.2 Track Reconstruction

In the reconstruction step of the simulation, an ideal pattern recognition is used, which means that every hit is associated to the correct track. As described in Chapter 2.2.4, the digitisation process creates *digis* for each MCPoint by considering detector thresholds and noise. In order to make the pattern recognition more realistic, all tracks that do not contain at least four digis from within the same subdetector are rejected.

In this study ideal PID is used and always assigns the correct particle type to each track. The PID could mismatch kaons for pions and may have difficulty to find neutral particles, but since the studied decay channel does not contain kaons or neutral particles in its final state, the usage of an ideal PID should not have a big influence on this study.

Figure 7.7 shows the number of hit points per final state particle track. They show a peak at around 30 hits per particle track which then decreases towards higher hit numbers with another sharp peak at around 50 hits per track. The second peak is the contribution of the FTS as it almost always creates around 40 hits when being hit.

As mentioned above only those tracks with at least 4 hits from within the same subdetector (MVD , STT , GEM , or FTS) are considered to be reconstructable. For each particle type the Monte Carlo energy minus the reconstructed energy has been calculated, and the mean values

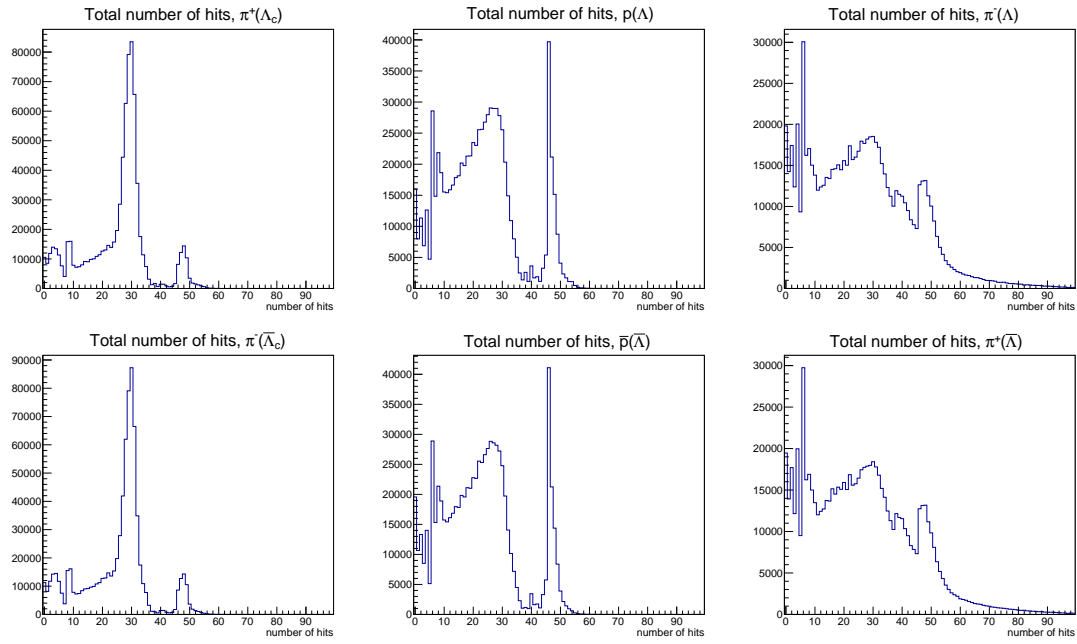


Figure 7.7: Distributions of the total number of detector hits per track, shown separately for each particle type.

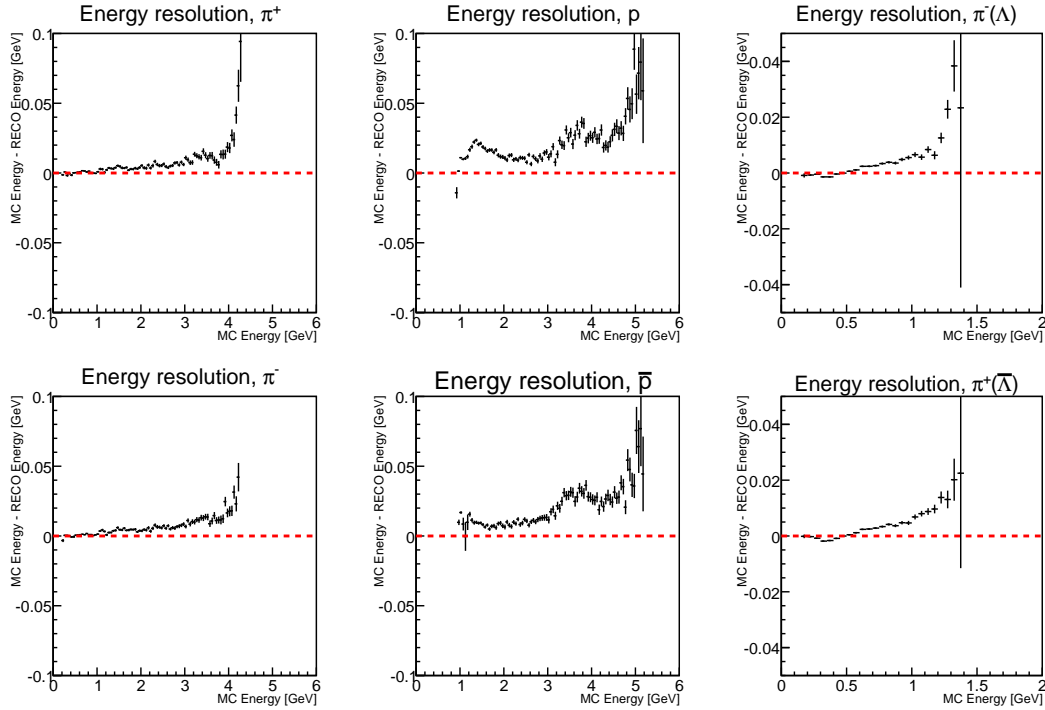


Figure 7.8: Systematic offset of the energy reconstruction per particle. The red dashed line marks the position of no systematic offset for better orientation.

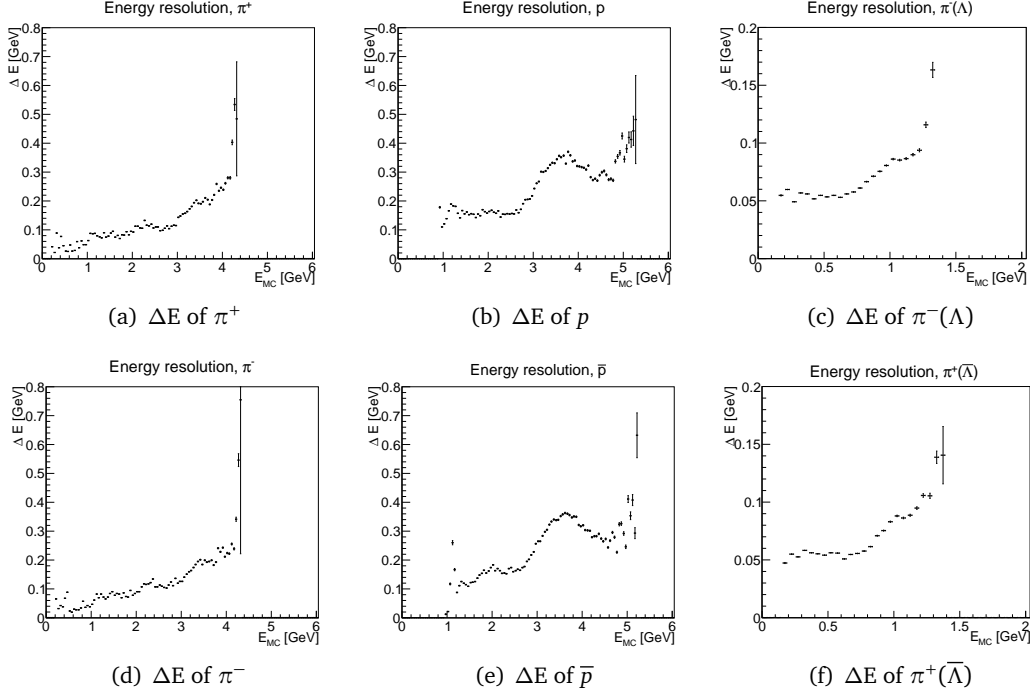


Figure 7.9: Statistical error of the energy reconstruction per particle.

are shown in Figure 7.8. Those represent the systematic offset in energy reconstruction for each particle type as the mean value should be 0 if only statistical errors are present.

For particles with a momentum close to zero, a negative systematic offset for $E_{reco.}$ is expected. This is because the reconstructed energy is always at least the mass-energy, it may deviate to higher values but not to lower values. For higher energies a positive value is expected as the particles may lose some energy due to multiple scattering on their way and therefore have less energy when reaching the next detector as it had initially. The same arguments apply to the systematic offsets of the reconstructed momenta of the particles, which can be found in Appendix C.

The statistical errors for the energy resolutions are calculated as the standard deviation from their systematic offsets and can be seen in Figure 7.9. The reconstructed momentum distributions in the centre of mass frame of the four final state particle types can be seen in Figure 7.10. The protons show the largest tail of background particles besides their peak. In the π^\pm momentum distributions to peaks are visible due to the two different origins of pions in this decay chain. The peaks at low momenta are created by those pions which originate from Λ and $\bar{\Lambda}$, while the peaks at $p_{\pi^\pm, cm} \approx 0.9 \text{ GeV}/c$ are created by those pions which originate from Λ_c and $\bar{\Lambda}_c$.

The reconstruction efficiency for the six final state particles is summarised in Table 7.1. Here, the numbers of found tracks in the table stand for the Monte Carlo truth matched track candidates, the efficiency is given in per cent. The efficiency for the π^\pm from the Λ and $\bar{\Lambda}$

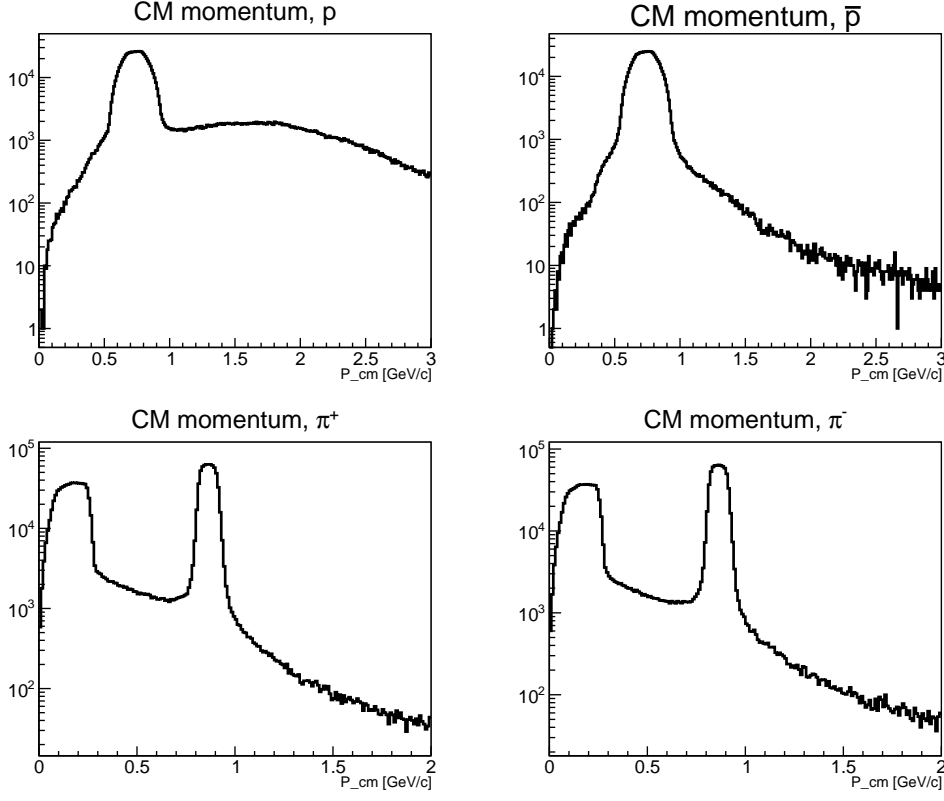


Figure 7.10: Momentum distributions of the four final state particle types in the centre of mass frame.

	ϵ
p	81.4 %
\bar{p}	79.9 %
$\pi^+(\bar{\Lambda}_c)$	82.2 %
$\pi^-(\Lambda_c)$	83.3 %
$\pi^+(\Lambda)$	75.4 %
$\pi^-(\bar{\Lambda})$	75.1 %

Table 7.1: Reconstruction efficiency for the six final state particles.

decays is lower than the efficiency for the π^\pm from the Λ_c and $\bar{\Lambda}_c$ decays, because of their lower momenta in laboratory frame.

7.2.3 Λ and $\bar{\Lambda}$ Reconstruction

For the reconstruction of the Λ particles all possible combinations of found p and π^- are taken as candidates, and for the $\bar{\Lambda}$ particles all combinations of \bar{p} and π^+ are taken as candidates. More secondary protons are produced than secondary antiprotons, therefore the combinatorial background for the Λ candidates is higher than for the $\bar{\Lambda}$ candidates. This can nicely be seen in the reconstructed mass distributions of the Λ and $\bar{\Lambda}$ particles which is shown in Figure 7.11.

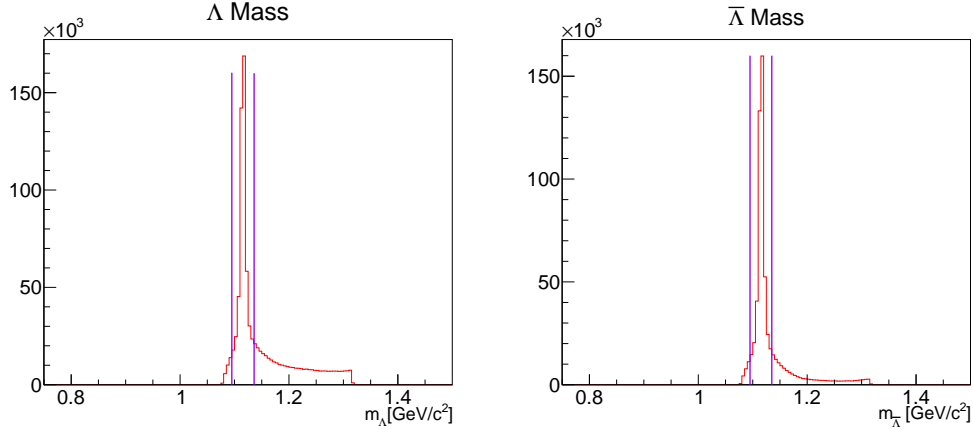


Figure 7.11: Reconstructed mass distributions of the Λ and $\bar{\Lambda}$. The purple lines indicate the cut position for accepted candidates.

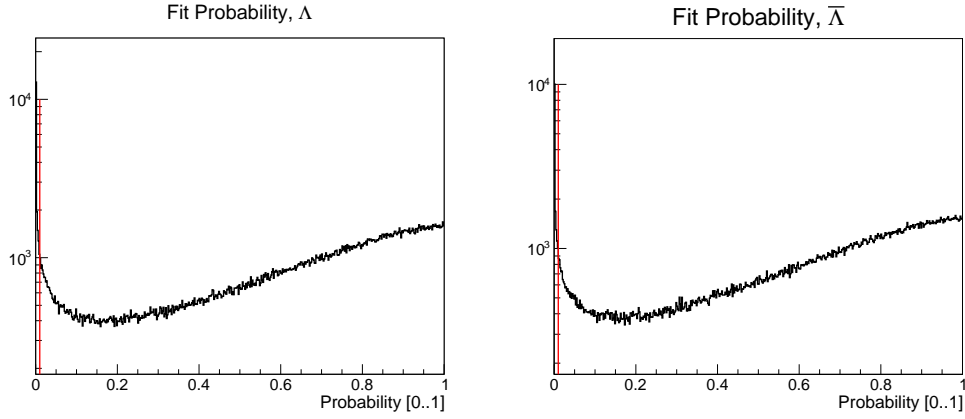


Figure 7.12: Probability distribution of the kinematic fits on the Λ and $\bar{\Lambda}$ candidates. The red line indicates the cut position for accepted candidates.

The purple lines indicate the cut positions for acceptance of the Λ and $\bar{\Lambda}$ candidates, their positions have been chosen to reject the mass regions that predominantly contain background.

After the mass cut has sorted out a large part of the combinatorial background, a kinematic fitter is applied to all remaining candidates. The applied fitter is defined by the PandaRoot class *PndKinFitter* and is used with a mass constraint. This means that the tracks of the candidate daughters are slightly modified within their measurement precision until their combined mass equals the Λ mass $m_\Lambda = 1115.68 \text{ MeV}/c^2$.

The fitter improves the track resolution for true Λ and $\bar{\Lambda}$ candidates as it forces them to have the correct mass. Furthermore, candidates with a poor fit probability ($\text{Prob} \leq 0.01$) can be rejected as their daughters are unlikely to form the correct Λ mass. The probability distribution together with the cut position can be seen in Figure 7.12. The slope in the probability distribution indicates that the parametrisation of the measurement errors has to be adjusted.

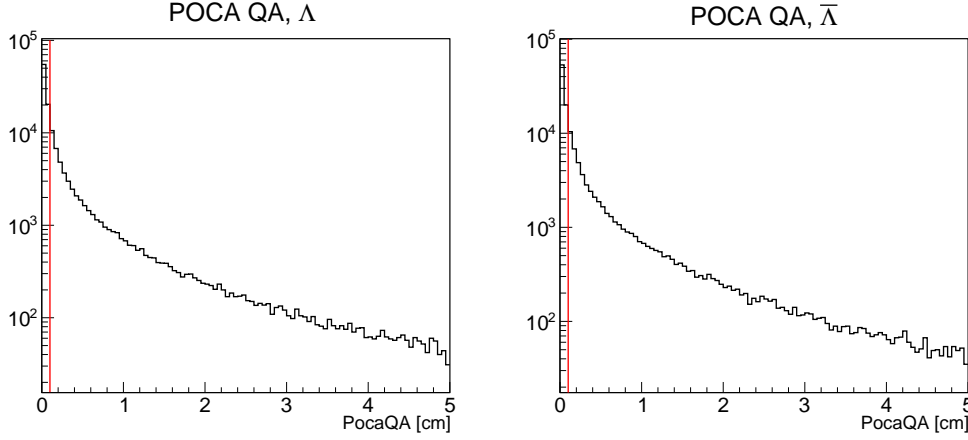


Figure 7.13: $PocaQA$ of Λ and $\bar{\Lambda}$. The red line at $PocaQA = 0.1$ cm indicates the cut position for accepted candidates.

The next step is to reconstruct the point of origin from the Λ and $\bar{\Lambda}$ candidates. This is done by the **Point Of Closest Approach (POCA)** method which takes the two helices of the candidate daughter tracks and calculates their overlapping point in the xy-plane. Typically two xy-positions are found in this way and the position with the smaller distance between the two helices in z direction is then taken to determine the **POCA** by taking the centre of the two helix-points on that xy-position. This distance between the helices in z direction is also returned as the **Point of closest approach Quality Assurance (PocaQA)**, an indicator how well the **POCA** vertex finder worked.

A small **PocaQA** value indicates a good reconstruction with a plausible vertex point. A large **PocaQA** value indicates a flawed reconstruction. The reason for a large **PocaQA** can be a poor track reconstruction of the p or π^- (or the \bar{p} or π^+), but it can also be that the two candidate daughters do not share the same origin and have falsely been combined to a Λ (or $\bar{\Lambda}$). The **PocaQA** values for Λ and $\bar{\Lambda}$ can be seen in Figure 7.13.

A cut that rejects all candidates with a large **PocaQA** should be applied to sort out the falsely combined candidates and to discriminate background events. The chosen cut position is $PocaQA_{cut} = 0.1$ cm and was determined by comparing the **PocaQA** distribution of the signal with that of background events from a **DPM** simulation. For the best **PocaQA** cut value, the following ratio has a maximum:

$$\frac{\left(\frac{N_{sig.,acc.}}{N_{sig.}}(PocaQA_{cut})\right)^2}{\frac{N_{bg.,acc.}}{N_{bg.}}(PocaQA_{cut})} \quad (7.1)$$

Here, $N_{sig.,acc.}$ is the number of accepted Λ or $\bar{\Lambda}$ candidates from the signal after all cuts have been applied. $N_{sig.}$ is the number of Λ or $\bar{\Lambda}$ candidates from the signal after all cuts but the cut on the **PocaQA** value have been applied. $N_{bg.,acc.}$ and $N_{bg.}$ are the corresponding values for the **DPM** events.

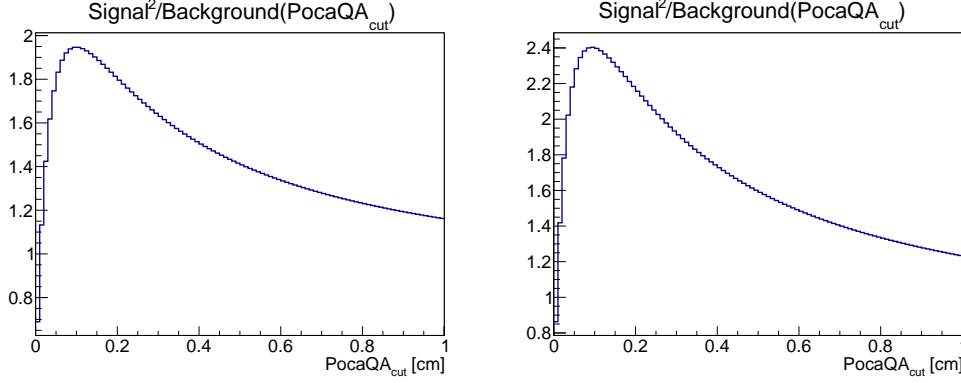


Figure 7.14: The squared ratio of accepted signal candidates divided by the ratio of accepted background candidates as a function of the **PocaQA** cut value. (left) Λ candidates, (right) $\bar{\Lambda}$ candidates.

In order to determine this ratio, Landau distributions have been fitted on the **PocaQA** distributions of the Λ and $\bar{\Lambda}$ candidates from signal and **DPM** events. The fit parameters are

	most probable value	σ
$\Lambda_{\text{sig.}}$	-0.08	$1.7 \cdot 10^{-5}$
$\bar{\Lambda}_{\text{sig.}}$	-0.08	$1.5 \cdot 10^{-5}$
$\Lambda_{\text{bg.}}$	-0.69	$2.83 \cdot 10^{-3}$
$\bar{\Lambda}_{\text{bg.}}$	-1.02	$4.51 \cdot 10^{-3}$

Table 7.2: Summary of the fit parameters from the Landau distribution fits.

summarised in Table 7.2. The ratios can now be calculated as:

$$\frac{\left(\frac{N_{\text{sig.,acc.}}(\text{PocaQA}_{\text{cut}})}{N_{\text{sig.}}}\right)^2}{\frac{N_{\text{bg.,acc.}}(\text{PocaQA}_{\text{cut}})}{N_{\text{bg.}}}} = \frac{\left(\frac{\int_0^{\text{PocaQA}_{\text{cut}}} p_{\text{sig.}}(x)dx}{\int_0^\infty p_{\text{sig.}}(x)dx}\right)^2}{\frac{\int_0^{\text{PocaQA}_{\text{cut}}} p_{\text{bg.}}(x)dx}{\int_0^\infty p_{\text{bg.}}(x)dx}} \quad (7.2)$$

The ratio of Equation 7.2 for Λ and $\bar{\Lambda}$ candidates both have their maximum at about $\text{PocaQA}_{\text{cut}} = 0.1$ cm and can be seen in Figure 7.14.

For candidates with a Monte Carlo truth match the reconstructed vertex resolution after the cuts have been applied is plotted and shown in Figure 7.15. The resolution is $\Delta z = 5$ mm in z direction and $\Delta xy = 1.3$ mm in the xy-plane. Additionally, a comparison of the decay vertices of Λ and $\bar{\Lambda}$ candidates from signal events with those from **DPM** events shows that in both cases the vertices have a peak around the interaction point. The comparison of the vertices from signal candidates to **DPM** candidates can be seen in Figure 7.16. While the **DPM** candidates show a rapid drop towards vertices off the interaction point, the candidates from signal events are more spread. Therefore, another cut has been applied on the distance of the Λ and $\bar{\Lambda}$ vertex position which rejects all candidates with a vertex close to the interaction point.

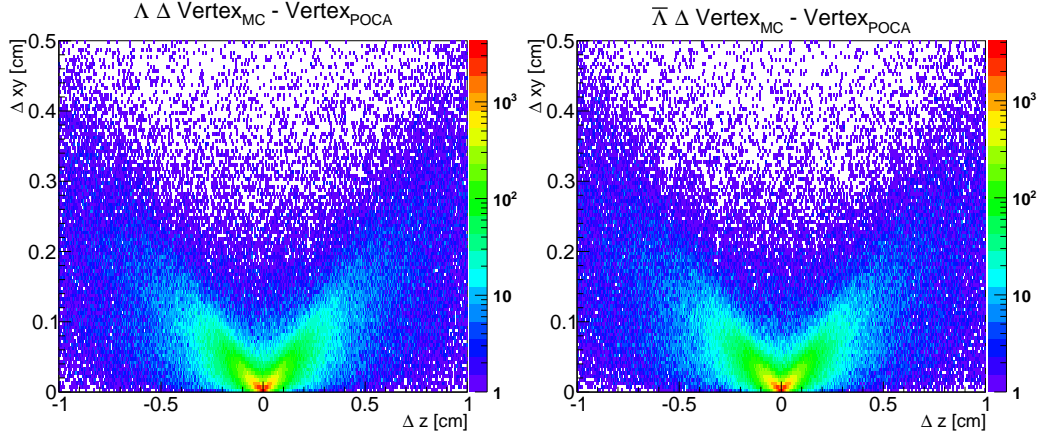
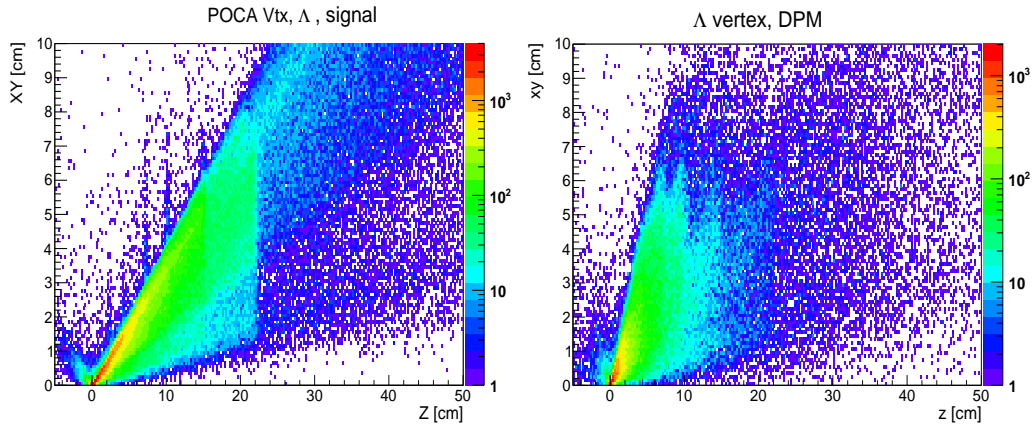
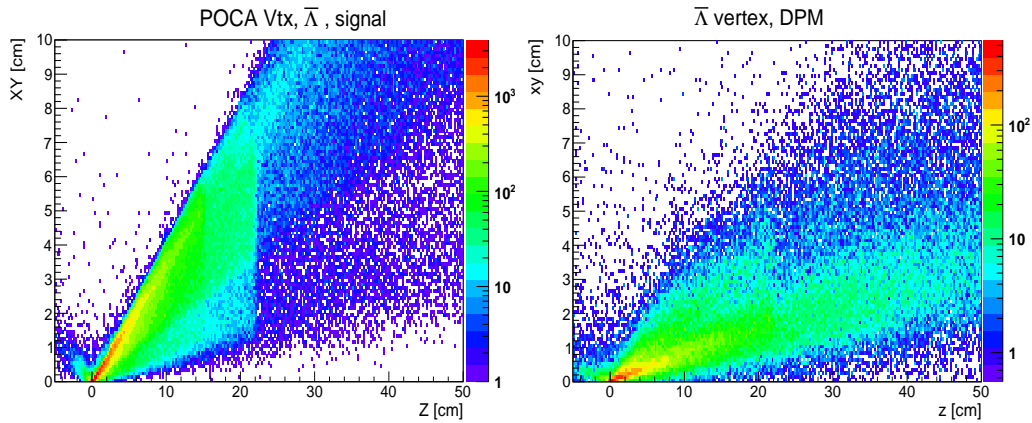


Figure 7.15: Vertex resolution of Λ and $\bar{\Lambda}$. The resolution in z direction is shown on the x-axis and the resolution in the xy -plane is shown on the y-axis.



(a) Vertex distribution of Λ candidates. left) from signal events, right) from DPM events



(b) Vertex distribution of $\bar{\Lambda}$ candidates. left) from signal events, right) from DPM events

Figure 7.16: Comparison between the vertices from signal and DPM events of the Λ and $\bar{\Lambda}$ candidates.

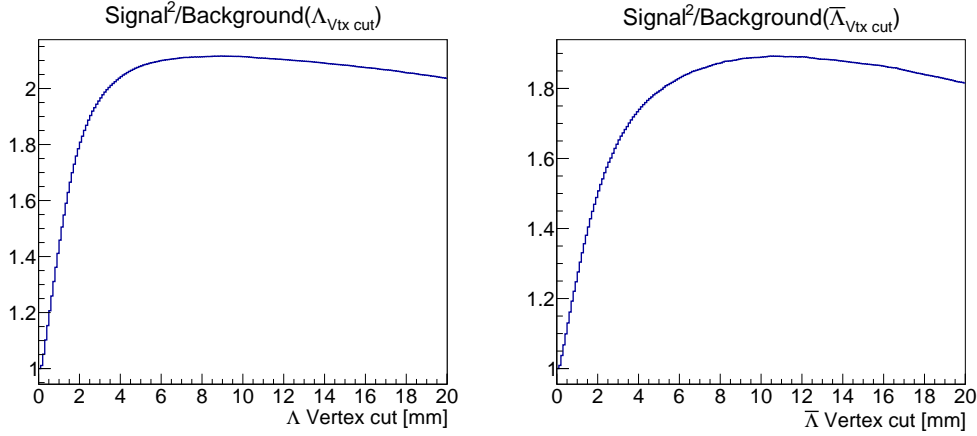


Figure 7.17: The squared ratio of accepted signal candidates divided by the ratio of accepted background candidates as a function of the Λ and $\bar{\Lambda}$ vertex position. (left) Λ candidates, (right) $\bar{\Lambda}$ candidates.

To determine the best cut position for the vertex distance, the squared signal to background relation is plotted versus the cut position which can be seen in Figure 7.17. For the Λ candidates the relation has a maximum at $\Lambda_{\text{Vtx cut}} \approx 9$ mm and for the $\bar{\Lambda}$ candidates a maximum can be found at $\bar{\Lambda}_{\text{Vtx cut}} \approx 11$ mm.

7.2.4 Λ_c and $\bar{\Lambda}_c$ Reconstruction

All combinations of reconstructed Λ and π^+ are taken as Λ_c candidates, and all combinations of reconstructed $\bar{\Lambda}$ and π^- are taken as $\bar{\Lambda}_c$ candidates. From the event generation in Chapter 7.1 the transverse to longitudinal momentum distributions of the final state particles from signal events is known.

All Λ_c and $\bar{\Lambda}_c$ candidates whose daughter particles do not fulfil the transverse to longitudinal momenta relation given by the event generation, are rejected. This is done by defining ellipse shaped cuts on the transverse to longitudinal momentum distributions of the reconstructed particles. The reconstructed transverse to longitudinal momentum distributions of the final state particles can be seen in Figure 7.18 for the daughter particles of Λ_c candidates and in Figure 7.19 for the daughter particles of $\bar{\Lambda}_c$ candidates.

The vertex of the Λ_c and $\bar{\Lambda}_c$ candidates has again been determined with a [POCA](#) finder. In this case we have a candidate that is composed of a neutral and a charged particle and the [POCA](#) finder calculates the overlapping point of a line and a helix in the xy-plane. This typically results in two points and again the point with the smaller distance between the two tracks in the z direction is chosen as vertex.

As the Λ_c and $\bar{\Lambda}_c$ particles have a short decay distance of in average $\sim 134 \mu\text{m}$ in beam direction and only $\sim 3 \mu\text{m}$ perpendicular to the beam line, a possible cut for the candidates is their reconstructed vertex position. Therefore, it is important to know the vertex resolution which is depicted in Figure 7.20. The resolution is $595 \mu\text{m}$ in z direction and $374 \mu\text{m}$ in the xy-plane for the Λ_c candidates. The $\bar{\Lambda}_c$ candidates have a resolution of $600 \mu\text{m}$ in z direction

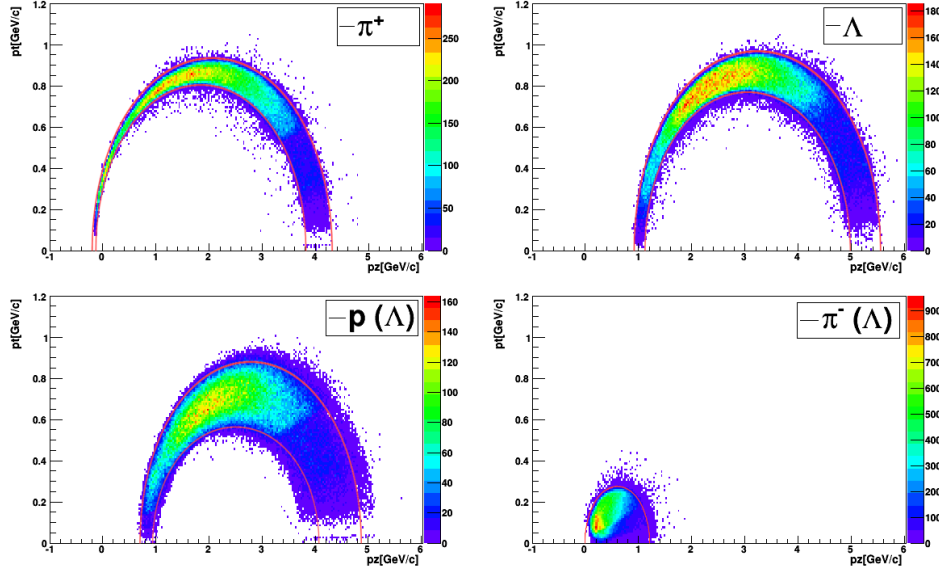


Figure 7.18: The longitudinal to transverse momentum distributions of the daughter particles of reconstructed Λ_c candidates. The red ellipse shaped lines indicate the cut positions for accepted candidates.

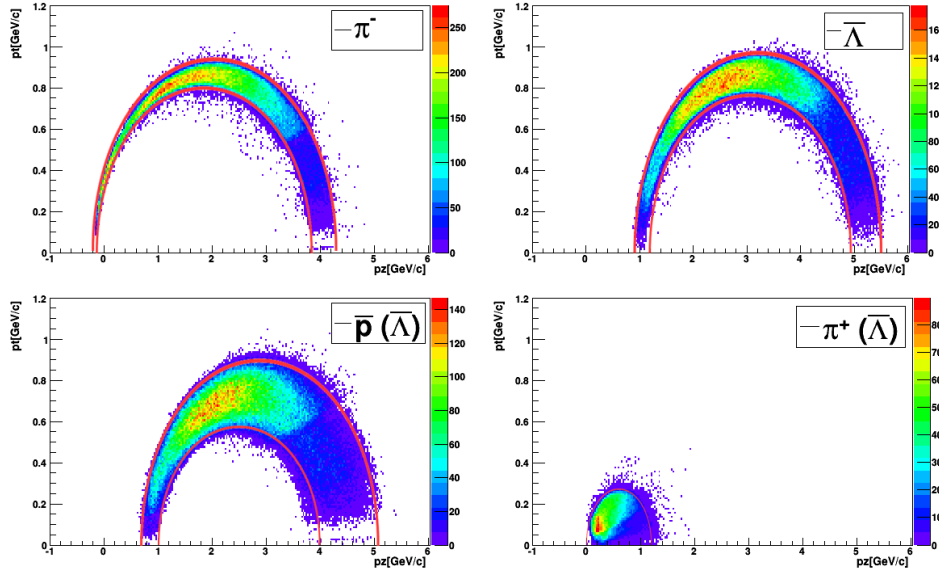


Figure 7.19: The longitudinal to transverse momentum distributions of the daughter particles of reconstructed Λ_c candidates. The red ellipse shaped lines indicate the cut positions for accepted candidates.

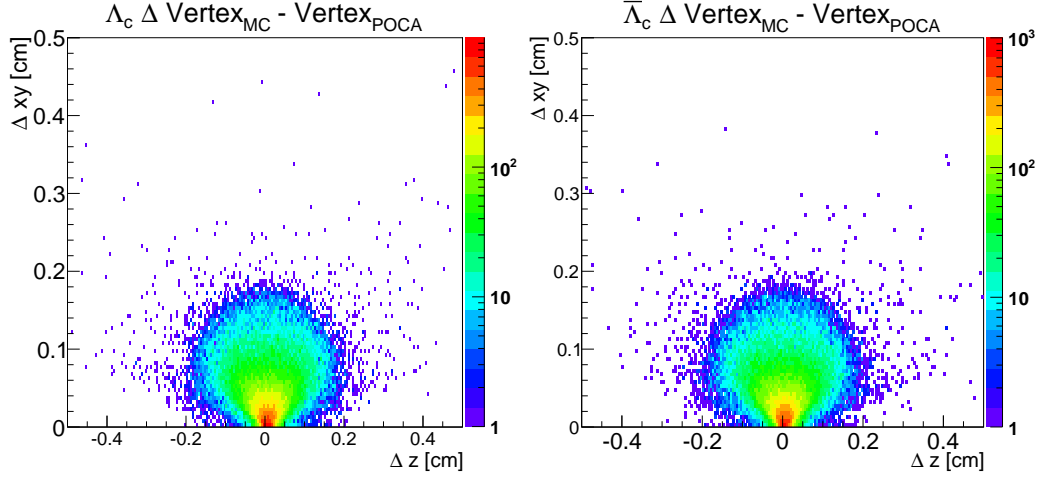


Figure 7.20: Vertex resolution of Λ_c and $\bar{\Lambda}_c$. The x-axis shows the Monte Carlo z vertex position minus the reconstructed z vertex position, and the y-axis shows the distance in the plane perpendicular to the z-axis between the Monte Carlo vertex position and the reconstructed vertex position.

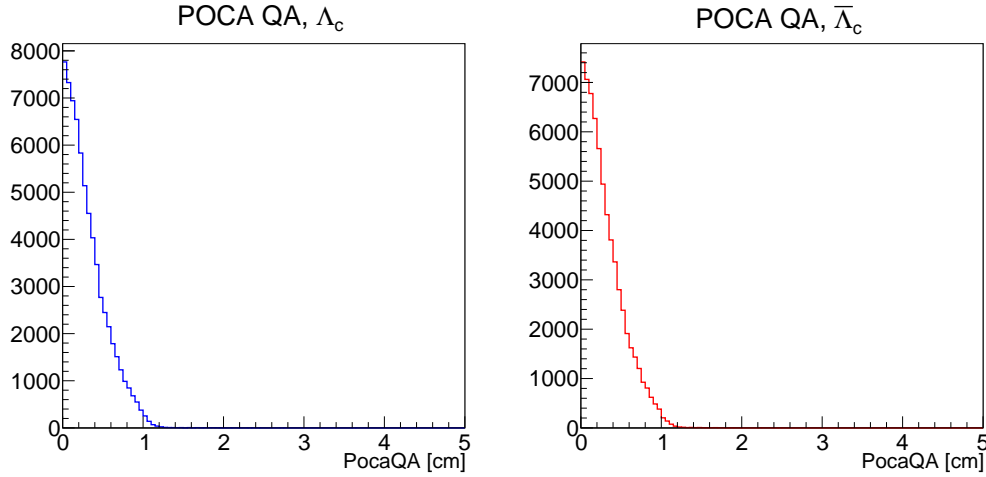


Figure 7.21: PocQA of Λ_c and $\bar{\Lambda}_c$.

and $373\mu\text{m}$ in the xy-plane. The chosen cut function is:

$$\frac{(z_{POCA} - 135\mu\text{m})^2}{(2\text{mm})^2} + \frac{R_{POCA}^2}{(1.75\text{mm})^2} \leq 1 \quad (7.3)$$

The function corresponds to an ellipse around the mean decay position with a 2 mm width in z direction and 1.75 mm width in the radial direction.

Figure 7.21 shows the PocQA distribution for the Λ_c and $\bar{\Lambda}_c$ candidates that survived the applied cuts. Those have already relatively small PocQA values. Furthermore, most of the falsely reconstructed candidates from signal events are already rejected by the previous cuts.

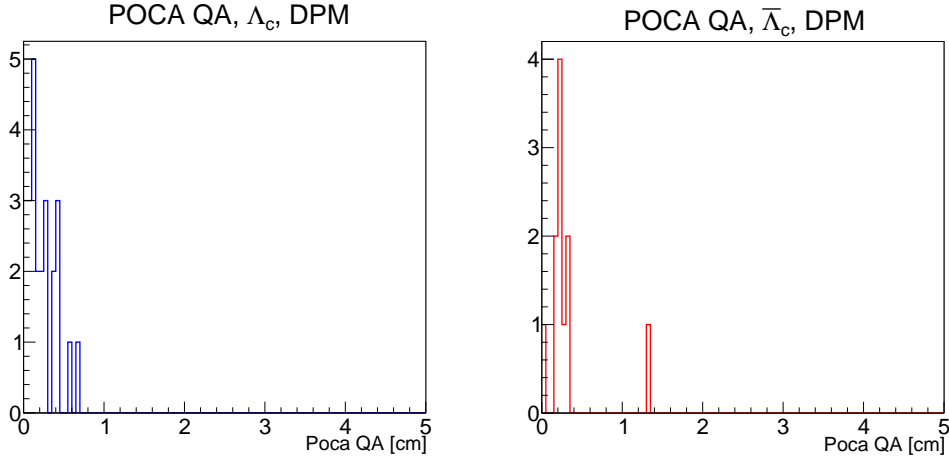


Figure 7.22: Λ_c and $\bar{\Lambda}_c$ candidate *PocaQA* distribution for DPM events.

Therefore, a selection on this value would only make sense, if this distribution is much broader for the background events. This is not the case as can be seen in Figure 7.22.

The energy resolution of the six final state particles shown in Chapter 7.2.2 took all found particles into account even though not all of them can survive the applied cuts. Figure 7.23 shows the systematic offset of the energy reconstruction from only those particles that survived all the cuts. And Figure 7.24 shows the statistical error of only those particles that survived all the cuts. As particles with bigger reconstruction errors are more likely to fail the cut conditions, predominantly those particles with low errors made it into these plots which results in a better resolution compared to the resolution of all particles shown above.

The last selection step for the Λ_c and $\bar{\Lambda}_c$ candidates is to remove possible ambiguities. This is done by using the PndKinFitter on the candidates with a mass constraint to the PDG mass entry for Λ_c , then only the candidate with the lowest χ^2 is accepted. This mass constraint fit is only used to select a candidate when an event provided two or more ambiguous candidates, it is not used for further reconstruction purposes, in particular not for the mass reconstruction.

Figure 7.25 shows the transverse to longitudinal momentum distributions of the reconstructed Λ_c and $\bar{\Lambda}_c$ candidates. Also here an ellipse-shaped cut has been applied on the transverse to longitudinal momentum distributions. A total of 67,522 Λ_c candidates survived the cuts of which all but 5 candidates are also Monte Carlo true Λ_c particles. Out of the $\bar{\Lambda}_c$ candidates 64,734 candidates survived the cuts with only 2 candidates which are not Monte Carlo true $\bar{\Lambda}_c$ particles. Taking the 798,000 simulated events into account, this corresponds to a reconstruction efficiency of 9.4% for the $\Lambda_c \rightarrow \pi^+ p \pi^-$ decay and 9.2% for the $\bar{\Lambda}_c \rightarrow \pi^- \bar{p} \pi^+$ decay.

Figure 7.26 shows the mass and momentum resolutions of the reconstructed Λ_c and $\bar{\Lambda}_c$ candidates. The results are summarised in Table 7.3. For each Λ_c and $\bar{\Lambda}_c$ candidate, the missing mass has been calculated and plotted in Figure 7.27. The missing mass has a peak at the Λ_c mass of $m_{\Lambda_c} = 2.29 \text{ GeV}/c^2$ in both cases. The widths of the two missing mass peaks is comparable to the widths of the two mass peaks.

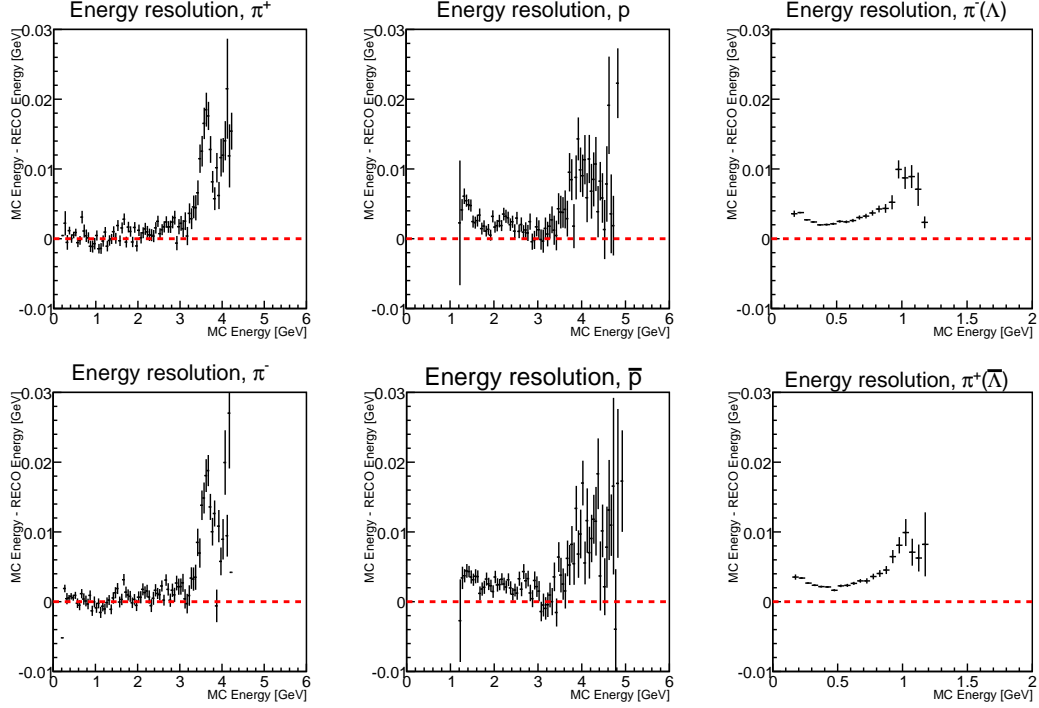


Figure 7.23: Systematic offset of the energy reconstruction per particle. Shown for all particles that survived the cuts for Λ_c or $\bar{\Lambda}_c$ candidates.

	ϵ	RMS_m	RMS_p
Λ_c	8.5 %	14.3 MeV/c ²	56.8 MeV/c
$\bar{\Lambda}_c$	8.1 %	14.5 MeV/c ²	57.2 MeV/c

Table 7.3: Reconstruction efficiency, and mass and momentum resolutions of the Λ_c and $\bar{\Lambda}_c$ signal events.

7.2.5 Exclusive $\bar{\Lambda}_c \Lambda_c$ Reconstruction

When both particles Λ_c and $\bar{\Lambda}_c$ have been reconstructed in an event their combined system can be compared to the initial beam conditions. Due to the fixed beam conditions the error in reconstructed total energy and momentum, and the missing mass of an event can be calculated when all final state particles have been found. The result can be seen in Figure 7.28.

Since $\bar{\text{PANDA}}$ will have well defined beam conditions from HESR , these initial beam conditions can be used to perform a kinematic fit on the reconstructed events. The class *Pnd4CFitter* of PandaRoot fulfils this purpose. The class takes the combined $\bar{\Lambda}_c \Lambda_c$ system and the initial beam plus target condition as input and then modifies all reconstructed final state candidates so that they coincide with the initial beam and target conditions.

For the majority of combined $\bar{\Lambda}_c \Lambda_c$ systems the fitter worked well so that no energy or momentum difference between the initial and final conditions is present. The distributions after using *Pnd4CFitter* can be seen in Figure 7.29 and both plots show a strong peak at zero.

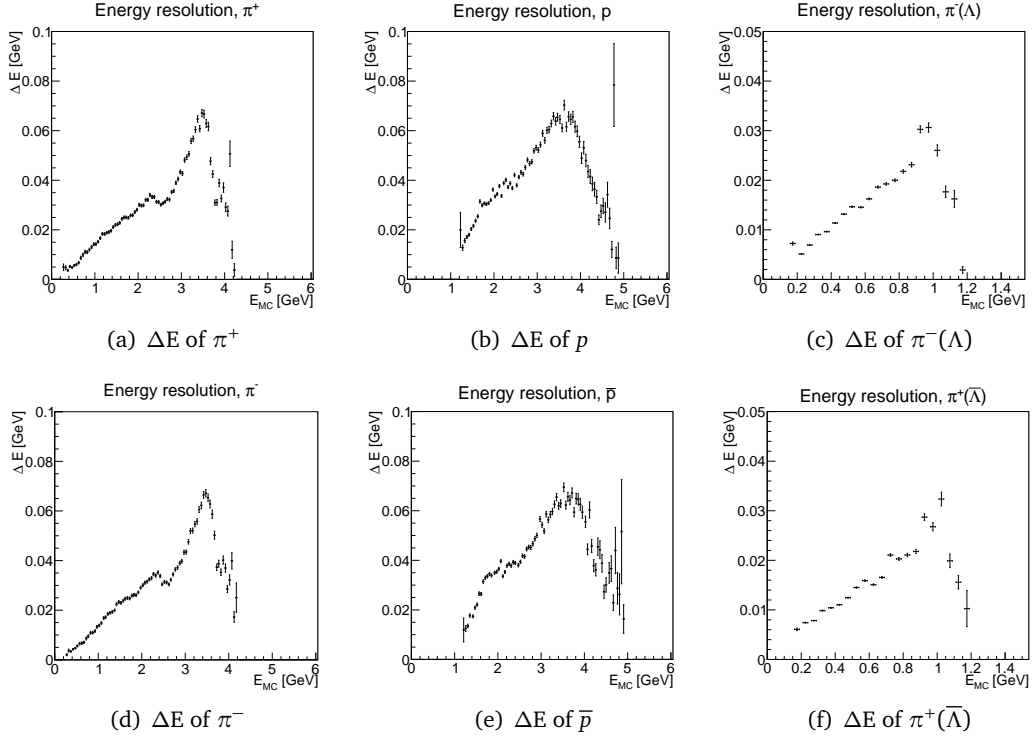


Figure 7.24: Statistical error of the energy reconstruction per particle. Shown for all particles that survived the cuts.

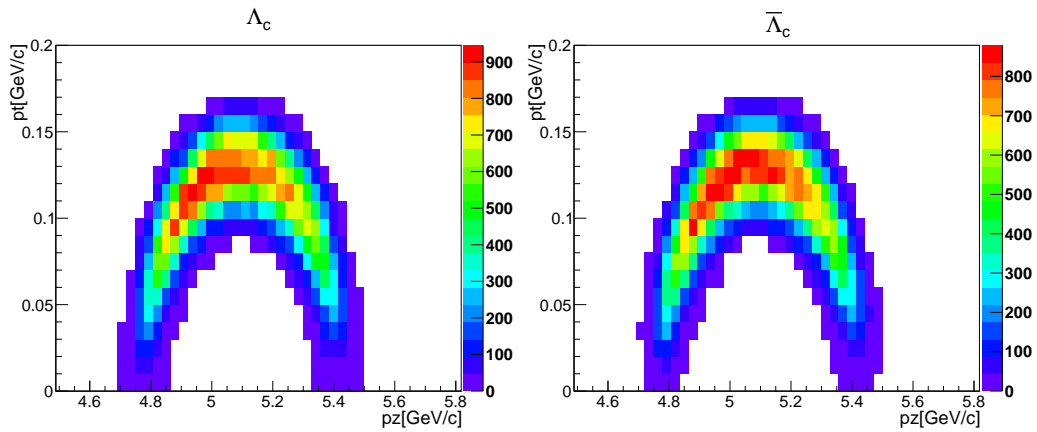


Figure 7.25: Distributions of the transverse momentum of the reconstructed Λ_c and $\bar{\Lambda}_c$ plotted versus their longitudinal momentum.

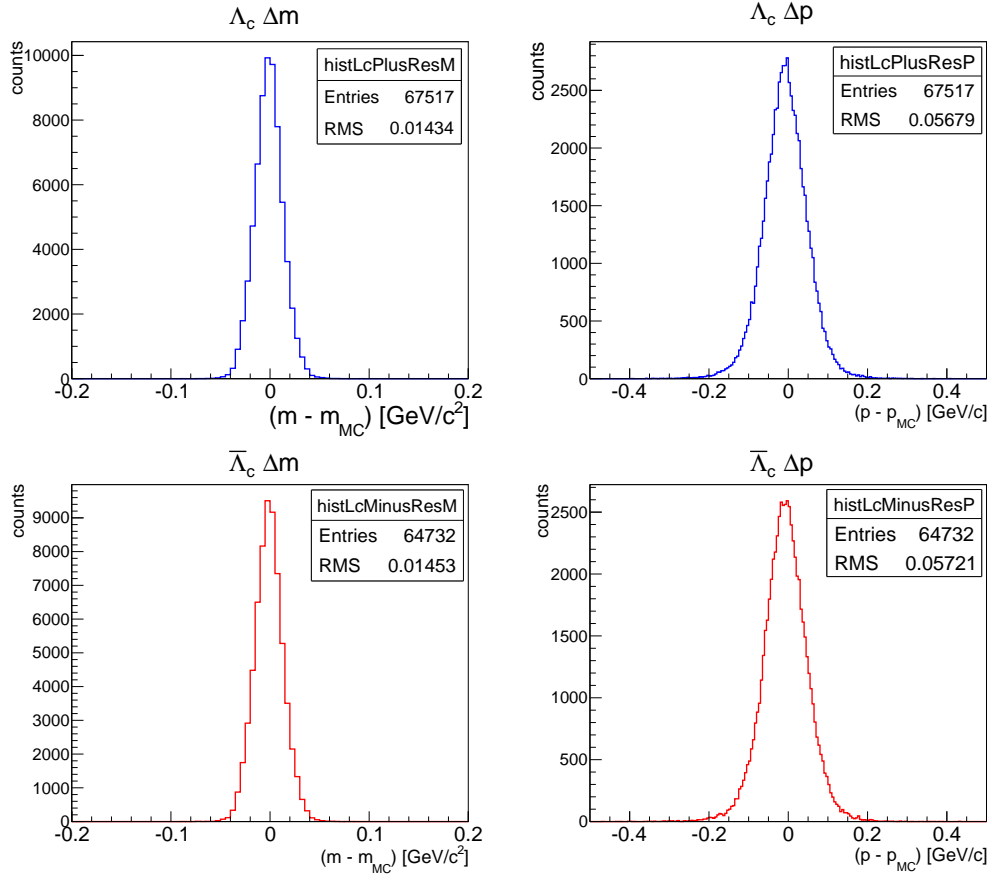


Figure 7.26: Resolution of the reconstructed mass and momentum of the Λ_c and $\bar{\Lambda}_c$.

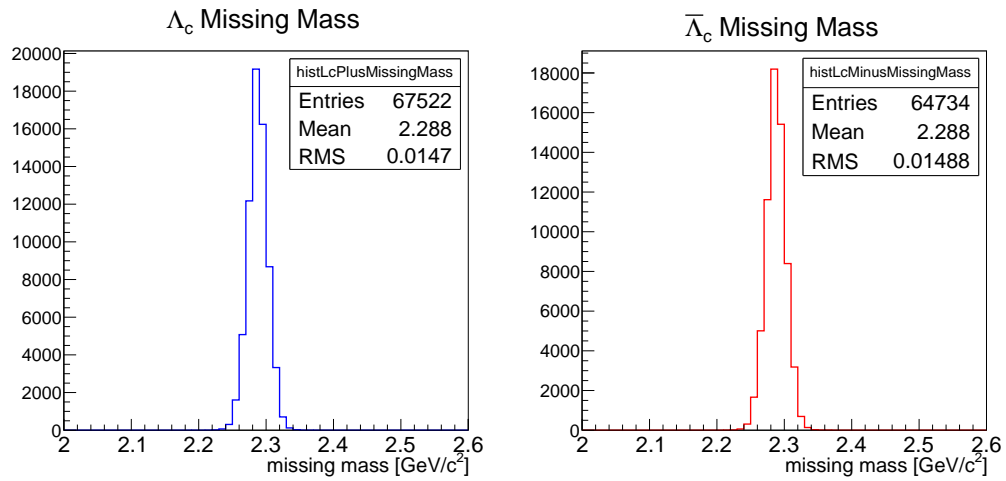


Figure 7.27: Missing mass of events with found Λ_c candidate (left) and found $\bar{\Lambda}_c$ candidate (right).

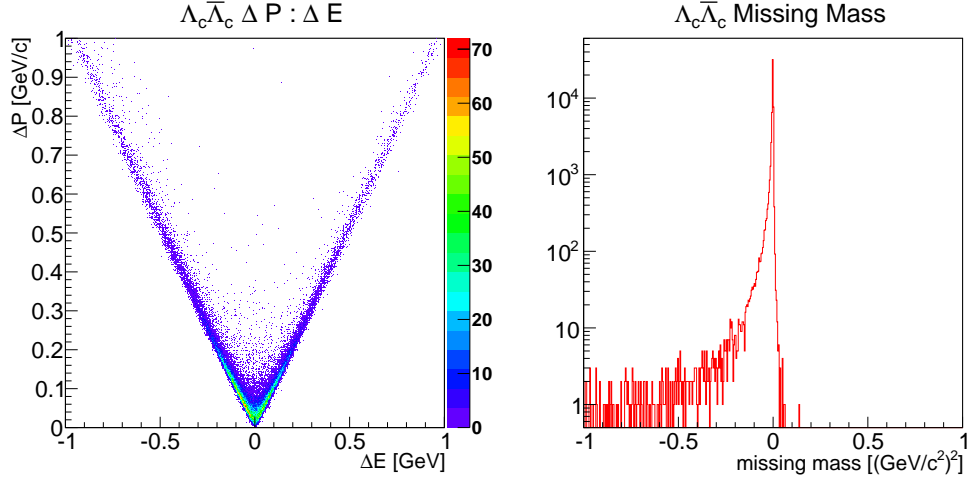


Figure 7.28: (left): Momentum and energy difference to initial momentum and energy of combined Λ_c and $\bar{\Lambda}_c$ events. (right): Missing mass distribution of combined Λ_c and $\bar{\Lambda}_c$.

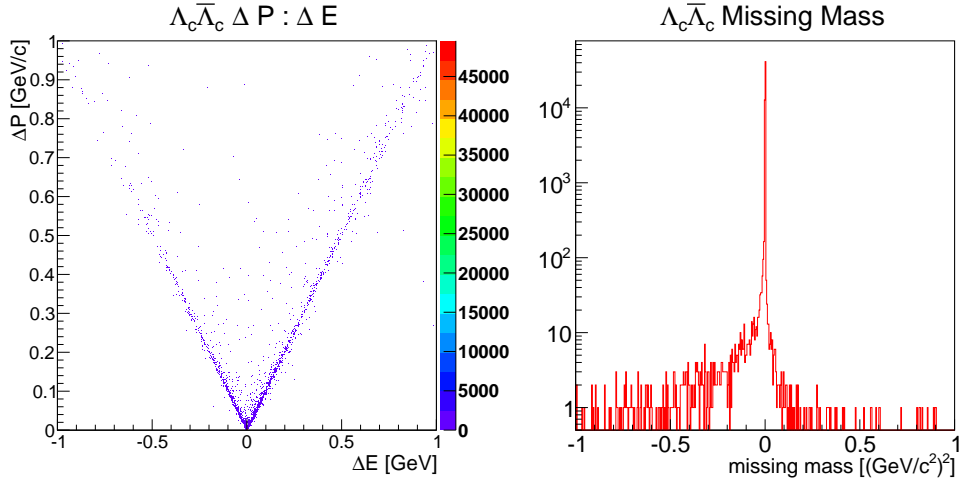


Figure 7.29: This figure shows results after using the Pnd4CFitter on the candidates. (left): Momentum and energy difference to initial momentum and energy of combined Λ_c and $\bar{\Lambda}_c$ events. (right): Missing mass distribution of combined Λ_c and $\bar{\Lambda}_c$.

Nevertheless, the fitter is not able to modify all tracks to match the initial conditions so that there are still some entries at other positions than zero. The fitter was also used to resolve ambiguities by accepting only the system with lowest χ^2 , this has been done for the unfitted results in Figure 7.28 as well.

With the same cuts applied as for the Λ_c and $\bar{\Lambda}_c$ candidates, a total of 5,990 combined $\bar{\Lambda}_c\Lambda_c$ systems pass the selection, which results in a reconstruction efficiency of 0.75 %. The exclusive measurement expects a much lower relative background, so that the cut parameters can be set less tight. With $\text{PocaQA}_{cut} = 5$ cm, no cuts on the transverse to longitudinal momentum distributions, and no cut on the Λ and $\bar{\Lambda}$ vertices, a total of 55,369 $\bar{\Lambda}_c\Lambda_c$ systems can be reconstructed. This makes a reconstruction efficiency of 6.9 %. The results shown in Figure 7.28 and 7.29 have been produced with the looser cut criteria.

7.2.6 $\bar{p}p \rightarrow \bar{\Lambda}_c\Lambda_c$ Cross Section

The cross section of $\bar{p}p \rightarrow \bar{\Lambda}_c\Lambda_c$ is still unknown, but a variety of predictions exist. For $p_{beam} = 10.2$ GeV/c predictions range from a few nb to several μb [68][69][70][71]. More information about the predictions are presented in Appendix D.

Due to this range of predictions on the cross section, an estimate of the amount of time needed to collect sufficient events to gain a significant signal that can be separated from the background fluctuation, is made for four cross sections, 5 nb, 100 nb, 500 nb, and $2\mu\text{b}$.

7.2.7 Non-resonant Background

Being able to reconstruct the signal events is a necessity for the measurement, but a real experiment will also produce many events from non-resonant reactions, which can result in falsely reconstructed events. In order to investigate the influence of these background events to the total measurement, the mass distribution of those falsely reconstructed events should be considered.

A total 235 million inelastic DPM background events have been simulated with the PndDp-mDirect event generator and the same antiproton beam momentum of 10.2 GeV/c as it has been used for the signal events. When applying the same cut parameters that were used for the signal reconstruction on the background events a total of 25 false Λ_c candidates and 11 false $\bar{\Lambda}_c$ candidates have been reconstructed. None of the 235 million DPM events passed the selection criteria for the exclusive reconstruction. Figure 7.30 shows the mass distribution of the falsely reconstructed Λ_c and $\bar{\Lambda}_c$ candidates. Especially the mass distribution for the Λ_c candidates indicates a peak around the actual Λ_c mass, this is because of the selection on the Λ_c and $\bar{\Lambda}_c$ candidates which drastically discriminates background events but also limits the possible mass range for background events.

As long as the background peak is broader than the signal peak, the signal peak can be measured on top of it if the number of reconstructed true candidates is significantly bigger than the statistical fluctuation of the number of background candidates in the same mass range. Figure 7.31 shows the signal mass overlayed on the background mass for four possible cross sections of $\bar{p}p \rightarrow \bar{\Lambda}_c\Lambda_c$. In order to compare signal and background, the background events

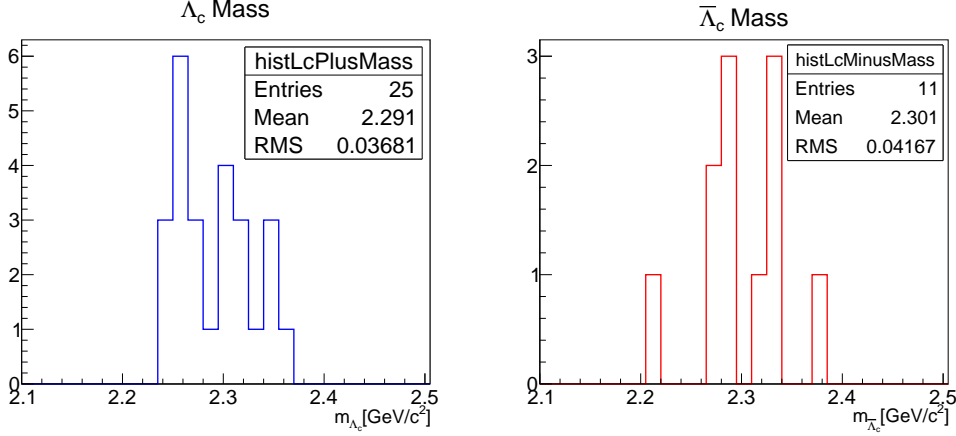


Figure 7.30: Λ_c and $\bar{\Lambda}_c$ candidate mass distribution for DPM events.

have been scaled by a factor f :

$$f = \frac{\sigma_{DPM} \cdot N_{sig.}}{N_{bg} \cdot \sigma_{\bar{p}p \rightarrow \bar{\Lambda}_c \Lambda_c} \cdot BR}; \quad (7.4)$$

Here, the background cross section is $\sigma_{DPM} = 42.2 \text{ mb}$, $N_{sig.} = 798,000$, $N_{bg} = 235 \text{ million}$, and the branching ratio is the product of the branching ratio for $\Lambda_c \rightarrow \Lambda \pi^+$ and $\Lambda \rightarrow p \pi^-$, $BR = 0.0107 \cdot 0.639$.

A three times higher number of signal than statistic fluctuation of the background is considered significant enough to discern the signal peak.

$$N_{true} \stackrel{!}{>} 3\sqrt{N_{false}} \quad (7.5)$$

The needed beam time t_b to fulfil Equation 7.5 is dependent on the cross section of $\bar{p}p \rightarrow \bar{\Lambda}_c \Lambda_c$ and can be calculated by:

$$t_b \cdot \mathcal{L} \cdot \sigma_{\bar{p}p \rightarrow \bar{\Lambda}_c \Lambda_c} \cdot \epsilon_{\Lambda_c} \cdot BR > 3 \cdot \sqrt{\mathcal{L} \cdot \sigma_{tot} \cdot \epsilon_{bg} \cdot t} \quad (7.6)$$

$$\Leftrightarrow t_b > \frac{9 \cdot \sigma_{tot} \cdot \epsilon_{bg}}{\mathcal{L} \cdot \sigma_{\bar{p}p \rightarrow \bar{\Lambda}_c \Lambda_c}^2 \cdot \epsilon_{\Lambda_c}^2 \cdot BR}$$

Here, a luminosity of $\mathcal{L} = 2 \cdot 10^{32} \text{ cm}^{-2} \text{ s}^{-1}$ is considered, which corresponds to the HL mode in HESR. Table 7.4 summarises the estimated time requirements for reaching that level of significance as well as the needed time to detect 1,000 Λ_c or $\bar{\Lambda}_c$ for the four possible cross sections.

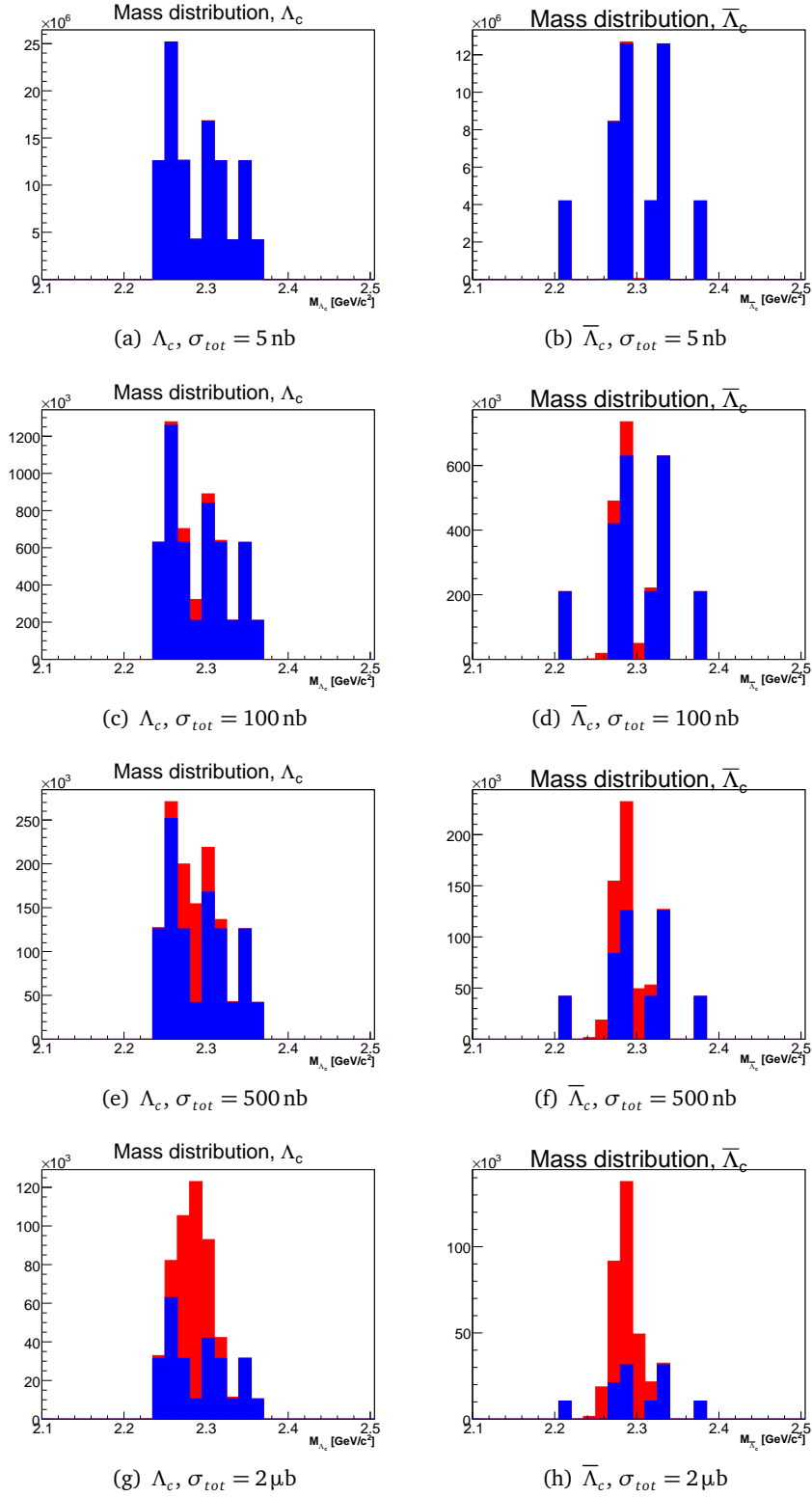


Figure 7.31: Signal to background mass peak of Λ_c and $\bar{\Lambda}_c$ for four possible total cross sections of $\bar{p}p \rightarrow \bar{\Lambda}_c \Lambda_c$.

	$\sigma_{\bar{p}p \rightarrow \bar{\Lambda}_c \Lambda_c}$	$N_{\text{true}} > 3\sqrt{N_{\text{false}}}$	$N_{\Lambda_c, \bar{\Lambda}_c} = 1000$
Λ_c	5 nb	277 d	19.9 d
$\bar{\Lambda}_c$	5 nb	134 d	20.9 d
Λ_c	100 nb	16.6 h	1 d
$\bar{\Lambda}_c$	100 nb	8.1 h	1 d
Λ_c	500 nb	39.8 min	4.8 h
$\bar{\Lambda}_c$	500 nb	19.3 min	5 h
Λ_c	2 μb	150 s	71.7 min
$\bar{\Lambda}_c$	2 μb	73 s	75.2 min

Table 7.4: Required beam time to detect $N_{\text{true}} > 3\sqrt{N_{\text{false}}}$ and to detect 1,000 Λ_c or $\bar{\Lambda}_c$.

7.3 Conclusion

With **PANDA**, it will be possible to detect the $\bar{p}p \rightarrow \bar{\Lambda}_c \Lambda_c \rightarrow \bar{\Lambda} \pi^- \Lambda \pi^+ \rightarrow \bar{p} \pi^+ \pi^- p \pi^- \pi^+$ decay chain. Up to now, 776 ± 55 detected $\Lambda_c \rightarrow \Lambda \pi^+$ events and 637 ± 34 detected $\bar{\Lambda}_c \rightarrow \bar{\Lambda} \pi^-$ events have been observed [72]. Depending upon the cross section of the reaction, this record may be broken within hours of **PANDA** operation, and observables ranging from the cross section and mass to angular distributions can be studied. A high amount of statistics would be great in order to measure the asymmetry parameters α_{Λ_c} and $\alpha_{\bar{\Lambda}_c}$, which can be determined by the angular distribution of the final state particles. If they are determined with sufficient precision, then the CP asymmetry parameter \mathcal{A} can be determined [72]:

$$\mathcal{A} \equiv \frac{\alpha_{\Lambda_c} + \alpha_{\bar{\Lambda}_c}}{\alpha_{\Lambda_c} - \alpha_{\bar{\Lambda}_c}} \quad (7.7)$$

In the worst case scenario, the measurement of this decay channel alone would not be sufficient to perform $\bar{p}p \rightarrow \bar{\Lambda}_c \Lambda_c$ measurements, but this decay channel could still contribute to a combined measurement together with other decay channels. For example, together with $\Lambda_c \rightarrow p K^- \pi^+$, which was investigated in [73]. For the exclusive measurement, rates between one event every 3.5 days up to > 100 per day are expected depending on the actual cross section.

Conclusion

8

Sensor Characterisation A test system for sensor characterisation and QA has been set up. High precision measurements of the sensor characteristics can be performed with the use of a dedicated test board. Also, Non-destructive characterisation and QA can be performed with a probestation. The leakage current and capacitive characteristics of the whole sensor as well as individual strips have been measured.

The test system can be used for characterisation of the final sensors which are expected to be delivered before the second half of 2015. As the final sensors have a smaller pitch, with the same dedicated test board every 75th strip of full length and every 30th strip of varying length can be contacted individually.

Spatial Resolution Improvement The charge distribution of two-strip clusters has been simulated and the possible improvement to the spatial resolution by using the η method has been analysed. In order to achieve this, one million muons have been simulated with the FairBoxGenerator at directions where the trapezoidal strip sensors are placed. From the digitisation of this data, the charge distribution of two-strip clusters has been extracted separately for different deposited energies. The same procedure has been done for the rectangular strip sensors with another set of one million muons.

Then, the η distributions for the trapezoidal and rectangular sensors have been determined and saved to a parameter file. The parameter file and the η method have been implemented to PandaRoot and used for the reconstruction of another set of one million muons in order to compare the achieved resolution with that of the CoG method.

Test Beam A first successful operation of the trapezoidal prototype sensors in a test beam has been done. After noise and ghost hit suppression, the hitmap showed a clear picture of the beam spot. The SNR has been determined for MIPs to be ~ 15.6 for the p-side strips of full length and ~ 18.2 for the n-side strips of full length. The short strips are estimated to reach a SNR of up to 60.

Also, the energy resolution has been determined, which is $\frac{\sigma_{dE}}{dE} \approx 4.5\%$ for deposited energies of more than 200 keV and has a peak at a deposited energy of about 75 keV with $\frac{\sigma_{dE}}{dE} \approx 11.5\%$.

Furthermore, the η distribution was measured and a method has been developed to correct the distribution for noise and threshold effects.

$p\bar{p} \rightarrow \Lambda_c \bar{\Lambda}_c$ **Simulation with PandaRoot** The decay channel $p\bar{p} \rightarrow \Lambda_c \bar{\Lambda}_c \rightarrow \Lambda \pi^+ \bar{\Lambda} \pi^- \rightarrow p \pi^- \pi^+ \bar{p} \pi^+ \pi^-$ has been investigated. In order to suppress background, strong selection criteria have been defined for the inclusive measurements of Λ_c and $\bar{\Lambda}_c$. The reconstruction efficiency reached with these selection criteria is 8.5 % (Λ_c) and 8.1 % ($\bar{\Lambda}_c$). For the exclusive measurement a looser set of selection criteria was chosen, so that a reconstruction efficiency of 6.9% has been reached. This is reasonable, as the background suppression factor for the exclusive measurement is approximately the product of the inclusive suppression factors.

Depending on the cross section of $p\bar{p} \rightarrow \Lambda_c \bar{\Lambda}_c$ at the $\bar{\text{PANDA}}$ momentum range, $\bar{\text{PANDA}}$ may be able to provide the best measurement of the asymmetry parameters α_{Λ_c} and $\alpha_{\bar{\Lambda}_c}$ for this channel. In any case, the channel may contribute to the overall $p\bar{p} \rightarrow \Lambda_c \bar{\Lambda}_c$ measurement even if the cross section is in the lower end of the predictions.

Parts of Chapter 4 and 6 are in the process of being published in [74].

Sensor Characterisation



A.1 Software

In Figure A.1 the GUI of the software can be seen with the *Connection and Settings* tab selected. From that tab the connection to the devices is controlled and basic parameters can be set. The software can loop over a frequency and volt range and a waiting time can be set to avoid the measurement of transient currents. A step size can be set for the loops. Additionally, when connected to the probestation it is also possible to repeat the measurement loops whilst shifting the position of the sensor in-between two measurement cycles, e.g. to measure the capacitance of different strips. The measurement routine runs in the following order:

1. If a bias voltage range was set, the first voltage is initiated on the source meter.
2. The software waits for a user defined amount of seconds to avoid the measurement of transient currents ($\sim 10 - 15$ s).
3. If a frequency range was set, the first frequency is initiated on the LCR meter.
4. The software waits for another user defined amount of seconds to let the LCR meter adjust to the new frequency ($\sim 1 - 2$ s).

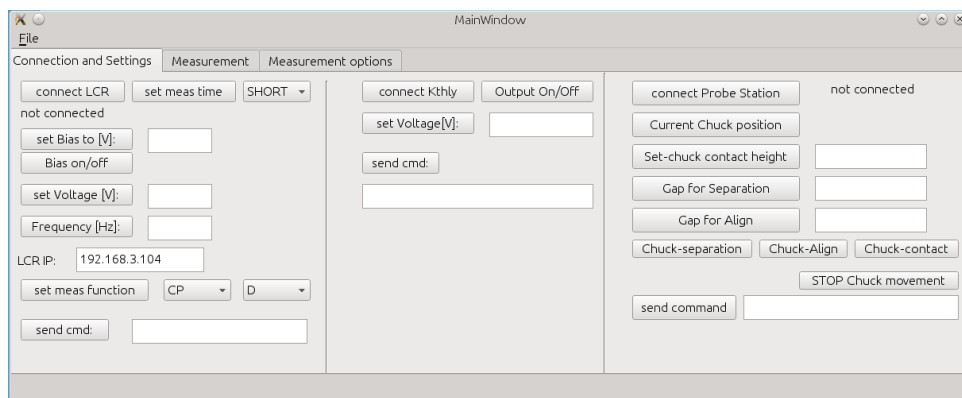


Figure A.1: Overview on the software GUI for the sensor characterisation measurements.

5. Measurement values are taken and written to a text file as well as into a text box in the GUI.
6. If a frequency range was set, the next frequency is initiated on the LCR meter.
7. Steps 4 to 6 are repeated until the end of the frequency range was reached.
8. If a bias voltage range was set, the next voltage is initiated on the source meter.
9. Steps 2 to 7 are repeated until the end of the bias voltage range was reached.
10. The bias voltage is ramped down to 1 V.
11. If a range of measurement positions was set, the probestation chuck is lowered to the align height.
12. The source meter's current measurement is used to determine whether the needles lost contact.
13. If the needles are still in contact the measurement routine aborts.
14. The chuck is moved to the next position.
15. The chuck is heightened to the contact height.
16. The source meter's current measurement and the LCR meter's capacitance measurement are used to determine whether the needles made contact.
17. Without contact the measurement routine aborts.
18. All previous steps are repeated until the last measurement position was reached.

Communication with Probestation The software communicates with the probestation via an embedded PC in the probestation. The command scheme is:

ID : COMMAND : PARAMETERS

While the ID can be any number, it is recommended to use a consecutive numbering, as the embedded system sends a reply to each command mirroring the provided ID. When each command is provided with a unique ID, a corrupted reply can directly be associated with its initial command by the mirrored ID. More information about the probestation interface and available commands can be found in [75].

SCPI SCPI is a standard set of commands of which a mandatory subset must be implemented in all devices that are called SCPI-compatible, while the rest of the command set can be implemented depending on the purpose of the device. All commands have the following structure:

KEYWORD₁ : [KEYWORD₂ : [KEYWORD₃ : [...]]] [PARAMETER]

Each command contains at least one keyword, but can contain more keywords in the order from general to specific, separated by colons. If a parameter is sent, the parameter comes last

and is separated from the keywords by a blank space, e.g. the command *SOURCE:VOLT 20* sent to the source meter will set the source meters voltage output to 20V [76].

If an answer from the device is requested the last keyword is followed by a question mark, e.g. *FETC?* sent to the LCR meter will make the LCR answer with the measurement results from the momentarily set measurement function [56].

A.2 Measurements of Prototype Sensors

Capacitance and leakage current measurements of 11 more sensors. Sensor 321589-6.1 shows

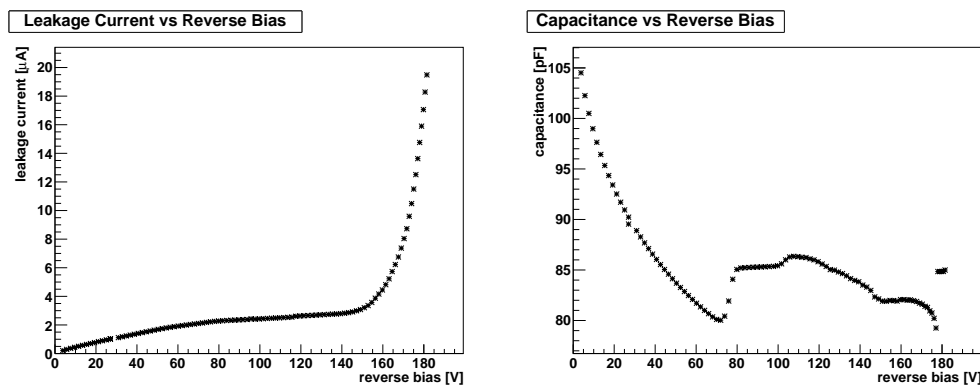


Figure A.2: Leakage current and capacitance of sensor 321589-6.1.

an unexpected capacitance curve as well as an early break through point and is considered to be broken. Besides the broken sensor, all sensors reached full depletion at about 100V to

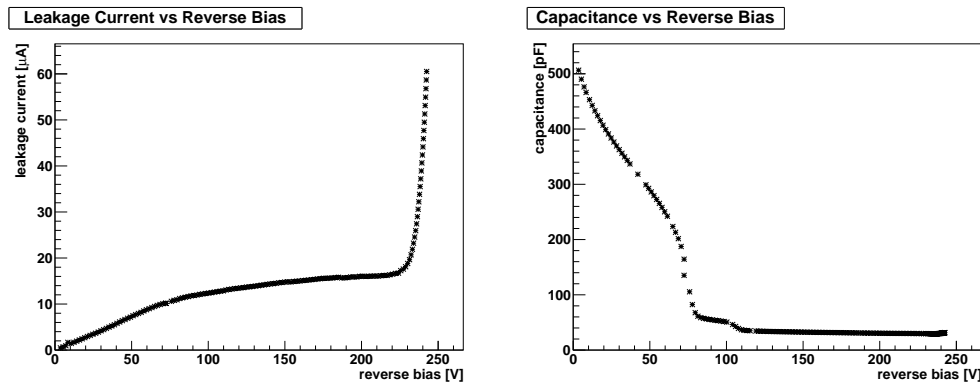


Figure A.3: Leakage current and capacitance of sensor 322635-7.1.

110V. The measurements with the sensors *.2 were taken by Ajay Kumar [77].

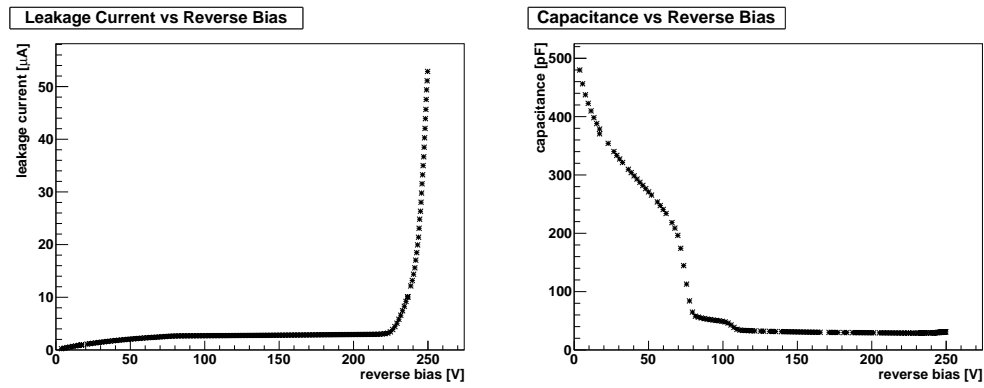


Figure A.4: Leakage current and capacitance of sensor 321589-8.1.

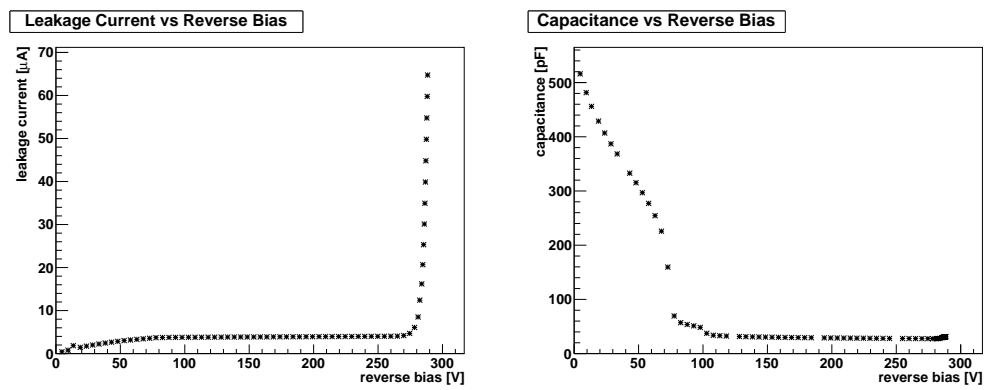


Figure A.5: Leakage current and capacitance of sensor 321589-5.2.

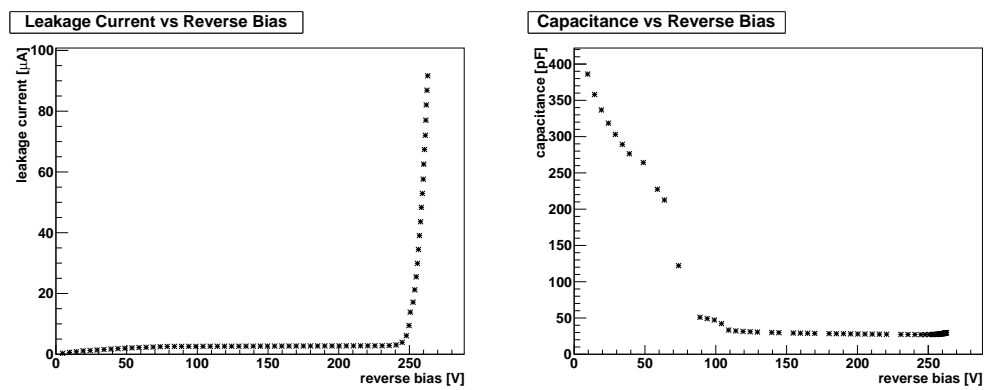


Figure A.6: Leakage current and capacitance of sensor 321589-6.2.

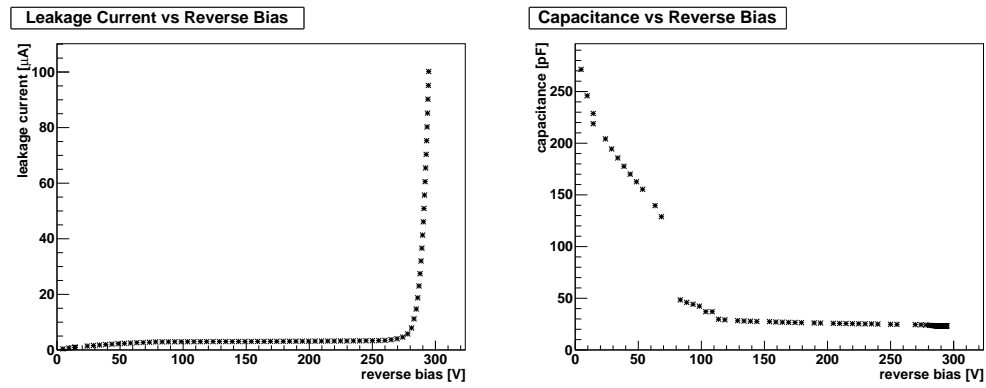


Figure A.7: Leakage current and capacitance of sensor 321589-7.2.

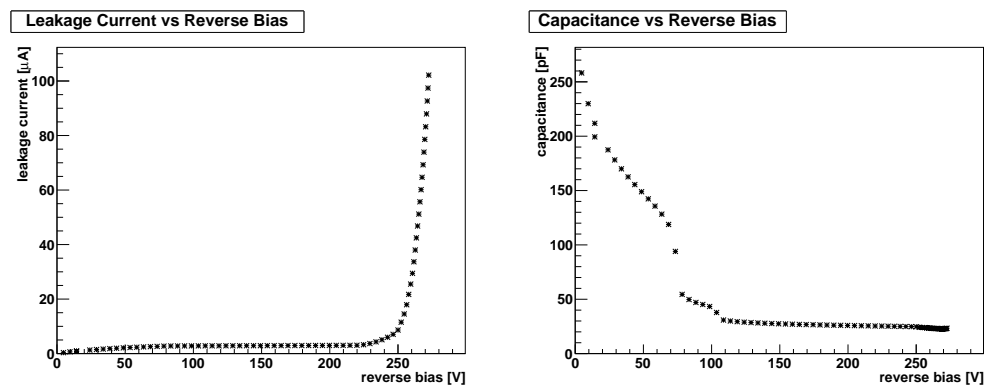


Figure A.8: Leakage current and capacitance of sensor 321589-8.2.

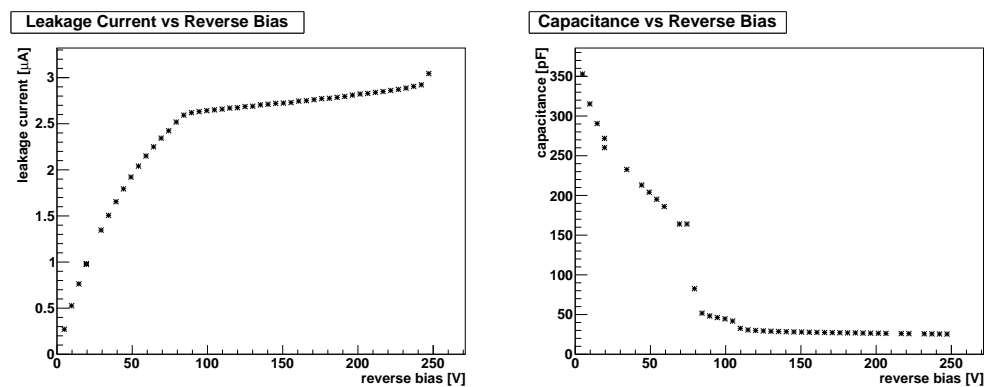


Figure A.9: Leakage current and capacitance of sensor 322635-5.2.

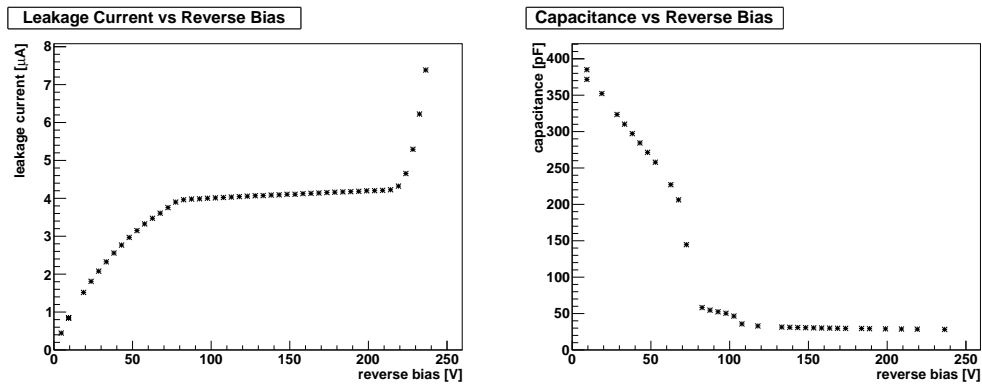


Figure A.10: Leakage current and capacitance of sensor 322635-7.2.

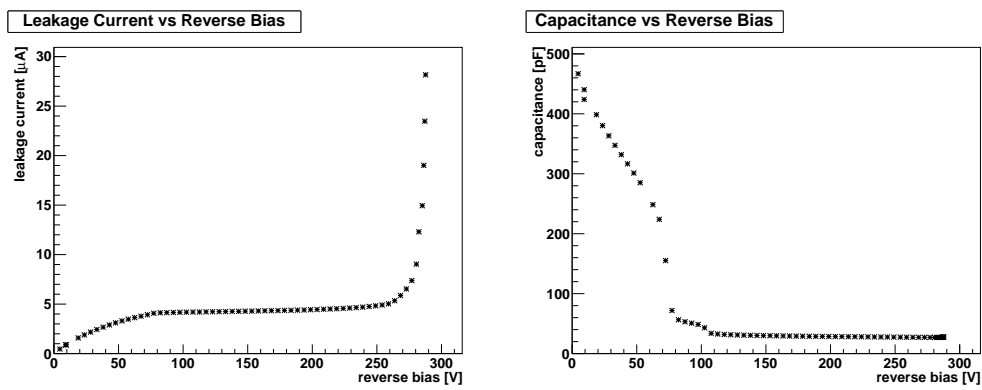


Figure A.11: Leakage current and capacitance of sensor 322635-8.2.

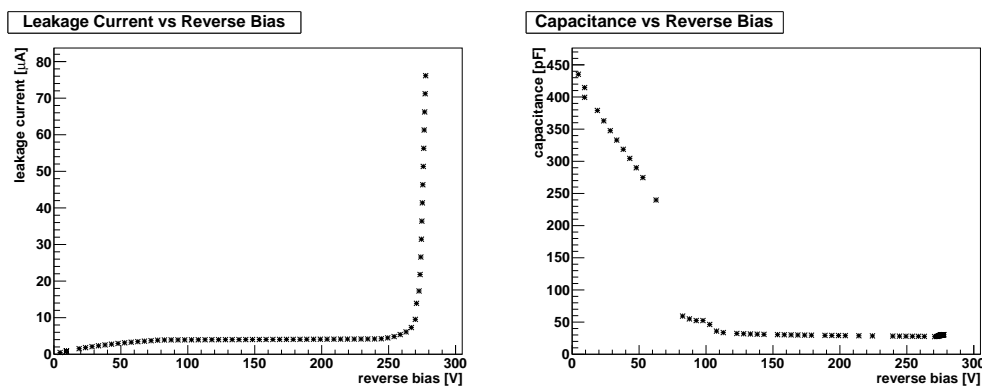


Figure A.12: Leakage current and capacitance of sensor 322635-9.2.

Results from December Test Beam

B

During the test beam in December a proton beam momentum of 2.95 GeV/c was used.

Deposited Energy Figure B.1 shows the deposited energy in the sensor for p- and n-side for each strip channel. Only the p-side shows some noise in the low ADC range. The cluster energy peaks at ~ 190 ADC for both p- and n-side as can be seen in Figure B.2. The n-side only shows the signal peak, while all noise entries seem to be below 50 ADC and have failed to reach threshold. The p-side clusters show a noise peak at about 60 ADC and a local minimum between the noise and signal peak at 95 ADC, which therefore has been chosen as a cut position for the data selection.

Start Frame The time difference between the trigger and the strip signal is shown in Figure B.3 for all channels. For the p-side the data selection rejects all signals with a start time < 150 ns or > 250 ns, and for the n-side all start times < 100 ns or > 200 ns are rejected.

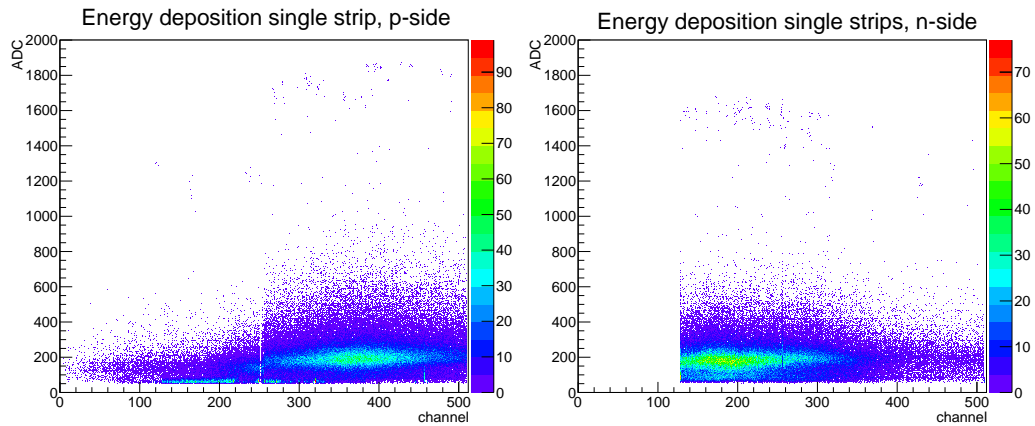


Figure B.1: Deposited energy per strip for the p- (left) and n-side (right).

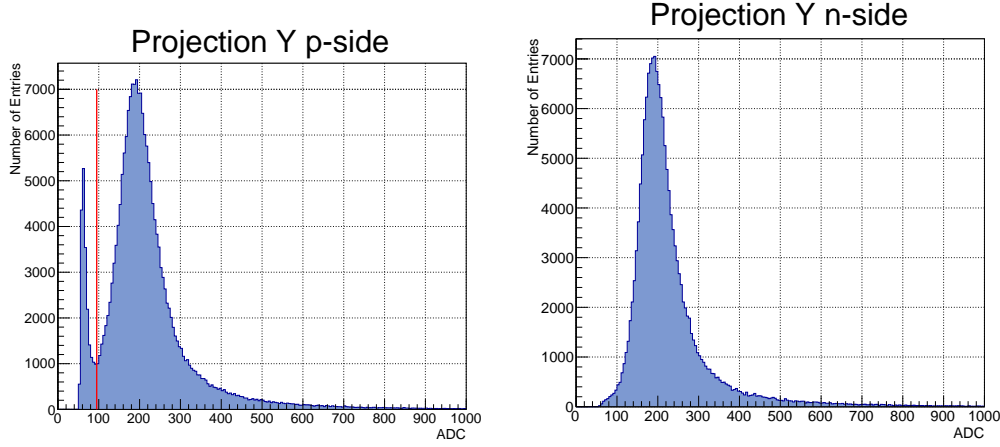


Figure B.2: Energy deposition per cluster for the p- (left) and n-side (right). The red line in the p-side cluster energy distribution indicates the data selection cut position.

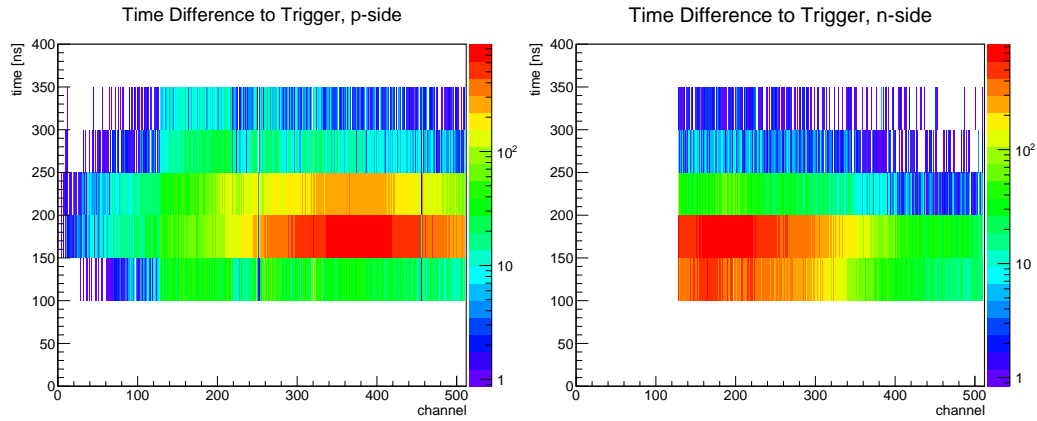


Figure B.3: Time difference between the trigger and the first strip signal above threshold. p-side (left), n-side (right).

p- to n-side Correlation The p- to n-side correlation together with an indication of the selected region is shown in Figure B.4(a). And Figure B.4(b) presents the ghost hit discrimination that is reached with that selection. From a total of 20,457 ghost hits 6,792 could be rejected by the selection on the p- to n-side correlation, which makes a suppression rate of 33.2%.

Hitmap The hitmap without and with data selection can be seen in Figure B.5. The difference between both is minor as only a small fraction of the entries on the p-side were noise entries, and there were almost no noise entries at all on the n-side.

Signal to Noise Ratio The SNR can be seen in Figure B.6 for all p- and n-side channels.

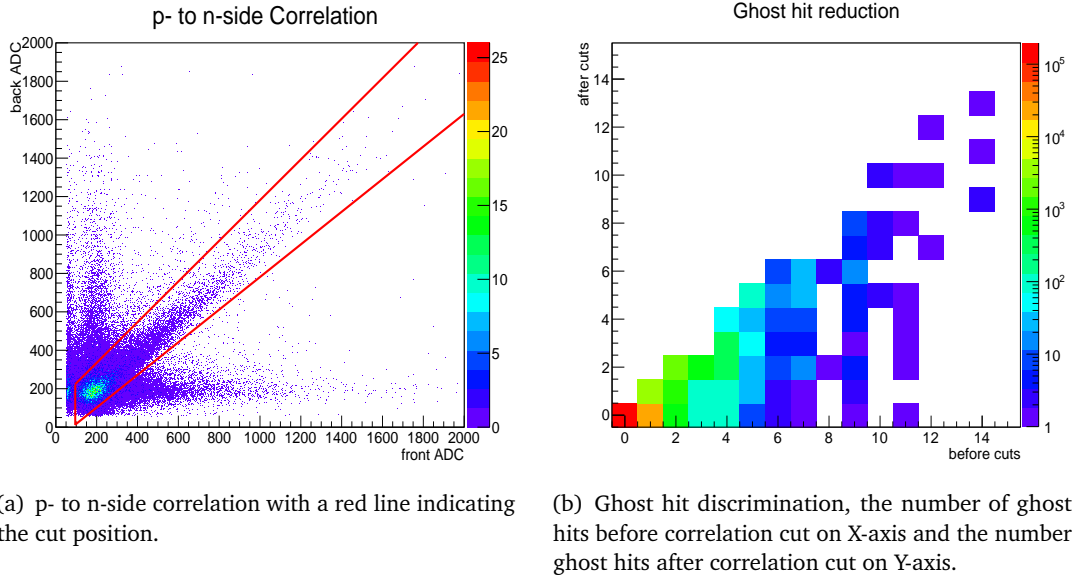


Figure B.4: Correlation between p- and n-side energy loss and ghost hit discrimination. (a) p- to n-side correlation with cut position, (b) ghost hit discrimination.

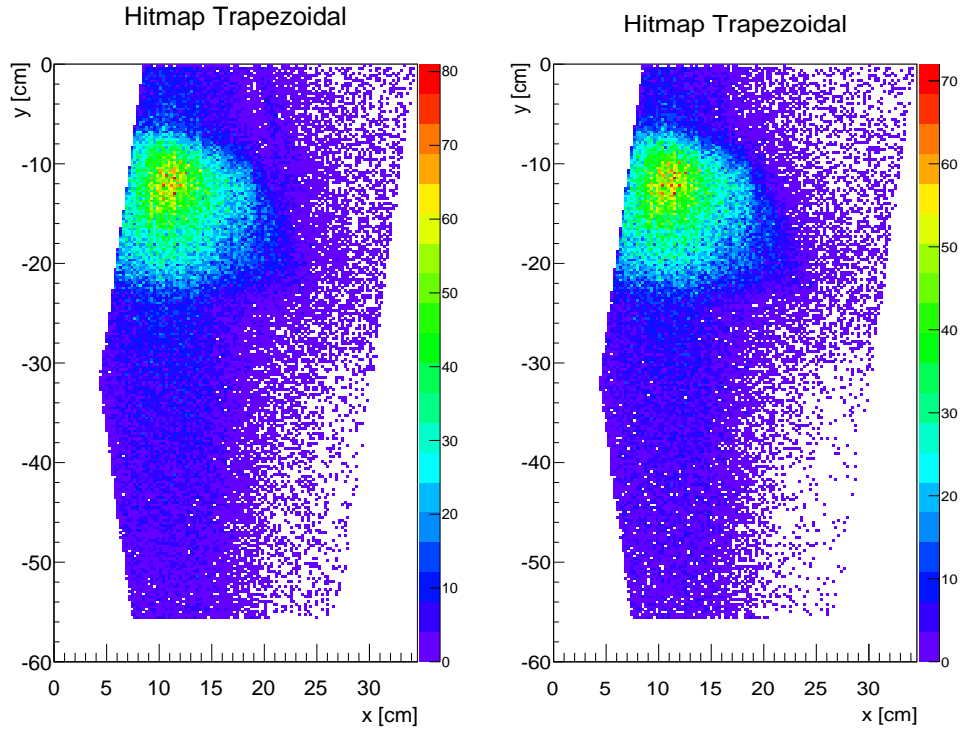


Figure B.5: The hitmap of the sensor, without (left) and with (right) data selection.

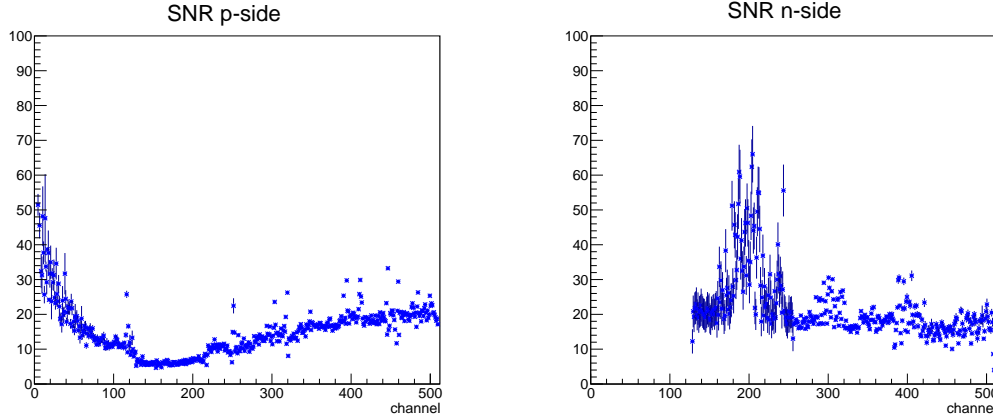


Figure B.6: The SNR for p- and n-side.

Timing Issues of p-side During the December test beam several technical issues prevented the taking of a larger data sample. One issue that could not be resolved during the December test beam was a timing problem between two of the APV25s and the DAQ. When the ADC digitises the data for each APV25 channel, their clock must be in sync. To do so, a phase shift can be applied to the ADC, so that the digitisation happens exactly during one clock cycle of the APV25. This phase shift could only be set globally for the whole ADC. Therefore, it is important that the signal delay from each APV25 to the ADC is of equal length.

Within the first hour of data taking, the signal from the two APV25s for channels 1 to 256 of the sensor's p-side got lost repeatedly. The reason for that was found in broken cables that connect the APV25 data from the supply board to the ADC system. The two cables have been replaced, but unfortunately no replacement cables of the original cables' length were available. Therefore, a relative time shift between those two APV25s and the other APV25s was established. The result of this was that those two APV25s were not totally in sync with the ADC anymore and the ADC split a part of each channel's signal with the signal of the next clock cycle. Because of the channel ordering scheme of the APV25 (see Equation 6.1), neighbouring clock cycles do not carry the signal of neighbouring strips, but of strip channels with a distance of 32, 88, or 119 channels.

Figure B.7 shows the correlation between strip channels. The expected figure would show a diagonal line, as every strip signal is always correlated with itself and maybe one or two direct neighbours in case of larger signal. All other entries should be randomly distributed as all other strip signals should not be correlated to the first signal. Nevertheless, Figure B.7 shows lines in parallel to the diagonal with a distance to it by 32, 88, and 119 channels in the area (1-128|1-128) and (129-256|129-256). Which is the consequence of the phase shift from those two APV25s.

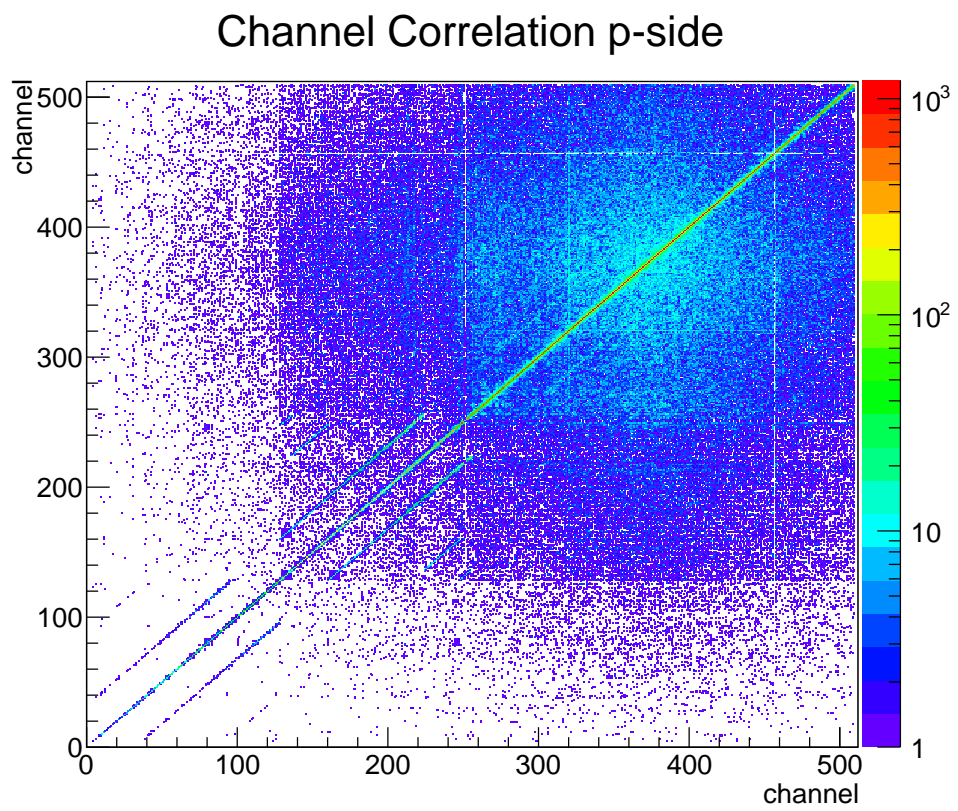


Figure B.7: Channel correlation of the p-side.

Momentum Resolution of the Final State Particles

C

The results for the momentum resolution of the final state particles are presented in this section. The systematic offsets have been calculated as the mean value of $P_{MC} - P_{reco}$. Here, P_{MC} is the Monte Carlo momentum as provided from the event generator and P_{reco} is the reconstructed particle momentum. The statistical errors are calculated as the standard deviations from the mean values.

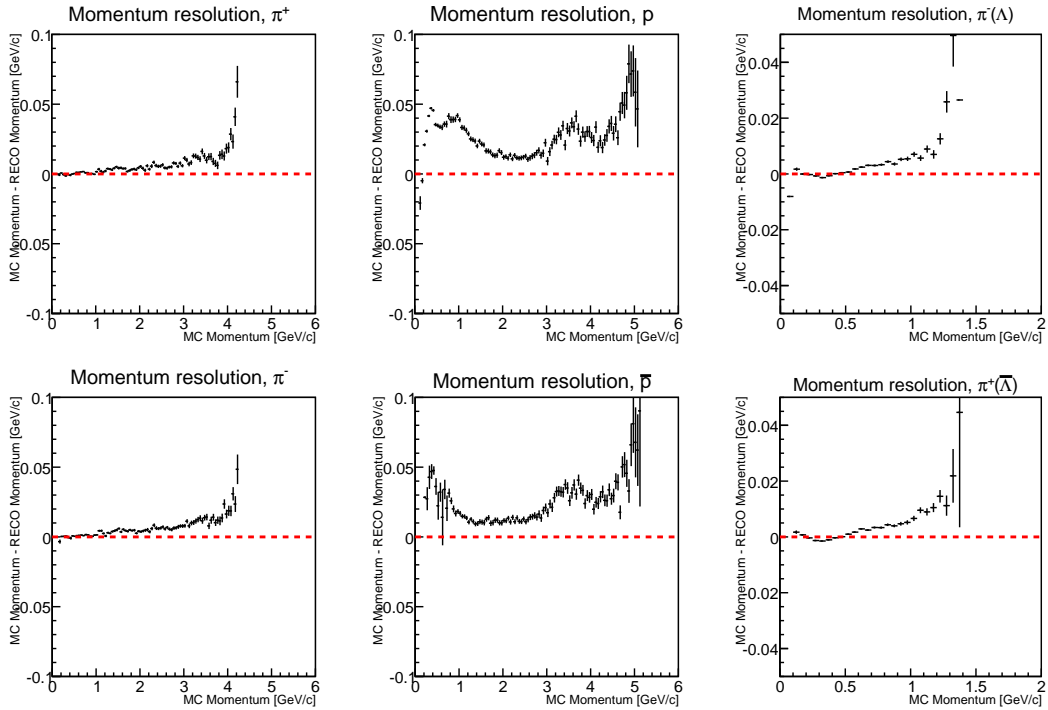


Figure C.1: Systematic offset of the momentum reconstruction per particle. The red dashed line marks the position of no systematic error for better orientation.

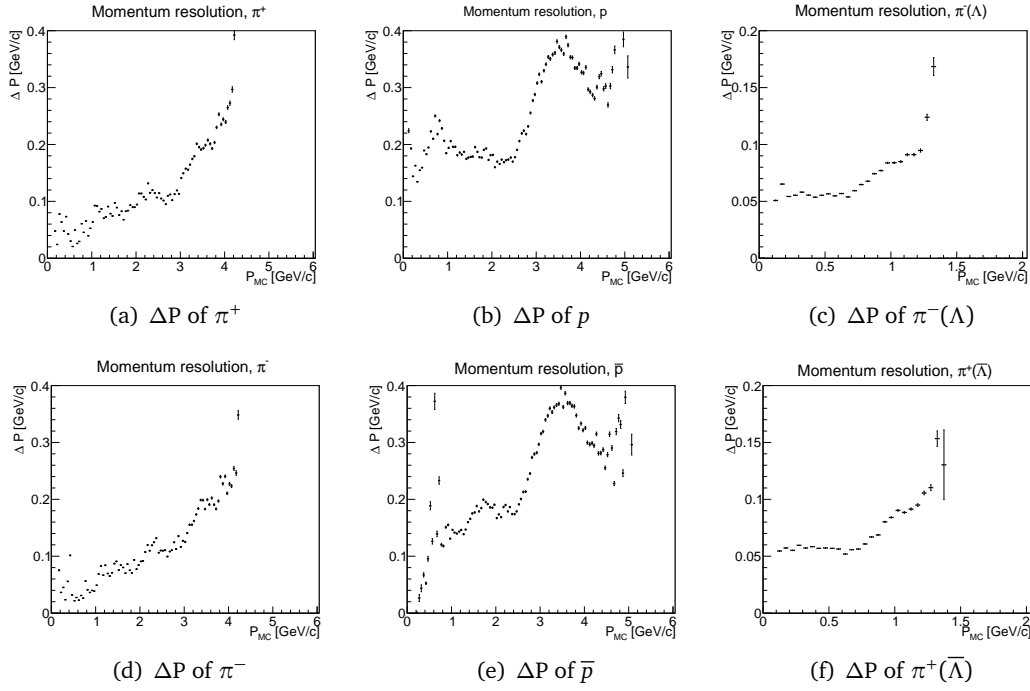


Figure C.2: Statistical error of the momentum reconstruction per particle.

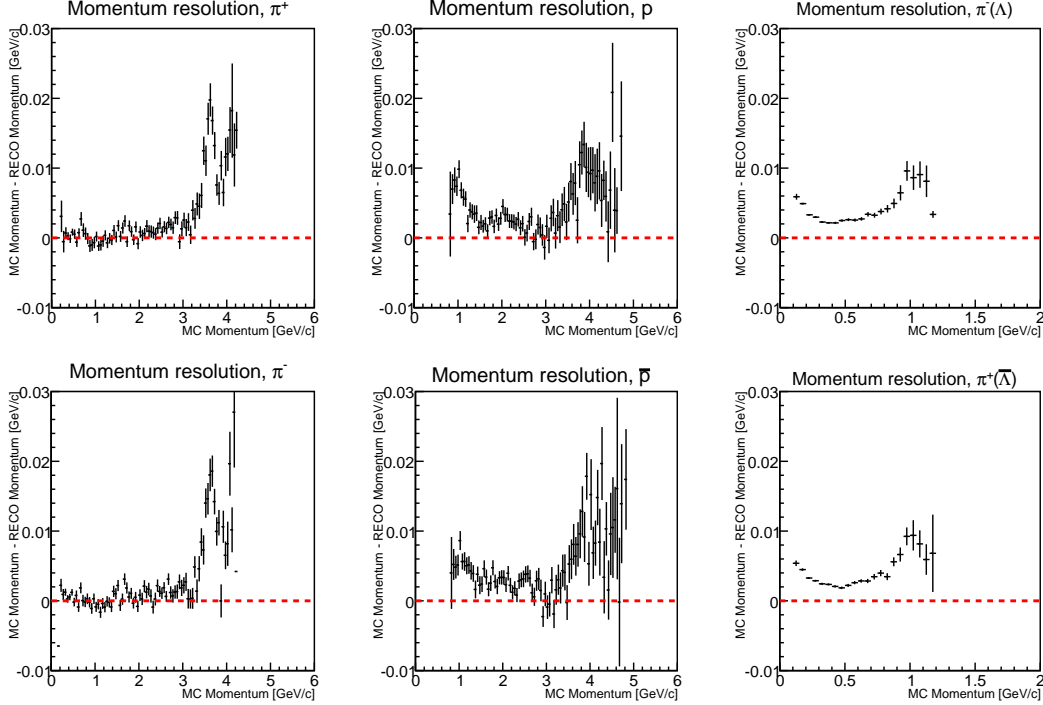


Figure C.3: Systematic offset of the momentum reconstruction per particle. Shown for all particles that survived a cut on the total momentum of Λ_c or $\bar{\Lambda}_c$ in their centre of mass frame as well as a cut on the mass of Λ or $\bar{\Lambda}$.

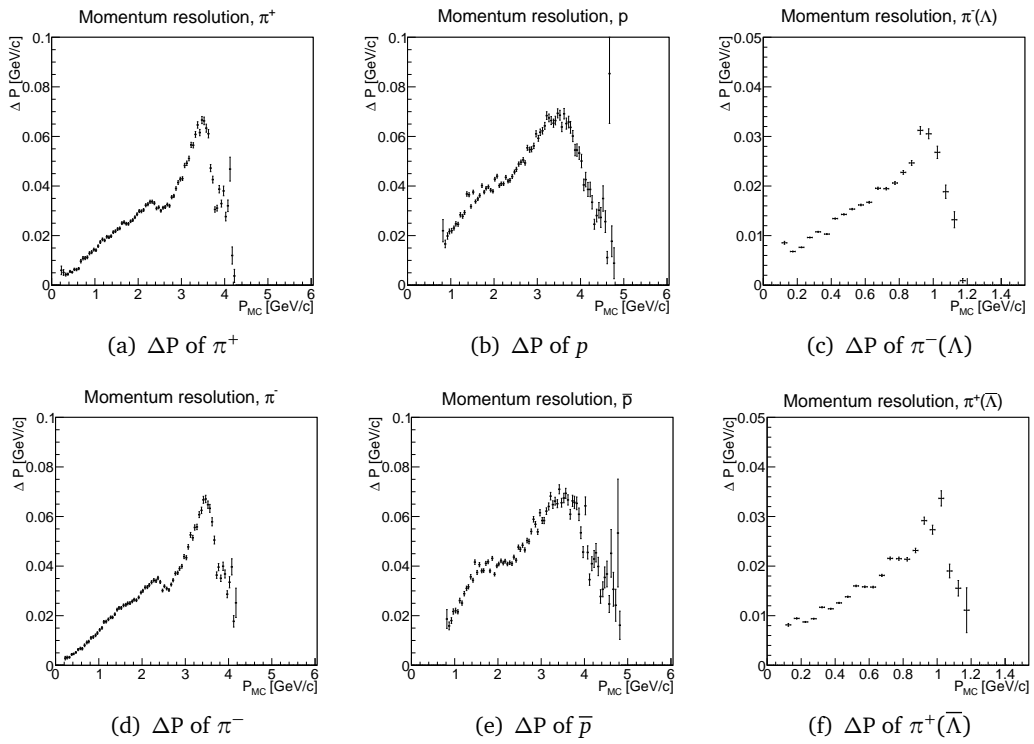
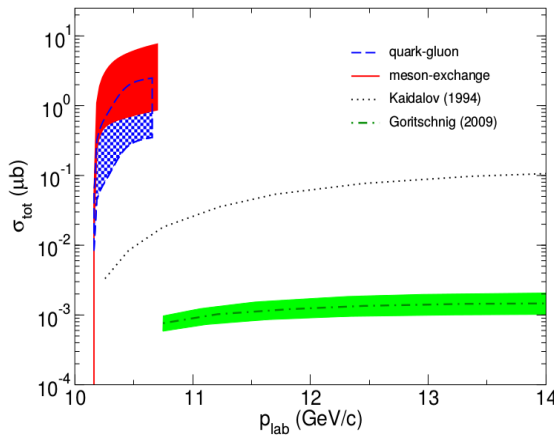


Figure C.4: Statistical error of the momentum reconstruction per particle. Shown for all particles that survived the cuts.

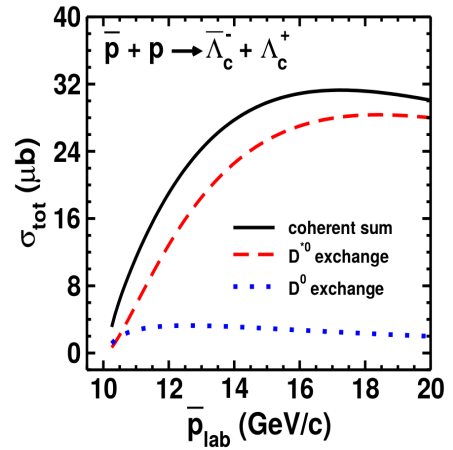
$\bar{p}p \rightarrow \bar{\Lambda}_c \Lambda_c$ Cross Section Predictions

D

The cross section predictions from [70] and [71] expect $\sigma_{\bar{p}p \rightarrow \bar{\Lambda}_c \Lambda_c}$ to be in the order of up to a few μb for an antiproton beam momentum of 10.2 GeV/c as can be seen in Figure D.1. In [68] and [69], the cross section $\sigma_{\bar{p}p \rightarrow \bar{\Lambda}_c \Lambda_c}$ is expected to be some nb, or at most a quarter μb as can be seen in Figure D.2.

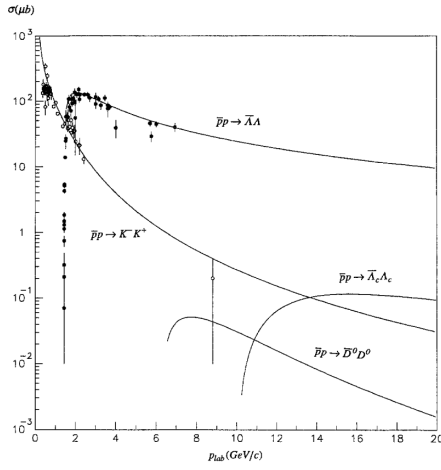


(a) This cross section prediction for $\bar{p}p \rightarrow \bar{\Lambda}_c \Lambda_c$ shows 0.1 μb to 2 μb at $p_{\bar{p}} = 10.2 \text{ GeV/c}$.

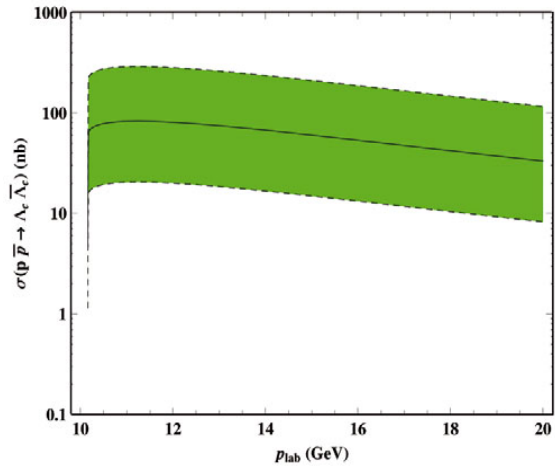


(b) This cross section prediction for $\bar{p}p \rightarrow \bar{\Lambda}_c \Lambda_c$ shows $\sim 3.5 \mu\text{b}$ at $p_{\bar{p}} = 10.2 \text{ GeV/c}$.

Figure D.1: Cross section predictions for $\bar{p}p \rightarrow \bar{\Lambda}_c \Lambda_c$. (a) [70], (b) [71].



(a) This cross section prediction for $\bar{p}p \rightarrow \bar{\Lambda}_c \Lambda_c$ shows $\sim 4 \text{ nb}$ at $p_{\bar{p}} = 10.2 \text{ GeV}/c$.



(b) This cross section prediction for $\bar{p}p \rightarrow \bar{\Lambda}_c \Lambda_c$ shows $\sim 20 \text{ nb}$ to $\sim 250 \text{ nb}$ at $p_{\bar{p}} = 10.2 \text{ GeV}/c$.

Figure D.2: Cross sections for $p\bar{p} \rightarrow \Lambda\bar{\Lambda}$ and $p\bar{p} \rightarrow K^+K^-$, and predictions for the cross sections of $\bar{p}p \rightarrow \bar{\Lambda}_c \Lambda_c$ and $p\bar{p} \rightarrow D^0\bar{D}^0$, (a) [68]. A cross section prediction for $\bar{p}p \rightarrow \bar{\Lambda}_c \Lambda_c$, (b) [69].

Bibliography

- [1] *Facility for Antiproton and Ion Research*. 2015. URL: <http://www.fair-center.eu/> (visited on 03/26/2015).
- [2] APPA-Collaborations. “Atomic and plasma physics, and applied sciences in bio, medical and material sciences (APPA) research pillar Science case”. In: (2012).
- [3] Volker Friese. *The CBM experiment at GSI / FAIR*. Nov. 2005. URL: <https://www-alt.gsi.de/documents/DOC-2006-Dec-91.html>.
- [4] Alexander Herlert for the NUSTAR Collaboration. “The NUSTAR program at FAIR Overview and present status of the project”. In: 71 (EPJ Web of Conferences 2014). DOI: 10.1051/epjconf/20147100064.
- [5] G. Clemente et al. “The FAIR proton linac: The first linac based on a room temperature CH-DTL”. In: *proceedings of ICFA ABDW HB2010* (2010), pp. 115–119. URL: <https://accelconf.web.cern.ch/accelconf/HB2010/papers/mopd26.pdf>.
- [6] FAIR. “Baseline Technical Report, Volume 2, Accelerator and Scientific Infrastructure”. In: (2006). URL: http://www.fair-center.de/fileadmin/fair/publications_FAIR/FAIR_BTR_2.pdf.
- [7] A. Lehrach et al. “Beam performance and luminosity limitations in the high-energy storage ring (HESR)”. In: *Nuclear Instruments and Methods in Physics Research Section A: Accelerators, Spectrometers, Detectors and Associated Equipment* 561.2 (2006), pp. 289–296. ISSN: 0168-9002. DOI: 10.1016/j.nima.2006.01.017.
- [8] R. Maier for the HESR Consortium. “The High-Energy Storage Ring (HESR)”. In: *Particle Accelerator Conference, New York*. 2011, pp. 2104–2106. DOI: 10.1109/RTC.2010.5750459.
- [9] *CAD-Renderings of the PANDA Detector*. 2015. URL: <https://panda-wiki.gsi.de/foswiki/bin/view/Detector/Pictures> (visited on 02/10/2015).
- [10] *Public Technical Progress Report*. Tech. rep. 2005. URL: http://www-panda.gsi.de/archive/public/panda_tpr.pdf.
- [11] K. K. Seth. “A Personal Journey Through Hadronic Exotica”. In: *Few-Body Systems* 45.2-4 (2009), pp. 85–90. DOI: 10.1007/s00601-009-0034-7.

- [12] S. Godfrey and N. Isgur. “Mesons in a relativized quark model with chromodynamics”. In: *Phys. Rev. D* 32 (1 July 1985), pp. 189–231. DOI: [10.1103/PhysRevD.32.189](https://doi.org/10.1103/PhysRevD.32.189). URL: <http://link.aps.org/doi/10.1103/PhysRevD.32.189>.
- [13] Paola Gianotti. “Results and perspectives in hadron spectroscopy”. In: *Physica Scripta* 2012.T150 (2012), p. 014014. DOI: [10.1088/0031-8949/2012/T150/014014](https://doi.org/10.1088/0031-8949/2012/T150/014014).
- [14] N. Brambilla et al. “Heavy quarkonium: progress, puzzles, and opportunities”. In: *The European Physical Journal C* 71.2 (2011), pp. 1–178. ISSN: 1434-6044. DOI: [10.1140/epjc/s10052-010-1534-9](https://doi.org/10.1140/epjc/s10052-010-1534-9).
- [15] M. Di Pierro and E. Eichten. “Excited heavy-light systems and hadronic transitions”. In: *Phys. Rev. D* 64 (11 2001), p. 114004. DOI: [10.1103/PhysRevD.64.114004](https://doi.org/10.1103/PhysRevD.64.114004).
- [16] Marius C. Mertens. “Der Panda Mikro Vertex Detektor: Endwicklung eines Labormesssystems, Simulation der MVD-Betriebsparameter sowie Untersuchung zur Auflösung der Breite des D_{s0}^* (2317)”. PhD thesis. Ruhr-Universität Bochum, 2010. URL: <http://www-brs.ub.ruhr-uni-bochum.de/netahtml/HSS/Diss/MertensMariusC/>.
- [17] E. Klempt and J.-M. Richard. “Baryon spectroscopy”. In: *Rev. Mod. Phys.* 82 (2 Apr. 2010), pp. 1095–1153. DOI: [10.1103/RevModPhys.82.1095](https://doi.org/10.1103/RevModPhys.82.1095). URL: <http://link.aps.org/doi/10.1103/RevModPhys.82.1095>.
- [18] E. Klempt and A. Zaitsev. “Glueballs, hybrids, multiquarks: Experimental facts versus QCD inspired concepts”. In: *Physics Reports* 454.1–4 (2007), pp. 1–202. ISSN: 0370-1573. DOI: [10.1016/j.physrep.2007.07.006](https://doi.org/10.1016/j.physrep.2007.07.006).
- [19] Ulrich Mosel. *Hadrons in Medium – Theory meets Experiment*. ECONFC070910:121,2007. 2008. eprint: [arXiv:0801.4970](https://arxiv.org/abs/0801.4970).
- [20] A. Sibirtsev et al. “Novel features of J/Ψ dissociation in matter”. In: *Physics Letters B* 484.1–2 (2000), pp. 23–29. ISSN: 0370-2693. DOI: [10.1016/S0370-2693\(00\)00635-3](https://doi.org/10.1016/S0370-2693(00)00635-3). URL: <http://www.sciencedirect.com/science/article/pii/S0370269300006353>.
- [21] N. Ikeno et al. “Formation of heavy-meson bound states by two-nucleon pick-up reactions”. In: *Phys. Rev. C* 84 (5 Nov. 2011), p. 054609. DOI: [10.1103/PhysRevC.84.054609](https://doi.org/10.1103/PhysRevC.84.054609). URL: <http://link.aps.org/doi/10.1103/PhysRevC.84.054609>.
- [22] Xiangdong Ji. “Generalized Parton Distributions”. In: *Annual Review of Nuclear and Particle Science* 54 (2004), pp. 413–450. DOI: [10.1146/annurev.nucl.54.070103.181302](https://doi.org/10.1146/annurev.nucl.54.070103.181302). URL: http://edwards1.phy.ohiou.edu/~inpp/nuclear_lunch/archive/2007/JiGPDs.pdf.
- [23] B. Povh, K. Rith, C. Scholz and F. Zetsche. *Teilchen und Kerne*. Springer Verlag, 1999. ISBN: 9783540659280.
- [24] Panda Collaboration. “Technical Design Report for the PANDA Target”. In: (2012). URL: http://www-panda.gsi.de/archive/TargetTDR/Targets_TDR.pdf.
- [25] W. Erni et al. “Technical design report for the PANDA Straw Tube Tracker”. In: *The European Physical Journal A* 49 (2013). DOI: [10.1140/epja/i2013-13025-8](https://doi.org/10.1140/epja/i2013-13025-8).
- [26] B. Voss et al. *The GEM-Discs for the PANDA experiment*. 2009. URL: <http://www-alt.gsi.de/informationen/wti/library/scientificreport2009/PAPERS/INSTRUMENTS-METHODS-58.pdf>.

- [27] C. Schwarz et al. “The Barrel DIRC of PANDA”. In: *Journal of Instrumentation* 7 (2012). DOI: 10.1088/1748-0221/7/02/C02008. URL: <http://www-alt.gsi.de/informationen/wti/library/scientificreport2009/PAPERS/INSTRUMENTS-METHODS-58.pdf>.
- [28] W. Erni et al. “Technical Design Report for the PANDA Micro Vertex Detector”. In: *ArXiv e-prints* (2012). arXiv: 1207.6581 [physics.ins-det].
- [29] W. Erni et al. “Technical Design Report for the PANDA Electromagnetic Calorimeter (EMC)”. In: *ArXiv e-prints* (Oct. 2008). arXiv: 0810.1216 [physics.ins-det].
- [30] H. Moeini et al. “Design studies of the PWO Forward End-cap calorimeter for PANDA”. In: *The European Physical Journal A* 49.11 (2013), pp. 1–22. ISSN: 1434-6001. DOI: 10.1140/epja/i2013-13138-0.
- [31] W. Erni et al. “Technical Design Report for the: PANDA Muon System”. In: (2012). URL: http://www-panda.gsi.de/archive/MuonTDR/Muon_TDR.pdf.
- [32] W. Erni et al. “Technical Design Report for the PANDA Solenoid and Dipole Spectrometer Magnets”. In: (2009). URL: <http://arxiv.org/pdf/0907.0169v1.pdf>.
- [33] M. Galuska et al. “Hough Transform Based Pattern Recognition for the PANDA Forward Tracking System”. In: *51st International Winter Meeting on Nuclear Physics, Bormio* (2013). URL: <http://inspirehep.net/record/1265424/>.
- [34] R. W. Novotny and the PANDA Collaboration. “The Electromagnetic Calorimetry of the PANDA Detector at FAIR”. In: *Journal of Physics: Conference Series* 404.1 (2012), p. 012063. DOI: 10.1088/1742-6596/404/1/012063.
- [35] M. Al-Turany et al. “The FairRoot framework”. In: *Journal of Physics: Conference Series* 396.2 (2012), p. 022001. DOI: 10.1088/1742-6596/396/2/022001. URL: <http://stacks.iop.org/1742-6596/396/i=2/a=022001>.
- [36] Rene Brun and Fons Rademakers. “Root - an object oriented data analysis framework”. In: *Nuclear Instruments and Methods in Physics Research Section A: Accelerators, Spectrometers, Detectors and Associated Equipment* A.389 (1996), pp. 81–86. DOI: 10.1016/S0168-9002(97)00048-X.
- [37] S. Spataro and the PANDA Collaboration. “The PandaRoot framework for simulation, reconstruction and analysis”. In: *Journal of Physics: Conference Series* 331.3 (2011), p. 032031. DOI: 10.1088/1742-6596/331/3/032031.
- [38] K.A. Olive and Particle Data Group. “Review of Particle Physics”. In: *Chinese Physics C* 38.9 (2014), p. 090001. URL: <http://stacks.iop.org/1674-1137/38/i=9/a=090001>.
- [39] Torbjörn Sjöstrand et al. “An introduction to PYTHIA 8.2”. In: *Computer Physics Communications* (Feb. 2015). In Press, Accepted Manuscript. DOI: 10.1016/j.cpc.2015.01.024.
- [40] Steffen A Bass et al. “Microscopic models for ultrarelativistic heavy ion collisions”. In: *Progress in Particle and Nuclear Physics* 41 (1998), pp. 255–369.
- [41] Vincenzo Fracassi. *Private communication*. 2014.

- [42] Fabian Hügging. “Development of a Micro Vertex Detector for the PANDA-Experiment at the FAIR Facility”. In: *Nuclear Science Symposium Conference Record, 2006. IEEE*. Vol. 2. 2006, pp. 1239–1243. DOI: [10.1109/NSSMIC.2006.356068](https://doi.org/10.1109/NSSMIC.2006.356068).
- [43] T. Stockmanns. *Private communication*.
- [44] William R. Leo. “Pulse Signals in Nuclear Electronics”. English. In: *Techniques for Nuclear and Particle Physics Experiments*. Springer Berlin Heidelberg, 1994, pp. 249–255. ISBN: 978-3-540-57280-0. DOI: [10.1007/978-3-642-57920-2_11](https://doi.org/10.1007/978-3-642-57920-2_11). URL: http://dx.doi.org/10.1007/978-3-642-57920-2_11.
- [45] G. Kramberger et al. “Superior radiation tolerance of thin epitaxial silicon detectors”. In: *Nuclear Instruments and Methods in Physics Research Section A: Accelerators, Spectrometers, Detectors and Associated Equipment* 515.3 (2003), pp. 665–670. DOI: [10.1016/j.nima.2003.07.021](https://doi.org/10.1016/j.nima.2003.07.021). URL: <http://www.sciencedirect.com/science/article/pii/S0168900203023441>.
- [46] Thanushan Kugathasan. “Low-Power High Dynamic Range Front-End Electronics for the Hybrid Pixel Detectors of the PANDA MVD”. PhD thesis. Universiti Turino, 2011. URL: <http://dottorato.ph.unito.it/Studenti/Tesi/XXIII/kugathasan.pdf>.
- [47] G. Mazza et al. “The ToPiX v4 prototype for the triggerless readout of the PANDA silicon pixel detector”. In: *Journal of Instrumentation* 10.01 (2015), p. C01042. URL: <http://stacks.iop.org/1748-0221/10/i=01/a=C01042>.
- [48] M. D. Rolo et al. “TOFPET ASIC for PET applications”. In: *Journal of Instrumentation* 8.02 (2013), p. C02050. URL: <http://stacks.iop.org/1748-0221/8/i=02/a=C02050>.
- [49] A. Goerres et al. “A free-running, time-based readout method for particle detectors”. In: *Journal of Instrumentation* 9.03 (2014), p. C03025. URL: <http://stacks.iop.org/1748-0221/9/i=03/a=C03025>.
- [50] R. Schnell et al. “The readout chain for the $\bar{\text{P}}$ ANDA MVD strip detector”. In: *Journal of Instrumentation* 10.02 (2015), p. C02003. URL: <http://stacks.iop.org/1748-0221/10/i=02/a=C02003>.
- [51] Thomas Würschig. “Design optimization of the PANDA Micro-Vertex-Detector for high performance spectroscopy in the charm quark sector”. PhD thesis. Universität Bonn, 2011. URL: http://www-panda.gsi.de/db/thesesDB/TW15-110719_2623a.pdf.
- [52] CiS Forschungsinstitut für Mikrosensorik und Photovoltaik GmbH. “Strahlungsdetektoren”. In: (2015). URL: http://www.cismst.org/fileadmin/user_upload/publikationen/pi_strahlungsdetektoren.pdf.
- [53] Simon M. Sze and Kwok K. Ng. *Physics of Semiconductor Devices, 3rd Edition*. Wiley, 2006. ISBN: 978-0-471-14323-9.
- [54] Louis C. Burmeister. *Convective Heat Transfer, 2nd Edition*. Wiley, 1993. ISBN: 978-0-471-57709-6.
- [55] Kurganov V.A. “Heat Transfer Coefficient”. In: (2011). DOI: [10.1615/AtoZ.h.heat_transfer_coefficient](https://doi.org/10.1615/AtoZ.h.heat_transfer_coefficient). URL: <http://www.thermopedia.com/content/841/>.

- [56] Agilent Technologies. *Agilent E4980A Precision LCR Meter User's Guide Second Edition*. 2006.
- [57] G. L. Bashindzhagyan and N. A. Korotkova. "Determining the Position of an Ionizing Particle in a System of Silicon Microstrip Detectors". In: *Instruments and Experimental Techniques* 49.3 (2006), pp. 331–341. ISSN: 0020-4412. DOI: [10.1134/S0020441206030055](https://doi.org/10.1134/S0020441206030055).
- [58] G. L. Bashindzhagyan and N. A. Korotkova. "The use of capacitive charge division in silicon microstrip detectors". English. In: *Instruments and Experimental Techniques* 49.3 (2006), pp. 318–330. ISSN: 0020-4412. DOI: [10.1134/S0020441206030043](https://doi.org/10.1134/S0020441206030043). URL: <http://dx.doi.org/10.1134/S0020441206030043>.
- [59] H.-G. Zaunick. "Developments toward a Silicon Strip Tracker for the PANDA Experiment". PhD thesis. Universität Bonn, 2012. URL: <http://hss.ulb.uni-bonn.de/2013/3185/3185.pdf>.
- [60] Robert Schnell. "Untersuchungen zu First-Level-Datenauslesestrukturen für den Siliziumstreifendetektor im Mikro-Vertex-Detektor von PANDA". Diploma thesis. Technische Universität Dresden, 2009. URL: http://panda.hiskp.uni-bonn.de/files/Diplomarbeit_RSchnell.pdf.
- [61] L. L. Jones et al. "The APV25 Deep Submicron Readout Chip for CMS Detectors". In: *Proc. 5th Conf. Electronics for LHC Experiments* (1999), pp. 162–166.
- [62] L. L. Jones. "APV25-S1 user guide version 2.2". In: (2001). URL: <http://cds.cern.ch/record/1069892/files/cer-002725643.pdf>.
- [63] M. Becker et al. "FPGA-based readout for double-sided silicon strip detectors". In: *Journal of Instrumentation* 6.01 (2011), p. C01008. URL: <http://stacks.iop.org/1748-0221/6/i=01/a=C01008>.
- [64] Karsten Koop. "FPGA-basierte Auslese von Silizium-Streifen-Detektoren". Diploma thesis. Technische Universität Dresden, 2009. URL: http://panda.hiskp.uni-bonn.de/files/Diplomarbeit_Koop.pdf.
- [65] C. Jacoboni et al. "A review of some charge transport properties of silicon". In: *Solid-State Electronics* 20.2 (Feb. 1977), pp. 77–89. ISSN: 00381101. DOI: [10.1016/0038-1101\(77\)90054-5](https://doi.org/10.1016/0038-1101(77)90054-5). URL: [http://dx.doi.org/10.1016/0038-1101\(77\)90054-5](http://dx.doi.org/10.1016/0038-1101(77)90054-5).
- [66] Frank Hartmann. *Evolution of silicon sensor technology in particle physics*. Springer, 2009. ISBN: 9783540250944. URL: <http://www.worldcat.org/isbn/9783540250944>.
- [67] R. Sarpeshkar, T. Delbrück, and C. A. Mead. "White noise in MOS transistors and resistors". In: *IEEE Circuits Devices Mag.* 9 (6 1993), pp. 23–29. DOI: [10.1109/101.261888](https://doi.org/10.1109/101.261888). URL: <http://ieeexplore.ieee.org/stamp/stamp.jsp?tp=&arnumber=261888>.
- [68] A. B. Kaidalov and P. E. Volkovitsky. "Binary reactions in $\bar{p}p$ collisions at intermediate energies". In: *Zeitschrift für Physik C Particles and Fields* 63.3 (1994), pp. 517–524. DOI: [10.1007/BF01580332](https://doi.org/10.1007/BF01580332). URL: <http://dx.doi.org/10.1007/BF01580332>.

- [69] A. Khodjamirian et al. “How much charm can $\overline{\text{PANDA}}$ produce?” In: *The European Physical Journal A - Hadrons and Nuclei* 48.3 (Mar. 1, 2012), pp. 1–12. ISSN: 1434-6001. DOI: [10.1140/epja/i2012-12031-8](https://doi.org/10.1140/epja/i2012-12031-8). URL: <http://dx.doi.org/10.1140/epja/i2012-12031-8>.
- [70] J. Haidenbauer and G. Krein. “Charm Production in Antiproton-Proton Annihilation”. English. In: *Few-Body Systems* 50.1-4 (2011), pp. 183–186. ISSN: 0177-7963. DOI: [10.1007/s00601-010-0126-4](https://doi.org/10.1007/s00601-010-0126-4). URL: <http://dx.doi.org/10.1007/s00601-010-0126-4>.
- [71] R. Shyam and H. Lenske. “Reaction $\overline{p}p \rightarrow \overline{\Lambda}_c^+ \Lambda_c^+$ within an effective Lagrangian model”. In: *Phys. Rev. D* 90 (1 July 2014), p. 014017. DOI: [10.1103/PhysRevD.90.014017](https://doi.org/10.1103/PhysRevD.90.014017). URL: <http://link.aps.org/doi/10.1103/PhysRevD.90.014017>.
- [72] J. M. Link et al. “Study of the decay asymmetry parameter and {CP} violation parameter in the $\Lambda_c^+ \rightarrow \Lambda \pi^+$ decay”. In: *Physics Letters B* 634.2–3 (2006), pp. 165–172. ISSN: 0370-2693. DOI: [10.1016/j.physletb.2006.01.017](https://doi.org/10.1016/j.physletb.2006.01.017). URL: <http://www.sciencedirect.com/science/article/pii/S0370269306000797>.
- [73] Simone Bianco. “Tracking and vertex reconstruction with the PANDA Micro-Vertex-Detector”. PhD thesis. Universität Bonn, 2013. URL: <http://hss.ulb.uni-bonn.de/2013/3296/3296.pdf>.
- [74] D. Deermann, T. Stockmanns, and J. Ritman. “Characterization of the PANDA MVD Trapezoidal Silicon Strip Sensors and their First Operation in a Proton Beam”. In: *Proceedings of Science* 213.277 (to be published in 2015). URL: http://pos.sissa.it/archive/conferences/213/277/TIPP2014_277.pdf.
- [75] SUSS MicroTec Test Systems GmbH. *ProberBench 6 Command and Interface Reference*, Rel. 6. 34. 2005.
- [76] Inc. Keithley Instruments. *2400 Series SourceMeter User’s Manual*, 2400S-900-01 Rev. K. 2011.
- [77] Ajay Kumar from the Indian Institute of Technology Indore. *Private communication*. September to November 2014.

Acronyms

Notation	Description
$\bar{\text{PANDA}}$	antiProton ANnihilation at DArmstadt
ADC	Analogue-to-Digital Converter
APPA	Atomic, Plasma Physics and Applications
ASIC	Application Specific Integrated Circuit
CAD	Computer-Aided Design
CBM	Compressed Baryonic Matter
CiS	Forschungsinstitut für Mikrosensorik und Photo- voltaik GmbH
CoG	Centre of Gravity
COSY	COoler SYNchrotron
CPT	Charge Parity Time
CR	Collector Ring
DAQ	Data AcQuisition
DIRC	Detector for Internally Reflected Cherenkov Light
DPM	Dual Parton Model
EMC	Electro-Magnetic Calorimeters
FAIR	Facility for Antiproton and Ion Research
FPGA	Field Programmable Gate Array
FS	Forward Spectrometer
FTS	Forward Tracking System
GEM	Gas Electron Multipliers
GPD	Generalised Parton Distributions
GSI	Helmholtz Centre for Heavy Ion Research
GUI	Graphical User Interface
HESR	High Energy Storage Ring

Notation	Description
HL	High Luminosity mode
HR	High Resolution mode
IIC	Inter-Integrated Circuit
LAAPD	Large Area Avalanche PhotoDiodes
MCPoint	Monte Carlo point
MDT	Mini Drift Tubes
MIP	Minimal Ionising Particle
MVD	Micro Vertex Detector
NUSTAR	NUclear STructure, Astrophysics and Reactions
PASTA	$\bar{\text{P}}$ ANDA STRip ASIC
PDG	Particle Data Group
PID	Particle IDentification
POCA	Point Of Closest Approach
PocaQA	Point of closest approach Quality Assurance
PWO	PbWO ₄
QA	Quality Assurance
QCD	Quantum ChromoDynamics
QED	Quantum ElectroDynamics
RESR	Recycled Experimental Storage Ring
RICH	Ring Imaging CHerenkov detector
SCPI	Standard Commands for Programmable Instru- ments
SM	Standard Model
SNR	Signal to Noise Ratio
STT	Straw Tube Tracker
Super-FRS	Superconducting FRagment Separator
TDR	Technical Design Report
TOF	Time-Of-Flight
TOFPET	Time-Of-Flight Positron Emission Tomography
ToPix	Torino Pixel
TS	Target Spectrometer
UrQMD	Ultrarelativistic Quantum Molecular Dynamics
VPTT	Vacuum Photo-TeTrodes

List of Figures

2.1	Overview on FAIR and the location of the different experiments. The existing part of the facility is shown in blue and the new parts which are currently under construction in red [1].	3
2.2	Schematic view on the p-LINAC [5].	5
2.3	Overview on HESR, with position of $\bar{\text{PANDA}}$, electron cooler, stochastic pickups and kickers, and $\bar{\text{p}}$ -injection. Picture taken from [8].	6
2.4	CAD representation of the $\bar{\text{PANDA}}$ detector [9].	7
2.5	This figure shows the accessible mass range of hadrons with antiproton beams in HESR. The necessary antiproton momenta for charmonium spectroscopy, potential charmed hybrids and glueballs, as well as the production of D meson pairs and the production of Σ baryon pairs for hypernuclear studies are indicated in the upper part. Figure taken from [10].	8
2.6	A comparison of positronium and charmonium spectra together with a ratio of their energy scales. Figure taken from [11].	8
2.7	This figure shows the charmonium spectrum. Constituent quark model predictions are indicated by solid lines [12], the observed conventional charmonium states are indicated by shaded lines, and several thresholds are shown by blue dashed lines. Newly discovered states, which are likely to have charm content, are placed in the column of their most probable quantum number assignment and are represented with red dots. The last column contains states, which may be exotic and do not fit to a $q\bar{q}$ quantum number assignment. Figure taken from [13].	9
2.8	The spectrum of D_s mesons with predictions shown as solid lines [12] and dotted lines [15]. The points represent experimental data for old measured states (black) and newly discovered states (red). Figure taken from [13].	10
2.9	The spectrum of glueball masses predicted by lattice QCD calculations [18].	12
2.10	CAD rendering of the target spectrometer. Figure taken from [9].	13
2.11	Schematic of the STT and its profile. Figures taken from [25].	15
2.12	Schematic of the components inside a GEM station. Figure taken from [26].	16
2.13	Schematic view on the EMC. Figure taken from [29].	17
2.14	Schematic view on $\bar{\text{PANDA}}$ with the muon system. Figure taken from [31].	18
3.1	An overview on the MVD, which shows its mechanical holding structure and sensor layers [41].	23

3.2	Mean specific energy loss per unit distance for different absorber materials, the momentum scale on the x-axis is scaled by the particle mass so that a combined measurement of p and $\frac{dE}{dx}$ can be used for PID. Figure taken from [38].	26
3.3	Distribution of the energy loss per unit distance for pions with a momentum of 500 MeV/c in silicon, calculated for several thicknesses of the absorber. Figure taken from [38].	27
3.4	Corner segments of the p-side from two sensor's are shown in this figure. Parts of the p-side strips, p-side bias ring, and guard rings can be seen. The two pictures were extracted from layout files given by CiS who also produced the sensors which are described in Chapter 4.1. a) with poly-silicon resistors, b) with punch through method.	30
3.5	Scheme of a hybrid pixel sensor. Graphic taken from [28].	31
3.6	Dual threshold scheme for PASTA. The lower threshold provides a fast time stamp and the higher threshold validates a hit and gives the second point for the ToT measurement [50].	32
3.7	The two MVD frame halves are mounted on the central frame separately with a three point fixation. The central frame includes fixation points to the beam pipe (a), target pipe (b), and rail system (c). Figures taken from [28].	33
3.8	Schematic of a larger pixel disc with its cooling tubes and connections to the depression system. Figure taken from [28].	34
4.1	Trapezoidal strip sensor geometry. Sizes are in mm. Figure taken from [51].	35
4.2	A picture of the probestation and the dedicated test board, which were used for sensor characterisation.	36
4.3	Photograph of a prober needle.	37
4.4	The corner of a sensor and a prober needle viewed with the videotracker from the probestation PC.	37
4.5	A picture of the LCR meter and the source meter used for the measurements in this chapter.	38
4.6	Schemes of the separation boxes for the LCR meter and source meter.	39
4.7	Leakage current of sensor 1 from wafer 8 (322635-8.1). The orange measurement was done in Jülich with the probestation and the purple measurement was done by CiS.	40
4.8	Stable sensor temperature as a function of the leakage current at room temperature.	41
4.9	Sensor capacitance at 100 kHz measured for bias voltages from 0 V to 160 V.	42
4.10	Capacitance per strip length of the p-side strips, measured with the probestation at 1 MHz	43
4.11	A section of the test board layout, with two contact lines for the majority of strips and some pads for the connection of individual strips. The blue area indicates the sensor.	43
4.12	Leakage current of sensor 1 from wafer 7 (321589-7.1). The orange measurement was done in Jülich with the test board and the purple measurement was done by CiS.	44
4.13	Sensor capacitance at 200 kHz measured for bias voltages from 0 V to 250 V.	45
4.14	Capacitance per strip length, measured above full depletion (150 V) with 200 kHz.	45

4.15	Capacitance per strip length. The red entries show measurements between individual p-side strips and the majority of n-side strips. The blue entries show measurements between individual n-side strips and majority of p-side strips.	46
4.16	In this figure the capacitance of an individual p-side strip shown in red and the capacitance of an individual n-side strip is shown in blue.	47
5.1	Simulated η distributions for two-strip signals for the trapezoidal and rectangular sensors. The colours indicate the number of entries per combination of η and charge, and the highest charge range contains all entries with a charge deposition greater or equal to 50,000 electrons. Figures c) and d) show the η distribution integrated over the charge deposition.	51
5.2	η to inter-strip position relations according to Equation 5.2. The colours indicate the inter-strip position from the centre of the left strip (0 or purple) to the centre of the right strip (1 or red). The white space indicates combinations of η and q that did not occur. The highest energy range contains all entries with energies greater or equal to 50,000 electrons.	52
5.3	These plots show the uniform distribution of the hit locations.	52
5.4	Inter-strip position distribution of two-strip signals separated for different energy ranges. The highest bin in the y-axis contains all entries with energies greater or equal to 50,000 electrons.	53
5.5	Plots of the η distributions after performing a correction due to the inhomogeneously distributed two-strip signals. Figures a) and b) show the η distribution per charge deposition range. Figures c) and d) show the η distribution integrated over the charge deposition.	54
5.6	Plots of the η to inter-strip position relations, after performing a correction.	54
5.7	η to inter-strip position relation together with the reconstructed relation (pink) and the linear relation which represents the reconstruction with the CoG method (brown), shown for two ranges of deposited charge and both sensor geometries. The plots on the left are for the trapezoidal sensors, and the plots on the right are for the rectangular sensor. The plots on the top are for the range of deposited charge from 22,501 to 25,000 e^- , and the plots on the bottom are for the range of deposited charge from 42,501 to 45,000 e^-	55
5.8	Inter-strip position distribution for two-strip clusters in the cluster charge range from 25,000 to 27500 e^-	56
5.9	Inter-strip position distribution for two-strip clusters with a simulated front end chip clock frequency of 300 MHz.	57
5.10	These plots show the spatial resolution in tangential and radial direction of the trapezoidal sensors for different combinations of p- and n-side cluster sizes. The numbers in the legend give the sizes of the two clusters that have been combined to a hit point. For better comparison all graphs in this figure are normalised to an area of 1.	58
5.11	These plots show the total resolution of the trapezoidal and rectangular sensors for different combinations of p- and n-side cluster sizes. The numbers in the legend give the sizes of the two clusters that have been combined to a hit point. All graphs in this figure are normalised to an area of 1.	58

6.1	Photographs of the mechanical setup for the test measurements.	62
6.2	Schematic of the readout chain.	62
6.3	The APV25's data output scheme. Figure taken from [62].	63
6.4	The APV25's data output, digitised and recorded over several frames.	64
6.5	A schematic view on the pitch adaptor with the matching pitch size for the APV25 chips at the top and the matching pitch size for the sensor at the bottom.	65
6.6	Photograph of the supply board with labels for the main components. The two white components on the dashed line are two of the transformer. Two more transformers are on the back side of the supply board.	67
6.7	Energy loss per strip signal measured in ADC channels.	68
6.8	Energy loss per cluster measured in ADC channels. a) and b) show the cluster energy vs the strip channel, while c) and d) show the projection on the y-axis together with a red line that indicates the software threshold.	69
6.9	Energy loss of two-strip clusters measured in ADC channels.	70
6.10	Energy loss per strip signal measured in ADC channels.	70
6.11	Distribution of the time difference between trigger and signal for p- and n-side. . .	71
6.12	Correlation between p- and n-side energy loss and ghost hit discrimination. a) shows the correlation and the position of the applied cut. b) shows the ghost hit discrimination.	72
6.13	The hitmap of the sensor, without (left) and with (right) data selection.	73
6.14	The output of a single APV25 for several frames. (a) p-side, (b) n-side.	74
6.15	Energy loss per cluster measured in ADC channels. a) and b) show the cluster energy vs the strip channel, normalised to the number of entries per channel. c) and d) show the most probable value of energy loss for each channel.	76
6.16	Energy loss per ADC channel for each strip channel, (left) p-side and (right) n-side. .	76
6.17	Energy difference between p- and n-side versus the energy sum of p- and n-side. . .	78
6.18	The absolute (left) and relative (right) energy resolution of sensor hits.	78
6.19	The measured noise in ADC channels during the time of measurement with the trapezoidal sensor.	79
6.20	Corrected noise in ADC channels.	81
6.21	This figure shows the signal to noise ratio for the p- and n-sides of the sensor. . . .	81
6.22	The mean SNR for different reverse bias voltages shown in red for the p-side and in blue for the n-side.	82
6.23	Probability functions $P_p(\eta, q)$ and $P_n(\eta, q)$ that indicate the probability for a two-strip cluster to be measured as a one-strip cluster by colour.	84
6.24	Contributions to the η distribution that have been lost due to noise. This result has been calculated by $N(\eta, q) \frac{P(\eta, q)}{1-P(\eta, q)}$	85
6.25	Plots of the corrected η distributions $N_{corr.}(\eta, q) = N(\eta, q) + N(\eta, q) \frac{P(\eta, q)}{1-P(\eta, q)}$ for p- and n-side.	85
6.26	η to inter-strip position relation for the p- and n-side. The colour scale indicates the inter-strip position, with purple representing the centre of the left strip and red the centre of the right strip. White areas are combinations of η and cluster charge that have not occurred.	86
7.1	The simulated Λ_c and $\bar{\Lambda}_c$ particles are isotropically distributed in their centre of mass system.	88

7.2	The simulated Λ_c and $\bar{\Lambda}_c$ particle's transverse to longitudinal momentum distributions.	88
7.3	The simulated decay length distributions of the Λ_c and $\bar{\Lambda}_c$ in the laboratory frame.	89
7.4	The simulated decay length distributions of the Λ and $\bar{\Lambda}$ in the laboratory frame. . .	89
7.5	This figure shows the proper time distributions of the Λ_c and $\bar{\Lambda}_c$, and the Λ and $\bar{\Lambda}$.	90
7.6	Distributions of the transverse momenta of the different decay products plotted versus their longitudinal momenta.	90
7.7	Distributions of the total number of detector hits per track, shown separately for each particle type.	92
7.8	Systematic offset of the energy reconstruction per particle. The red dashed line marks the position of no systematic offset for better orientation.	92
7.9	Statistical error of the energy reconstruction per particle.	93
7.10	Momentum distributions of the four final state particle types in the centre of mass frame.	94
7.11	Reconstructed mass distributions of the Λ and $\bar{\Lambda}$. The purple lines indicate the cut position for accepted candidates.	95
7.12	Probability distribution of the kinematic fits on the Λ and $\bar{\Lambda}$ candidates. The red line indicates the cut position for accepted candidates.	95
7.13	PocaQA of Λ and $\bar{\Lambda}$. The red line at PocaQA = 0.1 cm indicates the cut position for accepted candidates.	96
7.14	The squared ratio of accepted signal candidates divided by the ratio of accepted background candidates as a function of the PocaQA cut value. (left) Λ candidates, (right) $\bar{\Lambda}$ candidates.	97
7.15	Vertex resolution of Λ and $\bar{\Lambda}$. The resolution in z direction is shown on the x-axis and the resolution in the xy-plane is shown on the y-axis.	98
7.16	Comparison between the vertices from signal and DPM events of the Λ and $\bar{\Lambda}$ candidates.	98
7.17	The squared ratio of accepted signal candidates divided by the ratio of accepted background candidates as a function of the Λ and $\bar{\Lambda}$ vertex position. (left) Λ candidates, (right) $\bar{\Lambda}$ candidates.	99
7.18	The longitudinal to transverse momentum distributions of the daughter particles of reconstructed Λ_c candidates. The red ellipse shaped lines indicate the cut positions for accepted candidates.	100
7.19	The longitudinal to transverse momentum distributions of the daughter particles of reconstructed Λ_c candidates. The red ellipse shaped lines indicate the cut positions for accepted candidates.	100
7.20	Vertex resolution of Λ_c and $\bar{\Lambda}_c$. The x-axis shows the Monte Carlo z vertex position minus the reconstructed z vertex position, and the y-axis shows the distance in the plane perpendicular to the z-axis between the Monte Carlo vertex position and the reconstructed vertex position.	101
7.21	PocaQA of Λ_c and $\bar{\Lambda}_c$	101
7.22	Λ_c and $\bar{\Lambda}_c$ candidate PocaQA distribution for DPM events.	102
7.23	Systematic offset of the energy reconstruction per particle. Shown for all particles that survived the cuts for Λ_c or $\bar{\Lambda}_c$ candidates.	103
7.24	Statistical error of the energy reconstruction per particle. Shown for all particles that survived the cuts.	104

7.25	Distributions of the transverse momentum of the reconstructed Λ_c and $\bar{\Lambda}_c$ plotted versus their longitudinal momentum.	104
7.26	Resolution of the reconstructed mass and momentum of the Λ_c and $\bar{\Lambda}_c$	105
7.27	Missing mass of events with found Λ_c candidate (left) and found $\bar{\Lambda}_c$ candidate (right).	105
7.28	(left): Momentum and energy difference to initial momentum and energy of combined Λ_c and $\bar{\Lambda}_c$ events. (right): Missing mass distribution of combined Λ_c and $\bar{\Lambda}_c$	106
7.29	This figure shows results after using the Pnd4CFitter on the candidates. (left): Momentum and energy difference to initial momentum and energy of combined Λ_c and $\bar{\Lambda}_c$ events. (right): Missing mass distribution of combined Λ_c and $\bar{\Lambda}_c$	106
7.30	Λ_c and $\bar{\Lambda}_c$ candidate mass distribution for DPM events.	108
7.31	Signal to background mass peak of Λ_c and $\bar{\Lambda}_c$ for four possible total cross sections of $\bar{p}p \rightarrow \bar{\Lambda}_c \Lambda_c$	109
A.1	Overview on the software GUI for the sensor characterisation measurements.	113
A.2	Leakage current and capacitance of sensor 321589-6.1.	115
A.3	Leakage current and capacitance of sensor 322635-7.1.	115
A.4	Leakage current and capacitance of sensor 321589-8.1.	116
A.5	Leakage current and capacitance of sensor 321589-5.2.	116
A.6	Leakage current and capacitance of sensor 321589-6.2.	116
A.7	Leakage current and capacitance of sensor 321589-7.2.	117
A.8	Leakage current and capacitance of sensor 321589-8.2.	117
A.9	Leakage current and capacitance of sensor 322635-5.2.	117
A.10	Leakage current and capacitance of sensor 322635-7.2.	118
A.11	Leakage current and capacitance of sensor 322635-8.2.	118
A.12	Leakage current and capacitance of sensor 322635-9.2.	118
B.1	Deposited energy per strip for the p- (left) and n-side (right).	119
B.2	Energy deposition per cluster for the p- (left) and n-side (right). The red line in the p-side cluster energy distribution indicates the data selection cut position.	120
B.3	Time difference between the trigger and the first strip signal above threshold. p-side (left), n-side (right).	120
B.4	Correlation between p- and n-side energy loss and ghost hit discrimination. (a) p- to n-side correlation with cut position, (b) ghost hit discrimination.	121
B.5	The hitmap of the sensor, without (left) and with (right) data selection.	121
B.6	The SNR for p- and n-side.	122
B.7	Channel correlation of the p-side.	123
C.1	Systematic offset of the momentum reconstruction per particle. The red dashed line marks the position of no systematic error for better orientation.	125
C.2	Statistical error of the momentum reconstruction per particle.	126
C.3	Systematic offset of the momentum reconstruction per particle. Shown for all particles that survived a cut on the total momentum of Λ_c or $\bar{\Lambda}_c$ in their centre of mass frame as well as a cut on the mass of Λ or $\bar{\Lambda}$	126
C.4	Statistical error of the momentum reconstruction per particle. Shown for all particles that survived the cuts.	127

D.1	Cross section predictions for $\bar{p}p \rightarrow \bar{\Lambda}_c \Lambda_c$. (a) [70], (b) [71].	129
D.2	Cross sections for $p\bar{p} \rightarrow \Lambda \bar{\Lambda}$ and $p\bar{p} \rightarrow K^+ K^-$, and predictions for the cross sections of $\bar{p}p \rightarrow \bar{\Lambda}_c \Lambda_c$ and $p\bar{p} \rightarrow D^0 \bar{D}^0$, (a) [68]. A cross section prediction for $\bar{p}p \rightarrow \bar{\Lambda}_c \Lambda_c$, (b) [69].	130

Acknowledgements

At this place I want to show my gratitude to all the people that accompanied me during the last years.

Firstly, to professor James Ritman who took me into the Jülich group, made this work possible, and supported me on the way.

Secondly, to Tobias Stockmanns who was a very helpful mentor with an open door at all times.

Furthermore, to all of the IKP members who made great colleagues in professional as well as personal matters. Special thanks go to the $\bar{\text{P}}$ ANDA group: Albrecht, André, Andreas, Elisabetta, Frank, Harout, Huagen, Jim, Lu, Ludo, Qiang, Simone, and Tobias. Without you, it wouldn't have been even half of the fun!

Thanks also go to everyone who helped during the test beam. Particularly to the Bonn/Gießen group with Hans, Karsten, Max, and Robert.

I want to thank Thomas Sefzick for helping me with the probestation when it was broken.

I am happy that I always had the support of my family.

And last but not least, I want to thank my dear Cheng for encouraging me and for being the wonderful person she is.

Lebenslauf

Persönliche Daten

Name: Dariusch David Deermann
Geburtsdatum: 25.12.1985
Geburtsort: Siegburg

Schulbildung

07/1992-06/1996 Gemeinschaftsgrundschule Birk
07/1996-06/2005 Gymnasium Lohmar
Allgemeine Hochschulreife

Studium

10/2005-06/2011 Studium der Physik an der Universität Bonn
Diplomarbeit: „Charakterisierung von
Siliziumstreifendetektoren“

Promotion

10/2011-03/2015 Promotion im Fach Physik an der Universität
Bochum in Kooperation mit dem Institut für
Kernphysik am Forschungszentrum Jülich
Doktorarbeit: „Development of the $\overline{\text{PANDA}}$
MVD Trapezoidal Sensors and a Feasibility
Study of the $p\overline{p} \rightarrow \Lambda_c \overline{\Lambda}_c$ Reconstruction“